Phénomènes dépendants du spin dans des structures à un puits quantique CdMnTe à modulation de dopage de type-n

Francisco Jose Teran

Spin dependent phenomena in n-type modulation doped CdMnTe quantum well structures

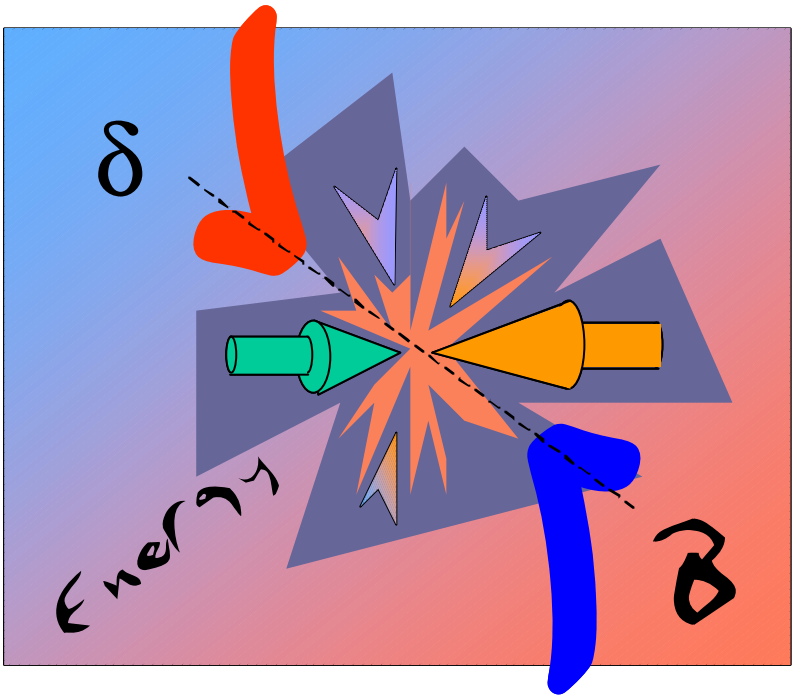

Francisco José TERAN GARCINUÑO

Grenoble High Magnetic Field Laboratory
CNRS-MPI/FKF

November 2001

Université Joseph Fourier –Grenoble 1

THESE

Présentée par

Francisco José TERAN GARCINUÑO

Pour obtenir le titre de

Docteur de l'Université JOSEPH FOURIER-GRENOBLE 1

Discipline : Physique

(Arrêtés ministériels du 5 juillet 1984 et du 30 mars 1992)

Phénomènes dépendants du spin dans des structures à un puits quantique CdMnTe à modulation de dopage de type-n

Soutenue le 23 novembre 2001 devant la commission d'examen :

President : *Joël Cibert*

Raporteurs: *Carlos Tejedor*
Denis Scalbert

Jacek Kossut

Directeur de thése : *Marek Potemski*

Thèse préparée au sein du

Laboratoire des Champs Magnétiques Intenses
CNRS-MPI/FKF Grenoble

I libri non sono fatti per
crederci, ma per essere
sottoposti a indagine.
Di fronte a un libro non
dobbiamo chiederci cosa
dica ma cosa vuole dire.

Guillermo de Baskerville

en "Il nome della Rosa"
de **Umberto Eco**

Remerciements

Il y a beaucoup de gens que j'aurais envie de remercier après avoir réussi à donner une forme de 'thèse' à mes quatre ans en France.

J'aimerais commencer par remercier *Marek Potemski* à qui je donne ma plus sincère reconnaissance pour ses doses de motivation et sa disponibilité quotidiennes, pour ses ressources et discussions infinies et sa patience, qui m'ont permis de déployer mes ailes bien au-delà des aires de la physique, pendant la durée de cette aventure alpine.

Je remercie *Joël Cibert* de m'avoir fait l'honneur de présider le jury de cette thèse ainsi que pour toutes les discussions scientifiques dont je me suis enrichi. Je remercie aussi *Carlos Tejedor* et *Denis Scalbert*, rapporteurs et *Jacek Kossut* d'avoir accepté de siéger dans ce jury. A tous, je tiens à exprimer ma gratitude pour l'attention portée au manuscrit de ce travail.

Je remercie M.*Peter Wyder* et M.*Gerard Martinez* de m'avoir accueilli au Laboratoire des Champs Magnétiques Intenses et pour le *S*outien offert dès ma première année de thèse.

Rien de ce qui est écrit ici n'aurait été possible sans la précieuse aide de *Duncan K. Maude* qui a toujours mis à ma disposition son **pack** de patience et de savoir-faire en expériences de magnéto-transport ainsi que pour rendre plus ***anglais*** mon espagnol scientifique. La même chose pour *Alia K. Hassan* avec qui j'ai été capable d'extraire la résonance des "pauvres" ions de Mn^{2+} des échantillons que *Grzegorz Karczewski* et *Tomasz Wojtowicz* nous ont fabriqués. **Dziekuje bardzo** à ces deux derniers pour le temps qu'ils ont passé à nous fournir **sur commande** une telle quantité d'échantillons. **Dziekuje bardzo** aussi à *Tomasz Andrearczyk* et *Jan Jaroszynski*, responsables de la **grâce** des contacts pour les expériences de transport. Merci aussi à Andy Sachrajda pour la lecture méticuleuse de ce manuscrit.

On oublie trop souvent qu'un laboratoire n'est rien sans des techniciens de grand talent. Je souhaite manifester mon entière gratitude à *Herbert Krath, Hans Dresler, Claude Mollard, Robert Pankow* et *Jürgen Spitznagel* dont les compétences, la disponibilité et la gentillesse ont été responsables de mes

résultats de magnéto-optique. Je tiens aussi à remercier *Jean Florentin* pour sa disposition et ses compétences pour la construction de l'insert RPE. Merci aussi à *Peter van der Linden* pour son *aide cryogénique* aux expériences **resistives**. Qu'ils en soient remerciés.

Je voudrais remercier *Luis Viña* de m'avoir montré où était la porte d'entrée du monde de la physique et pour les collaborations **UAM temps-résolu** grâce auxquelles j'ai profité des soirées longues et 'détendues' avec *M.D. Martin, Lola*, 'sino fuera por esos ratos...'.

J'ai une reconnaissance spéciale aussi pour *Pawel Hawrylak, Allan Mac Donalds, Andrzej Wysmolek, Roman Stepniewski* et *Zbysek Wilamowski*, mon grand-pére scientifique, pour le temps, toujours chargé, qu'ils m'ont dédié et les discussions desquelles je me suis enrichi.

Merci aussi à *Ronald Cox, Vincent Huard, Arek Wojs* et *Piotr Kossacki,* pour les nombreuses discussions, conseils et les bons moments que nous avons eu à Grenoble ou en conférences.

Cette thèse a bénéficié des expériences en spectroscopie infrarouge réalisées par *Marcin Sadowski* au début de ma thèse ainsi que des expériences de spectroscopie inter bande réalisées par *Ye Chen*. Merci pour l'**échange** des points **de vue**!

Par ailleurs, un grand MERCI à *Gislaine Meneroud*, lumière dans la jungle administrative, et *Sébastien Buisson*, gladiateur informatique.

Last but not least, j'ai une pensée émue pour tous mes camarades de chambrée : *Fred Thouvenin, Barbaros Ozylmal, Isabelle Claus, Patrick Dupré* et les soirées autour de l'imprimante, *Stef Jullian, Eric Chap, Fred Dupont, Clement 'Hombre' Faugeras, David Plantier,* ***illy****-Desrat, Lolito Rubaldo, Nono Pouydebasque, Jef de Marneffe, Daniel Kremer, Nicolas Freytag, David Schaeffer, Olivier Estibals, Anne Laure Barra, Carole Toia, Cédric Bardot, Markus Weiss* et *Clemence Koerdt*.

Una especial mención dedico a Daniel Huertas*,* Javier Román *y* Diego Lázaro *al pensar que siempre podré contar con ellos.*

A mi familia

Grenoble, le 23 novembre 2001

Francisco José Terán Garcinuño

Chapter 5

Chapter 6

Table of contains

Chapter 7

Introduction

Spin related phenomena have acquired renewed interest during the last few years, mostly due to the possibility of using the spin degree of freedom of electrons, nuclei, or artificial molecules for creating novel solid state devices that may lead to entirely new technologies.

Most of these future applications require a precise control of the different spin states. This implies a good understanding of the fundamental physics related to the spin properties, in particular, the properties of interacting spins of a different nature, such as for example, localized nuclear spins and delocalized carrier spins in metals or magnetic moments and delocalized carrier spins in magnetic semiconductors. The description of the exchange interaction in such hybrid systems involves a very large number of particles. The problem can be described by averaging the exchange effects and considering the interaction as an effective mean field induced by the ensemble of one type of spins on the second type of spin.

An example of an extensively studied system is the '*hyperfine*'-coupled spins of nuclei and of electrons in metals [Abragam]. The spin exchange interaction significantly modifies the intrinsic properties of both electronic and nuclear subsystems. The nuclear spin polarization produces the so-called "Overhauser shift"[1] first observed for the electron spin resonance of lithium [Guérdon-1959]. The nuclear spins induce an effective field felt by the electron spin, which increases the energy separation of the electron spin levels. The inverse effect[2] induced by the effective magnetic field due to spin polarization of the *electrons* leads to the so-called Knight shift of the nuclear spin resonance [Knight-1949]. The Knight shift represents a correction of 0.1% to the position of the nuclear magnetic resonance.

[1] Albert Overhauser was the first who theoretically predicted the influence of the nuclear polarization on electron spin excitations in 1953 [Overhauser-1953].

[2] W.D.Knight observed for first time in a shift of the nuclear magnetic resonance of divers metals.

A second example of a contact interaction between delocalized and localized spins, is the coupling between the free carriers and the localized magnetic moment of ions, e.g. transition metals (Fe, Mn, Cr). Both electronic and magnetic subsytems coexist in hybrid materials where a semiconductor lattice hosts a dilute number of ions with a large magnetic moment, such as Mn^{2+}. These compounds form a branch of the semiconductor materials often referred as diluted magnetic semiconductors (DMS) from which, CdMnTe is a representative example.

In DMS materials, the exchange interaction occurs between the conduction and valence ***s-p*** band electrons and the electrons from the ***3d*** shell of the magnetic ions. The polarization of the localized magnetic spins is already large at low fields which consequently amplifies the effective magnetic field that the spins of band electrons "*feel*". The modified energy separation of the electronic spin states analogous to the "Overhauser" shift, is referred to as the *giant Zeeman splitting*. In semiconductor nanostructures, the effective Zeeman splitting can be tuned by varying the Mn concentration, the sample dimensionality, the Mn temperature or the magnetic field [Furdyna-2000], and can reach values up to 100 meV for conduction band electrons in CdMnTe. The modification of the electronic spectrum by the ***sp-d*** exchange interaction is strongly reflected in the magneto-optical and the magneto-transport properties of DMS material [Furdyna-1988b].

The reciprocal effect of carriers on the Mn properties is much subtler than for the case of hyperfine coupling with nuclei. The effective magnetic field felt by a single Mn spin depends not only on the number of the carriers but also on whether the free carriers are electrons or holes [Story-1996]. In the case of holes the interaction effects are strong enough to induce a carrier-mediated magnetic ordering of the paramagnetic Mn spins [Haury-1997]. The role of the hole spin in the long distance interaction of Mn spins opens up prospects not only for tailoring the magnetic properties of Mn spins but also addressing the issue of the origin of the ferromagnetism [Dietl-2000]. In the case of electrons, these effects are less pronounced and their influence only slightly affects the magnetic properties of the Mn.

However, both the *giant Zeeman splitting* and the *Knight shift*, can successfully be described within a mean-field approach [Gaj-1978, Ferrand-2001] based on an average of the exchange interaction between the delocalized electrons and the randomly distributed localized magnetic moments. Within this approach, there are two consequent cases, which merit especial attention.

One case corresponds to the particular situation where the energy of the electronic and the magnetic excitations coincide $E^{e}_{Z} = E^{Mn}_{Z}$. Since both electronic and Mn spin excitations are excitation modes of the crystal, one

should expect a resonant appearance of perturbation effects, which may imply a description beyond the mean-field theory.

The second case corresponds to the cancellation of the Mn effective magnetic field by an external magnetic field. Since both, exchange and external, magnetic fields have opposite signs, they can compensate each other leading to a total effective magnetic field *felt* by the electron spin equal to zero. Therefore, this implies a vanishing of the energy separation between two electronic spin levels, i.e. $E^e_Z=0$. A resonant perturbation may also be expected when the energy of both electronic spin states is equal.

So far, there has been no systematic investigations of these effects, although they represent an important test for understanding the spin properties in DMS. The aim of this thesis is to verify the possible appearance of resonant perturbative effects at $E^e_Z = E^{Mn}_Z$ and at $E^e_Z=0$, in order to investigate possible discrepancies of the mean-field theory at these extreme limits. For such reasons, an exhaustive experimental study of the magnetic, transport and optical properties of doped CdMnTe quantum well structures have been performed. The results are presented in this thesis which is organized as follow.

In chapter 1, we briefly review the fundamental magnetic and electronic properties of CdMnTe, the material employed for the sample fabrication. The basis of the transport (quantum Hall effect) and optical properties (infrared, interband and Raman scattering spectroscopy) of 2D systems in a magnetic field is presented in a general form.

In chapter 2, a description of the different Cd(Mn)Te quantum well structures studied in this thesis is presented. In chapter 3, a preliminary characterization of doped magnetic (CdMnTe) and non-magnetic (CdTe) quantum well structures has been performed by means of cyclotron resonance measurements. The magnetic field dependence of cyclotron resonance allows us to determine the value of the effective electron mass for our samples.

In chapter 4, the magneto-transport properties of a 2DEG confined in a CdMnTe quantum well are investigated. In the low magnetic field region a strong influence of the giant Zeeman splitting is observed. A characteristic-beating pattern in the amplitude of the Shubnikov-de Haas oscillations in the magneto-resistance allows us to establish a model for describing the effective Zeeman energy. This model qualitatively describes the transport properties at low fields. The transport properties in the high magnetic field region where the effective Zeeman splitting is expected to vanish are then presented. An extensive study of the resistance minima evolution associated with filling factors $\nu=1,3,5$ indicates the existence of different regions in magnetic field where a opening of the spin gap is observed. Notably, we present evidence for Landau level anticrossing.

In chapter 5, the magnetic subsystem of Mn^{2+} ions is probed. We study the influence of free carriers in the quantum Hall regime on the magnetic properties of the Mn^{2+} ions by means of resistively detected electron paramagnetic resonance (EPR) in magnetic fields up to ~8 T. This study reveals a different influence of the carrier presence in low and high magnetic field regions. Whereas the mean-field theory reasonably describes the observed carrier effects on the Mn properties at low magnetic fields, it is not sufficient to account for the observations around 8T, where the electronic and magnetic excitation energies are comparable. A model based on the anticrossing of electronic and magnetic spin excitations is proposed in order to describe our experimental findings.

In chapter 6, spin flip processes in CdMnTe quantum well structures associated with the electronic and magnetic spins are investigated using inelastic light scattering. The magnetic field dependence of the electronic spin flip Raman shift complements our transport results related to the modeling of the electronic spin splitting, in particular under conditions of vanishing Zeeman energy where a non-zero spin gap is clearly observed. At the same time, the Raman spectroscopy supports the model of spin excitation anticrossing suggested by the EPR studies in chapter 5.

In chapter 7, two distinct optical spectroscopy studies are presented. In the first part, we use optical spectroscopy to probe the magnetic properties of our structures. The determination of the magnetic susceptibility at finite magnetic fields from luminescence studies of doped CdMnTe quantum wells at very low temperatures (down up to 75 mK) and very low magnetic fields ($B<$ 0.135 T) is presented. The method allows us to probe the Mn^{2+} ions located in the quantum well but is however not very accurate due to the large broadening of the emission lines. In the second part, we present a more detailed investigation of the optical properties, in particular, the evolution of the emission (PL) and absorption (PLE) with the electron density at zero field and under magnetic fields. The excitonic effects are found to persist for electron densities up to ~$6x10^{11}cm^{-2}$ when free particle-like transitions are also observed in our samples. Finally, the general conclusions of this thesis are presented.

Chapter 1

Fundamentals

Introduction

This introductory chapter reviews several topics which are necessary to facilitate the presentation and understanding of the original results discussed in the following chapters. We begin with a presentation of the basic information concerning the materials used during the investigations, summarizing their electronic and magnetic properties. We introduce the effect of spatial confinement and discuss the electronic states in "quasi-two-dimensional" semiconductor structures. The essential physics of a two-dimensional electron gas (2DEG) in a quantizing magnetic field is also presented. Finally, we discuss how the unique properties of a 2DEG in a quantizing magnetic field are reflected in the typical electrical transport and optical experiments.

1.1 Diluted magnetic semiconductors

Diluted Magnetic Semiconductors (DMS) are a branch of semiconducting compounds in which part of the constituent cations are replaced by ions with large magnetic moments such as Fe, Eu or Mn. Most of the DMS studied involve Mn ions incorporated in II-VI compounds [Furdyna-1988a] where the Mn is a neutral impurity. DMS are of great interest because they offer the interesting opportunity of integrating magnetic properties in semiconductor structures. These hybrid materials, such as, for example, CdMnTe which is our material of interest, can be considered as being composed of two subsystems: the localized magnetic ions with large spins and electronic states of the semiconductor host. Coupling between these subsystems have made DMS the focus of intense research activity providing many examples of interesting and exciting new effects.

1.1.1 Band structure of CdMnTe

Cadmium Telluride is a wide gap semiconductor (E_g = 1.606 eV at T=4.2 K [Furdyna-1988b]) which crystallizes in a zinc-blend structure (see Figure 1.1). Cd and Te ions are each located on one of the two face centered cubic (fcc) sub-lattices, shifted with respect to each other by a quarter of the cell diagonal. The crystallization is due to the tetrahedral ($s\text{-}p^3$) bonding which involves two valence ***s*** electrons of the group II element and six valence ***p*** electrons of the group VI element in order to form the conduction and valence band, respectively. The band extremes are located at the first Brillouin zone, Γ point (see insert of Fig.1.1). The conduction band Γ_6 is doubly degenerate (J=1/2). In the valence band, the spin-orbit coupling splits the quadruple Γ_8 (J=3/2) from the doublet Γ_7 (J=1/2) ($\Delta_{\Gamma 7\text{-}\Gamma 8}$ = 0.93eV). In CdMnTe, the Mn^{2+} ions randomly substitute the Cd ions. The zinc-blend structure is maintained for Mn concentration smaller than 77%. Beyond this point, the crystal phase is a mixture between zinc-blend and wurzite [Galazka-1980]. The gap of $Cd_{1-x}Mn_xTe$ in zinc blend structure changes approximately linearly with manganese composition [Lee-1984], from 1.606 to 2.73 eV at T=4.2 K (see Figure 1.2), which permits band structure engineering for the fabrication of good quality heterostructures [Datta-1985].

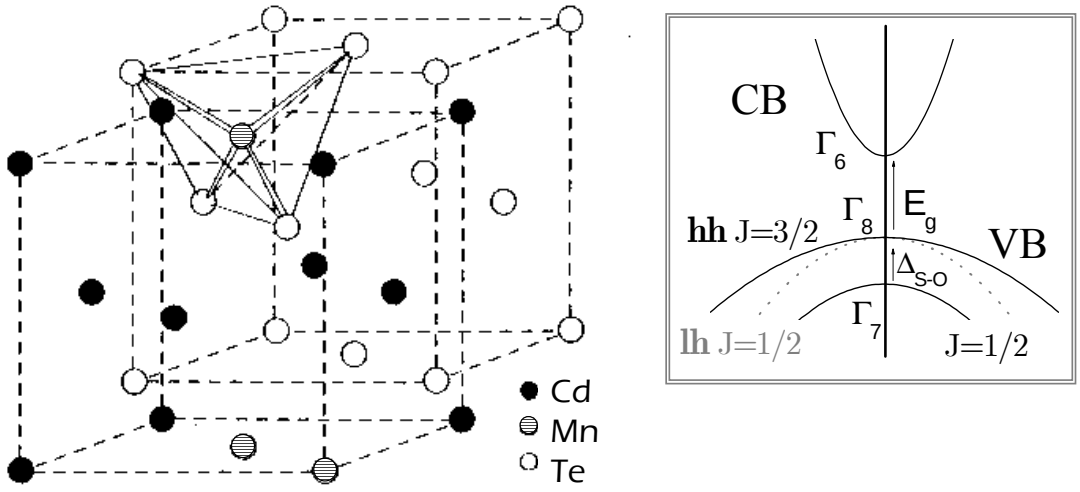

Figure 1.1.Zinc-blend crystal structure of $Cd_{1-x}Mn_xTe$. Conduction and valence band scheme indicating the band symmetry and the spin-orbit splitting.

1.1.2 Magnetic properties of CdMnTe

In a II-VI host lattice, the Mn^{2+} ions substitute group II cations and the isolated Mn^{2+} ion has a $3d^5$ configuration with the spins of the 3d electrons aligned in the ground state according to Hund's rules. Therefore, Mn^{2+} spin has, as a ground state, the six fold degenerate spin-multiplet ($^6S_{5/2}$) with S=5/2 and L=0. At finite manganese concentrations, the interaction between Mn^{2+} ions plays an important role. Studies of $Cd_{1-x}Mn_xTe$ mono-crystals have shown that many phases can be induced by tuning the Mn^{2+} concentration or the temperature: isolated ions (paramagnetic phase), clustering (pairs, triplets) [Shapira-1990] or magnetic ordering (spin glass or anti-ferromagnetic phase) [Galazka-1980] (see inset of Fig.1.2). Different Mn^{2+} concentrations imply distinct magnetic properties and distinct spin-spin interactions: the dipole-dipole interactions at long range and an anti-ferromagnetic super-exchange interaction at short range [Larson-1990]. The clustering of spins due to this anti-ferromagnetic interaction is responsible for the magnetic phases and for many interesting magnetic phenomena.

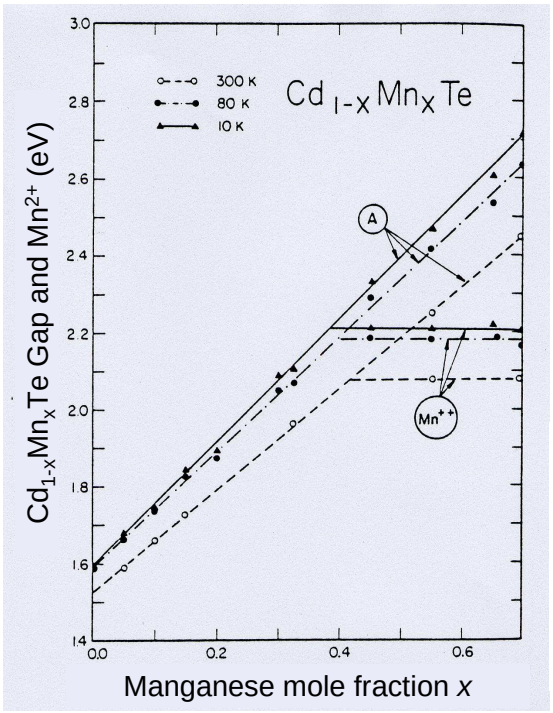

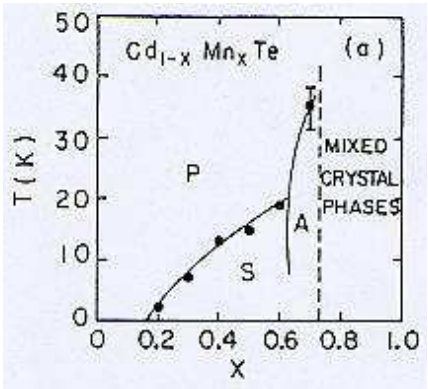

Figure 1.2. Left) Dependence of the energy gap on the Mn molar fraction [Lee-1984]. Above : Magnetic phase diagram for $Cd_{1-x}Mn_xTe$.
Legend: A: Anti-ferromagnetic, S: Spin-glass and P: Paramagnetic. [Galazka-1980].

In II-VI DMS, free carriers can be incorporated independently of the manganese doping. This provides the possibility of studying magnetic properties of the Mn^{2+} spin in a controlled free carrier environment. The reciprocal ***sp-d*** exchange interaction between the electronic spins and the magnetic spin makes it possible to consider the carrier presence (concentration) as a new axis of the magnetic phase diagram.

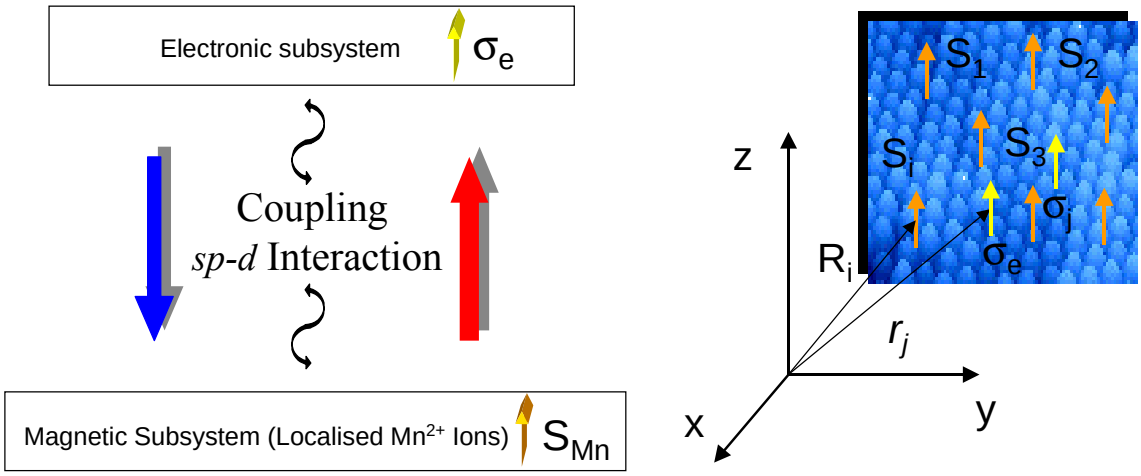

Figure 1.3. Left) Schematic diagram of the sp-d coupling between the electronic (conduction states) and the magnetic subsystem. Right) Schematic representation of the spatial distribution of carrier(σ_j) and magnetic (S_i)spins.

1.1.3 sp-d exchange interaction

When considering DMS it is convenient to distinguish two different subsystems. The first subsystem referred to as electronic includes the semiconductor band states (s-type conduction band and p-type valence band states). The second subsystem referred to as magnetic includes the localized d-states of Mn^{2+} ions. Both subsystems are coupled via an ***sp-d*** exchange interaction, as shown schematically in Figure 1.3. Such a coupling modifies the "intrinsic" properties that each system would have separately. Modifications of the electronic subsystem induced by the presence of the magnetic subsystem lead to very prominent effects which are relatively easy to observe. However, the changes of the properties of the magnetic system induced by the presence of band carriers (electron or holes) are subtler effects. This "asymmetry" is essentially due to the fact that typical DMS materials contain many more Mn^{2+} ions than free carriers. In a realistic CdMnTe sample it is probably difficult to

exceed the concentration of 10^{19} cm^{-3} of electrons (or holes) whereas a 1% concentration of manganese ($5x10^{20}$ cm^{-3} of Mn^{2+} ions) is easily achievable.

The investigations of the mutual interaction between band electrons and the 3d electrons of the substitution magnetic ions is responsible for many unique properties observed in DMS and have been rekindled by the interesting possibility of tuning the ***sp-d*** interaction by nano-structure engineering [Furdyna-2000, Crooker-1995, Haury-1997, Prechtl-2000, Mackh–1996].

There exist a large number of studies devoted to the ***sp-d*** interaction that probe the electronic systems but investigations focused on magnetic subsystems are much less common. For example it has been known for decades that the introduction of few percent of manganese in II/VI semiconductor dramatically changes their optical [Gaj-1978] as well as their transport properties [Jaczynski-1978]. Studies of magnetic subsystems affected by the presence of free carriers in semiconductor materials have been invoked only recently [Story-1986, Haury-1997].

The ***sp-d*** exchange interaction is described by the Kondo Hamiltonian:

$$\mathcal{H}_K = -\sum_{i,j} J(r_j - R_i)\vec{S}_i \cdot \vec{\sigma}_j \qquad \text{Eq.1.1}$$

where $\vec{S}_i$ is the spin operator for a Mn^{2+} site at the position R_i (see Fig.1.3) and $\vec{\sigma}_j$ is the spin operator of a carrier j in the position r_j. The sum is over all electrons and Mn^{2+} ions. $J_{i,j}(r_j\text{-}R_i)$ is the Kondo operator describing the exchange interaction. In the case of localized Mn spins and delocalized electrons such an operator can be approached by $J_{i,j}(r_j\text{-}R_i) \approx J_{sp\text{-}d}\delta_{ij}(r_j\text{-}R_i)$ where $J_{sp\text{-}d}$ is the carrier-Mn exchange coupling constant and $\delta_{ij}(r_j\text{-}R_i)$ is the Dirac delta function at the Mn site R_i.

However, the exchange coupling between a carrier j and a Mn i spin is usually described by a spin Hamiltonian H_{ij} in which the orbital part is averaged by the evaluation of the matrix elements between the orbital functions. Since the total wavefunction of the carrier is described by $\Phi = \psi(\vec{r})\chi$, i.e the product of orbital $\psi(\vec{r})$ and spin χ terms, the spin Hamiltonian H_{ij} takes the form:

$$\mathcal{H}_{ij} = \left\langle \psi_j \middle| \mathcal{H}_{sp-d} \middle| \psi_j \right\rangle = -j_{i,j}\vec{S}_i \cdot \vec{\sigma}_j \qquad \text{Eq.1.2}$$

where the exchange is now parameterized by the integral $j_{i,j}$ expressed by:

$$j_{i,j} = J_{sp-d}\left\langle \psi_j \left| \delta(r_j - R_i) \right| \psi_j \right\rangle = J_{sp-d} \cdot \left| \psi_j(R_i) \right|^2 = \\ = \left| \psi_j(R_i) \right|^2 \left\{ J_{sp-d} \cdot N_0 \right\} \cdot \Omega \qquad \text{Eq.1.3}$$

where $N_0=1/\Omega$ is the number of the elementary cells of volume Ω [volume units]. The value of the exchange integral $j_{i,j}$ is proportional to the amplitude of the electronic wave function which strongly depends on whether carriers are delocalized ($j_{i,j}$ reduced) or localized ($j_{i,j}$ increased). Positive (negative) values of $j_{i,j}$ corresponds to ferromagnetic (antiferromagnetic) coupling for the case of conduction electrons (valence holes). The dimension of the exchange integral $j_{i,j}$ is [energy], whereas $J_{sp\text{-}d}$ is [energy·cm^3]. The product $\{J_{sp\text{-}d}N_0\}$ is usually defined, in order to describe the exchange value for a given material. In the case of CdMnTe, the values of the ***s-d*** and ***p-d*** exchange coupling constant are $J_{s\text{-}d}\ N_0 = \alpha N_0 = 220$ meV and $J_{p\text{-}d}\ N_0 = \beta\ N_0 = -880$ meV [Gaj-1978].
Finally, the spin Hamiltonian of the whole system can be expressed in the Heisenberg form as:

$$\mathcal{H}_{sp-d} = -\sum_{i,j} j_{i,j} \vec{S}_i \cdot \vec{\sigma}_j \qquad \text{Eq.1.4}$$

*1.1.3.1 Effects of **sp-d** interaction on the **sp** electronic states: "Giant Zeeman splitting"*

In order to investigate how the electronic states can be modified by the presence of Mn^{2+} ions we consider a single $s(p)$ free electron(hole) with spin $\vec{\sigma}$, interacting with an ensemble of Mn^{2+} ions. Within this single electron approach, the corresponding spin Hamiltonian expressed by Eq.1.4 is now reduced to the sum over all lattice sites occupied by Mn^{2+} spins:

$$\mathcal{H}_{sp-d} = -\sum_{i}^{all\ Mn} j_i \vec{S}_i \cdot \vec{\sigma} \qquad \text{Eq.1.5}$$

For a free carrier interacting with a large number of Mn^{2+} spins, the exact location of each Mn^{2+} ion is unknown and calculating all exchange integrals j_i is impossible. However, the fact that the electronic wave function is very extended, so that the carrier sees a large number of Mn^{2+} ions at any one time

allows us to introduce a mean field approximation. We can therefore replace $\vec{S}$ by a thermal average $\langle \vec{S} \rangle$ taken over all Mn^{2+} sites. For a paramagnetic system, applying a magnetic field B in the z-direction, $\langle \vec{S} \rangle = \langle S_Z \rangle \vec{z}$ where $\vec{z}$ is the unit vector along z. With this assumption we have that the single electron spin Hamiltonian can be written as:

$$\mathcal{H}^{e}_{sp-d} = -\sigma_Z \sum_i j_i \langle S_z \rangle \qquad \text{Eq.1.6}$$

A second approach is possible, again because the electronic wave function spans a large number of lattice sites. We can replace the sum over all Mn sites R_i by a sum over every site of the lattice R in which a fraction of the Mn spin x_{eff} is attributed, where x_{eff} is the effective Mn concentration which interacts with the single carrier. Thus, Eq1.3 simplifies to give the sum over all the exchange integrals j_i to:

$$\left\langle \sum_i j_i \right\rangle = \{J_{sp-d} \cdot N_0\} \cdot x_{eff} \cdot \Omega \qquad \text{Eq.1.7}$$

Using, Eq.1.7, we can rewrite the effective ***sp-d*** Hamiltonian for a single carrier as:

$$\mathcal{H}^{e}_{sp-d} = -\{J_{sp-d} N_0\} x_{eff}\ \sigma_Z \langle S_Z \rangle \qquad \text{Eq.1.8}$$

where $\langle S_Z \rangle$ is proportional to the magnetization but has the opposite sign and can be well described by a (modified) Brillouin function $B_{5/2}(B,T)$ [Gaj-1978]:

$$\langle S_Z \rangle = - S_0 B_{5/2} (g^{Mn} \mu_B B / k_B(T+T_0)) \qquad \text{Eq.1.9}$$

where $S_0 = 5/2$, μ_B is the Bohr magneton and T_0 an effective temperature reflecting a long range residual anti-ferromagnetic interaction. Thus, the enhancement of the spin splitting for conduction band electrons due to the ***s-d*** exchange interaction is expressed by:

$$E^{e}_{s-d} = \{\alpha N_0\} x_{eff} S_0 B_{5/2} (g^{Mn} \mu_B B / k_B(T+T_0)) \qquad \text{Eq.1.10}$$

This term when added to the standard Zeeman term results in the total spin splitting for conduction band electrons:

$$E_Z = g^e \mu_B B + E^e_{s\text{-}d} = g^{*e} \mu_B B \qquad \text{Eq.1.11}$$

with

$$g^{*\,e} = (g^e + S_0 x_{eff} \alpha N_0 \cdot B_{5/2} (g^{Mn} \mu_B B / k_B(T+T_0)) / \mu_B B) \qquad \text{Eq.1.12}$$

where the last term is responsible for the so-called "giant Zeeman splitting". The exchange term $E^e_{s\text{-}d}$ can reach a maximum value of 100meV for x_{eff} =17% in bulk CdMnTe materials. Beyond this value, the anti-ferromagnetic d-d interaction effectively reduces the magnetization.

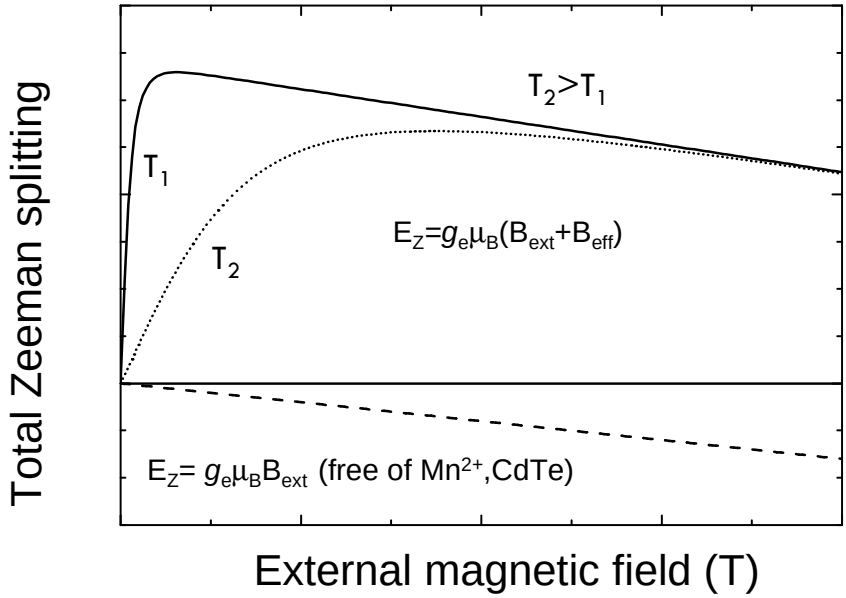

Figure 1.4. Magnetic field dependence of the total electronic Zeeman splitting in $Cd_{1-x}Mn_xTe$ for two temperatures. Electronic Zeeman splitting for CdTe (dash line).

The characteristic magnetic field dependence of the spin splitting for the conduction band electrons in CdMnTe is plotted in Figure 1.4. Due to the ***s-d*** term, the total Zeeman splitting is non-linear and strongly temperature dependent in contrast to the case of non-magnetic semiconductors. The total Zeeman energy results from the competition between two terms: the ***s-d*** term,

which is positive, and the standard Zeeman term, which has the opposite sign (negative g-factor in CdTe [Sirenko-1997]). At low fields, the spin splitting is mostly determined by the ***s-d*** term. The conventional Zeeman term becomes important at higher fields. The fact that the standard and the ***s-d*** contributions to the Zeeman term have opposite signs for the conduction band electrons in CdMnTe, creates the unique opportunity to investigate various phenomena under the specific condition of a vanishing g-factor (see, for example, chapter 4 and 6).

*1.1.3.2 Effects **s-d** interaction on **3d** electronic states: "Knight shift"*

In order to investigate the effect of free carriers on the magnetic subsystem, we consider a single Mn^{2+} ion, which interacts with free conduction electrons with spin $\vec{\sigma}_j$. As in the previous section, the corresponding spin Hamiltonian is now reduced to the sum over all lattice sites occupied by electron spins:

$$\mathcal{H}_{sp-d} = -\sum_{j}^{all\ e} j_j \vec{S} \cdot \vec{\sigma}_j \qquad \text{Eq.1.13}$$

The mean field approach can also be used in order to simplify the treatment of Eq.1.13. Similarly to the procedure described before, within the mean field approach, the effect of the ***s-d*** interaction on a single Mn^{2+} ion can therefore be expressed by:

$$\mathcal{H}_{s-d} = -S_Z \langle \sigma_Z \rangle \sum_j j_j \qquad \text{Eq.1.14}$$

The last term in Eq.1.14 implies an integration of the electronic wave function of all electrons on the Mn site at the R position. This term can be averaged as follows:

$$\left\langle \sum_j j_j \right\rangle = \alpha \cdot \left\langle \left| \psi_j(R) \right|^2 \right\rangle N_e \qquad \text{Eq.1.15}$$

where N_e is the number of electrons and $\Psi_j(R)$ is the orbital part of the electronic wavefunction and $\alpha = J_{s\text{-}d}/N_0$.

When the electrons are confined in a quantum well of width L_Z, populating

only the first electric subband, the evaluation of Eq.1.13 proceeds as follow. The wavefunction $\Psi_j(R)$ of an electron distribution in a sample of the area a, is described by:

$$\Psi(r)=\frac{1}{\sqrt{a}}e^{i\left(k_x x+k_y y\right)}\varphi(z) \qquad \text{Eq.1.16}$$

where $\varphi(z)$ is a normalized wavefunction in the confinement (z) direction of the first electric subband. Now, the total ***s-d*** exchange coupling is proportional to:

$$\left\langle \sum_j j_j \right\rangle = \frac{\alpha}{a}\cdot\left|\varphi(z)\right|^2 N_e \qquad \text{Eq.1.17}$$

This expression can be rewritten in terms of the sheet electron density n_e, considering $N_e = n_e/a$. Finally, the ***s-d*** energy of the single Mn^{2+} ion due to the exchange interaction with the 2D electrons is expressed by:

$$\begin{aligned} E^{Mn}{}_{s-d} &= -m_S\left\langle\sigma_Z\right\rangle\alpha\left|\varphi(z)\right|^2 n_e = \\ &= -m_S\left\langle\sigma_Z\right\rangle\{\alpha N_0\}\left|\varphi(z)\right|^2\frac{n_e}{N_0} \end{aligned} \qquad \text{Eq.1.18}$$

where N_0 is again the number of cells per unit volume and m_S is the projection of the magnetic quantum number corresponding to the projection of the z-component of the magnetic moment of the Mn spin S=5/2.

The energy term given by Eq.1.17 has to be added to the Zeeman energy corresponding to the energy separation distance between the split levels of the 3d electrons under magnetic field in absence of free carriers. The presence of a magnetic field in the z-direction lifts the degeneracy of the 3d state of Mn^{2+}. This state splits into six components with different magnetic moment projections m_S. The energies of each split level given by $E_{Mn} = m_S\, g^{Mn}\mu_B B_Z$ are schematically shown in Figure 1.5. The total spin splitting of Mn^{2+} ion interacting with free carriers can now be expressed as follows:

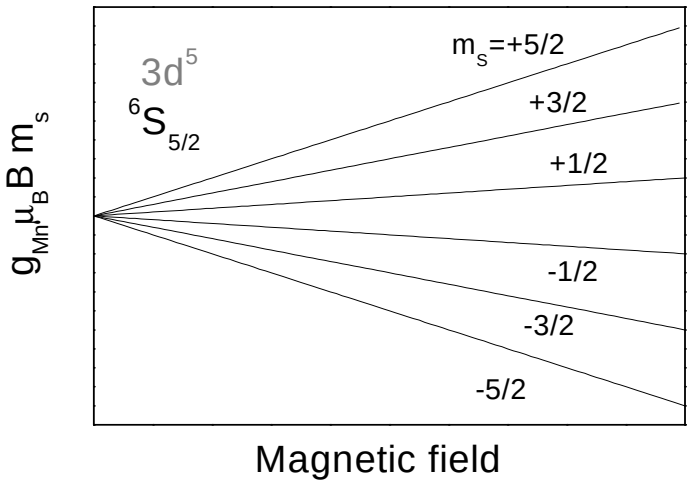

Figure 1.5. Magnetic field dependence of the electronic 3d-shell states of the isolated Mn^{2+} ion. The different levels represent distinct spin states m_S for the paramagnetic Mn^{2+} ion.

$$E_{Mn} = m_S\, g^{Mn} \mu_B B_Z + E^{Mn}{}_{s\text{-}d}$$

$$= g^{Mn} \mu_B (B_Z + B_k)\, m_S \qquad \text{Eq.1.19}$$

with

$$B_K(z) = -\frac{\langle \sigma_Z \rangle \{\alpha N_0\} |\varphi(z)|^2}{g^{Mn} \mu_B} \frac{n_e}{N_0} \qquad \text{Eq.1.20}$$

where B_K is the so-called "Knight shift" by analogy to the well known carrier effect on the position of nuclear magnetic resonance in metals [Knight-1949]. B_K is a function of the position in the z-direction, but for a given subband it is common for each electronic state k_x, k_y. Experimentally, the Knight shift of paramagnetic spins was first observed in Mn doped bulk lead compounds by Story [Story-1996]. The Knight shift in DMS quantum well structures will be discussed in Chapter 5.

The mean value of the "Knight shift" induced by 2D electrons can be estimated by assuming $|\varphi(z)|^2 = 1/\ L^*_z$, where L^*_z is the effective width of the well. Thus:

$$B_K(z) = -\frac{\{\alpha N_o\}}{g^{Mn}\mu_B}\frac{n_e}{L^*_Z N_o}\langle\sigma_Z\rangle \qquad \text{Eq.1.21}$$

To estimate the order of magnitude of the expected shifts we have calculated that for $n_e = 5.9\text{x}10^{11}\text{cm}^{-2}$ electrons occupying a single electric subband in a CdMnTe ($g^e = -1.6$, $\alpha N_0 = +220$ meV), $L^*_Z = L_z/2 = 5$ nm, and the lattice parameter of CdTe 6.48Å, we obtain $B_K = 746$ G for the case of a complete spin polarization of electrons in the lowest spin level $m_\sigma = -1/2$. The expected values of B_K are small but nevertheless accessible by, for example, EPR experiments.

1.2 Confinement effects on the electronic states

With the development of sophisticated growth techniques such as molecular beam epitaxy (MBE), it is now possible to fabricate semiconducting structures whose size is comparable to the atomic scale. The properties of such structures become size and shape dependent. The ability of modern technologies to make solid-state systems in which such conditions are realized opens up opportunities to investigate systems with reduced dimensionalities [Chemla-1993]. With a suitable combination of ultrathin layers of different semiconducting materials it is possible to realize nano-structures with quantum well energy profiles. In such structures the carrier motion is constrained in a plane and its energy spectrum is governed by quantum mechanics. The improvements resulting from modulation doping techniques [Dingle-1978] enabled structures to be made containing high mobility carriers that form a 2-D metallic system [Störmer-1979]. In the following, we briefly review the effects of the spatial confinement on the energy bands and the corresponding density of states in thin semiconductor layers. Finally, the quantization of the motion of two-dimensional electrons in a magnetic field will be described.

1.2.1 Quantum confinement and density of states

Electrons forming a 2DEG move freely along a plane (x,y) while their perpendicular motion (z) is restricted. Such a situation is achieved for carriers subjected to a potential barrier $V_C(z)$. New states arise due to the spatial confinement associated with the quantization in the z-direction forming subbands E_i (H_i) for the conduction (valence) band (see Figure 1.6). For low electron concentrations, at low temperatures and/or for deep potential wells the

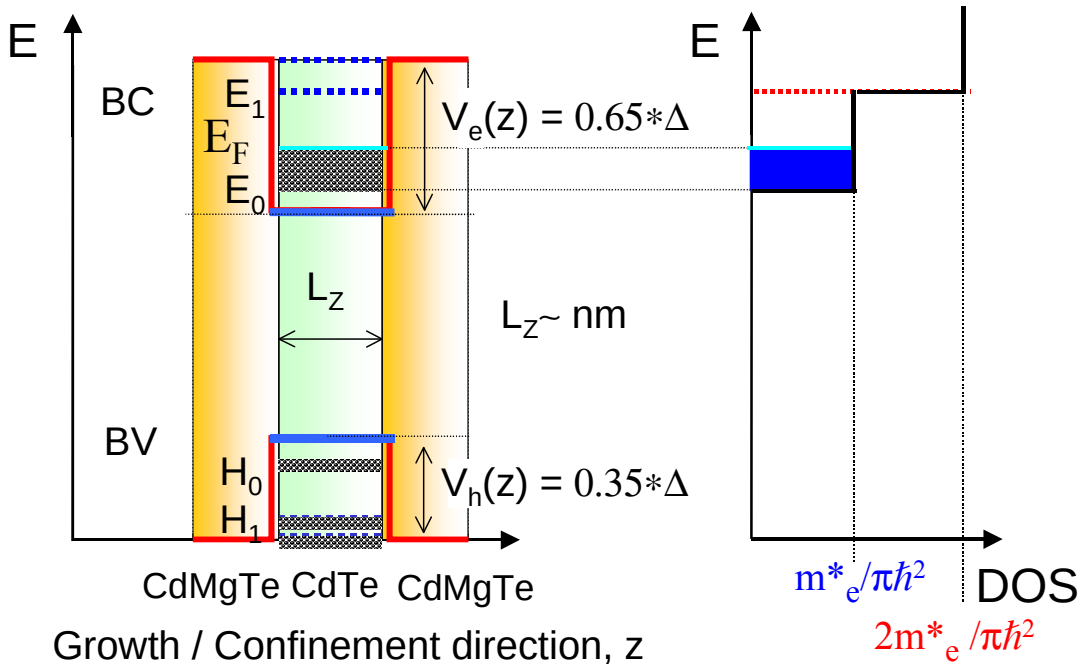

Figure1.6: Left) Representative schema of the energy levels in type I quantum well structures. Δ is the difference of CdTe and CdMgTe gap values. Right) Energy dependence of the density of states for the conduction band.

electrons occupy the lowest subband and their wave function tends to zero in the confinement direction. Thus, the motion of a electron with an effective mass m^*_e confined in a V(z) well potential is determined by the Hamiltonian:

$$\mathcal{H}_c = \frac{\vec{p}^2}{2m^*e} + V(z) \qquad \text{Eq.1.22}$$

As the potential well only acts in the z-direction, the electron is free to move in the x-y plane. The eigen-values resulting from the solution of the Hamiltonian are:

$$E(k_X, k_Y, i) = \frac{\hbar^2 (k_X^2 + k_Y^2)}{2m^*_e} + E_i \qquad \text{Eq.1.22}$$

where E_i are the size quantized states, the electric subbands of the well potential. For a symmetric, infinite quantum well of width L_z they are given by:

$$E_i = \frac{\hbar^2 \pi^2}{2m^*_e L_Z{}^2}(i+1)^2 \qquad \text{Eq.1.23}$$

The conduction and valence bands are structured in electric subbands with index i=0,1,2,..where i=0 is the ground state.

The density of states (DOS) for each subband does not depend on the energy E, contrary to the 3D case [Ando-1982]. In the ideal 2D case, each subband equally contributes to the total DOS, which can be written as a sum of the respective subband DOS:

$$\rho^{2D}(E) = \frac{m^*}{\pi\hbar^2}\sum_i \theta(E - E_i) \qquad \text{Eq.1.24}$$

where θ(x) is the Heavyside function. The energy dependence of the DOS is shown in Fig.1.6.

1.2.2 Landau quantization

The laws of electrodynamics establish that a charged particle under a magnetic field $\vec{B} = \vec{\nabla} x \vec{A}$, experiences a Lorentz force. Classically, the charged particle executes an orbital motion. The quantum mechanical description of this motion implies that the energy of the orbit of radius ℓ_B is quantized.

The momentum of a charged particle under a magnetic field is given by:

$$\vec{p} = \vec{p}_{kin} + \vec{p}_{field} = \hbar\vec{k} - \frac{e\vec{A}}{c} \qquad \text{Eq.1.25}$$

where $\vec{p}$ is the momentum operator $\vec{p} = -i\hbar\vec{\nabla} = \hbar\vec{k}$, e is the electron charge and c is the speed of light.

Considering an electron, with mass m^*_e moving with a momentum k in a plane x-y under the presence of a magnetic field perpendicular to the plane B_Z, the Hamiltonian which describes the motion is given by:

$$\mathcal{H} = \frac{1}{2m_e^*}\left(\hbar\vec{k} - \frac{e\vec{A}}{c}\right)^2 + V(z) + H_Z \qquad \text{Eq.1.26}$$

where H_Z denotes the carrier spin interaction term. Within the Landau gauge, the potential vector is $\mathbf{A}=(0,B_Z x,0)$ and Eq.1.26 is separable into electric and magnetic field parts which simplifies the calculation of the eigen-values :

$$E^{i,N} = E_N + E_i + E_Z \qquad \text{Eq.1.27}$$

where E_Z is the Zeeman energy, E_i are the electric subband position Eq.1.23 and E_N comes from the orbital motion in the x-y plane.

$$E_N = (N + 1/2)\hbar\omega_c \qquad \text{Eq.1.28}$$

where $\omega_C = eB_Z/m^*_e$ is the cyclotron energy and N is the quantizing index which takes integer values 0,1,2,...where N=0 corresponds to the lowest energy state.

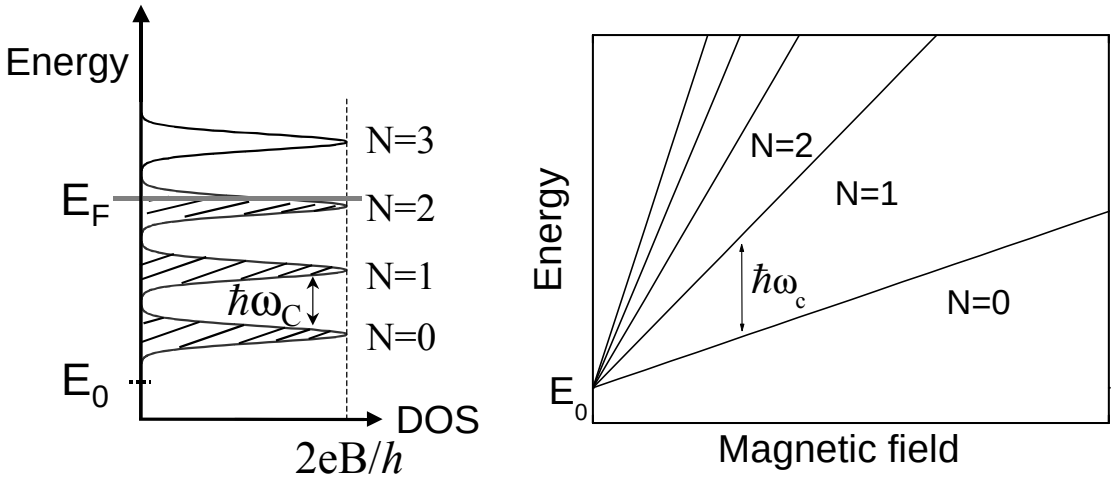

Figure 1.7. Left) Occupation of Landau Levels at a given magnetic field B. Right) Magnetic field dependence of the Landau levels. Spin splitting is neglected in the figures.

Whereas at zero field, the motion is only quantized in the z-direction of the confinement potential: $k_Z \rightarrow \pi(i+1)^2/L_Z$, on applying a magnetic field, the motion in the plane x-y is also quantized: $(k_x^2 + k_y^2)/2m^*_e \rightarrow (N+1/2)\hbar\omega_C$. Consequently, the zero field 2D density of states condenses for each electrical subband E_i into a series of equally spaced δ-functions centered at the Landau energy E_N and separated by $\hbar\omega_C$, as schematized in Figure 1.7. The degeneracy D of each Landau level is the same and varies with the magnetic field as:

$$D = eB_Z/h \qquad \text{Eq.1.29}$$

assuming that the spin degeneracy is lifted. In real systems, impurities and disorder lead to a broadening of the otherwise discrete Landau levels. The exact shape of broadened Landau levels is difficult to establish. It is commonly assumed that Landau level broadening is proportional to the square root of the magnetic field. This assumption is strictly correct for the case of broadening caused by short range potential fluctuations due to randomly distributed impurities [Ando-1974a].

An important concept in the physics of 2DEGs in quantizing magnetic fields is the distinction between localized and delocalized states, introduced for the first time by Aoki et al. [Aoki-1977]. This concept is crucial for understanding quantum Hall phenomena. Delocalized states are those which contribute to electronic transport and are located in the center of the broadened Landau levels. The localized states which are in the tails of Landau levels do not contribute to the longitudinal conductivity but are responsible for the appearance of quantum Hall plateaus in the Hall resistance.

At low temperatures, the single particle states are populated by electrons up to the Fermi level E_F respecting the Pauli exclusion principle. In the 2D case, E_F is proportional to the carrier density n_e as $E_F=n_e\pi\hbar^2/m^*_e$.

Under a magnetic field, it is convenient to define a filling factor given by:

$$\nu = \frac{hn_e}{eB_Z} \qquad \text{Eq.1.30}$$

The filling factor ν corresponds to the number of occupied spin Landau levels. Landau quantization is the origin of various phenomena with an oscillatory behaviour which is periodic in the inverse magnetic field. The induced oscillations in the position of the Fermi energy are essential for many interesting effects (see Figure 1.8). Since the degeneracy of each Landau level increases with the magnetic field, more and more electrons occupy states in the lower Landau levels resulting in a depopulation of the upper, partially occupied level. If the latter is completely empty the Fermi energy drops down by an amount $\hbar\omega_C$ (neglecting broadening and spin splitting), into the subsequent Landau level which now starts to be partially empty. At integer filling factors, the Fermi energy lies in the middle of a gap separating the highest occupied level from the level just above, recovering its zero field value (the dash line).

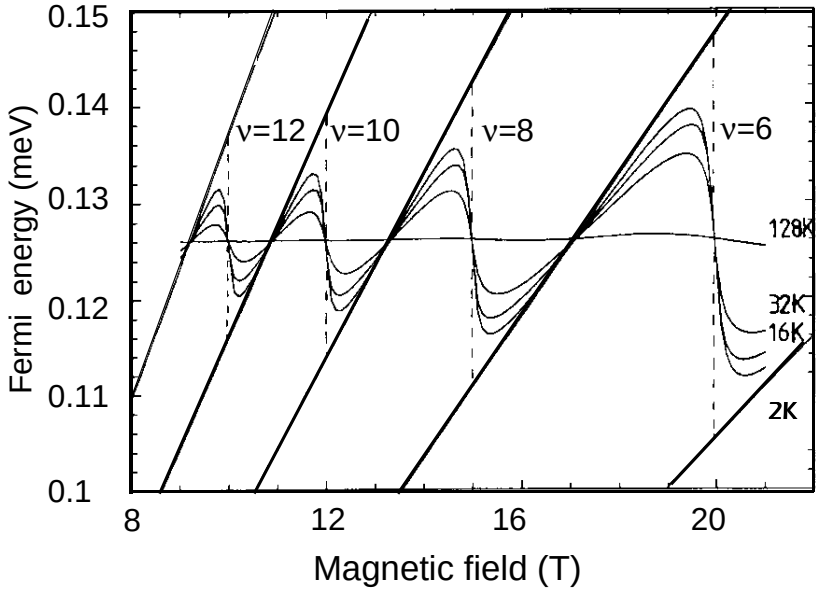

Figure 1.8. Illustration of the magnetic field dependence of Fermi energy position for different temperatures.

1.2.3 Spin polarization of 2D electrons

Once the Landau levels are spin resolved, i.e. the Zeeman energy is much larger than the level broadening, the spin polarization is given by the normalized difference of the number of electrons in spin up and down Landau levels:

$$\mathcal{P} = \frac{n_\uparrow - n_\downarrow}{n_\uparrow + n_\downarrow} \qquad \text{Eq.1.31}$$

Since the occupation of spin-up and spin-down levels changes with magnetic field, the spin polarization will change as well. At odd filling factors, $\mathcal{P}$ will be non zero and its value is $1/\nu$ in the ideal case. At even filling factors there are the same number of occupied spin-up and -down levels, and therefore $\mathcal{P}=0$ (see Figure 1.9). Within this simple picture, $\mathcal{P}=1$ at any fields above the filling factor one. It should be noted that the physics of spins of 2D electrons in the regime of the quantum Hall effect has recently become of a renewed interest.

These investigations have been stimulated by the possibility of the formation of complex spin-texture like ground states and the existence of

specific charged excitations known as "Skyrmions"[Barret-1995, Sondhli-1993, Fertig-1994]. The electron-electron exchange interaction is essential for QHE spin physics. This interaction is responsible for the fact that the thermodynamical spin gaps at odd filling factors are usually bigger that the "bare Zeeman gap" [Nicholas-1988]. This interaction is also responsible for the quantum Hall ferromagnetism. Ferromagnetism can occur since at odd filling factors any small perturbation of the system may lead to the opening of the spin gap (spontaneous spin polarization). Thus, even if the bare Zeeman splitting, $g^e\mu_B B$, is zero one expects, at odd filling factors the spin gap to be opened by electron-electron interactions. The expected "exchange gaps" ($\Delta=\frac{e^2}{\varepsilon}\sqrt{\frac{e\pi B}{2\hbar}}$ for $\nu=1$ [Bychkov–1981, Kallin-1984]) can be huge compared to the bare Zeeman splitting. The experimental values are known to be very sensitive to the disorder present in the sample. The effects of electron-electron interactions are therefore difficult to observe in low mobility samples.

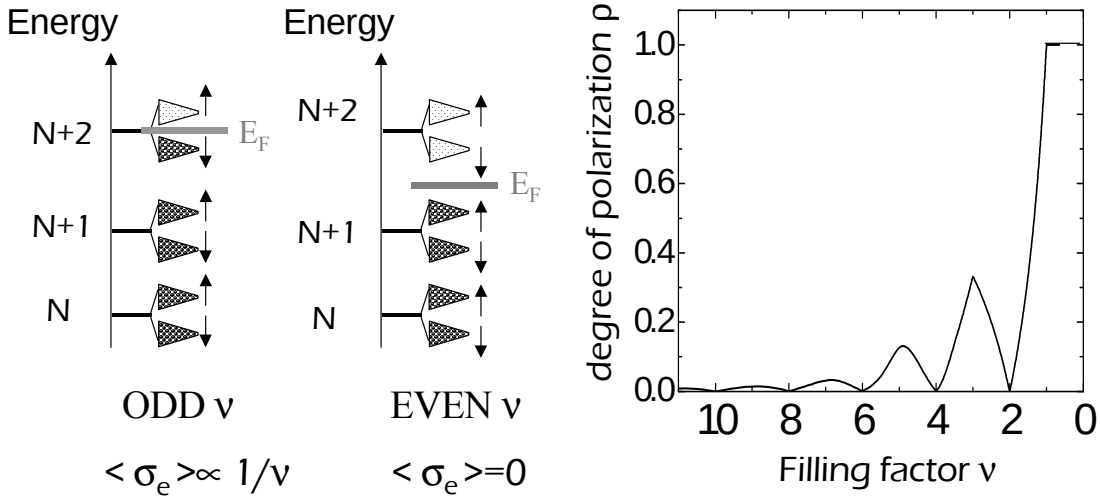

Figure 1.9. Left) Schematic representation of the Landau level occupation at odd and even filling factors. Right) Filling factor dependence of the degree of polarization $\mathcal{P}$.

1.3 Electrical transport properties of 2D electrons under magnetic field

The most conventional probe of the properties of a 2DEG is the

measurement of its resistivity. The physics of the quantum Hall effect, merited the Nobel Prize for K. von Klitzing in 1985 and for H. Störmer, D. Tsui and R. Laughlin in 1998. In spite of the fact the Quantum Hall Effect has been extensively investigated for more than 20 years, it still remains as one of the most fertile and active topics in solid state physics. In this section we will shortly review the electrical transport properties of a 2DEG in magnetic fields.

1.3.1 Electrical transport

The behavior of 2DEG electrons in an electric field are similar to those in a metal, where electrons are free particles subjected to the Pauli principle. The momentum of an electron is related to the wave-vector by $m^*_e \boldsymbol{v}=\hbar \boldsymbol{k}$. In an electric field $\boldsymbol{E}$, the force on an electron of charge e is given by Newton's second law:

$$m^*_e \frac{d\vec{v}}{dt} + \frac{m^*_e}{\tau}\vec{v} = e\vec{E} \qquad \text{Eq.1.32}$$

where τ is a phenomenological average scattering time introduced to account for the scattering of electron by impurities and phonons. These elastic collisions lead to a stationary regime. In such steady state under electric field, the Fermi surface is displaced at a uniform rate in $\mathbf{k}$ space by a constant applied electric field given by:

$$\vec{k}(t)-\vec{k}(0) = e\vec{E}t/\hbar \qquad \text{Eq.1.33}$$

If the field is applied at time t=0, the center of the Fermi circle originally at $\boldsymbol{k}=0$ will be displaced in the steady regime to a new center at:

$$\delta\vec{k} = eE\tau/\hbar \qquad \text{Eq.1.34}$$

This implies a drift velocity:

$$\vec{v}_d = e\vec{E}\tau/m^*_e \qquad \text{Eq.1.35}$$

and a current density for a carrier density n_e given by $\mathbf{j}=n_e e\mathbf{v}_d$. In fact, this is nothing more than Ohm's law from which we can extract the expression for conductivity or resistivity:

$$\sigma_0 = n_e e^2 \tau / m^*_e \quad \text{or} \quad \rho_0 = 1/\sigma_0 = m^*_e / n_e e^2 \tau \qquad \text{Eq.1.36}$$

This result within the Drude model [Ashcroft] seems logical since the charge transport is favored by the number of charges (n_c) but diminished by their mass. At low temperatures, τ describes the time during which the electric field acts on the carriers before a collision. This time is related to the electron mobility $\mu = e\tau/m^*_e$.

1.3.2 Magneto-transport

Applying an external magnetic field **B**, the Lorentz force introduces additional changes to the electron motion. From Eq.1.32 we are led to the equation of motion for electrons at the Fermi surface:

$$m^*_e \frac{d\vec{v}}{d\ t} + \frac{m^*_e}{\tau}\vec{v} = -e\left[\vec{E} + (\vec{v} \times \vec{B}/c)\right] \qquad \text{Eq.1.38}$$

For a static magnetic field lying along the z-direction, in a steady state in a static electric field, the drift velocity is given by:

$$v_x = -\frac{e\tau}{m^*_e} E_x - \omega_c \tau v_y$$

$$v_y = -\frac{e\tau}{m^*_e} E_y + \omega_c \tau v_x \qquad \text{Eq.1.39}$$

$$v_z = -\frac{e\tau}{m^*_e} E_z$$

where ω_C is the cyclotron frequency defined in Eq.1.28. Similarly to Eq.1.36, it is possible to extract the corresponding conductivity (or resistivity) tensor

$$\sigma = \frac{\sigma_0}{1+(\omega_C \tau)^2} \begin{pmatrix} 1 & -\omega_C \tau \\ \omega_C \tau & 1 \end{pmatrix} \qquad \text{or}$$

$$\rho = \frac{1}{\sigma_0}\begin{pmatrix} 1 & \omega_C\tau \\ -\omega_C\tau & 1 \end{pmatrix} \qquad \text{Eq.1.40}$$

From such a classical model, we can conclude:

-$\rho_{XX}=\rho_{YY}=1/\sigma_0=\rho_0$ are independent of magnetic field.

-$\rho_{XY}=-\rho_{YX}$ = $B/n_e e$ are proportional to the magnetic field as Hall determined in 1879 [Ashcroft].

Experimentally, both components of the resistivity can be independently measured using the Hall bar geometry (see insert Figure 1.10).

1.3.2.1 Quantum Hall effect

According to the classical model, the magnetic field dependence of the transversal resistance is linear $R_H=B/n_e e$, exactly as Edwin Hall observed on applying a longitudinal current through a metal bar under a perpendicular magnetic field. This has traditionally been used as a convenient method to determine the density n_e and nature (sign) of the carriers.

However, the quantum Hall effect surprisingly breaks the linearity (see Fig.1.10), with broad resistance regions (plateaus) of constant conductivity with quantized values $h/\nu e^2$ in the vicinity of filling factors ν. The QHE manifests similar features (plateaus and resistance minima) for integer [Von Klizting-1980] and fractional filling factors [Tsui-1982]. Whereas the Integer regime is easily described as a consequence of a quantized energy spectrum due to the 2D confinement plus the Landau/spin quantization, the fractional QHE requires a more sophisticated explanation. Laughlin proposed that electron-electron interactions lead to a gap in the DOS at high magnetic fields for high mobility systems [Laughlin-1983].

In the integer regime, the associated QHE features appear at specific magnetic fields B_ν (see Fig.1.10), when the filling factor ν is an integer and the Fermi level lies in the gap between two Landau levels. Under this condition there are no states available in the vicinity of the Fermi energy. Therefore, at these singular positions in the magnetic field, the electron system is rendered incompressible and its transport parameters (R_{XX}, R_{XY}) assume quantized values [Laughlin-1981]. Localized states in the tails of each Landau levels, extend the range of quantized transport from a set of precise points in B_ν to finite range of B, leading to observed plateaus in the Hall resistance and a wide regions of vanishing magneto-resistance [Prange-1990].

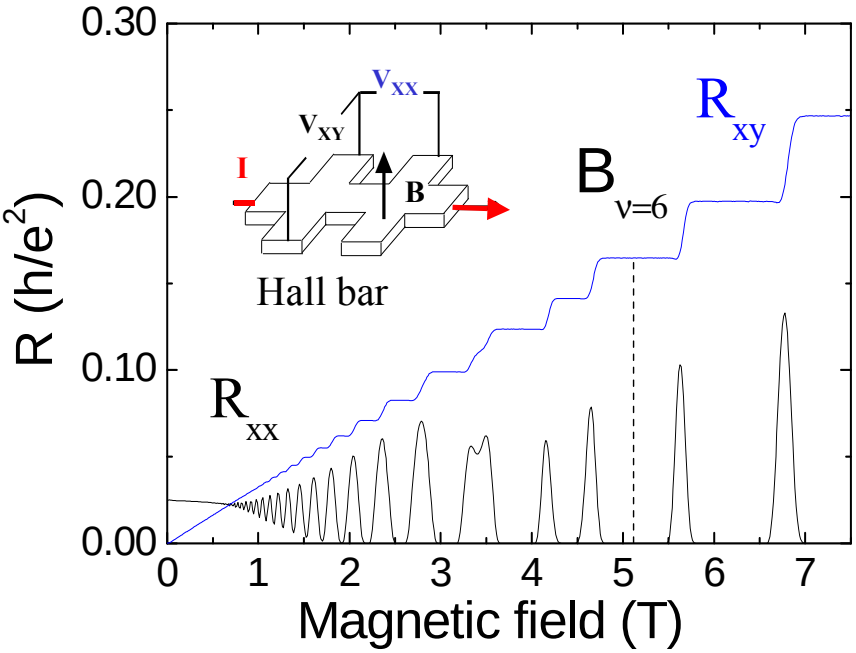

Figure 1.10. Longitudinal (R_{XX}) and transversal (R_{XY}) resistance of a 2DEG confined in GaAs quantum well structure as a function of magnetic field at low temperature. Insert: measurement conditions for a Hall bar.

The remarkable feature of the plateau quantization is the fundamental nature of the parameters involved. The particular semiconductor material does not play any role neither do the dimensions of the Hall bar. The accuracy of the experimental plateau value agrees with a manifestly simplistic theory to the quite incredible accuracy of a few parts in 10^8 which allows one to determine the fine structure constant α or to use the quantum resistance h/e^2 as the metrological standard of electrical resistance.

1.3.2.2 Shubnikov de Haas oscillations

Another phenomena linked to the quantization of the electronic motion in 2D under strong magnetic field is the oscillatory behavior of the longitudinal component of the resistivity (see Fig.1.10). Similar magneto-oscillatory behavior was first observed in the magneto-resistance of Bismuth metal by de Haas and Shubnikov [Shubnikov-1930].

The classical model expressed in Eq.1.40 does not imply any magnetic field dependence for the longitudinal resistivity, since it assumes τ constant what is

only true in the low field regime. At high fields $1/\tau \propto DOS(E_F)$ [Abrikosov-1988] which implies $\rho_{XX} \propto DOS(E_F)$ [Van der Burgt-1995]. Therefore, the oscillatory behavior of the longitudinal resistance of a 2DEG is simply a macroscopic consequence of the Fermi energy oscillations: maxima are observed when the Fermi energy lies in the middle of the extended states of a Landau level (maximum of DOS) and minima are observed when E_F resides in the middle of a gap, i.e. when there is an exact integer number of occupied Landau levels. Under such condition, no quasi-elastic scattering can occur at low temperatures; all states below Fermi energy are occupied and electrons require an energy equivalent to the gap in the DOS (neglecting broadening) to be scattered to the next unoccupied Landau level. In this case, $\rho_{XX}=0$ and ρ_{XY} is given by the classical collision value (Eq1.40). Considering Eq.1.30, we can therefore write that at integer filling factors ν:

$$\rho_{XY} = \nu \frac{h}{e^2}; \rho_{XX} = 0$$

The oscillatory behavior has a frequency directly related to the carrier density n_e which may be expressed by:

$$\Delta(1/B) = 1/B_\nu - 1/B_{\nu-1} = e/hn_e \qquad \text{Eq.1.41}$$

where B_ν is the magnetic field position of the resistance minima associated with filling factor ν. For an ideal 2D system, the plot of the inverse of the minima magnetic field positions as a function of their associated integer filling factors is a straight line whose slope gives the carrier density n_e. This may be used as complementary method other than the slope of the low field Hall resistance as a way to experimentally determine the carrier density.

In summary, the transport features are the results of transitions between alternating metallic and insulator behavior; i.e. the Fermi level alternates from being within a Landau / spin band to being in a cyclotron or spin gap. These integer quantum Hall effect (IQHE) states occur at integer filling factors ν and display the quantization of the Hall resistance to $h/\nu e^2$, as indicated in Fig.1.10. The IQHE is the result of the quantization conditions for non-interacting 2D electrons in magnetic field [a].

[a] In the case of high mobility systems or special conditions [Daneshvar-1997, Koch-1993], the gaps may be enhanced by electron –electron interaction, as outlined in the 1.2.3 section.

1.4 Optical properties of 2D electrons under magnetic fields

A powerful method to investigate the response of a 2DEG in the Quantum Hall regime is magneto-optics. The modern arsenal of optical spectroscopy enables one to study 2D electron systems without contacts to the material, in a way that complements the transport experiments. The interband spectroscopy allows one to probe the density of states below as well as above the Fermi energy (see Figure 1.11) giving access to a wider range of electronic states than transport experiments. Far infrared transmission reflects the single particle DOS around the Fermi energy [Nurmiko and Pinczuk-1993]. The electronic transitions between the highest occupied and the adjacent Landau levels (intra-band transitions) require an energy equal to the cyclotron energy ($\hbar\omega_C$). Although infrared absorption gives precise values of the cyclotron energy, it is hardly applied to measure the spin gap whose excitations are associated with spin-flip processes. In the electric dipole approximation valid for infrared absorption, such spin-flip processes are forbidden, a restriction not applicable to inelastic light scattering. In an electronic system these spin-flip transitions occur across an excitation gap which corresponds to a total spin separation energy (Zeeman energy). The inelastic light scattering can also probe crystal excitations related to magnetic impurities present in the crystal.

In this section, we review the basis of the inter and intra-band spectroscopy and a general theoretical background of Raman spectroscopy.

1.4.1 Far infrared spectroscopy

Since Abstreiter and coworkers [Abstreiter-1974] measured the cyclotron resonance of a 2DEG confined in a MOSFET for first time, the far infrared spectroscopy has become a standard technique to characterize 2D electron systems. The principle information available from the cyclotron resonance spectrum at a given magnetic field is the effective electron mass. The resonance position is proportional to the magnetic field strength and according to Kohn's theorem [Kohn-1961] is not affected by the electron-electron interactions in translationally invariant systems. Within the single particle picture, the cyclotron resonance of a 2DEG appears as an ensemble of electronic transitions between the Landau levels in the vicinity of the Fermi energy in the conduction band as shown in Fig.1.11.

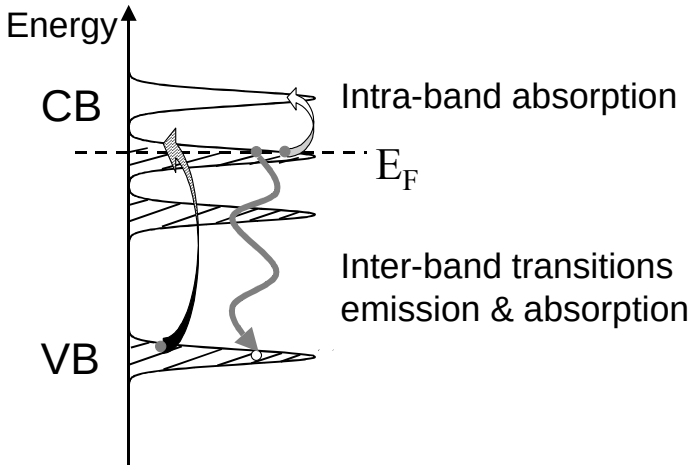

Figure 1.11. Possible optical processes include inter-band (emission and absorption) and intra-band (cyclotron resonance) Landau level transitions. Spin splitting is neglected in the figure.

As results of the broadening of the Landau level, the cyclotron resonance has a width described by electron scattering processes. One possibility of interpreting the dynamic mechanism implied in the description of the line-width lies within the Drude model described in the section 1.3. This model assumes all electrons participate in the cyclotron resonance (not only those in the vicinity of the Fermi energy) and each electron individually obeys Eq. 1.38 with $\boldsymbol{E}$ as the electric field of the light. This model implies that cyclotron resonance is clearly observed when $\omega_C\tau << 1$, where ω_C is the cyclotron frequency [Koch-1976]. Assuming a vanishing extension of the 2D electron layer along the confinement direction, Chiu et al. [Chiu-1976] demonstrated that the transmission line given by the Drude model results:

$$\frac{T(B)}{T(0)} = \frac{T_+(B)+T_-(B)}{2T(0)} \qquad \text{Eq1.42}$$

with

$$T_\pm(B) = \left(\frac{2}{1+\sqrt{\varepsilon}}\right)^2 \frac{1+(\omega \pm \omega_c)^2\tau^2}{(1+\Gamma\tau)^2+(\omega \pm \omega_c)^2\tau^2} \qquad \text{Eq.1.43}$$

where $T_{\pm}(B)$ is the transmission of cyclotron-resonance-active (-) and inactive (+) polarized light, ε is the dielectric constant, ω_c is the resonance energy and

$$\Gamma = \frac{\mu_B c n_e e^2}{m^*_e (1+\sqrt{\varepsilon})} \qquad \text{Eq.1.44}$$

is a parameter containing the electron concentration n_e and the effective electron mass m^*_e. Within this approach, we notice that for a given carrier concentration, the integrated intensity of the absorption is constant and proportional to the carrier concentration.

1.4.2 Inter-band spectroscopy

The inter-band magneto-optical technique on quantum wells structures is an important spectroscopic tool for investigating either occupied states or empty states looking at the emission or absorption of photons. Both phenomena are related to electronic transitions involving conduction and valence states (inter-band).

1.4.2.1 Emission Spectroscopy

1.4.2.1.1 Photoluminescence

In an ideal semiconductor, the principle of photoluminescence (PL) is the excitation by optical illumination of electrons from the valence (leaving a hole) to the conduction band. Since the system tends to equilibrium, both particles relax towards the lowest empty states in *k*-space by non-radiative processes. They then recombine across the gap emitting a photon (see Figure 1.12) at $\boldsymbol{k}$=0 preserving the momentum conservation. The photon energy corresponds to the energy separation between the electron (initial) and hole (final) states involved in the transition.

1.4.2.1.2 Photoluminescence excitation

With the availability of continuously tunable lasers, a new kind of emission spectroscopy becomes possible which consists of measuring the evolution of the PL as a function of the excitation energy (see Fig.1.12). The luminescence intensity increases resonantly when the excitation energy coincides with the absorption level. Actually, the photo-luminescence excitation (PLE) is accepted as a pseudo-absorption technique.

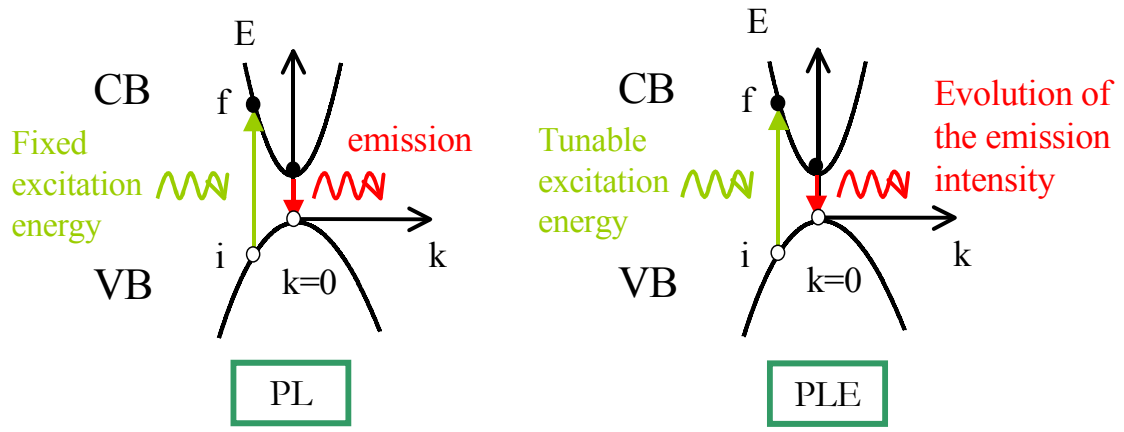

Figure 1.12. Schematic representation of the principles of PL and PLE.

1.4.2.2 Character of the inter-band transitions

The inter-band optical emission and absorption spectra are strongly influenced by the presence of the carriers. Many theoretical [Hawrylak-1991, Brown-1996] and experimental [Huard-2001, Eytan-1998,] works have considered how the optical properties of a semiconductor quantum well structure evolve with the density of carriers.

1.4.2.2.1 Excitonic transitions: neutral and charged excitons

The optical properties of undoped semiconductor quantum well structures are dominated by excitons. The absorption of a photon in a semiconductor creates an electron in the conduction band and a hole in the valence band. They attract each other due to the Coulomb force forming an 'atomic' exciton i.e. bound electron-hole pair X = e+h. The excitonic states are described by hydrogen-like levels [MacDonald-1986] with a ground state energy shifted by the exciton binding energy E_b with respect to the gap energy. The emission and absorption lines are narrow (few meV). Under a magnetic field, the excitonic states show a typical diamagnetic behaviour at low fields (see Figure 1.13) accounted by the hydrogenic model [MacDonald-1986].

In the case of a low excess density of electrons (or holes), an exciton can capture an additional electron (or hole) to form a charge exciton or trions, $X^{-(+)}$=X+e(h). In spite of the fact that Lampert predicted [Lampert-1958] the existence of such a three particle complex over 40 years ago, the first observation in CdTe quantum wells was only made recently [Kheng-1993].

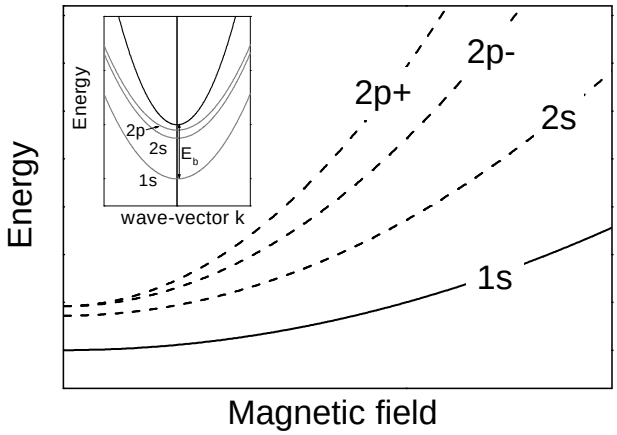

Figure 1.13. Illustrative representation of the magnetic field dependence of excitonic states. Insert: Conduction band (solid line) and exciton (dotted) dispersion relations E-k.

The binding energy of the third particle increases with spatial confinement [Thilagam-1997] and is about 2meV for a 10nm thick quantum well. The formation of negatively charged trions implies electrons with different spins:

$$X^- \rightarrow e\uparrow + e\downarrow + h\Uparrow$$

where $\uparrow$ and $\downarrow$ represent electron spins $\pm 1/2$ and $\Uparrow$ hole spin$+3/2$. The recombination and formation processes therefore obey the selection rules represented in Figure 1.14. From these selection rules, it is evident that the creation (absorption) process of X^- depends on the polarization of the electron gas. In contrast, the emission polarization of X^- depends on the hole polarization. An external magnetic field or temperature can modify the hole and 2DEG polarization and consequently trion formation [Jeukens-2001].

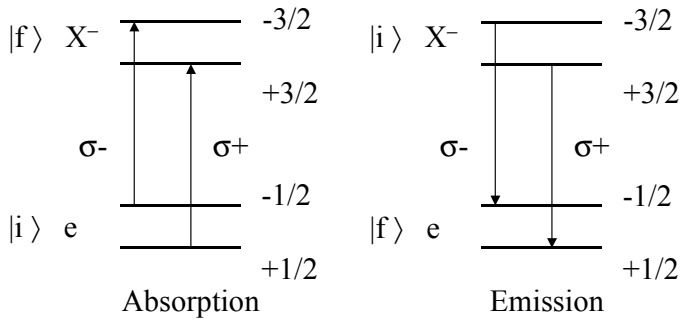

Figure 1.14. Schema of the allowed optical transitions, absorption (left) and emission (right) for $e + h\nu \leftrightarrow X^-$. The spin of is the hole spin, the two electron being spin-paired.

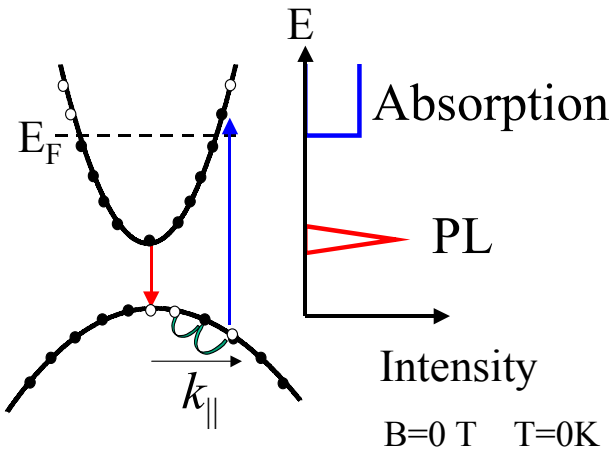

Figure 1.15. Schematic illustration of the expected emission and absorption spectra of an ideal and non-interacting 2DEG.

1.4.2.2.2 Inter-band transitions

Coulomb effects are screened when adding carriers. In the case of a non-interacting 2DEG (free carriers), the emission occurs from the bottom of the conduction band in the ***k***-space whereas the absorption starts above the Fermi energy, as shown in Fig.1.15. The shift between the emission and absorption edges is the Moss-Burstein shift and it is a standard method for the determination of the Fermi energy:

$$E_F = (E_{onset} - E_{Gap})\left(1 + \frac{m^*_e}{m^*_h}\right)^{-1} \qquad \text{Ec.1.45}$$

In a magnetic field, the zero-field DOS condenses into Landau levels labeled by N. Inter-band Landau level transitions occur from there obeying selection rules for momentum conservation ($\Delta N=0$) and spin ($\Delta\sigma=+/-1$).

1.4.3 Spin flip Raman scattering processes

Although most of the light traveling through a medium is either transmitted or absorbed following the standard laws of reflection and refraction, a very tiny fraction is scattered in all directions by dislocations, atomic vibrations or the fluctuations of the spin density inside the medium [Yu-

Cardona]. Whereas absorption or emission are first order processes which involve one photon participating in an electronic transition, the inelastic light scattering is a second order process involving two photons (see Figure 1.16). When the initial photon hits the crystal, the light-matter interaction gives back a scattered photon with different energy and momentum with respect to the initial one. The Raman spectroscopy constitutes an experimental method to investigate elementary excitations of matter based on the consideration of the energy and momentum differences between the two photons. In DMS, the Raman scattering has proved to be a high resolution technique in discovering and delineating two types of spin excitations [Ramdas-1988]: electronic transitions within the Zeeman multiplet of ground state of Mn^{2+} split by an external magnetic field and the spin flip of conduction band electrons describing orbits under magnetic field.

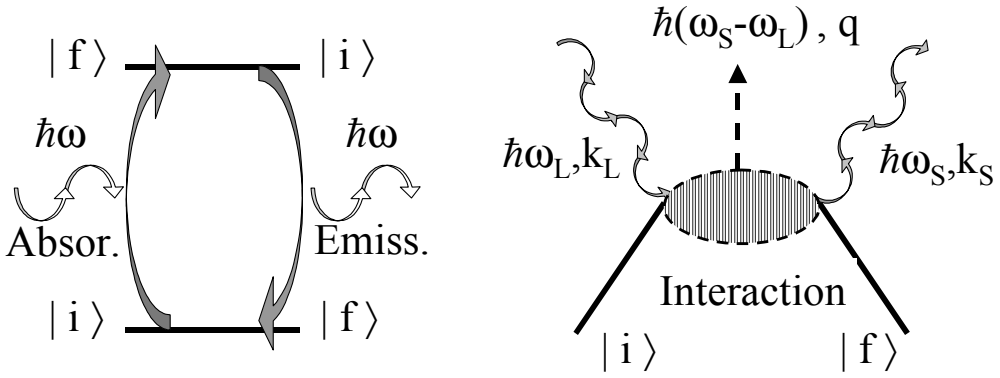

Figure 1.16. Illustrations of photons involved in inter-band transitions (left) and light scattering processes (right).

1.4.3.1 Electronic spin flip

Spin Flip Raman Scattering (SFRS) from conduction electrons was first suggested by Wolf [Wolf-1966] involving light scattering from Landau levels in semiconductors. The electric field of the incident radiation of energy $\hbar\omega_L$ interacts via spin-orbit coupling with a spin in a magnetic field B and induces a spin flip $\uparrow \Rightarrow \downarrow$ with the energy of the scattered light shifted to $\hbar(\omega_L - \omega_Z)$ (Stokes shift) where $\hbar\omega_Z$ is the electronic Zeeman energy. The energy of the scattered light is therefore tunable by the magnetic field. This was firstly observed by Slusher [Slusher-1967] for conduction electrons in InSb. In DMS, SFRS was first observed in wide gap CdMnTe [Nawrocki-1980]. The electronic structure probed by SFRS results from the combined effect of the external field B and Mn^{2+} magnetization according to Eq.1.6.

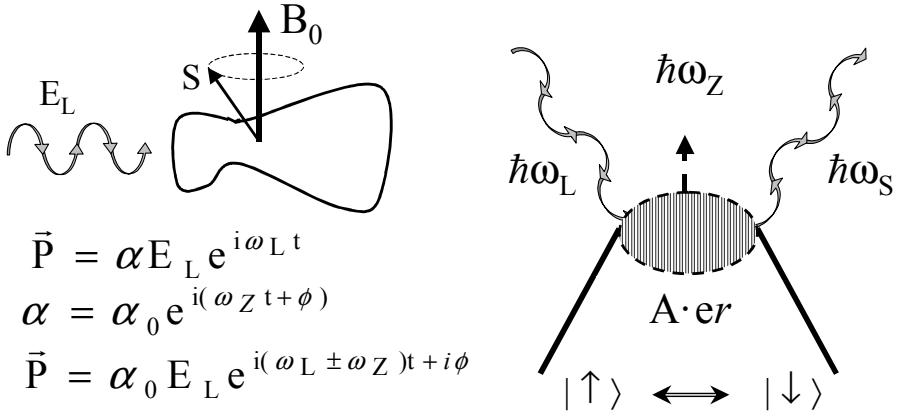

$$\vec{P} = \alpha E_L e^{i\omega_L t}$$
$$\alpha = \alpha_0 e^{i(\omega_Z t + \phi)}$$
$$\vec{P} = \alpha_0 E_L e^{i(\omega_L \pm \omega_Z)t + i\phi}$$

Figure 1.17. Classical picture of SFRS. Spin-Orbit coupling drags a charge cloud around at spin precessional frequency ω_Z, thus modulating the polarizability and giving rise to side-bands $\omega_L \pm\omega_Z$. Refined schema of the light scattering process by the spin fluctuations (dipole interaction).

A classical picture of SFRS is illustrated in Figure 1.17. The spin precesses in an external magnetic field B at the Zeeman frequency ω_Z and drags around a charged cloud tied to it by spin orbit coupling. Thus, the incident light sees a polarizability α modulated at ω_Z and a polarization is induced with a frequency $\omega_L - \omega_Z$ which then radiates at this frequency (also $\omega_L + \omega_Z$, anti-Stokes shift). This is analogous to the vibrational scattering due to the modulation of α by vibration frequencies (Phonon scattering processes). The spin – orbit coupling is the handle via which the electric field of the light couples to the spin. The electric field $E_L \cos \omega_L t$ of the incident laser light admixes the electronic excited states $|N\rangle$, Landau levels N, into the states $|\uparrow\rangle$ and $|\downarrow\rangle$ through a set of virtual electric dipole transitions described by the Hamiltonian [Geschwind-1984]:

$$\mathcal{H} = \left(\frac{\alpha}{2} e^{-i(\omega_L - \omega_S)t} + \frac{\alpha^*}{2} e^{i(\omega_L - \omega_S)t} \right) \sigma \cdot (E_L \times E_S) \qquad \text{Eq.1.46}$$

where α^* is the complex conjugate of α, $\boldsymbol{\sigma}$ are the Pauli matrix and S denoted the scattered frequency and electric field. From the vector product of $\boldsymbol{E_L x E_S}$ in Eq.1.46, the selection rules for cubic symmetry can be deduced. The σ has off-diagonal elements corresponding to a spin flip transition which can be observed when the resulting polarization components of the product $\boldsymbol{E_L}$ **x** $\boldsymbol{E_S}$ are perpendicular to the magnetic field direction. In this geometry, considering a

magnetic field in z-direction the **Stokes** (Anti-Stokes) lines are σ+(-) polarized for **cross polarization** of the L and S electric field. No Raman scattering occurs when the polarizations of the incident and scattered radiation are parallel. The scattering event is enhanced under resonant conditions [Wolf-1966]. When the energy of the incident light is close to the initial state energy of the electron, i.e. states above band-gap or exciton states (for instance in neutral or charged excitons), the perturbation theory breaks-down and the scattering probability (cross section) is increased.

1.4.3.2 Magnetic Spin flip

The incomplete d-shell of the Mn^{2+} ions in DMS gives rise to a variety of properties in which their localized magnetic moments play important roles, either individually or collectively through their mutual interactions. Therefore, the electronic spin-flip transitions between 3d-levels should differ for the individual Mn^{2+} ions in comparison to the features associated to magnetic ordered phases. Here, we consider only the paramagnetic phase where Raman scattering is associated with spin flip transitions between adjacent sublevels of the multiplet $^6S_{5/2}$. At zero field, the crystal field is too small to observe any splitting among the multiplet states. However, the application of an external magnetic field lifts the six-fold degeneracy of the ground state, as indicated in Fig.1.5. The selection rules for the observation of the magnetic excitations are given by Eq.1.46. Fleury and Loudon [Fleury-1968] considered a two step process with an intermediate state corresponding to one of the excited states of the Mn^{2+} ions (L=1,S=5/2) as the responsible mechanism for Raman scattering. Figure 1.18 shows the mechanism for the Stokes component of the Raman line. For the Stokes component, an incident photon of energy $\hbar\omega_L$ and polarization σ+ induces a virtual electric dipole transition (red arrow) between initial and a intermediate state which differ by $\Delta m_J(Mn^{2+})=+1$; it is followed by a second electric dipole transition (blue arrow) between the intermediate and final states with $\Delta m_J(Mn^{2+})=0$. This is accompanied by the emission of a scattered photon of polarization z and energy $\hbar\omega_S = \hbar\omega_L - \hbar\omega_{PM}$ with $\hbar\omega_{PM} = g^{Mn}\mu_B B$, represented in Fig.1.5. At the end of this process the Mn^{2+} ions is in an excited state within the Zeeman multiplet differing from the initial state by $\Delta m_S=+1$. Notice that the entire phenomenon is Electron Paramagnetic Resonance (EPR) observed as a Raman shift. Similar processes can be visualized for the anti-Stokes component.

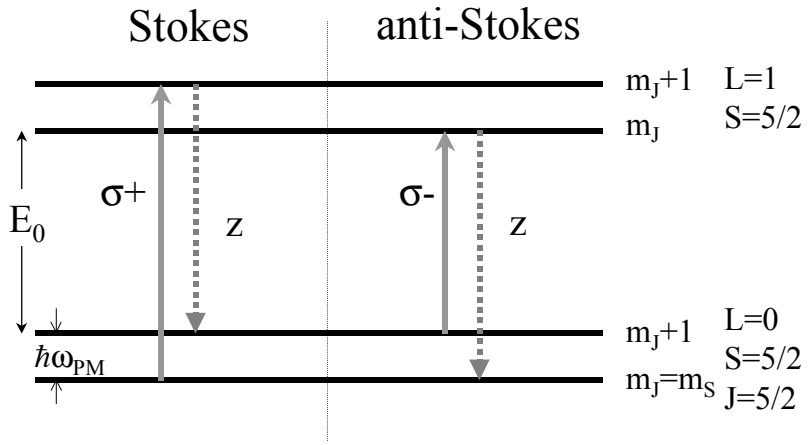

Figure 1.18. Raman mechanism for the ω_{PM} line involving the internal transitions of the Mn2+ ion. The arrows indicate virtual electric dipole transitions. The energy level scheme is not scaled, the energy difference between the excited and ground states E_0 is much greater than $\hbar\omega_{PM}$.

Chapter 2

Sample structure

Introduction

Since the early use of MOSFET structures for the formation of quasi-two-dimensional electron gases (2DEG's), the mobility values have dramatically increased more than 1000 times mainly due to the introduction of the modulation doping concept in III-V structures. This improvement has mainly been achieved by a careful design of spacer layers, which separate the ionized donors away from the electron gas sheet. In recent years, there has been an increased interest in the optical and transport properties of 2DEGs in II-VI based nanostructures [Landwehr-2000]. The interest arises from the fact that II-VI compounds generally have larger exciton binding energy values. In addition such materials allow one to independently incorporate magnetic ions and carriers. This offers an unique opportunity for studying the exchange interaction between high mobility carriers and localized magnetic spins.

2.1 Sample structure

All samples studied in this thesis were grown by molecular beam epitaxy by Grzegorz Karczewski and Tomasz Wojtowicz in the department of **Growth and Physics of Low Dimensional crystals**, Institute of Physics, Warsaw. Elemental sources of Cd, Te, Mg, Mn, and Mg and a compound source of ZnI_2 (iodine) for donor doping were used for growing layered structures on semi-insulating (100) GaAs substrates. The samples consist of a single 10nm-thick quantum well $Cd_{1-X}Mn_XTe$ embedded in $Cd_{0.8}Mg_{0.2}Te$ [Karczewski-1998] as shown in Figure 2.1. Since the introduction of Mg enhances the energy gap of the barrier (16 meV/%), the composition of the barrier can be determined from photoluminescence measurements. For 20% Mg composition, the offset for the

conduction band (70% of the difference in band gap between the well and the barriers [Kuhn-Heinrich-1993]) provides a good confinement.

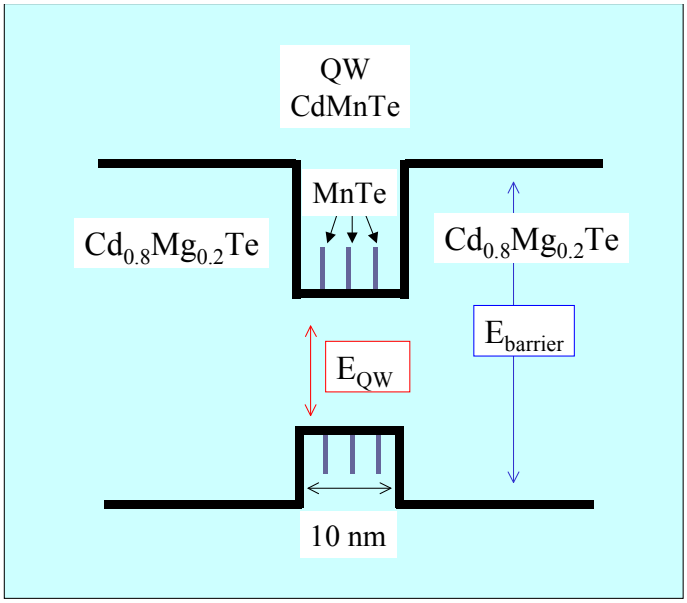

Figure 2.1 : Schematic energy profile of a $Cd_{0.8}Mg_{0.2}Te/Cd_{1-X}Mn_XTe$ quantum well structure.

Two types of samples were used for the investigations: CdTe (without Mn) and $Cd_{1-X}Mn_XTe$ (containing Mn). In the wells containing Mn, the magnetic ions were digitally introduced in a few monolayers, in order to have a strong overlap of the wave-functions between the confined states and the localized magnetic ions. The distribution of magnetic local moments in the well is hence a short period superlattice of CdTe/MnTe where, the latter are separated by 3 nm as shown in Fig.2.1. The value of the effective Mn concentration x_{eff} was experimentally estimated from the giant Zeeman energy determined by transport, interband optics, or Raman data, as will be shown in the next sections.

The carriers were introduced in the well by modulation doping. The 2DEG is formed by placing on one side of the well iodine doped $Cd_{0.8}Mg_{0.2}Te$ layers separated 10 nm from the quantum well by an intrinsic $Cd_{0.8}Mg_{0.2}Te$ *spacer*. The asymmetric doping induces an electric field, which bends the quantum well potential as schematically illustrated in Figure 2.2.

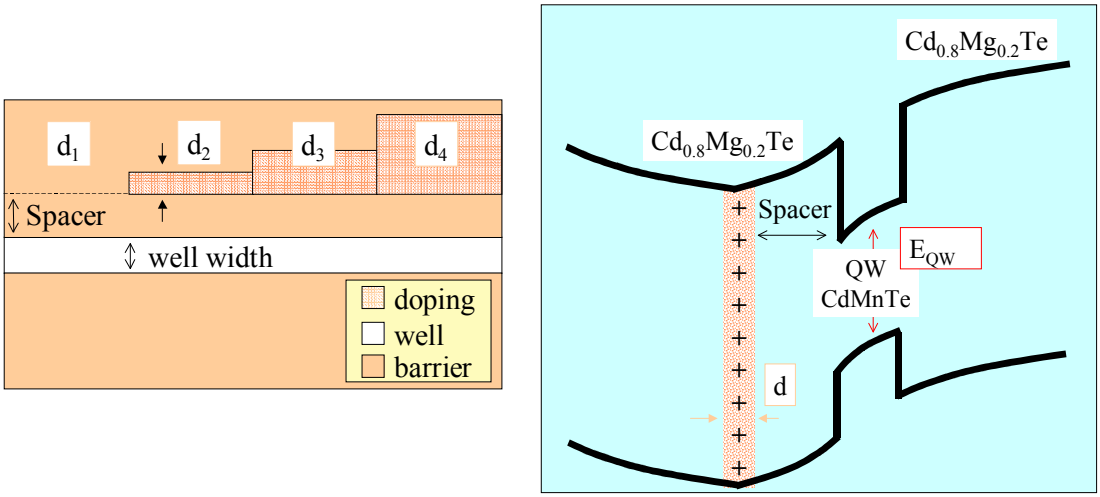

Figure 2.2 : L) Schematic illustration of the spatially different doping intensity profile in a $Cd_{0.8}Mg_{0.2}Te/Cd_{1-X}Mn_XTe$ quantum well structure. d_i indicates the doping layer thickness for the region of carrier concentration n_i. R) Schematic energy profile of a doped $Cd_{0.8}Mg_{0.2}Te/Cd_{1-X}Mn_XTe$ quantum well structure.

Different carrier concentrations are obtained by varying the thickness of the iodine doped $Cd_{0.8}Mg_{0.2}Te$ layers *d*. For a specific reason described in Chapter 7, a special modulation doped CdMnTe quantum well structure was grown. The 'polish speciality' [Wojtowicz-1998] in growing the quantum structures is based on a spatial in-plane profiling of different doping intensities. The precisely controlled gradient of the thickness, *d,* of the remotely doped region along one of the directions perpendicular to the growth axis of the sample results in separated spatial regions with different doping level as shown in Figure 2.3. Thus, the same structure results in 4 different samples with different carrier concentrations: from nominally undoped up to several $10^{11}cm^{-2}$. Moreover, the particular design structure of these samples allows us to additionally control the electron concentration by laser illumination. The carrier concentration can be increased by a factor of 2 by illuminating with different laser power above the barrier with respect to the case in which the excitation energy is below the barrier. Intermediate concentrations can be reached by simultaneous illumination of a line below 700 nm (obtained by a tunable Titanium sapphire laser) and an Ar^+ line. Extremely low powers (~10 $\mu W/cm^{-2}$) of the Ar^+ line remarkably increases the carrier concentration up to a saturation value. Beyond, saturation high power illumination depletes the quantum well.

Chapter 3

Far infrared spectroscopy studies

Introduction

Far infrared transmission studies of a 2D electron system confined in quantum well structures under quantizing magnetic fields probe the cyclotron gap excitation and complement electrical transport studies [Koch-1976]. In this chapter, we show how far infrared spectroscopy allows a useful characterization of the free carrier system notably in order to determine the carrier effective mass, concentration and mobility.

3.1 Cyclotron resonance study

The properties of two-dimensional electron systems in II-VI compounds are not as well known as those of their counterparts in III-V systems, which have been investigated intensively during the last 20 years. In addition, the introduction of magnetic ions such as Mn^{2+} into these compounds opens the possibility for interesting new phenomena. One such possibility is observing the situation in which the exchange interaction enhanced spin splitting of a Landau level coincides with the energy separation between adjacent Landau levels (cyclotron energy, $\hbar\omega_C$). As we will present in chapter 4, transport properties show features related to such energy coincidence.

3.1.1 Experimental details

Here, we present the results of a preliminary far infrared cyclotron resonance (CR) study performed on a series of $Cd_{1-x}Mn_xTe$/CdMgTe modulation doped quantum wells with characteristics as described in chapter 2. Transmission measurements were performed at 2K under magnetic fields up to 13T.

The electron concentrations and manganese contents of the samples used in the study obtained by optical measurements are summarized in Table 1:

Sample	Electron concentration	Mn content
101097A	3.0×10^{11} cm^{-2}	0.3%
100997A	5.9×10^{11} cm^{-2}	0.3%
072497A	5.7×10^{11} cm^{-2}	0
072897A	6.3×10^{11} cm^{-2}	0

Table 1

The far-infrared transmission of the samples was measured using a Bruker 113v Fourier Transform Spectrometer. A doped Ge bolometer, kept at low temperature, was used to record the transmitted energy. The spectra were normalized by the zero-field spectrum of a given sample; thus the results presented here are in the form:

$$S(\nu) = T(\nu, B)/T(\nu, B=0)$$

3.1.2 Spectrum shape

Figure 3.1 shows typical transmission curves for all the samples at a magnetic field $B = 8.5T$. The cyclotron resonance transitions of the two-dimensional electron gas are clearly visible for all samples. Lower carrier concentration samples ($<3x10^{11}cm^{-2}$) did not show resonant absorption. The most regular peak may be observed for sample 072897A. The other samples both with and without Mn in the well, exhibit a large shoulder on the low-energy side, which evolves into a clearly resolved split-off peak for the low-concentration sample (101097A) which is largest at around 8.6T. This clear departure from the single peak spectrum does not appear to resemble the often-found "anomalous" cyclotron resonance splitting which typically show anti-crossing behaviour and a transfer of oscillator strength between the split-off peaks. In this case the splitting is invisible at low fields; it grows gradually as the magnetic field approaches 8.6T and then disappears again at higher fields. The area under both peaks, shown in Figure 3.2 as a function of the magnetic field, may be considered a measure of the number of electrons involved in each process. Its behaviour suggests that the two processes are not independent, there is a decrease of the area of the main peak at the maximum of the satellite peak. Only the relative changes of the areas are

plotted in Fig.3.2, but the sum of the areas remains constant in the region of magnetic field where both peaks undergo changes.

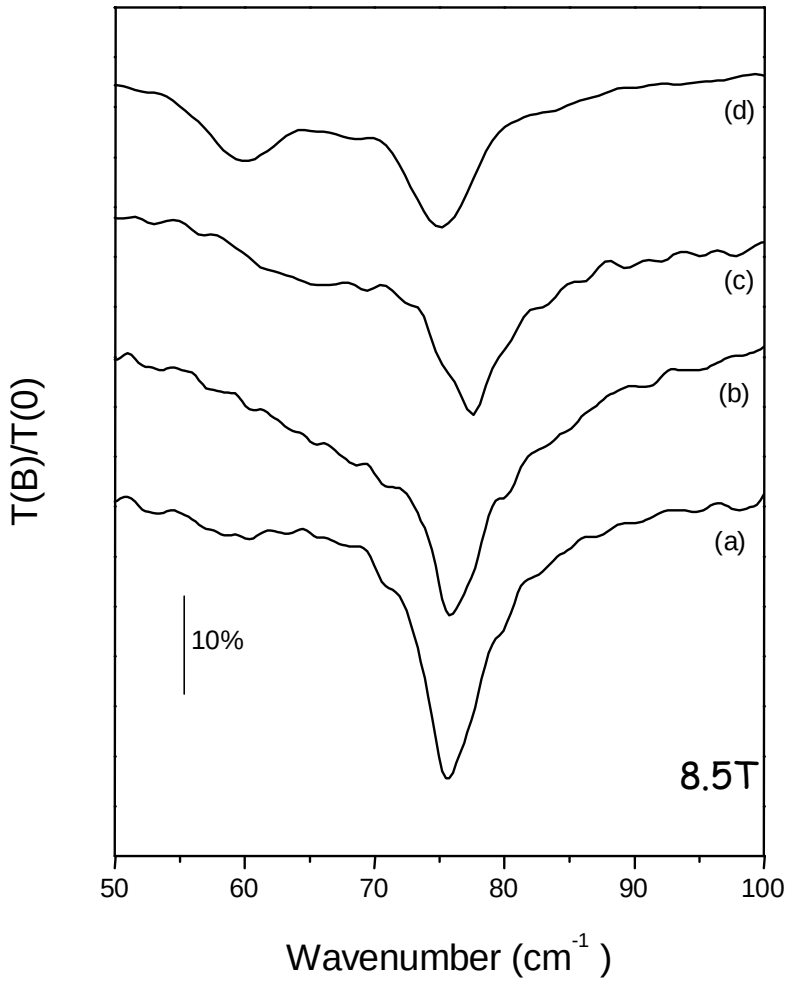

Figure 3.1 : Plots of normalised transmission versus wavenumber for different samples, at a magnetic field of 8.5T. The spectra have been shifted for clarity. a)– sample 072897A; b)–sample 072497A; c)– sample 100997A; d)– sample 101097A.

The low-energy shoulders observed in the other samples (see Fig.3.1) appear to move parallel to the main CR peak as a function of magnetic field, although a precise determination of their position is not easy. Their presence also makes it difficult to reasonably describe the lineshape with a formula derived from a simple Drude model [Chiu-1976], with the exception of sample 072897A, where this procedure works quite well. Within such a description, the exhibited single CR peak may be reasonably well approximated by the shape of a

2D CR given by Eq.1.43. When this expression is used to fit the spectra of sample 072897A, an electron concentration of $n_s = 6.2x10^{11}$ cm^{-2} and a scattering time of $\tau = 2.8x10^{-12}$ is found. The effective mass was taken from a fit of the dependence of CR position on magnetic field. This concentration agrees well with that deduced from the magnetic field dependence of photoluminescence spectra (see table 1). However, a single CR peak is clearly not sufficient to describe the traces for the other samples.

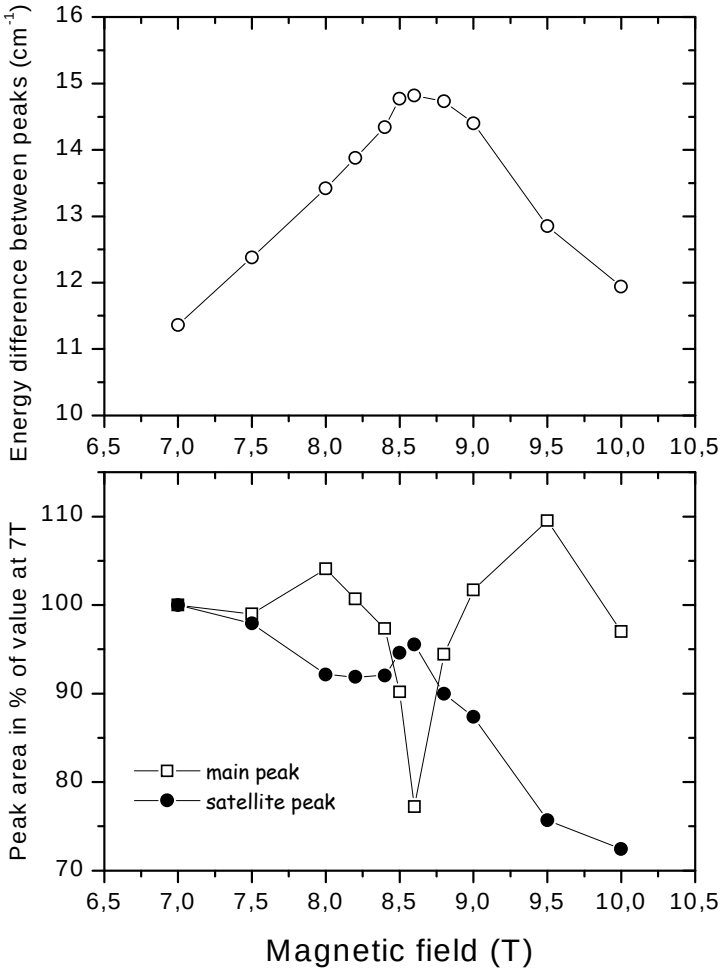

Figure 3.2 : a) Energy difference between the two peaks as a function of the magnetic field. b) Relative changes of the area of both peaks as a function of the magnetic field.

In the low-field behaviour of the CR, for the samples containing Mn the dependence of resonance position on magnetic field does not show any trace of

Zeeman and the cyclotron energy coincidence. Cyclotron resonance experiments have recently shown to be sensitive [Karczewski-2001] to the interaction between both resonances leads to an anti-crossing behavior. In our case, as we will show in next chapter, such energy coincidence is expected for magnetic fields lower than B =1.2 T at T=2 K, region which remains out of the sensitivity of our detector.

3.1.3 Effective mass determination

From the energy position of the main CR peak as a function of the magnetic field we determine the electron effective masses for the samples as shown in Figure.3.3. The mass values are found to be between $0.106m_0$ and $0.110m_0$. The effective mass tends to increase with decreasing electron concentration as is shown in Table 2.

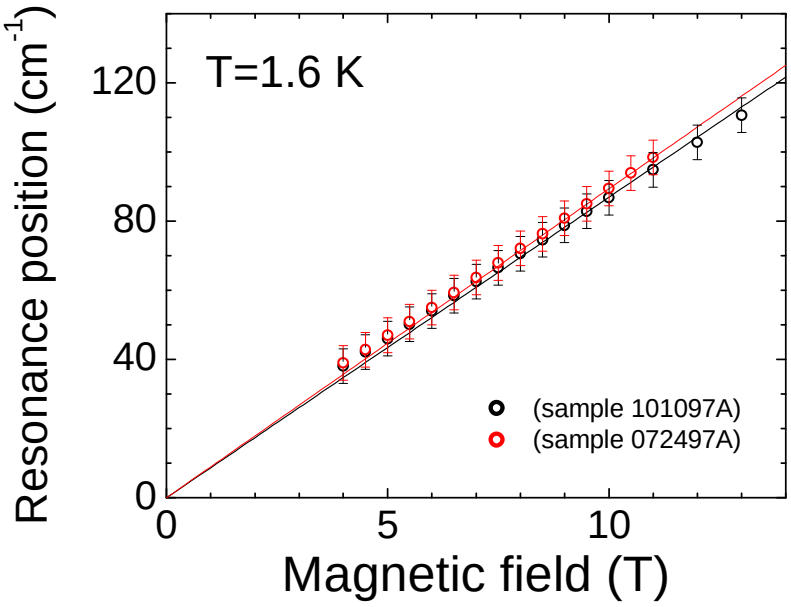

Figure 3.3 : Magnetic field dependence of the resonance position for the different samples (circles). The solid lines represent the corresponding linear fit $\hbar\omega_C$ from which the effective mass is extracted for each sample.

An accurate determination of the effective masses is useful for the subsequent analysis of the magnetic field evolution of emission lines in the optical studies described in chapter 7. Also, in the transport studies the effective mass is a crucial parameter for understanding the magneto-transport properties of a 2DEG confined in a magnetic quantum well, as described in chapter 4.

Sample	Electron mass
101097A	$(0.110 \pm 0.007)\ m_0$
100997A	$(0.108 \pm 0.007)\ m_0$
072497A	$(0.106 \pm 0.007)\ m_0$
072897A	$(0.107 \pm 0.007)\ m_0$

Table2

Conclusions

The cyclotron resonance studies of a 2DEG in CdTe and CdMnTe quantum wells shows clearly resolved CR peaks in the transmission spectra, which yield values of the effective mass around $0.11m_0$, i.e. within expected limits for the edge of conduction band of CdTe [Marple-1963]. The effective mass decreases slightly with increasing carrier concentration. The carrier concentration found from a fit of the Drude formula for the sample 072897A, $n_e=6.2x10^{11}cm^{-2}$, is in good agreement with the value $6.3x10^{11}cm^{-2}$ deduced from luminescence measurements.

Chapter 4

Electrical transport properties of a 2DEG confined in DMS quantum well structures

Introduction

Since the first observation of the Quantum Hall Effect (QHE) in Si-MOSFETS in 1980 by Klaus von Klitzing and coworkers [Von Klitzing-80], the remarkable quantum behavior of two-dimensional electron systems has revealed a vast amount of new, interesting and largely unexpected physics.

Experimentally, most of the subsequent fundamental discoveries and advances in our understanding in QHE research have been performed using GaAs/(AlGa)As based structures. At low temperatures, the electrical transport properties of a 2DEG confined in a GaAs quantum well structure show the typical QHE field dependence in the integer regime as shown in the Figure 4.1. The longitudinal resistance (R_{XX}) oscillates as a function of the magnetic field showing maxima and minima which become more pronounced for higher magnetic fields, whereas the Hall resistance (R_{XY}) evolves from a linear behaviour at low magnetic field to develop quantized $\boldsymbol{n}e^2/h$ plateaus which coincide with the R_{XX} minima appearance. The R_{XX} minima are periodic in inverse magnetic field (1/B) and occur when the filling factor ν is an integer $\boldsymbol{n}$, providing the corresponding gap in the density of states at the Fermi level is sufficiently well defined. In fact, such transport features result from periodic transitions between alternating metallic and insulating behaviour, i.e. from a situation where the Fermi energy lies within a Landau level to a Fermi energy lying in a gap between spin split Landau levels, respectively. Thus, from the minima positions, the number of Landau levels (occupied) below the Fermi level may be determined.

In the high field region where the spin and cyclotron gaps in the density of states are well pronounced one can see minima in R_{XX} and plateaus in R_{XY}

related to consecutive (odd and even) integer values of filling factor. However, at low fields where the disorder plays a crucial role in the definition of the gaps in the density of states, the Zeeman gaps are not resolved. Under such conditions only minima associated with even filling factors are observed. This behaviour is typical for quantum Hall systems in which the Zeeman energy increases linearly with applied magnetic field and is always significantly smaller than the cyclotron energy.

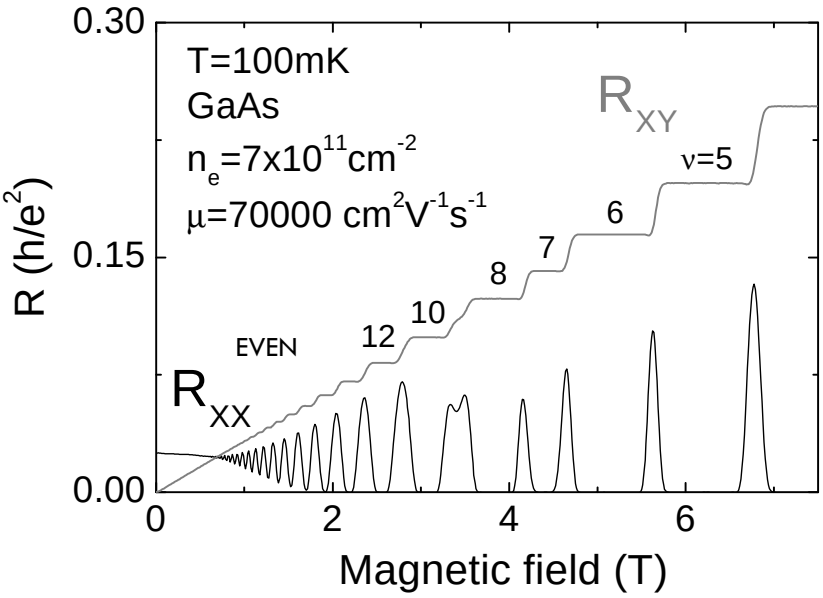

Figure 4.1: Magnetic field dependence of R_{XX} and R_{XY} at T=100 mK for a 2DEG with $n_e=7x10^{11}$ cm^{-2} confined in a GaAs quantum well. Data courtesy of Duncan K. Maude.

In this chapter, we study the magneto-transport properties of a 2DEG confined in a CdMnTe quantum well. In a first part we present the study in the low field region which reflects a strong influence of the giant Zeeman splitting. The observation of nodes of the amplitude of the magneto-resistance at very precise magnetic field allows us to establish a model for describing the effective Zeeman energy with which we quantitatively describe the transport properties at low fields. In a second part, we study the transport properties in the high field region where the effective Zeeman splitting is expected to vanish. An extensive study of the resistance minima evolution associated with filling factors ν=1,3,5 indicates different regions in magnetic field where a crossing and anticrossing behaviour of the spin Landau levels is observed. A possible explanation supported by Raman experiments will be discussed.

4.1 Studies in the low magnetic field region

4.1.1 Landau level crossing effects: beating pattern

As described in chapter 1, Diluted Magnetic Semiconductors offer the interesting possibility of enhancing the electronic spin splitting via the ***s-d*** exchange interaction between the spins of conduction band states and the localized magnetic moments. The total effective electronic Zeeman energy (spin splitting) results from the competition between Zeeman and exchange terms. In the low magnetic field regime, the exchange term predominates and the spin splitting energy acquires the maximum value. With increasing magnetic field, the standard Zeeman energy becomes larger what decreases the total effective Zeeman energy. Therefore, there is a transition to a regime where the cyclotron energy is larger than the total effective Zeeman energy as in systems free of Mn. Such strong non-linear behavior of the spin splitting is expected to significantly affect the transport properties of a 2DEG confined in DMS quantum wells.

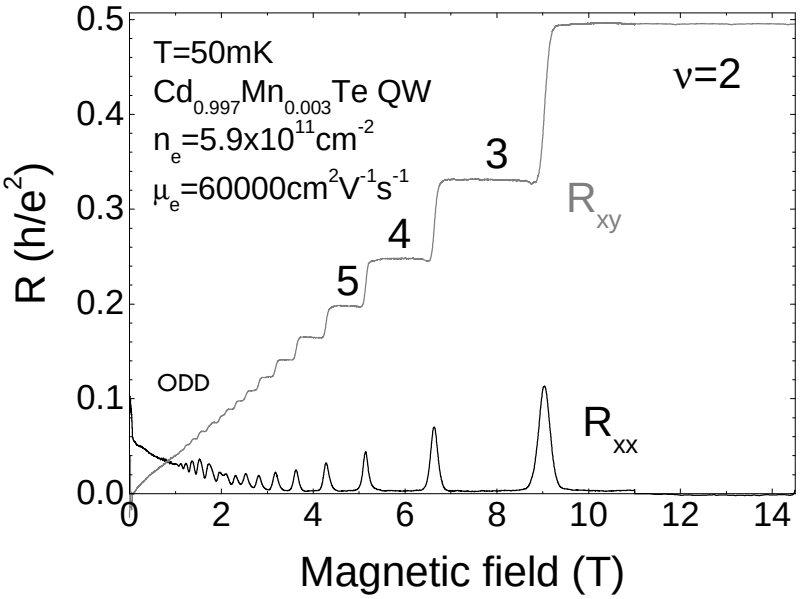

Figure 4.2: Magnetic field dependence of R_{XX} and R_{XY} resistance at T=500mK for a 2DEG with $n_e=5.9\cdot10^{11}$ cm^{-2} confined in $Cd_{0.997}Mn_{0.003}Te$ quantum well.

In Figure 4.2, the Hall (R_{XY}) and longitudinal (R_{XX}) resistance of our high quality CdMnTe quantum well measured at 50mK and for magnetic fields up to 15T are presented. The transport experiment were performed using a Hall bar of

0.5x1 mm (see insert Fig.4.2). The magnetic field dependences of the two resistance components manifest a relative well-defined Landau quantization at low temperatures. R_{XY} presents a large number of well-developed plateaus corresponding to both odd and even filling factors. The rather broad Hall plateaus indicates the disorder present in the Mn doped ternary quantum well [Jaroszynski –1998]. The R_{XX} magnetic field dependence presents well pronounced Shubnikov de Haas oscillations with minima corresponding to filling factors as high as 53 clearly visible (see Figure 4.3 for an expanded view of the low field region). Here odd filling factors are strikingly well resolved at lower fields in contrast to the domination of even filling factors in GaAs structures.

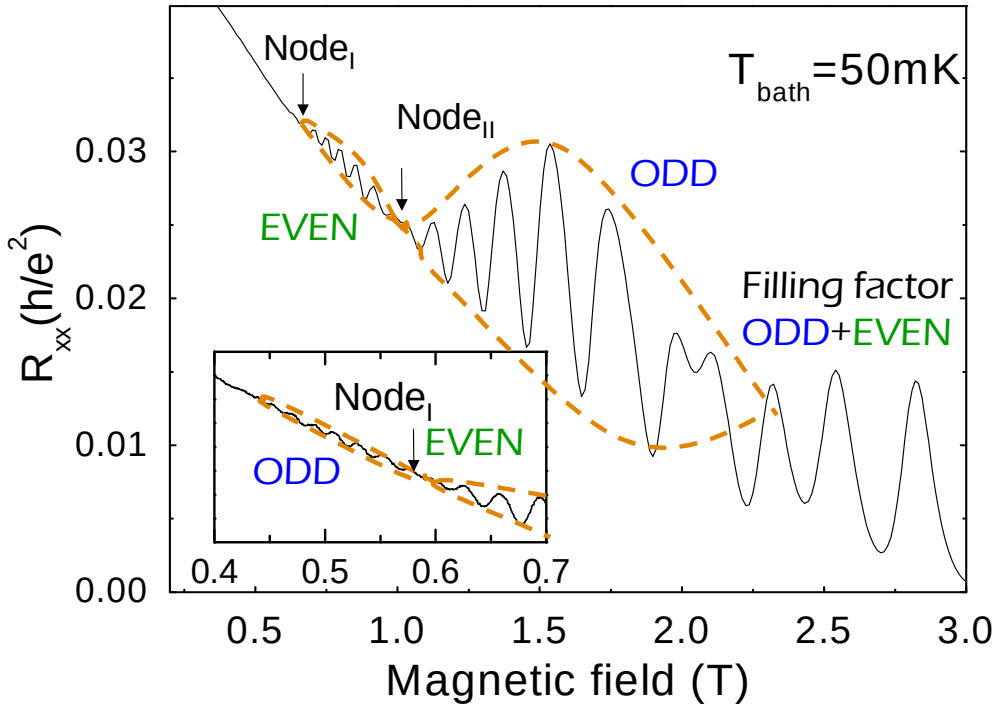

Figure 4.3: Shubnikov de Haas oscillations in R_{xx} at low magnetic fields clearly showing the beating pattern and the existence of nodes. Insert: Detail amplified for clarity of the R_{XX} in low field range.

A closer inspection of the low magnetic field region reveals that R_{XX} minima are clearly observable down to very low fields (down to ~0.5 T for odd filling factors) and the existence of magnetic field regions with different parity of the filling factor associated to the resistance minima. Below ~0.6T only odd filling factors are observed (ν=53-43). In the range ~0.6-1.0T only even filling factors (ν=42-24) can be seen while between ~1.0-2.0 T the minima correspond to odd

filling factors (ν=33–13). Finally above ~2.0 T both odd and even filling factors are resolved (ν=12,11,..,2). Despite the fact that well defined Landau quantization is essential for the formation of a gap in the density of states at the Fermi energy, the Landau level broadening is sufficiently large to suppress resistance minima corresponding to even or odd filling factors depending on the magnetic field range considered. In Figure 4.4, the plot of the reciprocal magnetic field positions of the resistance minima versus filling factor shows the expected linear dependence from whose slope we can determine after Eq.1.34 the 2D-carrier concentration $n_e = 5.9 \times 10^{11} cm^{-2}$.

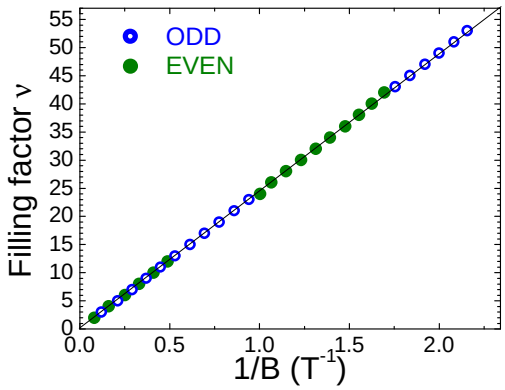

Figure 4.4: Filling factor versus inverse magnetic field position of the minima in R_{xx}. Notice the change in parity of filling factor at the node positions.

The plot also shows magnetic field regions with different parity: starting from low magnetic field the parity is initially odd, then even, once again odd before, at high magnetic fields both odd and even filling factors are resolved. At the same time, a clear beating-like modulation of the amplitude of the Shubnikov de Haas oscillation measured at T = 50 mK is seen in the Figure 4.3. At each transition between odd and even parity a minimum of the amplitude (node) is observed in the envelope of the oscillations. Two nodes labeled as $Node_I$ (~0.6T) and $Node_{II}$ (~1T) are clearly seen at very well defined magnetic field positions. The error in determining the node position is less than the difference in magnetic field between the minima on the upper and lower field side of the node. This value is about 30 mT for $Node_I$ and 80 mT for $Node_{II}$ at 50 mK. Moreover, the node positions are very sensitive to the electron temperature of the system.

On heating the system, the nodes move towards lower fields in distinct temperature ranges as shown in Figure 4.5. $Node_I$ moves from the vicinity of 0.6T at 50 mK to ~0.5 T at 450 mK before the temperature damping effects smear out the

oscillations in this field range. $Node_{II}$ is much less sensitive to temperature and no appreciable change in its position is observed for temperatures below 400 mK. Above 400 mK, $Node_{II}$ shifts to lower magnetic field before damping effects start to smear the oscillations around a temperature of 1 K. Due to the temperature-induced motion of the nodes, the extension and locations of the different parity regions changes with on increasing temperature. As a consequence, the resistance minima at the low field side of the nodes are transformed into maxima and the maxima transformed into minima with increasing temperature as can be seen in Fig.4.5.

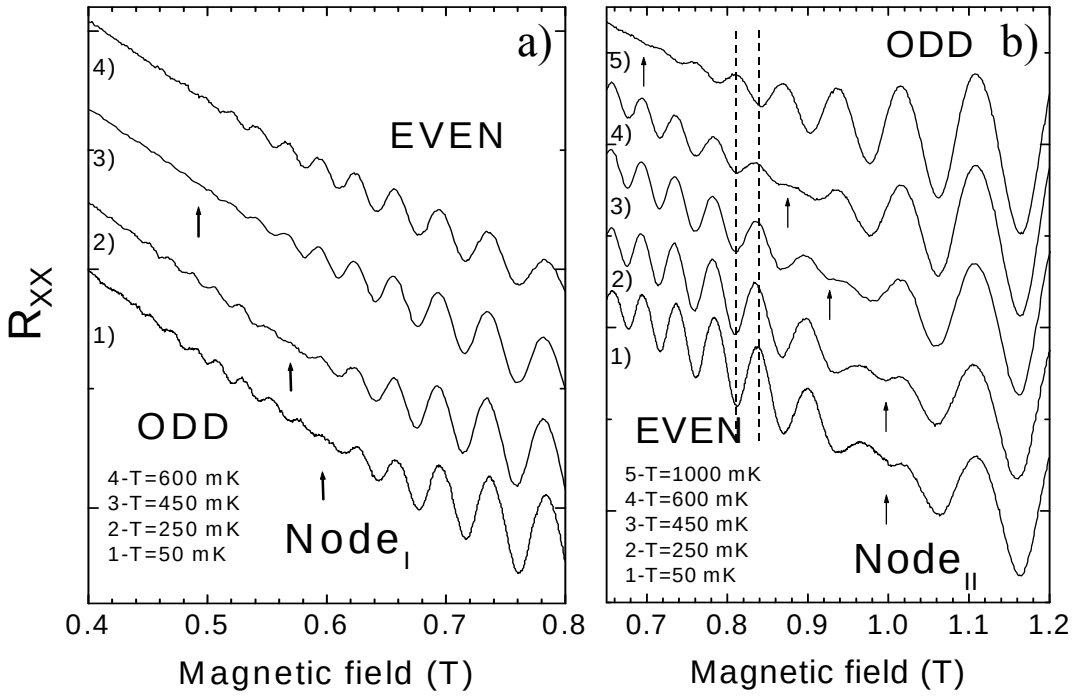

Figure 4.5: Temperature dependence of the magnetic field position of the a) $Node_I$ between 50-600 mK. B) $Node_{II}$ between 50-1000 mK.

Previous investigation of electrons in DMS quantum wells considered how the oscillation shape and plateau appearance are affected by the crossing of Landau levels of different spin states [Gerschütz –1996]. However, the rather low mobility and the higher temperatures at which the measurements were performed limited the investigation to the high (B>2T) magnetic field regime. In order to understand the unusual transport behavior observed in our sample one needs to take into account the specific evolution of the Landau level spectrum due to the non-linear variation of the Zeeman energy with applied magnetic field.

For such DMS materials, the spin splitting is expected to be several times larger than $\hbar\omega_c$ at low fields. Let us consider for example a specific magnetic field B_3 for which $E_Z=3\hbar\omega_c$. The corresponding Landau level occupancy is sketched in Figure 4.6a). Close to B_3 the three lowest energy levels are consecutive Landau levels with the same spin. At higher energies, opposite spin levels from different Landau levels overlap. Thus, when the Fermi energy lies in a well defined gap in the density of states the resistance minima will be associated with an odd filling factor. In contrast for even filling factors close to B_3 the density of states at the Fermi energy is predicted to be a maximum. For magnetic fields close to B_2 (Fig.4.6b) for which $E_Z=2\hbar\omega_c$ the lowest energy levels are two consecutive Landau levels with the same spin. Well defined gaps in the density of states at the Fermi energy and therefore minima in the resistance occur for even filling factors. Finally for magnetic field close to B_1 (Fig.4.6c) for which $E_Z=\hbar\omega_c$, well defined minima in the resistance are expected for odd filling factors. Thus, the parity of the filling factor associated to the R_{XX} minima around B_3,B_2 or B_1 depends simply on the number of lowest Landau levels with the same spin.

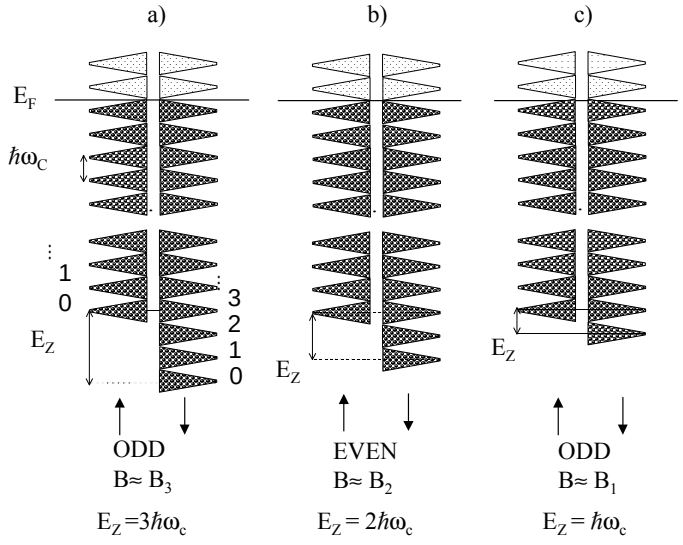

Figure 4.6: Schematic Landau level distribution at the particular magnetic field position $B_{1,2,3}$. It can clearly be seen that the parity of the filling factor corresponding to a minima in R_{xx} depends on the number of filled Landau levels when the Fermi energy (E_F) lies in a gap in the density of states. In the vicinity of those $B_{3,2,1}$ magnetic fields, the amplitude of the longitudinal resistivity shows well pronounced oscillations.

With increasing magnetic field the system will evolve towards the more usual situation in which the lowest energy levels of the system are the N=0 spin

up and spin down Landau levels. This redistribution of the Landau levels will inevitably lead to successive coincidences between spin-up and spin-down Landau levels with different angular momentum which will have a profound influence on the amplitude of the resistance oscillation.

Close to the coincidence points corresponding to $E_Z=(N+1)\hbar\omega_c$ (for N=0,1,2,..) the SdH oscillations are well defined because Fermi energy lies in well defined gaps due to the Landau level overlap. However, this is not the case for the intermediate situations between B_{N+1} and B_N, for instance between B_3 and B_2. The Landau level occupancy for an intermediate magnetic fields $B_{5/2}$ where $E_Z=5/2\hbar\omega_c$ is illustrated in Figure 4.7. Due to the Landau level broadening, no gaps occur in the density of states at the Fermi energy for both odd and even filling factors and the resistance oscillations are suppressed (node) because the Landau levels of a given spin lie in the cyclotron gap of the Landau levels with opposite spin. In general, such node condition satisfies the energy coincidence $E_Z = (N+½)\ \hbar\omega_c$ with N=0,1,2, corresponding to $B_{N+½}$. In samples with lower disorder, rather than nodes, a doubling of the frequency corresponding to the simultaneous observation of odd and even filling factors would be expected. This is indeed what is observed at higher magnetic fields (B>2T) when the cyclotron gap is larger than the disorder induced Landau level broadening. Thus, no node is observed for magnetic fields corresponding to $E_Z=1/2\hbar\omega_c$ since both odd and even filling factors give well defined minima in the resistance.

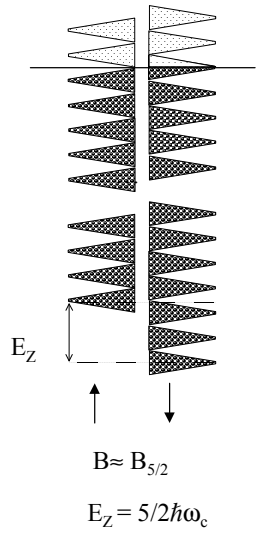

Figure 4.7: Schematic Landau level distribution at the particular magnetic field position $B_{5/2}$. When Fermi energy lies in a cyclotron gap at this particular $B_{5/2}$ magnetic field, no gap in the total density of states exists for any filling factor and the amplitude of R_{XX} shows damped oscillations.

4.1.2 Modeling the Zeeman Energy

Due to the well defined magnetic field position at which the nodes occur, the energy coincidence condition for the occurrence of nodes can be used to experimentally determine the effective electronic Zeeman energy. From the ratio $B_{NodeI}/B_{NodeII} = 0.6\ T/1\ T = 3/5$ it is easy to determine the value of N=1 for which $E_Z = (N+½)\ \hbar\omega_c$ is satisfied at B=0.6T by writing $(N+½)/(N+3/2) = 3/5$. Here we assume E_Z is identical for both node positions, which is a good approximation at low magnetic fields and low temperatures where the exchange term is saturated and dominates the total effective Zeeman energy. Thus, we determine that the energy coincidence $E_Z = 5/2\ \hbar\omega_c$ is satisfied at B_I=0.6T, and $E_Z = 3/2\ \hbar\omega_c$ at B_{II}=1T at 50mK. The temperature dependence of the node positions can then be compared with the predicted temperature dependence of the electronic spin splitting (see chapter 1) given by:

$$E_Z(B,T) = E_{s\text{-}d}B_{\frac{5}{2}}(B,T+T_0) + g_e\mu_B B \qquad \text{Eq.4.1}$$

where $B_{5/2}(x)$ is the modified Brillouin function which describes the ***s-d*** exchange term [Gaj-1976] and g_e the CdTe electronic g factor. For the node condition, we

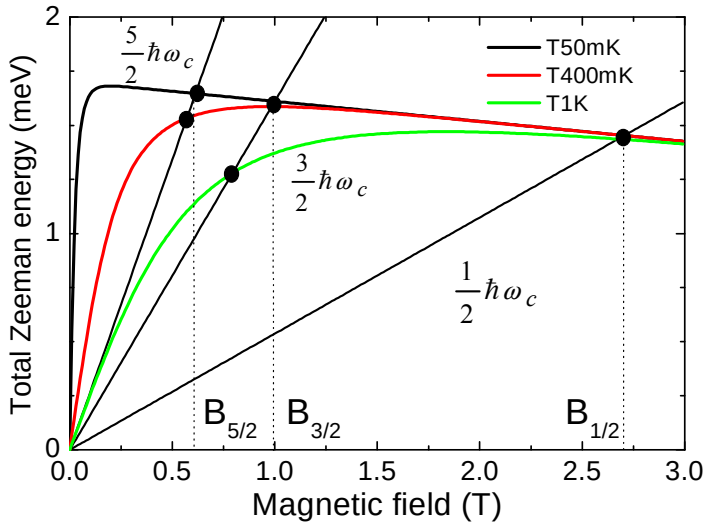

Figure 4.8: Magnetic field dependence of the calculated spin splitting at different temperatures. Half integer (1/2, 3/2, 5/2) of $\hbar\omega_c$ are shown for comparison. The crossing points ($B_{1/2}$, $B_{3/2}$, $B_{5/2}$) correspond to regions of damped oscillations in R_{xx} (nodes). The node conditions move toward low magnetic fields when temperature is increased.

have assumed an electron mass of $m^*_e=0.107m_0$ measured by cyclotron resonance and an effective temperature T_0 constant and equal to 0.18 K, since there is not any contribution of Mn pairs within such temperatures and magnetic field range [Shapira-1990]. The only fitting parameter is the amplitude of the exchange term E_{s-d} which is found to be 1.7 meV in good agreement with the optically measured spin splitting. Using $E_{s-d} = 5/2\ N_o\alpha x_{eff}$ this allows us to estimate the effective Mn concentration $x_{eff} \approx 0.3\%$ in the well. In Figure 4.8, the resulting Zeeman energy is plotted as a function of magnetic field in comparison with $E_Z = (N+½)\,\hbar\omega_c$. It should be noticed that our assumption (E_Z at B_I = E_Z at B_{II}) is quite realistic at T=50mK.

In addition to an externally applied magnetic field, temperature can also be used to modify the Mn spin polarization and thus to tune the electronic spin splitting. At higher temperatures a larger applied magnetic field is required to saturate the Mn spin system and therefore the crossing points in Fig.4.8 are expected to shift towards lower magnetic fields. This explains the shift of the node positions to lower field with increasing temperature as observed in Fig.4.5. From the node condition and using our model for the Zeeman energy, we can easily calculate the magnetic field positions which satisfies the energy coincidence $E_Z = 5/2\ \hbar\omega_c$ and $E_Z = 3/2\ \hbar\omega_c$ for each temperature. The measured magnetic field positions of the nodes as a function of temperature are shown in Figure 4.9. The expected dependence calculated using a Brillouin function with the same parameters as before is shown by the solid lines. The agreement between theory and experiment is quite remarkable. The simple model correctly predicts the node positions and temperature dependence. Thus, the node position can be used as a

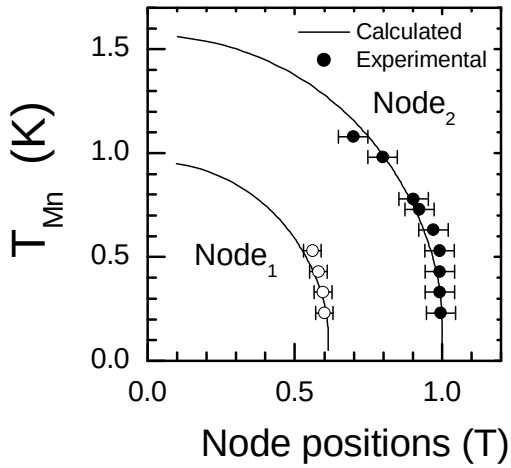

Figure 4.9: Temperature dependence of the node positions in R_{xx}. The solid curves are calculated as described in the text using a Brillouin function to describe the polarization of the Mn system.

thermometer for the effective temperature of the Mn spin system $T_{Mn}=T_{bath} + T_0$. Another direct consequence of the shift in the node position with temperature is the transformation of minima in the resistance into maxima (and vice - versa). This is entirely due to the ***s-d*** exchange induced change in the electronic spin splitting. A redistribution of electron on the Landau levels can be obtained by increasing the temperature at a fixed magnetic field as shown schematically in Figure 4.10. Thus, the resistance change from a minimum to maximum, for instance at B=0.81T (see Fig.4.5), upon increasing the temperature from T=50mK to 1K and can be explained simply by the redistribution of the carrier population in the electronic states as the effective Zeeman energy varies. Decreasing the effective Zeeman energy with respect to the cyclotron energy, the Fermi energy moves from a gap (resistance minima) to a partially full Landau level (resistance maxima). Note however, that the carrier density and therefore the filling factor is temperature independent over the range of temperatures investigated. Experimentally this is easily verified since the magnetic field position of the high field Shubnikov de Haas oscillations remained unchanged.

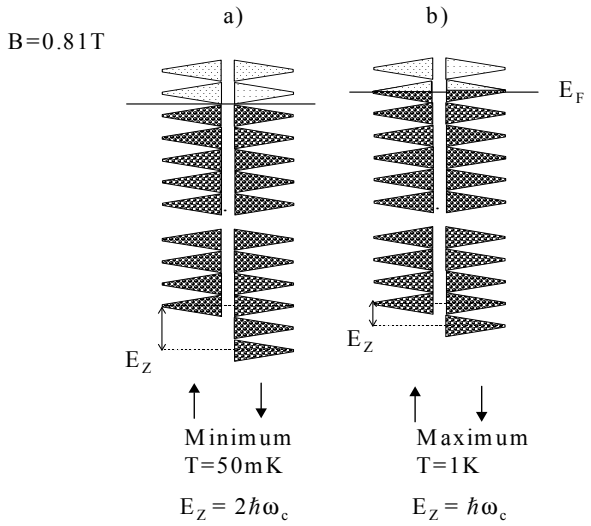

Figure 4.10: Schematic Landau level distribution at the particular magnetic field position B=0.81T corresponding to a minima of R_{XX} for two temperatures.

4.1.3 Simulations of the Density of States

The quantum transport properties of the 2DEG confined in a DMS quantum well are relatively well understood and this allows us to establish a very simple and precise model for the Zeeman energy at low fields. A first step consists of writing all

the latter ideas in equations for describing the competition between the effective cyclotron and spin gaps which determines the distinct beating pattern in the Shubnikov-de Haas oscillations and the magnetic field regions with different parity. For our purposes it is sufficient to consider the description of the density of states for our 2D-electron system surrounded by the magnetic environment. Since the longitudinal resistivity is simply proportional to the density of states at the Fermi energy [Van der Burgt-1995], a qualitative description of our observations can be obtained from a simple simulation of the DOS (details presented in Appendix 2).

Figure 4.11a shows the comparison between the experimental (shifted vertically for clarity) and the calculated data. The agreement is quite remarkable. The simulation is able to closely reproduce the node positions and the modulation of the amplitude of the resistance oscillations. The calculated DOS show minima at the same magnetic field (filling factors) values as the data so that our simple model also correctly reproduces the observed parity changes in different magnetic field regions. The node positions are also properly reproduced when the temperature is increased as can be seen in Figure 4.11b, which shows the measured resistance and calculated DOS at 600mK.

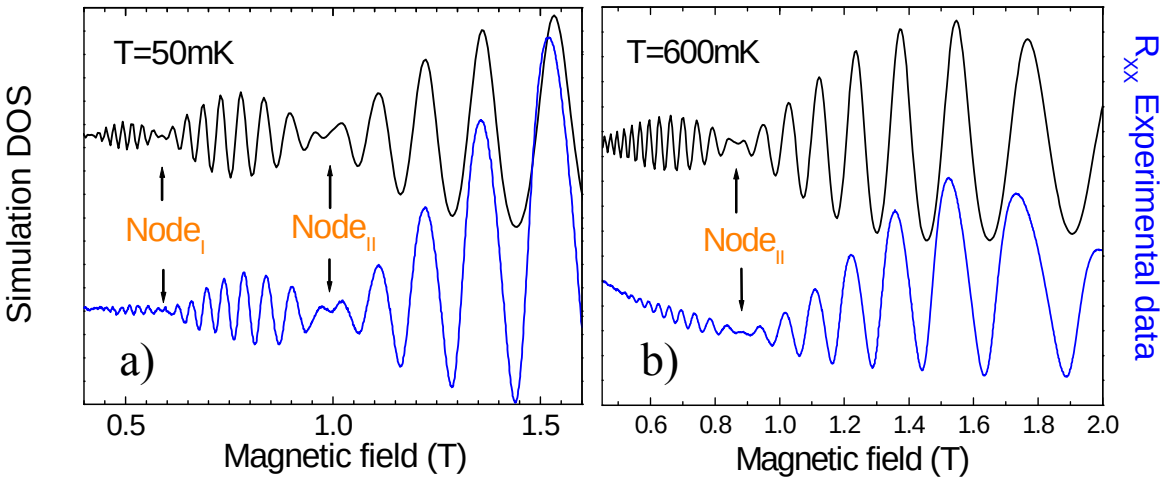

Figure 4.11: Comparison of the calculated Density of States at the Fermi energy with the experimental Shubnikov de Haas oscillations at T=50 mK (a) and at T=600 mK (b).

Thus, we can conclude that the qualitative description of the longitudinal resistivity confirms our ideas concerning the effect of the non linearity of the electronic spin splitting on the quantum transport properties of a 2DEG.

4.1.4 Tuning the Zeeman energy

The ***s-d*** exchange interaction allows to tune the electron spin splitting in a number of different ways. One possibility is to change the Mn temperature via the interaction with the free carriers. Köning and co-workers [Köning-2000] have shown that the free carrier presence is one of the main channels of energy transfer towards the Mn subsystem due to the strong ***s-d*** coupling. Thus, hot carriers can efficiently increase the temperature of the magnetic subsystem. Increasing the current through the sample [Nachwei-1999] generates hot carriers in non equilibrium with the lattice temperature. Since hot carriers are injected, the Mn temperature increases and the node positions can be used as a thermometer to monitor the warming effects. In the Figure 4.12, the current dependence of the $Node_{II}$ position at T=50mK is shown. Increasing the current through the sample is equivalent to increasing temperature as shown in the Fig.4.5. Using the node position as a thermometer it is possible to determine the Mn temperature T_{Mn} corresponding to the applied current. To a good approximation T_{Mn} is found to scale linearly with current *over the limited current range investigated*. The node positions are plotted in Figure 4.13 versus applied current and the equivalent Mn temperature.

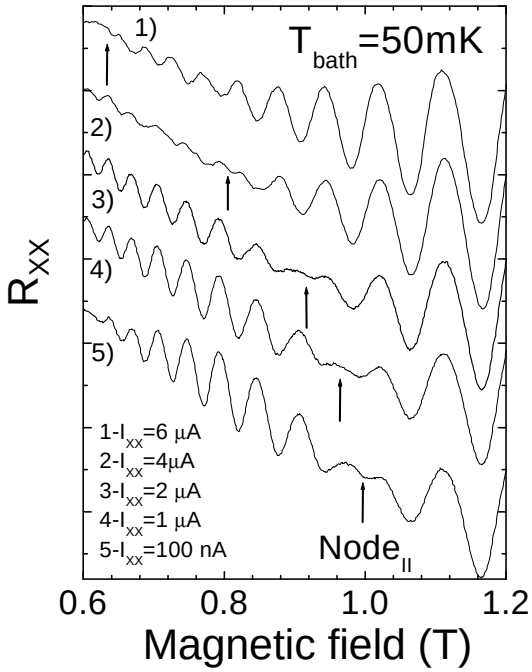

Figure 4.12: Current dependence of the magnetic field position of the $Node_{II}$ at T=50 mK.

Another important point which can be treated from this data is the thermal equilibrium between the lattice, the 2DEG and the Mn subsystem. The thermodynamic principles state that when three different caloric reservoirs are in thermal contact, a heat transfer occurs from the hotter to the colder reservoir in order to establish thermal equilibrium. In solids, the thermal exchange is characterized by the phonon spectrum of the lattice. However, in a diluted spin system such as a DMS the spin-phonon coupling is not the most efficient channel to recover equilibrium [Struzt-1991]. In fact, the efficiency of the spin-lattice relaxation is extremely low in case of very diluted DMS ($x_{eff} < 5\%$) where the Mn spins are isolated entities [Dietl-1995]. An alternative relaxation route can be efficiently mediated by the free carriers, avoiding the difference in the temperature between lattice and Mn subsystem. Recently, [Scherbakov-2000, Köning-2000] the role of the free carriers on the Mn spin relaxation channels have investigated.

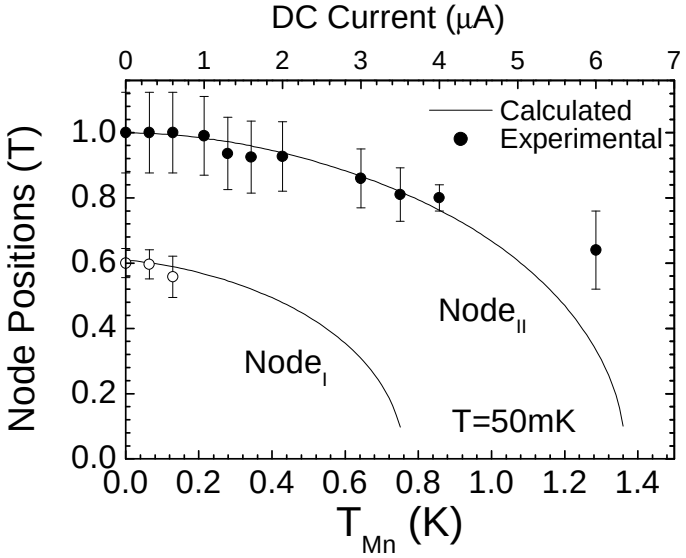

Figure 4.13: Current dependence of the magnetic field position of the nodes in R_{xx} in comparison with the calculated temperature dependence as described above at T=50mK.

The energy-transfer channels between those three different reservoirs in the DMS are schematically represented in the inset of the Figure 4.14. The relevant Mn relaxation channels are not known with any certainty in spite of the fact they constitute a key-point for the spin dynamics in DMS. The lattice represents an infinite bath with respect the Mn and 2DEG subsystems. The phonon coupling between the free carriers system and the lattice dominates the electron-lattice relaxation channel. However, the isolated Mn spin subsystem is weakly coupled with the lattice [Dietl-1995]. Only the clustering of the Mn ions or Mn-Mn pair interactions

can dramatically enhance the efficiency of the coupling of the Mn subsystem to the lattice. Thermal equilibrium is therefore achieved by the mediation of the 2DEG reservoir so that free carriers are responsible for the cooling or warming of the Mn spins.

In fact, from the resistance data for different currents it is possible to estimate the carrier temperature (T_e) by comparing the widths of the high field minima with those from the temperature dependence data at the lowest current (I_{XX}=100 nA). Therefore, T_e can be compared with the Mn temperature (T_{Mn}) for each current as shown in Fig.4.14. The data clearly indicates that the free carrier and Mn subsystem are in a very good thermal contact: the hot carriers efficiently heat the Mn subsystem. The small tendency of the carriers to be slightly warmer than the Mn^{2+} ions may results from the fact T_{Mn} is extracted from the node positions at low fields which could differ at high fields. However, we do not have any real proof the lattice temperature does not change with increasing current. Further investigations to determine with certainty the dominant relaxation channel are required.

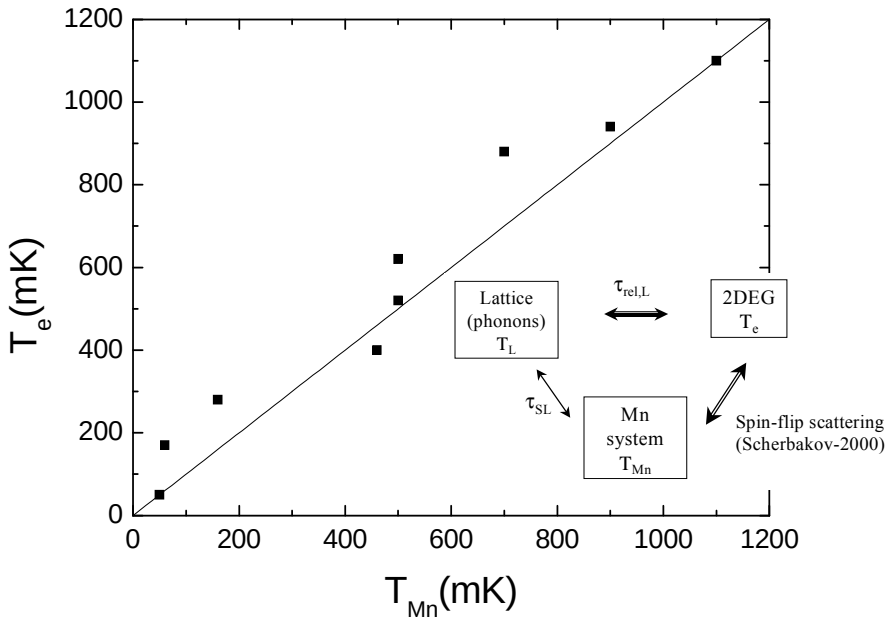

Figure 4.14: Representation of the carrier temperature as a function of the Mn temperature. The solid line denotes T_e=T_{Mn}. Inset: Different energy reservoirs that participate in the Mn heating process in DMS. The relaxation channels responsible for the heating of the Mn systems are denoted by arrows. The most effective channels are shown by double arrows.

Nevertheless, the measure of the Mn temperature that the node positions offer is an efficient method to monitor the electronic spin splitting and consequently the carrier polarization at low magnetic fields.

4.2 Transport studies at high magnetic fields: quantum Hall states at vanishing Zeeman splitting

In the preceding part of this chapter, we have analyzed the transport data obtained at low magnetic fields which can be successfully used to investigate the electron spin splitting. This data supports the idea that in DMS materials the main contribution to the electron spin splitting corresponds to two components: one resulting from the "mean field" ***s-d*** interaction term and the second one resulting from the "bare" Zeeman term. We found that at low magnetic fields, the main contribution for electronic spin splitting is due to the ***s-d*** interaction whereas the "bare" Zeeman contribution is relatively small. However, this is not the case at high magnetic fields. As can be seen in Fig.4.8, the exchange term E_{s-d} saturates at a relatively low magnetic field (the exact value of which depends on the temperature), whereas the "bare" Zeeman splitting increases linearly with field. Since in CdMnTe, the ***s-d*** exchange and the usual Zeeman terms have opposite signs, the total Zeeman splitting (referred in the following as Zeeman splitting, E_Z) is a decreasing function of the magnetic field (once the exchange term becomes saturated) as shown in Figure 4.15. Therefore, there exists a particular magnetic field for which the Zeeman splitting is expected to be zero. Such a situation creates the interesting possibility to investigate quantum Hall phenomena for the specific case of vanishing electron Zeeman splitting.

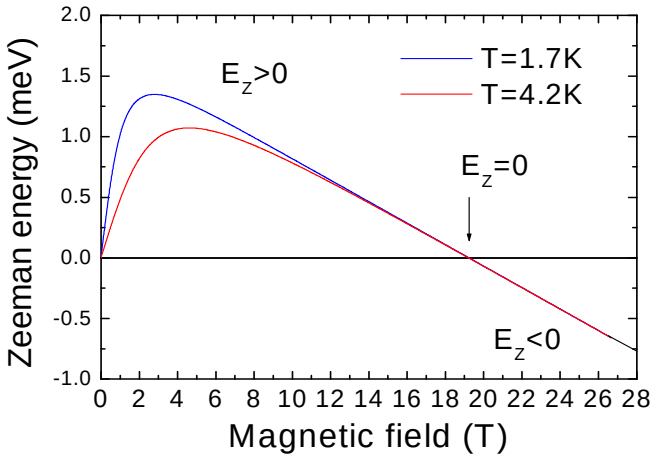

Figure 4.15: Magnetic field dependence of the calculated Zeeman energy at two temperatures.

The studies presented here are complementary to the transport investigations of GaAs/GaAlAs based structures in which the electronic g-factor can be tuned through

zero by application of hydrostatic pressure [Maude-1996]. The later investigations have revealed interesting phenomena related to the interplay between Zeeman and electron-electron interactions in the quantum Hall regime. The role of spin in the quantum Hall effect is still not completely clear and our experiments give some new insight into this subject. The clear advantage of our systems, with respect to III-V structures, is the wider range over which the Zeeman splitting can easily be tuned. Simply by tilting the plane of the 2D electron sheet with respect to the magnetic field direction, we tune the electronic g-factor from positive values to negative values passing through zero independently of filling factor. The disadvantage lies in the inherent low mobility (quality) of the 2DEG, which might be improved in the future. The quantum Hall effect scales with the filling factor, i.e. it depends on the magnetic field component perpendicular to the 2D plane. However, the Zeeman splitting is determined by the total magnetic field. Thus, tilting the magnetic field allows us to obtain the $E_Z=0$ condition for a wide range of filling factors $5<\nu<3/2$.

We start with a description of the transport data under normal field conditions (B perpendicular to the plane of the 2DEG) when the $E_Z=0$ condition is reached around $\nu=3/2$. Subsequently, we will focus on the specific case when $E_Z=0$ at $\nu=3$, and the case $E_Z=0$ at $\nu=5$, before finally discussing a more general case.

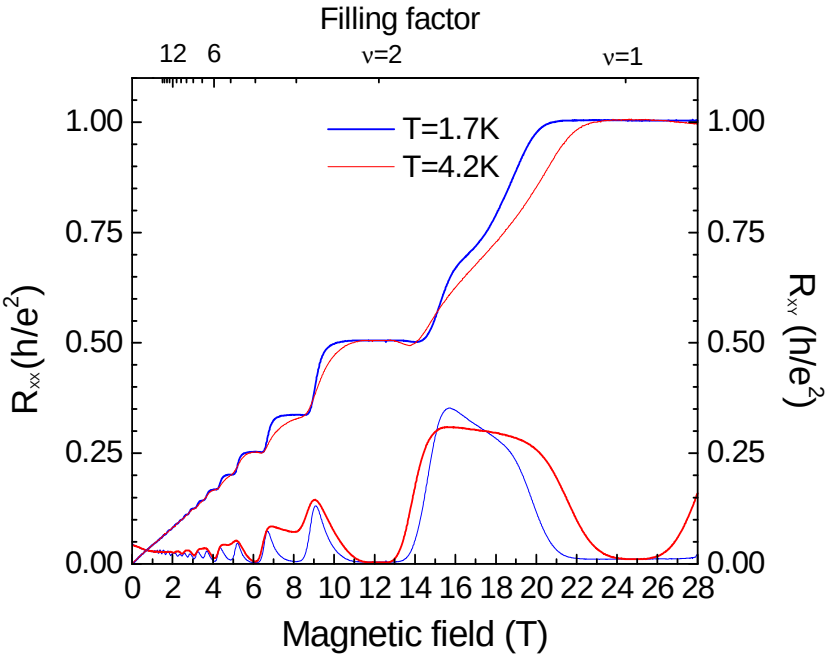

Figure 4.16: Magnetic field dependence of the longitudinal (R_{XX}) and transverse (R_{XY}) resistance for our sample 100997A at T=1.7 K (blue line) and T=4.2 K (red line).

4.2.1 Vanishing Zeeman splitting in the vicinity of filling factor ν=3/2

The Zeeman splitting E_Z expected from the low-field transport model is plotted in Fig.4.15 for two temperatures and for magnetic fields up to 28 T. The spin splitting is calculated using Eq.4.1 assuming $E_{s\text{-}d}$=1.7 meV for the ***s-d*** exchange energy and g=-1.6 for bare electron g-factor in CdTe. As can be seen, the predicted zero value of E_Z occurs at 18.5T. For this particular magnetic field position we would expect important consequences on transport properties of the 2DEG. In Figure 4.16, we show the magnetic field dependence of the longitudinal R_{xx} and transverse R_{xy} resistances measured at two different temperatures (1.7 and 4.2K) over a wide range of magnetic fields. This data was obtained under normal field conditions, i.e. the direction of the applied magnetic field is perpendicular to the 2D plane. Focusing our attention on the R_{xx} maxima around ν=3/2 we observe that the resistance maxima is composed of two peaks which are well pronounced at T=1.7K. At the same time, the Hall resistance shows a clear kink around B=18.5 T, which resembles the development of a quantum Hall plateau.

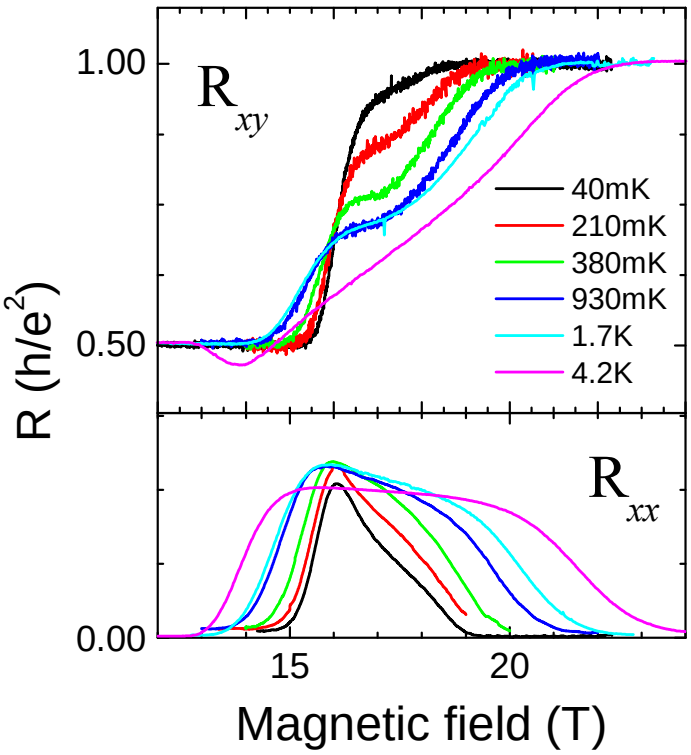

Figure 4.17: Temperature dependence of the R_{XX} and R_{XY} in the vicinity of ν=3/2.

The temperature dependence (40 mK - 4.2 K) of the anomalous behavior of the resistance in the vicinity of 18.5 T is presented in Figure 4.17. As can be seen, our anomaly is quite markedly pronounced at intermediate temperatures but somehow washes out at the lowest temperature. The resistance of our "quantum Hall plateau" apparently changes with temperature which is a first indication that this plateau cannot be related to a 4/3 fractional quantum Hall state.

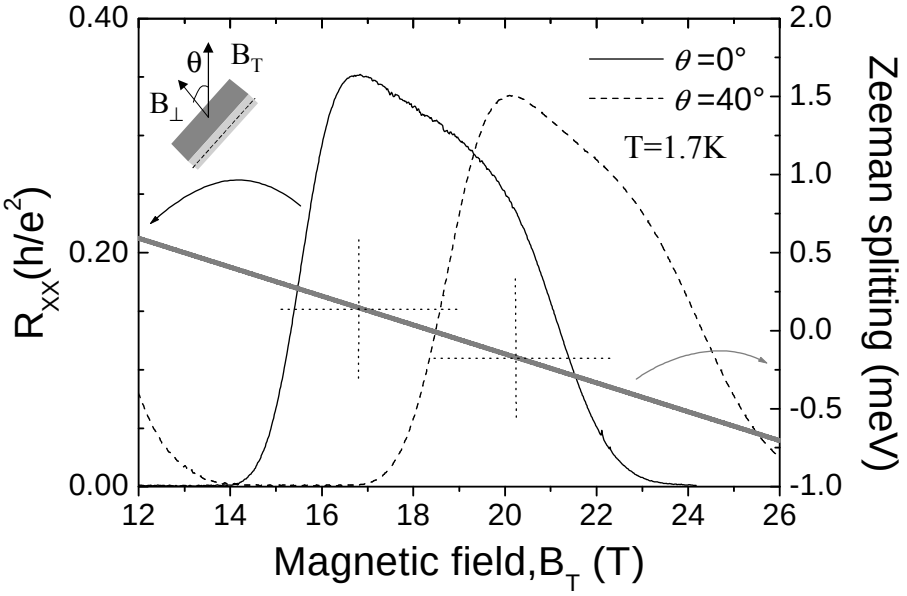

Figure 4.18: Longitudinal resistance R_{XX} (black lines) as a function of the total magnetic field for two angles θ=0 (solid line) and θ=40° (dotted line) at T=1.7K. Calculated Zeeman energy as a function of the total magnetic field (gray line). Inset: experimental geometry.

More information is provided by experiments in tilted magnetic fields. The experimental configuration and the effect of tilting the magnetic field on the transport properties are shown in Figure 4.18. The normal direction of the 2D plane is tilted by an angle θ with respect to the total magnetic field B_T. Tilting the magnetic field shifts the resistance maxima associated to ν=3/2 towards higher values of the total magnetic field. This is because the quantum Hall effect scales with filling factor which is determined by the magnetic field component $B_\perp = B_T\cos\theta$ along the direction perpendicular to the plane of the 2DEG. On the other hand, the Zeeman splitting is given by the total magnetic field B_T and therefore tilting the magnetic fields allows us to tune the Zeeman energy with respect to filling factor as shown in Fig.4.18. In the following we represent the data as a function of the perpendicular magnetic field component $B_\perp$. In such

representation the filling factor is fixed with respect to the horizontal scale but Zeeman energy which depends on the total field is different for each tilt angle θ.

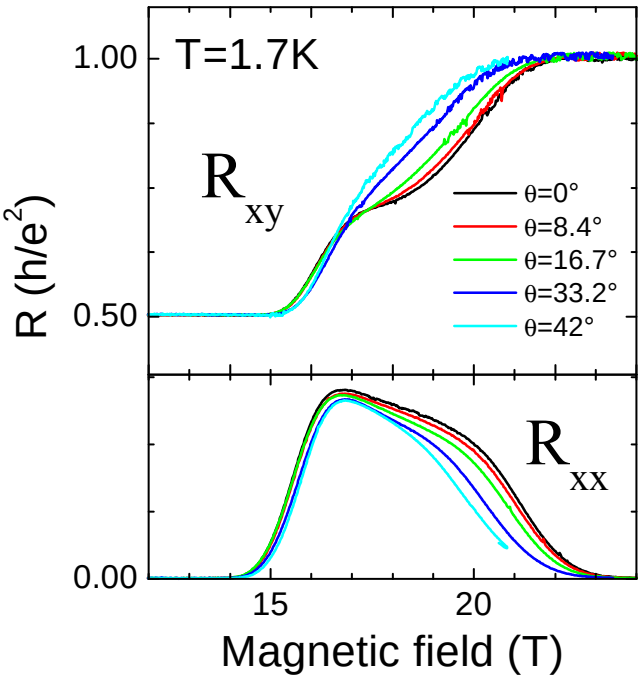

Figure 4.19: Angle dependence of the longitudinal (R_{XX}) and transverse (R_{XY}) resistance as a function of perpendicular magnetic field in the vicinity of ν=3/2.

The traces of R_{xx} and R_{xy} measured at T=1.7K in the high field region for different tilt angles are shown in Figure 4.19. The anomaly around $B_{\perp}$ =18.5 T disappears when the Zeeman energy is sufficiently large. We therefore attribute this anomaly to the expected vanishing of the spin gap. However, these data do not reflect such a vanishing. In a first approximation, we may interpret both peaks in the R_{xx} resistance as corresponding to the situation where Fermi level is located in the center of the (broadened) Landau level. The longitudinal resistance is proportional to the density of states at the Fermi energy. A vanishing of the electron Zeeman splitting would imply a perfect overlap of spin up and spin down Landau levels. Consequently a doubling of the density of states at the Fermi energy, as compared to the case of well separated spin split levels would lead to an increase (doubling) of the resistance which is not the case. The zero Zeeman energy E_Z=0 is expected to coincide with filling factor ν=3/2 for a tilt angle θ=40 ° .

As shown in Fig.4.19, no dramatic changes occur, which is first indication that the spin gap does not completely close under the considered experimental

conditions. The data is more consistent with an anticrossing of the spin-up and spin down Landau levels. However, an analysis of evolution of the resistance maxima is complex and therefore not always very convincing in contrast to the analysis of the resistance minima, which have a physical meaning in terms of activation gaps. As expected, the E_Z =0 condition does not influence resistance minima corresponding to a cyclotron gap around ν=2. For this reason we turn our attention to the higher filling factors.

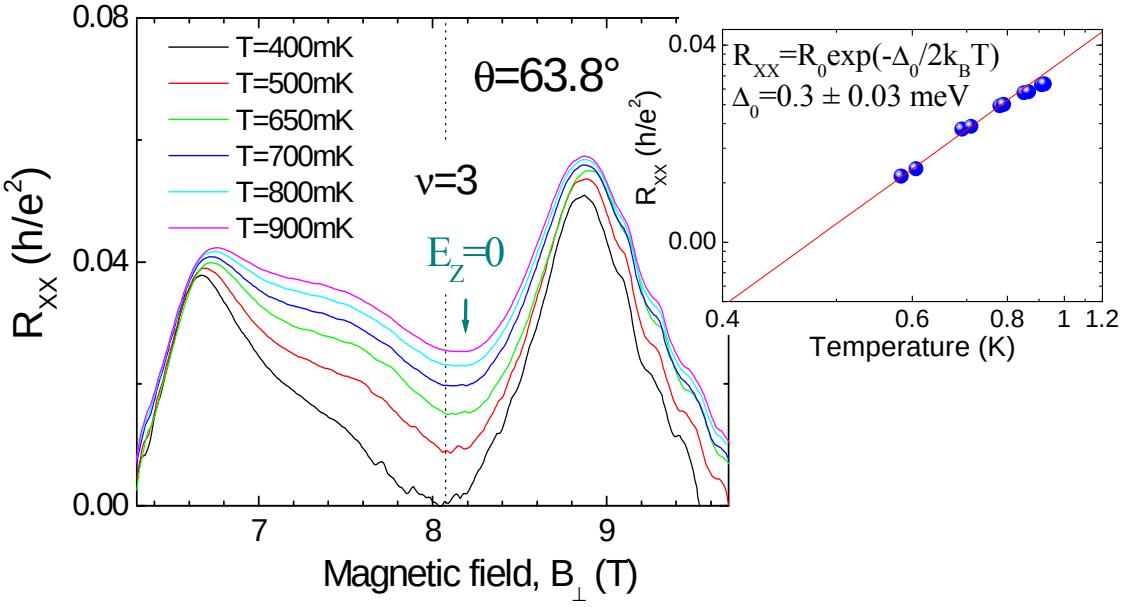

Figure.4.20: Temperature dependence of longitudinal (R_{XX}) around ν=3 for a tilted angle θ=63.8°. At such angle the expected E_Z=0 occurs near 8.1 T (blue arrow). Inset: Arrhenius plot of resistance at ν=3 versus temperature. The red line is a least square fit to the experimental data points.

4.2.2 Vanishing Zeeman splitting in the vicinity of filling factor ν=3

The coincidence of E_Z=0 and the ν=3 is reached by tilting the magnetic field an angle around θ=64 ° as shown in Figure.4.20. The longitudinal resistivity shows a well pronounced minimum at low temperatures (400 mK) which clearly indicates the existence of a small but non zero spin gap. A conventional method of determining the quantum Hall energy gaps is the analysis of the temperature activation of the resistance at the minimum of R_{xx}. The method is based on the assumption that:

$$R_{xx} \propto \sigma_{xx} \propto exp(-\Delta_S/2k_BT) \qquad \text{Eq.4.2}$$

where the spin gap Δ_S, often referred to as the activation gap, can be directly read from the slope of the Arrhenius plot: ln R_{xx} vs 1/T. As shown in the inset to Fig.4.20, the R_{xx} at the ν=3 minimum shows a thermally activated behaviour. The deduced spin gap at conditions of vanishing Zeeman gap (E_Z=0) is $\Delta_S = 0.3 \pm 0.03$ meV.

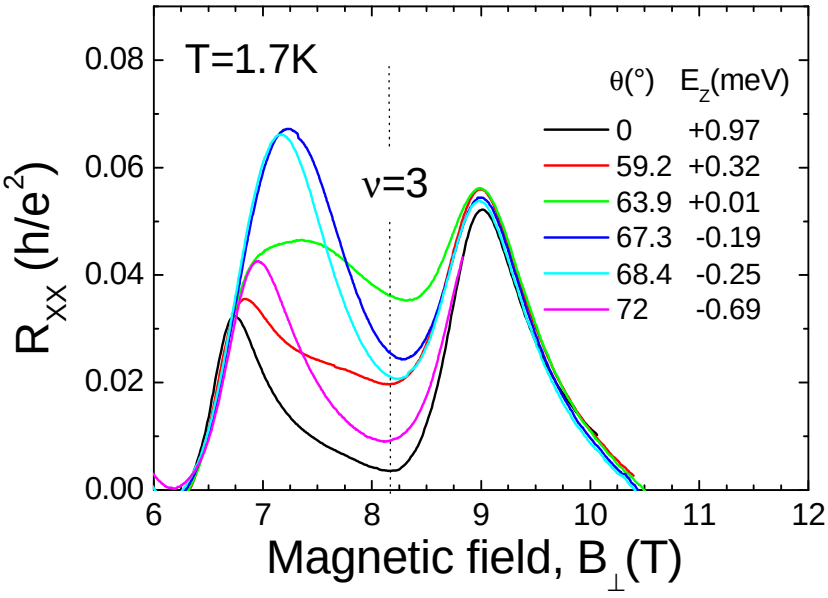

Figure 4.21: Angle dependence of the longitudinal resistance (R_{XX}) as a function of perpendicular magnetic field in the vicinity of filling factor ν=3 at T=1.7K. The values of the effective Zeeman energy (E_Z) at the ν=3 position (dotted line) are indicated for each angle.

Moreover, an interesting evolution of the longitudinal resistance is observed when the E_Z=0 condition is tuned through the ν=3 minima. The traces of R_{xx} at different tilted angles obtained at T=1.7 K are shown in Figure 4.21. The minimum is least pronounced for the curve for which $E_Z \cong 0$ meV (θ=63.9 °) but recovers when $|E_Z|$ is increased by tilting the sample away from this angle. Assuming a thermally activated behavior we can write:

$$R_{xx}\,(\nu=3\,) = R_0 \cdot exp(-\Delta_S(E_Z)/2kT) \qquad \text{Eq.4.3}$$

Calculating the expected E_Z for each tilted angle at the magnetic field position of ν=3 ($B_\perp$=8.17T) we can estimate the ν=3 spin gap for a wide range of

E_Z. We use a value of R_0=27.1kΩ determined from the Arrhenius plot under E_Z=0 conditions in Fig.4.21. Rewriting Eq.4.3 the spin gap:

$$\Delta_S(E_Z) = 2kT(-ln\,(R_{xx}\,(\nu=3\,)) + ln\,(R_0))) \qquad \text{Eq.4.4}$$

can be determined for fixed temperatures from the experimental value of R_{XX} at ν=3 for the different tilt angles. The resulting Δ_S at different tilted angle, i.e. different E_Z value, is shown in Figure 4.22. The values of Δ_S obtained for different temperatures all collapse onto the same Δ_S vs E_Z dependence which validates the assumption of thermally activated behavior. As expected, Δ_S is a minimum for tilt angle of θ=64 ° ($B_\perp$ =8.11 T, B_T=18.5 T), in good agreement with the expected value for which E_Z=0 from our model based on the low field data. Either side of E_Z =0, Δ_S increases approximately linearly.

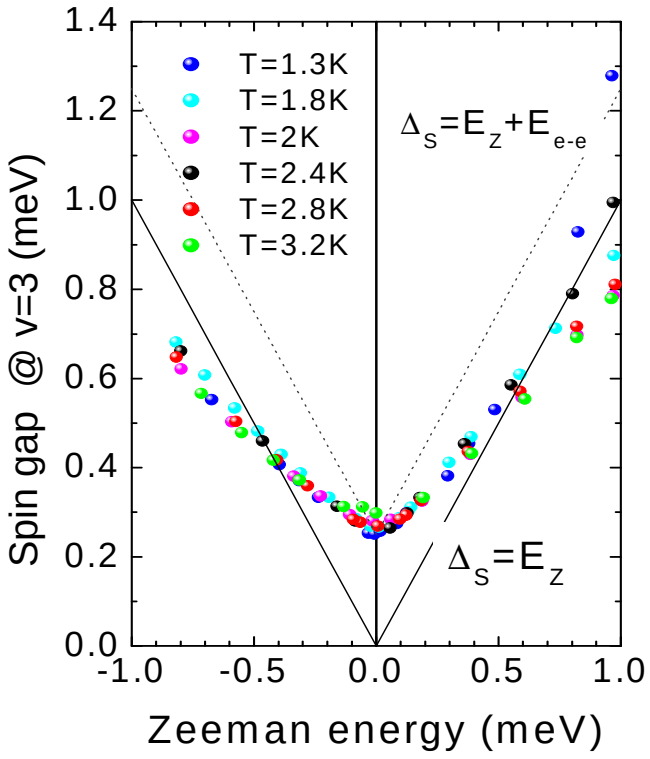

Figure 4.22: Deduced spin gap as a function of the Zeeman energy at filling factor ν=3 for different temperatures. The solid and dot lines represent two distinct spin gap dependence: $\Delta_S=E_Z$ and $\Delta_S=E_Z+E_{e\text{-}e}$.

This is a clear experimental evidence that the ν=3 spin gap remains open even when the Zeeman energy is zero. At first sight, the observation of a finite spin gap at vanishing the effective Zeeman energy ($E_Z = 0$) for the case of a quantum Hall state at odd filling factor is not very surprising. Transport experiments on 2DEG's in GaAs/GaAlAs quantum wells under hydrostatic pressure have shown similar phenomenon at filling factor ν=1 [Maude-1996]. In the case of a high quality 2DEG, the key point in the physics of the quantum Hall regime at odd filling factors is electron-electron exchange interactions. These interactions are responsible for many observed phenomena, the most well known being the so called g-factor enhancement [Usher-1990, Leadly-1998] at odd filling factors which is routinely observed in transport measurements of 2DEGs in GaAs-based structures. Roughly speaking the electron-electron exchange interaction leads to a ferromagnetic ordering of the electronic spins at odd filling factors and therefore any small perturbation opens the spin gap even if the "bare" Zeeman gap is zero.

Assuming that electron-electron exchange interaction plays a role in our case we would, in the first approximation, expect that the dependence of the spin gap on the Zeeman gap is $\Delta_S = E_{e\text{-}e} + E_Z$ (see dotted line in Fig.4.22), with $E_{e\text{-}e}$ as the electron-electron exchange interaction term which is constant for a given filling factor. Our activated transport method to determine the spin gap can be criticized but any corrections accounting for broadening effects would result in a steeper linear $\Delta_S(E_Z)$ dependence and not a shallower one as experimentally observed. We notice, however, that such an interpretation does not fully agree with our data since $\Delta_S \approx E_Z$ when $E_Z >> 0$. We are unable to completely reject the possibility that the non-zero spin gap at ν=3 under vanishing Zeeman energy conditions is due to electron-electron interactions.

Beside, we can also observe in Fig.4.22 that the Zeeman energy dependence of the spin gap shows an asymmetry. Δ_S grows more slowly for negative E_Z (large tilt angles) than for positive. Such behaviour could be related to the uncertainty of our "activation method" to determine the spin gap, which can be influenced by Landau level broadening. However, it still remains as an open question.

4.2.3 Vanishing Zeeman splitting in the vicinity of filling factor ν=5

In contrast to the ν=3 case, the effects of the vanishing Zeeman splitting at ν=5 are easier to understand. As shown in Figure 4.23, at high tilt angles when the Zeeman energy becomes very small the ν=5 minimum R_{xx} is simply washed out. The R_{xx} maxima around ν=11/2 and 9/2 which are clearly observed at large Zeeman energies, merge together into a broader maximum around ν=5 when Zeeman gap becomes smaller. At the same time, the amplitude of the resistance maxima almost

doubles. Assuming that R_{xx} is proportional to the density of states at the Fermi energy, such a behaviour is simply the manifestation of the perfect overlap of the spin split levels at small values of Zeeman splitting. In other words, there are strong indications for the closing of the spin gap at the ν=5 quantum Hall state.

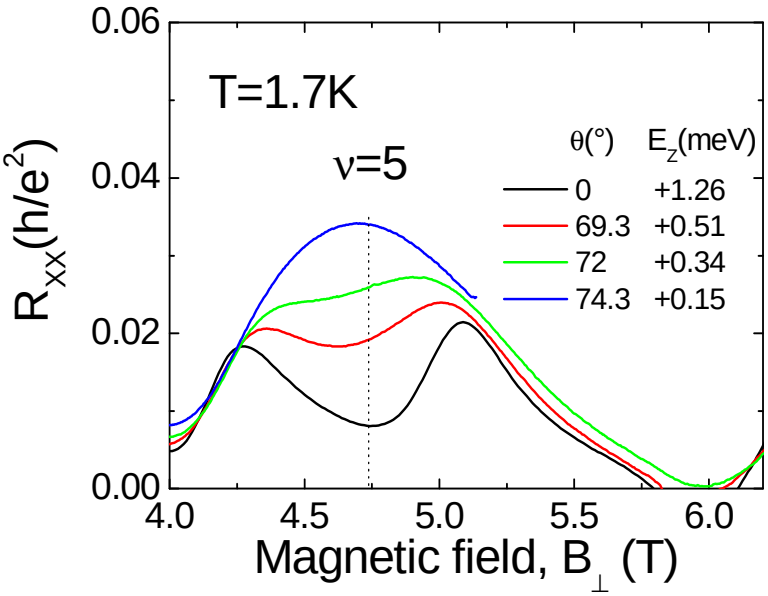

Figure 4.23: Angle dependence of the longitudinal resistance (R_{XX}) as a function of perpendicular magnetic field in the vicinity of filling factor ν=5 at T=1.7K. The values of the effective Zeeman energy (E_Z) at the ν=5 position (dotted line) are indicated for each angle.

4.2.4 Vanishing Zeeman splitting at arbitrary filling factor 3/2 ≲ ν ≲ 5: anticrossing spin levels

In Figure 4.24, we have regrouped the data of the longitudinal resistance measured at 1.7K under conditions of vanishing Zeeman splitting (indicated by labelled arrows) around filling factors ν=3/2, 5/2, 3, 7/2, and 5. There, it can be clearly seen that closing the Zeeman gap leads to a closing of the spin gap in the case of filling factor ν=5 (see f-Fig.4.24). However, this is not the case for ν=3 (arrow d), where the spin gap remains open for any value of Zeeman splitting. The three other R_{XX} traces (b), (c) and (e), show the evolution of the R_{XX} in case the E_Z=0 condition occurs around ν=3/2, 5/2, and 7/2. The essential observation, for our further discussion, is that the resistance maxima of the ν ≈ 3/2 and 5/2 are very weakly influenced by the E_Z=0 condition whereas the ν ≈ 7/2 maximum

roughly doubles in amplitude. Such a different behavior anticipates the conclusion that for conditions corresponding to E_Z=0, the spin gap remains open in case of filling factors $\nu \approx 3/2$ and $5/2$ but closes at $\nu \approx 7/2$.

In order to understand the different behaviour around filling factors $\nu = 3$ and $3/2$ with respect to ν =5, let us recall the basis of the quantum Hall effect in the metallic phase, starting from a distinction between localized and extended states and their distribution in the Landau levels. We assume a Gaussian broadening of width Γ for the Landau levels. In the center of each Landau level there exists a band of extended states, whose broadening is also Gaussian of width $\Gamma_{del}<\Gamma$. For each Landau level the number of the extended states is a fixed fraction of the total number of states (localized and delocalized).

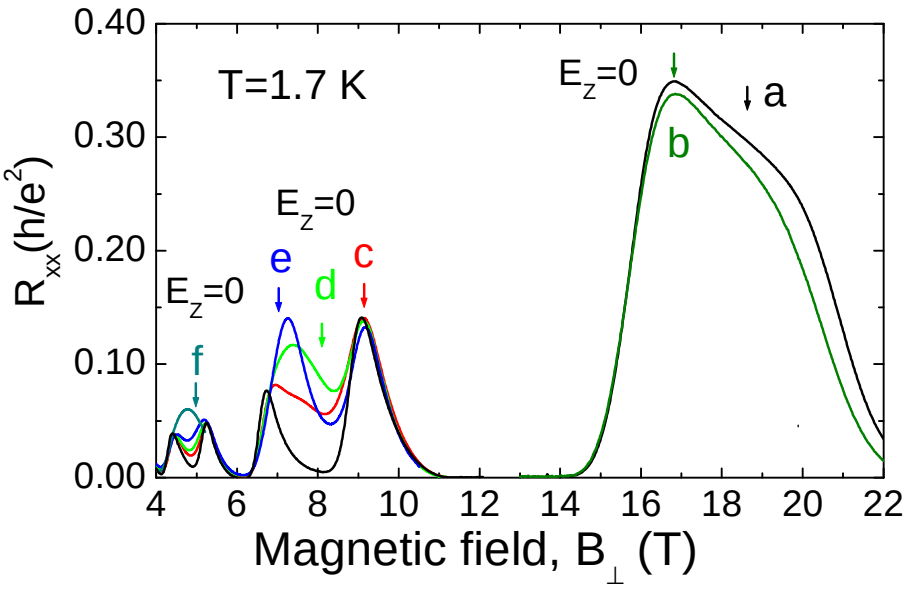

Figure 4.24: Angle dependence of the longitudinal resistance (R_{XX}) as a function of perpendicular magnetic field at T=1.7K for different E_Z=0 coincidences: a) E_Z=0 at 18.5T (black) b) E_Z=0 at 16.8 T (olive) c) E_Z=0 at 9.2 T (red) d) E_Z=0 at 8.2T (green) e) E_Z=0 at 7.3 T (blue) f) E_Z=0 at 5.1T (navy).

The longitudinal resistance shows a maxima when the Fermi level is located in the center of the Landau level. In this situation, the system states in a metallic phase in which only electrons occupying extended (delocalized) states at the Fermi energy participate. One consequence of our model is that the perfect overlap between two spin split Landau levels leads to a doubling of the density of states which in turn would result in a two-fold increase of the resistance as

compared to the case of spin split Landau levels. Thus, within this model we expect that closing the spin gap would result in an overlap of Landau levels and consequently it will imply a doubling of the resistance maxima. Our observation shows that this is indeed the case around filling factor $\nu \approx 7/2$ but not in the case of filling factors $\nu \approx 3/2$ and $5/2$.

Initially, we focus our attention on the case of R_{xx} maximum around $\nu \approx 3/2$. In this case the Fermi energy is expected to be located in the vicinity of the center of the upper branch of the N=0 Landau level. We schematically sketch this in Figure 4.25L. The situation there corresponds to the well separated spin levels and the Fermi energy is located slightly below the center of the upper spin level. Reducing the energy splitting Δ_0 between the center of Landau levels leads to an *upwards shift* of the Fermi level with respect to the center of the upper spin branch. The effect is trivial and results from the decrease of the available density of states at lower energies when the levels overlap and the tails of the lower spin Landau level is pushed up through the Fermi energy.

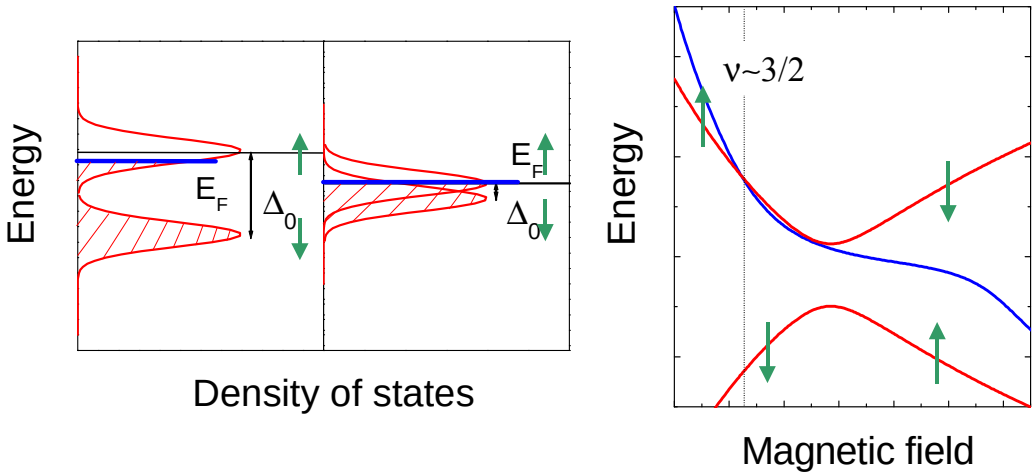

Figure 4.25: Left) Schematic illustrations of the Landau level mixing on the Fermi energy position in the vicinity of ν=3/2. Right) Schematic representation of the Fermi energy position with respect to the center of the spin Landau levels (N=0,↑↓) which anticross as a function of the magnetic field in the vicinity of ν=3/2.

This however is quite essential for understanding of a specific character of the change of Fermi energy with the magnetic field, which is schematically illustrated in Fig.4.25R. In this figure, red traces represent the anticrossing spin levels and the blue line represents the Fermi energy. The Fermi energy crosses the center of the upper spin level around filling factor $\nu \approx 3/2$. Increasing the magnetic

field leads to a progressive downwards shift of the Fermi level with respect to the center of the upper spin branch. However, the effect of approaching both spin levels when increasing magnetic field pushes the Fermi level up. Therefore, the effect of increasing degeneracy (i.e. magnetic field) and at the same time approaching both spin levels results in a non-monotonic behaviour of the Fermi energy position. The exact behaviour of the Fermi level between filling factor 2 and 1, depends very much on the parameters, such as broadening of Landau levels and the amplitude of the anticrossing gap. One possibility is that Fermi energy remains anomalously pinned to the center of the upper spin branch over a wide range of magnetic field. Another possibility is that the Fermi energy crosses twice the center of the upper spin branch, entering in the region of localized states at intermediate magnetic fields as shown in Fig.4.25R. In the first case, the R_{xx} would result in anomalously wide $\nu \approx 3/2$ maxima. The second one would result in a two maxima in R_{xx} with possibility of developing of the quantum Hall plateau in between the two R_{xx} peaks. We believe such a situation agrees with our experimental observations concerning the wide R_{xx} feature with two maxima around $\nu \approx 3/2$ together with a plateau around 4/3 shown in Fig.4.16.

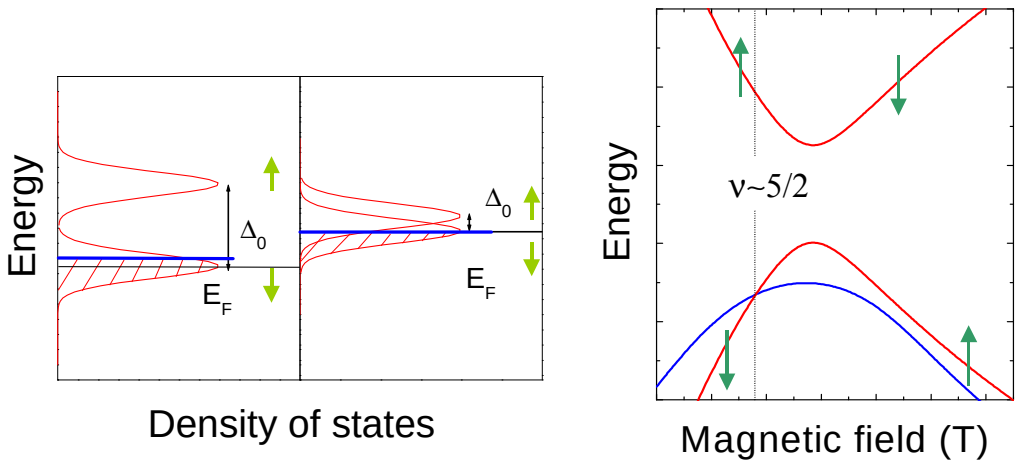

Figure 4.26: Left) Schematic illustrations of the Landau level mixing on the Fermi energy position in the vicinity of ν=5/2. Right) Schematic representation of the Fermi energy position with respect to the center of the spin Landau levels (N=1,↑↓) which anticross as a function of the magnetic field in the vicinity of ν=5/2.

The 'floating' of the Fermi energy induced by approaching the spin levels is distinctly different in case of filling factor $\nu \approx 5/2$. The Fermi energy is now located in the vicinity of the center of the lower spin branch of the N=1 Landau level, as

schematically shown in Fig.4.26L. Reducing the energy separation Δ_0 between the center of the spin Landau levels adds density of states at lower energies which consequently pushes the Fermi level down. Now, the effect of increasing the degeneracy of the Landau levels (increasing magnetic field) and the effect of approaching the spin levels induce a variation of the Fermi level in the same direction. Both effects push the Fermi level down. The resulting Fermi energy crosses quickly and only once through the center of the lower spin branch (see Fig.4.26R).

The different behaviour of the Fermi energy in the anticrossing region in the vicinity of filling factor 5/2 and 3/2 explains the asymmetry in the evolution of the R_{XX} maxima shown in Fig.4.24. In both cases the spin levels clearly anticross and no effect of the doubling of the resistance peak are observed at any value of E_Z.

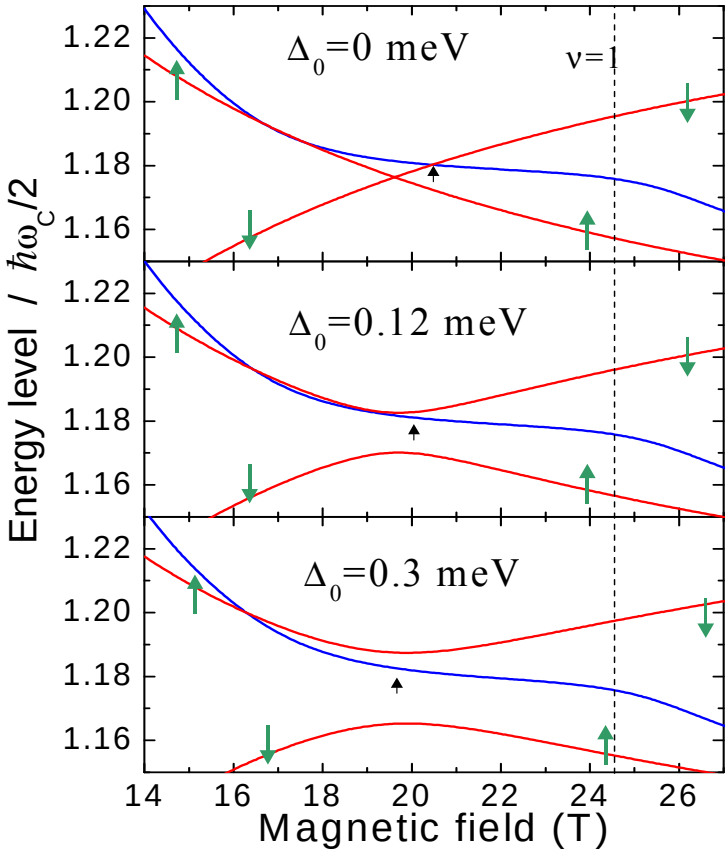

Figure 4.27: Magnetic field dependence of the calculated Fermi energy (blue line) and energy of the N=0-spin levels (red line) position for different values of Δ_0 at T=2K. The energy position of the lowest spin split Landau level is divided by $\hbar\omega_C/2$ for clarity. Black arrows indicate the magnetic field position where a satellite maximum has been observed in Fig.4.28.

However, the manner of anticrossing is slightly different in both cases. At $\nu \approx 3/2$ the longitudinal resistance is sensitive to the anticrossing developing an extra maxima together with a plateau in the Hall resistance, whereas at $\nu \approx 5/2$ the anticrossing is more pronounced leading to no change in the resistance.

4.2.5 Results of numerical simulation of longitudinal resistance

The qualitative discussion of the observed effects presented above allows us to present a more quantitative description of the experimental results. We assume that R_{XX} is proportional to the density of extended states at the Fermi energy and simulate the anticipated anticrossing of spin levels using a simple perturbation approach (see Appendix 2 for more details). The common parameters used in all the simulations presented below are: Γ=0.15meV, Γ_{del}=0.075 meV, an electron effective mass $m^*_e=0.107m_0$, electron concentration $n_e=5.9\cdot10^{11}cm^{-2}$, exchange constant E_{s-d}=1.7meV, T_0=180mK and g_e=-1.6. The simulated R_{XX} traces depend strongly on the "anticrossing parameter" Δ_0, which represents the gap between two spin sublevels in the case of vanishing Zeeman splitting. This is a consequence of the fact that this parameter essentially modifies the 'floating' of the Fermi level with respect to the center of the Landau bands. The influence of the amplitude of the parameter Δ_0 on the position of the Fermi energy around filling factor $\nu \approx 3/2$, under normal field conditions (zero tilt angle) is shown in Figure 4.27. The corresponding traces corresponding to the calculated dependence of R_{XX} are represented in Figure 4.28.

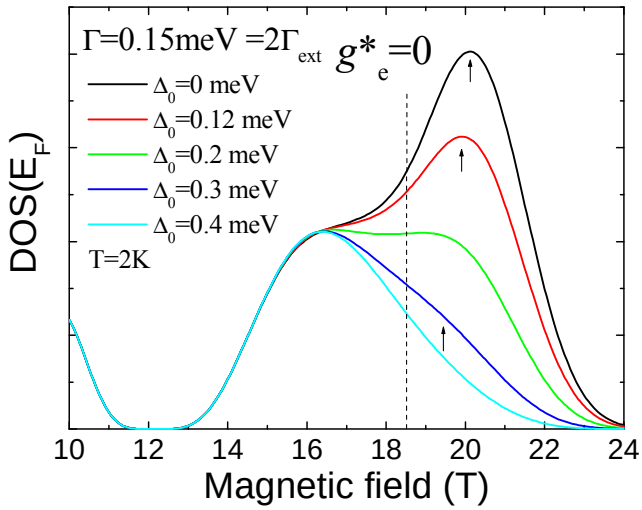

Figure 4.28: Magnetic field dependence of calculated $DOS_{ext}(E_F)$ for different values of Δ_0 at T=2K. The dash line indicates the position of g*=0.

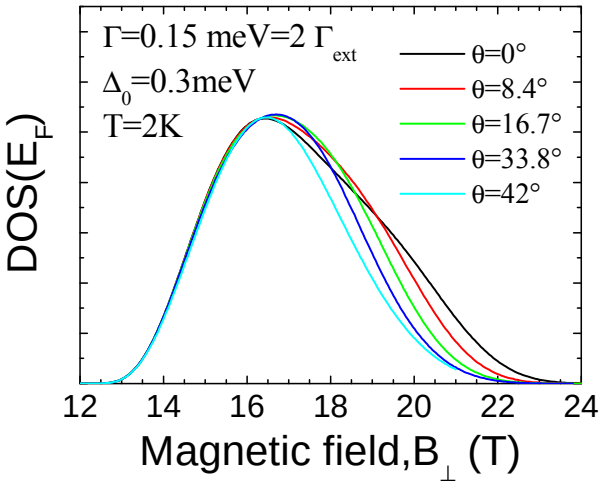

Figure 4.29: Angle dependence of the calculated $DOS_{ext}(E_F)$ in the vicinity of ν=3/2 for a constant Δ_0 = 0.3 meV and T=2K.

Comparing these traces with the experimental results for θ=0° shown in Fig.4.19, it can be seen that a value Δ_0=0.3meV best reproduces the experimental data. Using this value, we model the resistance R_{xx} traces for different tilted angles as shown in Figure 4.29. The simulations are in a good agreement with the experimental data presented in Fig.4.19. They correctly predict the observed broadening at the R_{XX} maxima on the high field side.

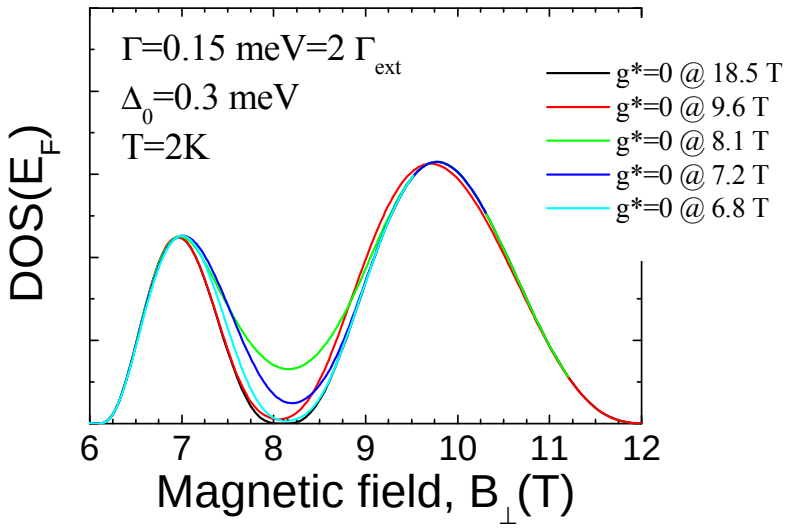

Figure 4.30: Calculated $DOS_{ext}(E_F)$ in the vicinity of ν=3 with Δ_0 = 0.3meV at T=2K. The zero Zeeman energy (g*=0) is noted for each plot.

Now, we turn to the discussion of the shape of the resistance traces obtained in the range of filling factors $4 < \nu < 2$ whose experimental results were shown in Fig.4.21. Using the same constant parameter Δ_0=0.3 meV, the simulation results are shown in Figure 4.30. The simulations are able to roughly reproduce the behavior of the resistance peak around $\nu \approx 5/2$, but it clearly fails in reflecting the doubling of the amplitude of resistance maxima around $\nu \approx 7/2$. The observation of doubling of the amplitude of the resistance peak requires an overlap of the extended states of the two spin components of the Landau level.

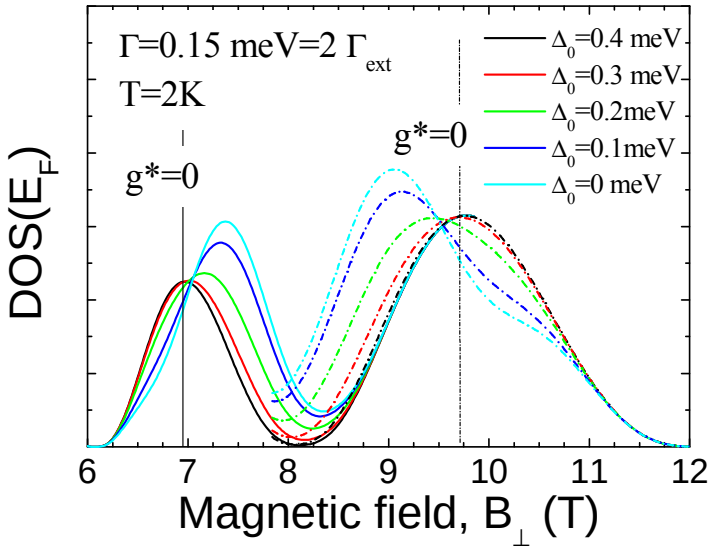

Figure 4.31: Calculated $DOS_{ext}(E_F)$ for different values of Δ_0 at two angles in the vicinity of ν=3 at T=2K. The zero Zeeman energy (g*=0) occurs at the resistance maxima associated to ν=7/2 (solid lines) and ν=5/2 (dash-dot lines).

In Figure 4.31, we show that only small values of the parameter Δ_0 (<0.2 meV) can explain the increase of the R_{xx} resistance peak around $\nu \approx 7/2$ under conditions of vanishing Zeeman splitting. However, such a small values of Δ_0 cannot explain the behaviour of the $\nu \approx 5/2$ resistance peak whose value should remain almost unchanged (see Fig.4.21). There-fore, to explain the experimental data we are forced to assume that in this range of filling factors ($5/2 \lesssim \nu \lesssim 7/2$), Δ_0 changes rapidly with magnetic field (filling factor). A linear change of Δ_0 is unable to explain the experimental results. However, assuming that Δ_0 abruptly increases from zero around filling factor 5/2 (B=7 T) and then saturates at

higher magnetic field, we are able to reproduce the experimental results. The simulations presented in Figure 4.32 are obtained assuming:

$$\Delta_0 = 0.1 \cdot (B - B_0)^{1/2}\ meV \qquad \text{Eq4.5}$$

where B_0=7 T and Δ_0=0 for B < B_0. They fairly well reproduce the experimental observations shown in Fig.4.21.

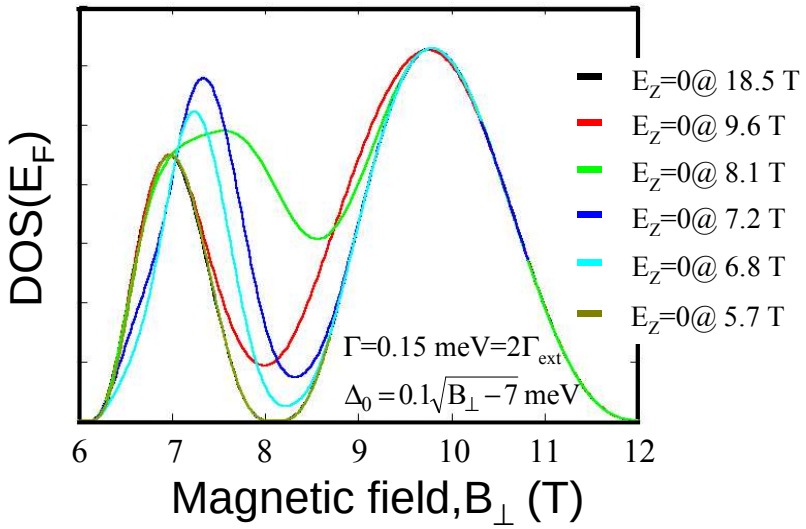

Figure 4.32: Angle dependence of the calculated $DOS_{ext}(E_F)$ in the vicinity of ν=3 considering $\Delta_0 = f(B_\perp)$ at T=2K. The zero Zeeman energy (g*=0) is noted for each plot.

To complete our simulations we consider the longitudinal resistance around filling factor ν = 5 and show that it is possible to roughly reproduce the experimental results (see Fig.4.23) assuming Δ_0 =0 in our simulations as shown in Figure 4.33.

Our numerical simulations support the qualitative description of the experimental data presented in the preceding paragraph and allow us to estimate the amplitude of spin gap for E_Z=0 in the range of filling factors 5/2 ≲ ν ≲ 7/2 and around ν = 3/2. As shown in Figure 4.34, we conclude the spin gap is very likely closed at filling factors ν ≳ 7/2, but appears to be abruptly open around ν = 7/2, takes a value of about 0.2 meV at ν =3, is of about 0.25 meV around ν ≲ 5/2 and 0.3 meV around ν =3/2.

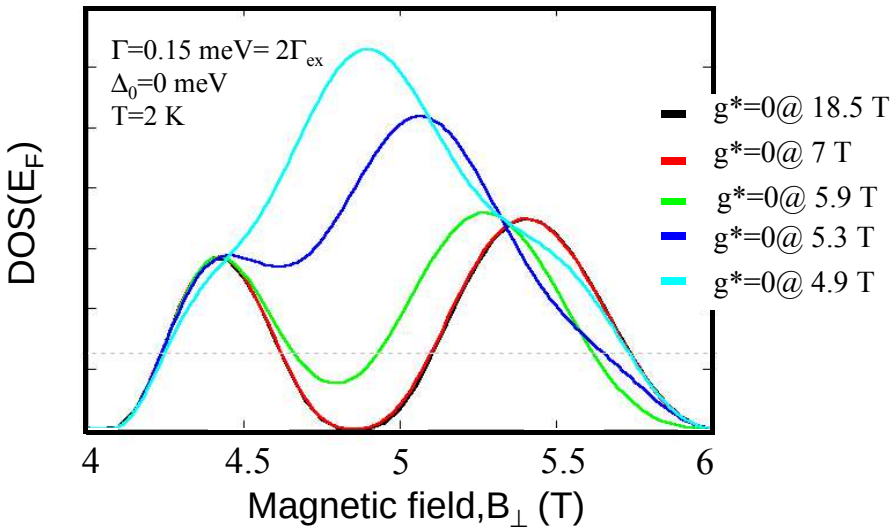

Figure 4.33: Angle dependence of the calculated $DOS_{ext}(E_F)$ as a function of perpendicular magnetic field in the vicinity of ν=5 for $\Delta_0 = 0$ at T=2 K. The magnetic field position of the zero Zeeman energy (g*=0) is labeled for each plot.

Conclusions

Transport phenomena on 2DEG coupled to Mn^{2+} ions in a CdMnTe quantum well have been studied. The results at low magnetic fields can be well understood within the usual model for DMS materials which predicts the giant Zeeman splitting described by the mean-field spin polarization of Mn^{2+} ions as well as by the "bare" Zeeman effect. The low field transport data in combination with the results of cyclotron resonance measurements allow us to precisely determine the ***s-d*** exchange energy and to study the effective temperatures of the manganese spins.

In the high field range we observe that closing the ***s-d*** Zeeman splitting does not necessary imply closing the spin gap. Independently of the condition of vanishing Zeeman splitting the spin gap always remains open for filling factors $5/2 \lesssim \nu \lesssim 7/2$ and around $\nu = 3/2$. We have considered the possibility that the opening of the spin gap under conditions of vanishing Zeeman splitting observed in our sample might be due to the electron-electron exchange interaction. However, measurements of the spin gap versus Zeeman energy at filling factor $\nu = 3$ are not in agreement with this hypothesis.

In order to understand the different evolution of the distinct resistance maxima and minima with E_Z, we consider two distinct methods depending on whether the system lies in an insulator phase (at odd integer quantum Hall sta-

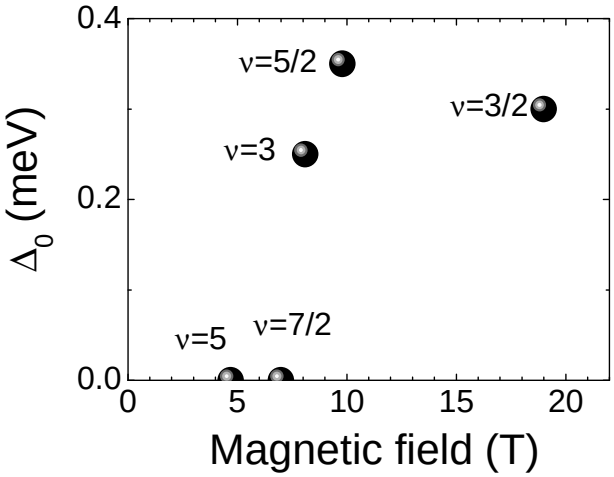

Figure 4.34: Magnetic field dependence of the calculated spin gap Δ_0 at given filling factors ν.

tes, ν=3 and 5) or in a metal phase (at half odd integer quantum Hall states ν=3/2, 5/2 and 7/2). In a first case, an analysis of the temperature activation of the resistance at the minimum of R_{xx} allows us to quantitatively determine the spin gaps. In the second case, one shall reason in terms of DOS. Any overlap between two spin split Landau levels leads to an increase of the resistance as compared to the case of spin split Landau levels, and therefore to a resistance increasing. Thus, the effect of opening or closing the spin gap by tuning the Zeeman splitting can be translated into the effect of anticrossing or crossing of the spin split Landau levels. In fact our data can be more deeply understood when using our model for the longitudinal resistance and simulating the effect of non vanishing spin gap by anticrossing of spin levels.

Measurements of the spin gap in samples with different electron concentrations are needed to clarify the origin of the observed effect. We have not been able to find another sample with good quality electrical contacts, which are apparently extremely difficult to prepare in case of II/VI structures. The spin gaps have been however measured on another sample using Raman scattering experiments. These results will be presented in Chapter 6.

Chapter 5

Electron paramagnetic resonance of Mn^{2+} ions coupled to a 2DEG

Introduction

In the previous chapter, we have focused our attention on band electrons, which exhibit a giant Zeeman splitting at low magnetic fields. However, due to the reciprocal coupling between the electronic and magnetic system, an inverse phenomenon is also expected. The amplitude of the spin splitting between the multiplet states of the paramagnetic Mn^{2+} ions should be sensitive to the free carrier spin polarization. Under such conditions, the magnetic properties observed in DMS will no longer depend only on temperature and Mn^{2+} concentration but also on the presence of free carriers [Galazka-1980, Story-1986, Dietl–1997,Yang-1999]. Recent studies have demonstrated that ferromagnetism of Mn^{2+} spins can be carrier-mediated in p-type II-VI [Ferrand –2000, Haury-1997] as well as in III-V materials [Ohno-1998]. Story and co-workers [Story-1996] determined the free carrier induced shift, similar to the well known Knight shift for nuclear spins, in the Electron Paramagnetic Resonance (EPR) spectra of Mn^{2+} in 3D DMS lead compounds. In a theoretical work, Yang et al. [Yang-2000] have pointed out that measurements of the Knight shift offer interesting possibilities in the case of 2D systems. An interesting point is the character of the ***sp-d*** interaction for the case of Mn^{2+} ions interacting with carriers subjected to the quantum Hall regime.

In this chapter, we present the investigations of Mn^{2+} spins by means of electron paramagnetic resonance measurements. We expect that spin splitting of the Mn^{2+} ions interacting with a 2DEG is not a simple linear function of the magnetic field and search for the limitations of the simple mean-field approach to better describe our system. We show that indeed the Mn^{2+} spin splitting is not linear with the magnetic field. The observed deviations from a linear dependence are difficult to explain when only taking into account the effect of the "usual" Knight shift induced by the electron spin polarization, expected from the mean

field approach. A possible explanation of our experimental results is based on a phenomenological model which assumes an additional interaction between the mean-field spin excitations of Mn^{2+} ions and free electrons.

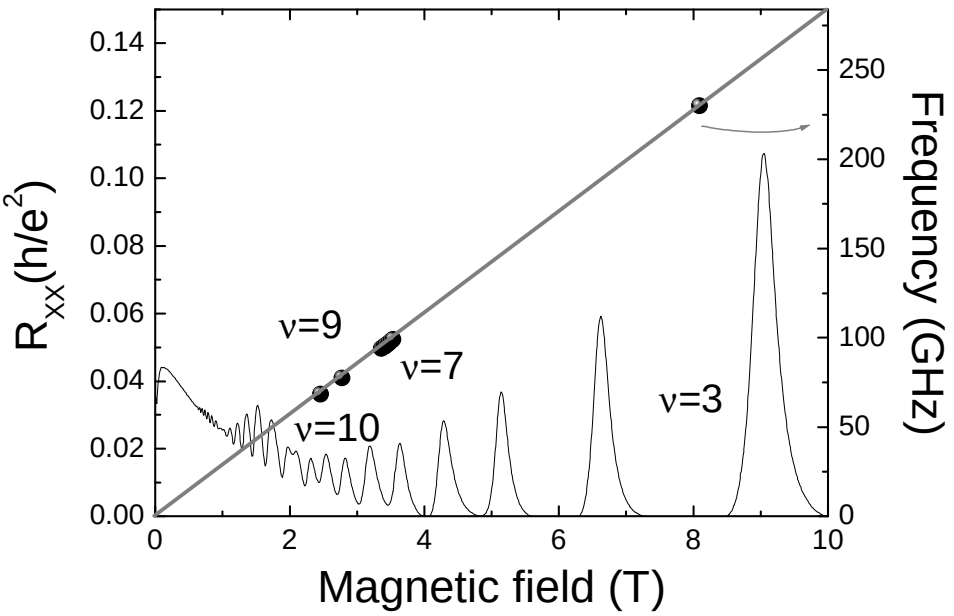

Figure 5.1: Longitudinal resistance R_{XX} as a function of magnetic field at low temperatures (left axis). Magnetic field dependence of the resonant frequencies for Mn2+ ions in the vicinity of ν=10,9,7 and 3 (right axis).

5.1 Experimental details: Resistively detected EPR

The sample used for the experiments was taken from the same wafer studied in chapter 4 (sample 100997A). The active part of the structure consists of a 10 nm-thick CdMnTe quantum well structure. The modulation doping of the structure results in the formation of a 2DEG whose carrier concentration is $5.9x10^{11}cm^{-2}$. The effective Mn concentration in the well is about 0.3%. Our aim is to study the multi-frequency EPR signal of the Mn^{2+} ions embedded in the well. However, this is a difficult task to achieve using conventional EPR methods. Although, a standard EPR spectrometer (at 9GHz) can detect down to 10^{10} spins, this number has to be increased up to 10^{15} spins, for higher resonant frequencies. In our case, the number of Mn^{2+} spins in our quantum well is around $5x10^{13}$. A special method for high field EPR needs to be applied. Therefore, we chose here the possibility of detecting the EPR signal via the resonant changes of the

longitudinal resistivity of a 2DEG under microwave illumination, i.e. resistively detected EPR. In addition to the increased sensitivity, the advantage of this technique is also its selectivity. Using resistive detection, we exclusively probe Mn^{2+} ions in the well and not the residual Mn which could be spread over the rest of the structure. The experiments were performed at helium temperatures (1.7 K – 4.2 K), using carcinotrons and Gunn diodes as the microwave sources. Our two different carcinotron systems are operating in the frequency range 53-79 GHz and 78-120 GHz, whereas Gunn diodes used in experiments supply fixed frequencies of 95, 115 and 230 GHz. The EPR signal has been found for the microwave frequency of 230 GHz, and around ~95, ~77.4, and ~68.4 GHz. Accordingly, the EPR resonances have been observed around B ~ 8.1, 3.4, 2.8 and 2.45 T, implying roughly a g-factor equal to 2 for our resonance. The resonance field positions correspond to the vicinities of the minima in the longitudinal resistance associated with filling factors ν=3,7,9, and ν=10, respectively (see Figure 5.1).

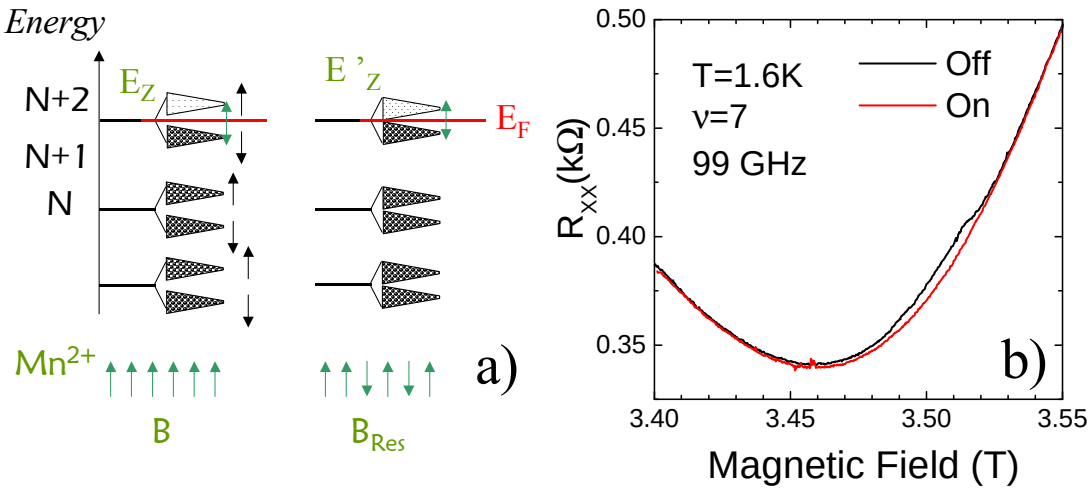

Figure 5.2: a) Schematic representation of the Zeeman gap squeezing at the resonant absorption of the microwave irradiation by the Mn subsystem at a given magnetic field. b) Longitudinal resistance R_{XX} near to ν=7 at T=1.6K with and without 99GHz microwave irradiation as a function of magnetic field.

Due to the *s-d* exchange coupling, any perturbation of the magnetic subsystem is expected to affect the transport properties of the 2DEG. As illustrated in Figure 5.2a, the longitudinal resistivity R_{XX} should be sensitive to the change in the gap between the Landau levels. The change of the Mn^{2+}

magnetization induced by the continuous microwave irradiation (see Figure 5.2a), will therefore be reflected in changes of R_{XX}. This allows us to probe the magnetic subsystem by measuring the resistivity of the 2DEG. The Mn^{2+} ions absorb the microwave irradiation when the energy distance between two Mn^{2+} spin sublevels, $g^{Mn}\mu_B B$, is equal to the energy $h\nu$ of the microwaves, where ν is the frequency.

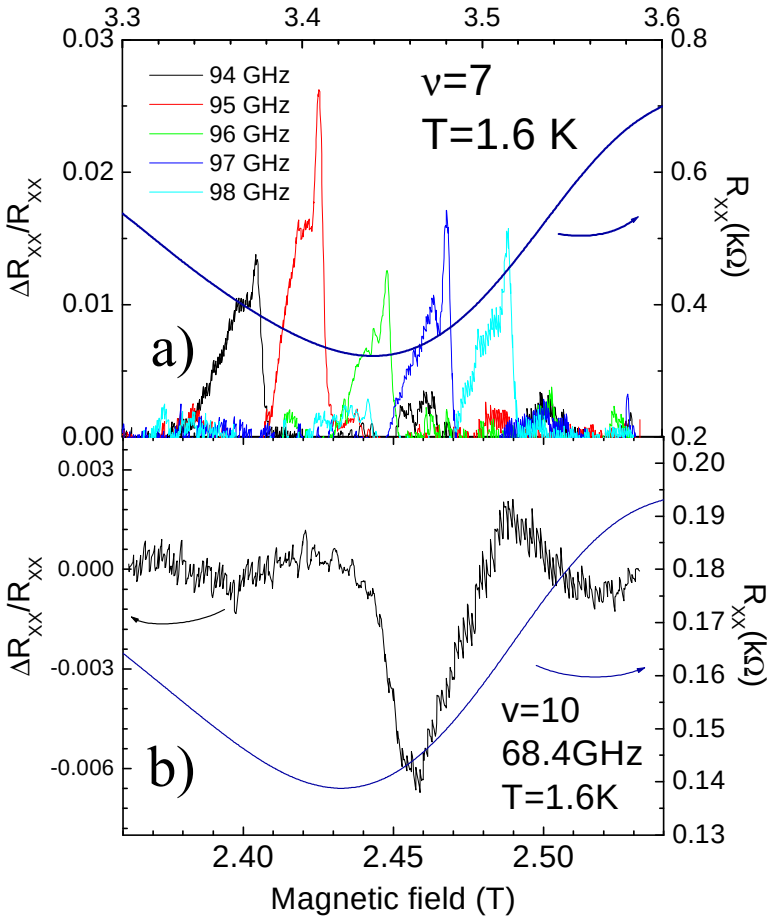

Figure 5.3: a) Relative change of the longitudinal resistance $\Delta R_{XX}/R_{XX}$ (left axis) at T=1.6K for different microwave frequencies near to ν=7. The R_{XX} in absence of microwaves (blue line) is presented for comparison with the resonant position. b) Relative change of the longitudinal resistance $\Delta R_{XX}/R_{XX}$ (left axis) at T=1.6K for 68.4GHz microwave illumination near to ν=10.

Under microwave illumination under resonant conditions, we expect to perturb the thermal equilibrium of the Mn^{2+} spins. The spin polarization of the Mn^{2+} ions will be decreased which results in a reduction of the electronic spin gap, and will in turn be reflected in the change of the resistance of the 2DEG. As

expected, a resonant change of the R_{XX} is observed (see Fig.5.2b). We obtain the EPR spectrum by subtracting a baseline corresponding to the resistivity measurement ($R_{XX}(B)$) without microwaves. The resonance position closely follows the variation of the microwave frequency as shown in Figure 5.3a. The reduction of the spin gap by the resonant Mn depolarization leads to a positive amplitude of the EPR at odd filling factors. However, a resonant decrease is observed at even filling factors as shown in Fig.5.3b, since the cyclotron gap is enhanced by the a reduction of the spin gap (see Fig.5.2a). In the experiments we used two types of microwave sources. The advantage of carcinotrons is the possibility to tune the frequency but these microwave sources are quite unstable both in power and frequency. Most of the data discussed below were therefore obtained using Gunn diodes operating at 95 and 230 Ghz.

We have placed a "g-factor marker" close to the sample which consists of a DPPH powder sample. Its EPR spectrum is well known and serves to calibrate the magnetic field precisely and therefore to determine the absolute value of the Mn^{2+} g-factor. An Allen-Bradley carbon resistance was used as a bolometer in order to detect the EPR spectrum of DPPH. More details about the construction and installation of the "g-factor marker" are given in Appendix 3. The experimental arrangement allows us to simultaneously measure the Mn^{2+} and DPPH resonances.

The experiments show that the observed EPR resonance has quite different behavior if measured at low or high magnetic fields.

5.2. EPR resonance at low magnetic fields

5.2.1 Line shape: temperature dependence

In Figure 5.4, the manganese resonance near B~3.4 T (ν~7) is shown for two temperatures. At this magnetic field and low temperatures (4.2 K-1.6 K) the spins of the Mn^{2+} ions are almost completely polarized. At T=4.2K the resonance shows a rather symmetric shape and is composed of six equally intense and equidistant lines. The signal observed at T=4.2 K corresponds to a characteristic EPR spectrum of Mn^{2+} with a well resolved hyperfine structure [Deigem-1967]. Due to the strong localization on the ion site of the 3d shell, each spin state (S_Z) shown in Fig.1.5 splits into six sublevels (AS_ZI_z, where I_z = -5/2, -3/2, ..., +5/2) as a consequence of the hyperfine coupling with the Mn nuclear spin I=5/2 (see insert Fig.5.4b). The observed hyperfine-split components correspond to different allowed transitions ($\Delta m_{S,i\text{-}f}=\pm 1$, $\Delta m_{I,i\text{-}f}=0$ [Goldstein-1966]) between states with distinct nuclear spin projections I_z, indicated by arrows in the insert of the

Fig.5.4b. The separation between hyperfine split components estimated from our spectra is 48.6×10^{-4} cm^{-1}, in agreement with the hyperfine constant $\boldsymbol{A}= 57.5 \times 10^{-4}$ cm^{-1} reported for bulk CdMnTe [Deigen-1967].

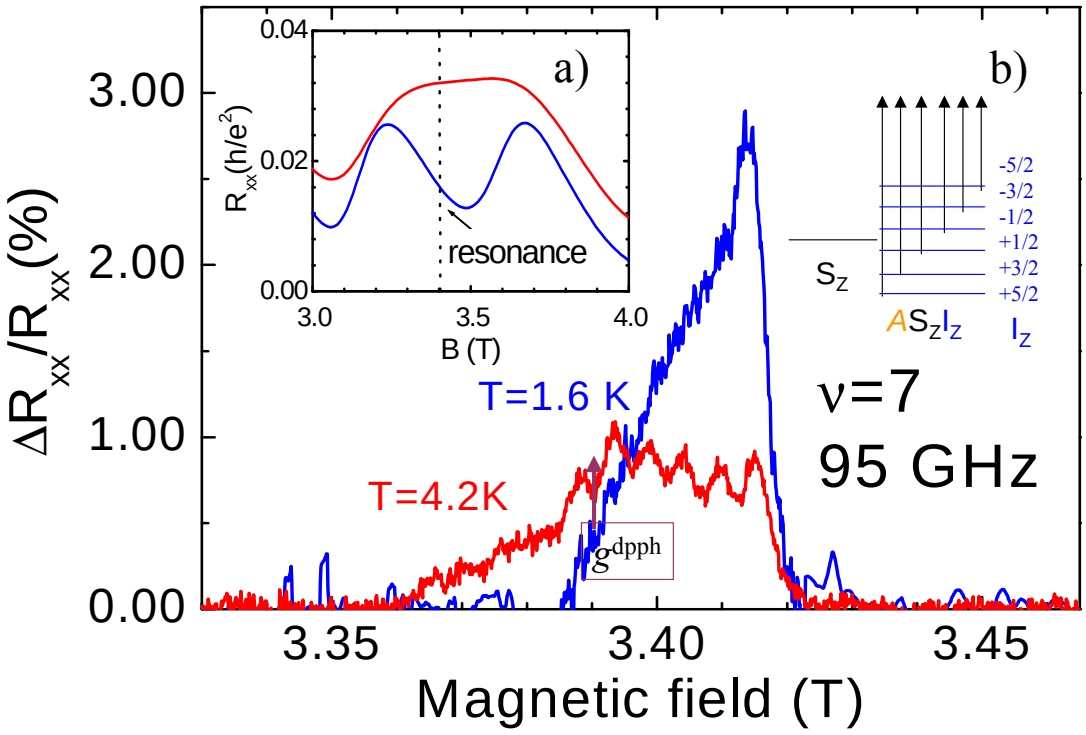

Figure 5.4: Relative change of longitudinal resistance $\Delta R_{XX}/ R_{XX}$ with and without microwave illumination at 95GHz at two different temperatures near to ν=7.The arrow indicates the DPPH resonance position. Inset: a) R_{XX} for T=4.2K and 1.6K without microwave illumination. Notice the appearance of the minimum associated to ν=7 with decreasing the temperature. b) Schematic representation of the allowed transitions between Mn^{2+} states after accounting the Hyperfine interaction.

On decreasing the temperature (T=1.6 K), the resonance shape becomes asymmetric. The amplitudes of the hyperfine components are far from being equally intense: those components at low fields decrease or even disappear, whereas the high field components gain intensity. At first sight, this would seem to indicate an appreciable polarization of the Mn nuclear spins. However, we believe that this must be a dynamical effect since the temperature is too high to expect such a large polarization of Mn nuclear spins in thermal equilibrium.

5.2.1.1 Effect of the dynamical nuclear spin polarization

In order to account for the dynamical polarization of the Mn nuclei and its sensitivity to the temperature in the range 4.2 K-1.6 K, we consider three spin subsystems in our sample as shown schematically in Figure 5.5: 1) spins of the Mn^{2+} nuclei, 2) spins of the Mn^{2+} ions and 3) spins of the free carriers. The presence of the free electron spins seems to be essential for the observed effects since no nuclear spin polarization has been observed in undoped CdMnTe at these temperatures [Lambe-1960]. Although nuclear spin relaxation can be expected to be a slow process [Berg-1990], EPR measurements on undoped CdMnTe do not usually show the effect of nuclear spin polarization [Deigen-1967]. We therefore consider that direct spin flip-flop processes between the spins of the Mn^{2+} ions and their nuclei are inefficient. For these reasons, we propose the possibility of a dynamical nuclear polarization mediated by the free carriers spins [Paget-1977].

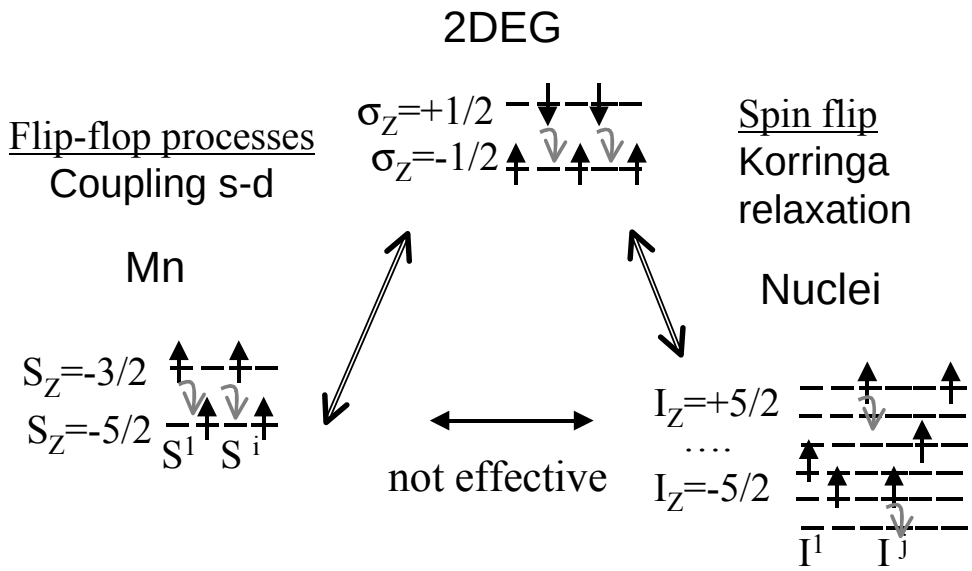

Figure 5.5: Schematic representation of the inter-coupling between the three subsystem: 2DEG, Mn^{2+} magnetic spins and nuclei. The arrows indicate the relaxation processes between them.

We can interpret this as follows. The nuclear spins may be dynamically polarized via a two-step flip-flop process. The microwave pumped spins of Mn^{2+} ions relax their spins via a flip-flop process with the free-electrons spins [Koning-2000] subsequently, the band electrons relax their spins via a flip-flop processes with the nuclear spins. In this way, the nuclear spin system can be dynamically

polarized depending on the rate of the nuclear spin relaxation. To explain our data, we further speculate that the nuclear spin relaxation in the sample is determined by the Korringa process [Korringa-1950]. The flip-flop process between the Mn nuclear spins and the free electrons spins may only involve electrons in the vicinity of the Fermi energy and their efficiency is therefore proportional to the density of states at the Fermi energy [Berg-1990]. One can consequently deduce that the rate of nuclear spin relaxation can be suppressed at low temperatures when R_{XX}, which is proportional to density of states at the Fermi energy, clearly decreases (see insert Fig.5.4a).

5.2.2. Resonance position

As shown in Fig.5.4, at low fields the Mn^{2+} EPR spectrum is seen on the high field side of the DPPH signal. Considering g=2.0036 for DPPH, we deduce a Mn g-factor = 1.9993 for both temperatures since the position of the spectrum is weakly dependent on temperature. In the case of ν =7, and only focusing on the highest field hyperfine satellite, a shift towards lower fields of only about 20 G is deduced on decreasing the temperature from 4.2 K to 1.6 K. The small temperature driven shift is not surprising. It could be related to a small change in the electron spin polarization under these experimental conditions. We have not found any change either in the shape or in the resonance position when varying the sweep rate (between 1 and 7 G/s) or the sweep direction of the magnetic field.

5.3. EPR spectra at high fields

At high fields, in the vicinity of filling factor ν=3 (B ~8 T) the resonance is detected as a single line. The shape of this single line has a width (~250 G) at the lowest temperature (1.6 K) which corresponds to the maximum spacing between the hyperfine split components which are not resolved. However, in contrast to the low field regime, the resonance position in this high field regime is at a lower field with respect to the position of the DPPH marker resonance. This clearly indicates that the magnetic field dependence of the Mn^{2+} EPR is not a linear function. Moreover, the spectrum is also much more sensitive to the temperature variation: i) it becomes twice as broad when decreasing the temperature from 4.2 K to 1.6 K, ii) the position of the Mn^{2+} signal shifts towards lower fields as temperature is lowered. This is seen in Figure.5.6, where the EPR spectra measured in the vicinity of ν=3 are depicted. At the same time, a second resonance simultaneously appears very close to the DPPH resonance position at

T=1.6K. A shift as large as 250 G is observed for the main resonance when the temperature decreases from 4.2 K down to 1.6 K, indicating an increase of the Mn^{2+} spin splitting. Possible reasons for the change of the Mn^{2+} spin splitting beyond the linear field dependence are discussed below.

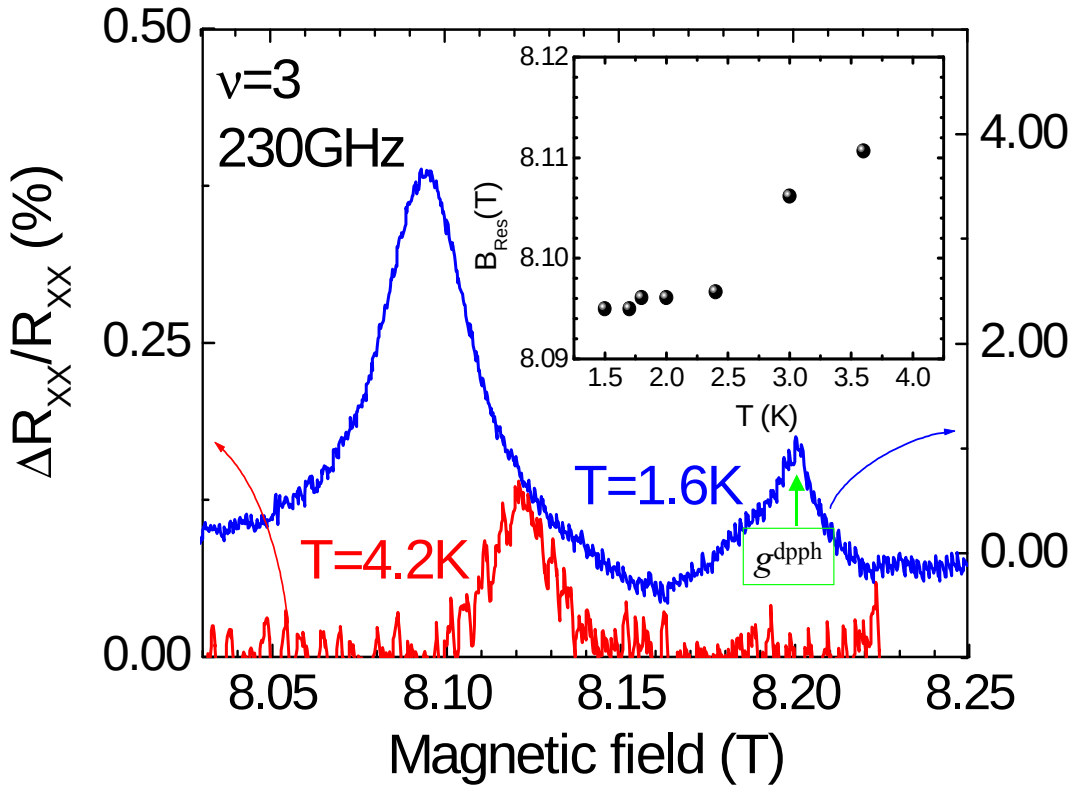

Figure 5.6: $\Delta R_{XX}/ R_{XX}$ for a microwave illumination at 230 GHz, at two different temperatures in the vicinity of filling factor ν=3. The arrow indicates the DPPH resonance position. Inset: temperature shift (solid circles) of the Mn^{2+} EPR positions.

5.4 Resonance position as a function of the magnetic field: Anomalous " Knight shift"

Our data concerning the position of EPR spectra at different magnetic fields can be analyzed in two different ways in order to emphasize the deviation of the resonance position from the linear field dependence. This deviation can be represented either as the change (increase in our case) of the Mn g-factor, or as the appearance of an extra magnetic field (expected in the first approximation to

be induced by the spin polarization of the carriers). In the first case, the g-factor can be directly determined from the EPR spectrum simply using the microwave frequency ν and the magnetic field position of the resonance. From the resonance condition:

$$h\nu = g^{Mn}\,\mu_B B_R \qquad \text{Eq.5.1}$$

we obtain the values shown in Figure 5.7 (open circles) at the lowest temperature T=1.6 K. Although all the obtained values differ from the Mn^{2+} g-factor measured in bulk CdMnTe, g=2.005 [Deigen-1967] the differences are small. It is however extremely surprising that a large change (up to 2%) in the Mn^{2+} g-factor is observed between EPR spectra measured at low fields and those detected around 8.1T. Story et al. [Story-1996] showed that a similar change was observed at 3.5 T in a bulk lead compound but with doping level of 10^{20} holes/cm^3 which represents an extreme requirement for shifting the g-factor value.

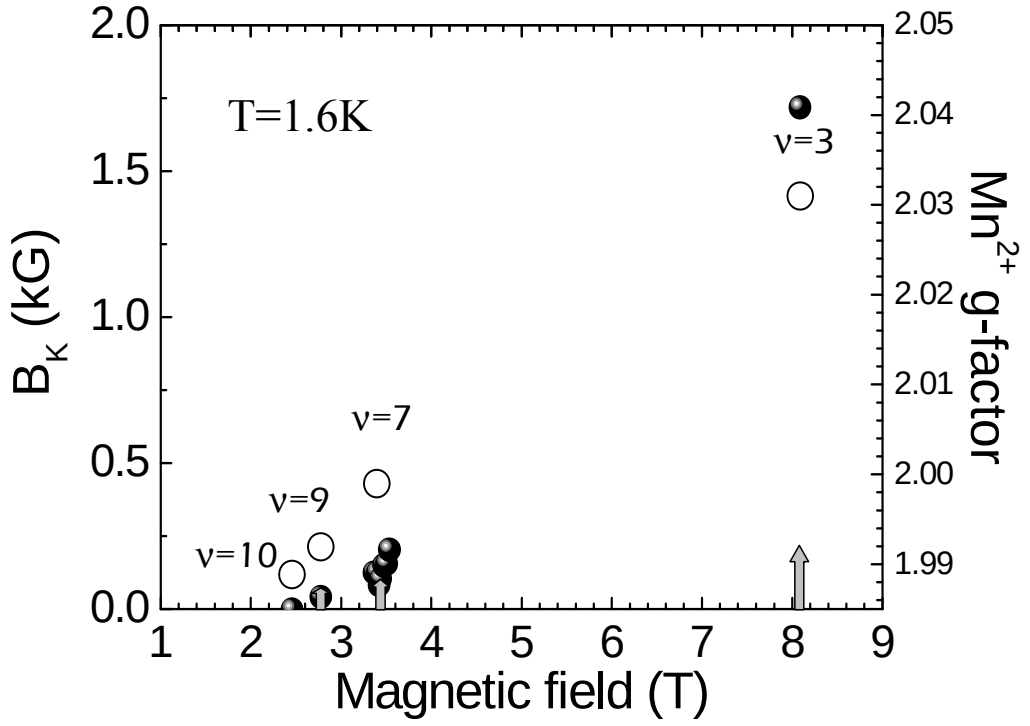

Figure 5.7: Experimental values (solid circles) of the Knight shift B_K (left side) derived from Eq.5.2 for the different resonances near to ν=10,9,7 and 3 at T=1.6K. The expected values (gray arrows) of B_K are plotted by comparison. Experimental values (empty circles) of the Mn^{2+} g-factor (right side) derived from Eq.5.1 for the different resonances near to ν=10,9,7 at T=1.6K.

An alternative way to interpret the resonance position is to account for the fictitious field B_k, which can naturally be considered as being related to the spin polarization of the 2DEG (i.e. "Knight shift). The equation describing the resonant field is then rewritten in the following way:

$$B_K = h\nu/g\mu_B - B \qquad \text{Eq.5.2}$$

Considering, g as the bare Mn^{2+} g-factor and B_R as the resonant magnetic field $B_R=B+B_K$, where B is the external magnetic field (precisely monitored by the marker EPR signal in our experiments). We assume $B_K=0$ at filling factor $\nu=10$ where a negligibly small electron spin polarization contribution is expected. This allows us to determine a "bare" manganese g-factor $g^{Mn}=1.990$. The B_K values obtained for different filling factors at the lowest temperature (T=1.6 K) are shown in Fig.5.7 (solid circles) and listed in Table 1. It is clearly observed that B_K increases non linearly with the external magnetic field. Whereas at low fields, B_K values are reasonably small (B_K=38 G and 130 G for spectra measured at ν=9 and 7, respectively), at high fields around 8.1T B_K is as large as 1700 G. As will be discussed later, such a value is unexpectedly large.

As shown before our low field transport experiments indicate that the mean field approach is applicable in the low field limit. It seems logical to use same approach to describe the effects of the carriers on the Mn subsystem.

According to Eq.1.21, the value of the "Knight shift" within the mean field approach can be calculated. Thus, considering the characteristic parameters of our system, i.e. αN_{Mn}=220meV, $n_e=5.9\cdot10^{11}cm^{-2}$, $N_{Mn}=1.5\cdot10^{22}cm^{-2}$, $|\varphi(z)|^2=1/5$ nm^{-2} and $\langle\sigma_\nu\rangle = \frac{1}{2}\cdot 1/\nu$ we calculate the B_K values. The results for different filling factors are shown in Table 1 for comparison with the experimental values:

B_K(measured)	B_K(calculated)	ν
0 G ± 10G	0 G	10
38 G ± 10G	83 G	9
130 G ± 10G	107 G	7
1700 G ± 10G	249 G	3

Table 1

The expected "Knight shifts" accounted for the spin polarization of a 2DEG, indicated by the height of the gray arrows in Fig.5.7, are calculated for an

ideal electron gas. This means that our calculations of B_K in Table 1 are already overestimated, since the Landau level broadening contributes to diminish the magnetization of the free carrier subsystem $<\sigma_V>$. At low fields, our model is able to reproduce a Knight shift of the same order of magnitude as the experimental observed values. However, at high fields, the prediction is almost one order of magnitude smaller than the observed value. This means that our model based on the mean field approach is not sufficient to reproduce the EPR position at high fields. In fact both the large "Knight shift" and the pronounced temperature dependence of the resonance position observed in the EPR spectra around B=8.1T are very surprising.

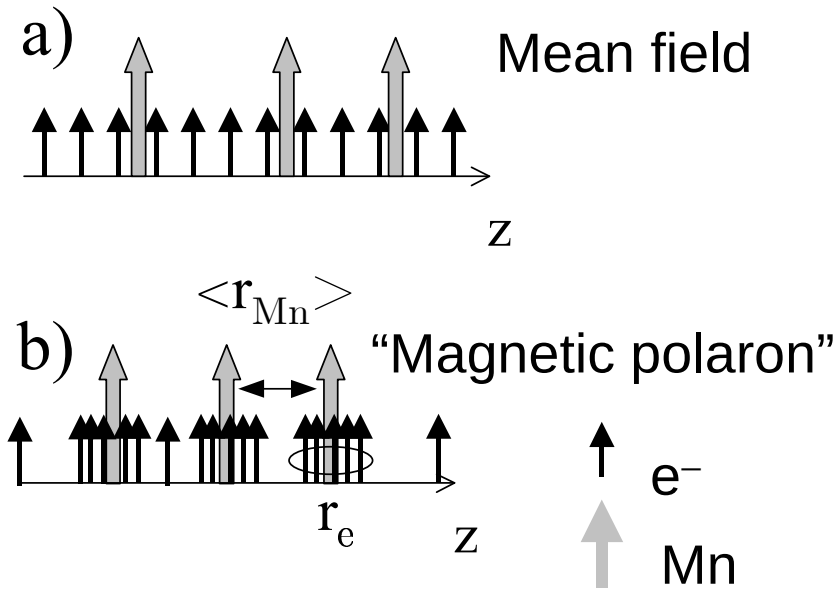

Figure 5.8: Schematic illustration of a) homogenous carrier distribution with respect to Mn^{2+} ions in case of the mean field approach or b) distinct local carrier distribution per to Mn^{2+} ion in case of magnetic polaron formation. In reality $N_{Mn} >> N_e$.

5.5 Discussion: electron-spin localization as the origin of the large "Knight shift"?

To account for the large amplitude of the "Knight shift" observed in our EPR spectra measured around B=8.1T we first consider the possibility of a non-uniform distribution of electronic spins. It seems plausible to assume that the

"Knight shift" could be enhanced with respect to its mean value, if the electron spin density is for some reasons increased at the Mn^{2+} sites. Such an effect would resemble the formation of a magnetic polaron (denser clouds of electron spins at the Mn^{2+} sites) [Wolff-1988] (see Figure 5.8a) or a spin density wave with a maxima at the Mn^{2+} sites. At a first sight such localization effects would not be surprising under the conditions of the quantum Hall effect which are satisfied for our resonance measured around B=8.1T (filling factor 3). However, if the electrons are localized on Mn^{2+} sites the localization length should be smaller than the mean distance $<r_{Mn}>$ between Mn^{2+} sites. On the other hand, a typical localization length $<r_e>$ expected for electrons in quantum Hall regime might at most be of the order of the magnetic length ℓ_B but not smaller. We estimate that under our experimental conditions $<r_{Mn}>$= 3nm, which is significantly smaller than ℓ_B=10nm. We therefore conclude that the effects of electron-spin localization on Mn^{2+} sites are a rather improbable explanation for our experimental results.

5.6 Discussion: Model of interaction between mean-field spin excitations of Mn^{2+} and free electrons

As mentioned in chapter 1, the *s-d* interaction in terms of the simple mean field approach implies that the original spin excitations for the Mn^{2+} ions $\vec{S}$ (whose energy is equal to $g^{Mn}\mu_B B_{ext}$) and for the conduction band electrons $\vec{\sigma}$ (with energy equal to $g^e\mu_B B_{ext}$) are replaced by the modified-ones $g^{Mn}\mu_B(B_{ext}+B_K)$ and $g^e\mu_B(B_{ext}+B_{eff})$, respectively. The effective magnetic fields B_{eff} and B_K are correspondingly proportional to the Mn^{2+} ion and free electron spin polarizations and can be considered as the usual "Overhauser" and "Knight" shifts, respectively. Within the simple mean field approach whose interaction term is driven by $J_{s-d}\vec{S}\cdot\vec{\sigma}$, these modified spin excitations are proper modes of the hybrid electron-magnetic system and as such do not couple with each other. Any extension beyond the first order $J_{s-d}\vec{S}\cdot\vec{\sigma}$ term could be a possible cause of the effective interaction between these already modified (by the mean field) modes. In what follows, we assume such a possible interaction and we confront our data with the proposed model. This procedure should be regarded as purely phenomenological. It should, however, be noticed that the arguments for interpreting the EPR data using this model are strongly supported in the following chapter by Raman scattering data obtained on similar samples.

In order to phenomenologically account for further terms in the *s-d*

interaction we assume that the spin excitations for Mn and conduction electrons are coupled via an interaction of strength δ_1. The new resulting modes E of the system correspond to $E_\pm$ which are given by the solution of the simple secular equation:

$$\begin{vmatrix} E - E_e & \delta_1 \\ \delta_1 & E - E_{Mn} \end{vmatrix} = 0 \qquad \text{Eq.5.3}$$

with

$$E_\pm = (E_e + E_{Mn})/2 \pm \{(E_{Mn} - E_e)^2/4 + \delta_1^2\}^{1/2} \qquad \text{Eq.5.4}$$

where $E_{Mn} = g^{Mn}\mu_B(B_{ext}+B_K)$ and $E_e = g^e\mu_B(B_{ext}+B_{eff})$. For further considerations we neglect the small value of B_K and assume that $E_{Mn} = g^{Mn}\mu_B(B_{ext}+ B_K) = g^{Mn}\mu_B B_{ext}$.

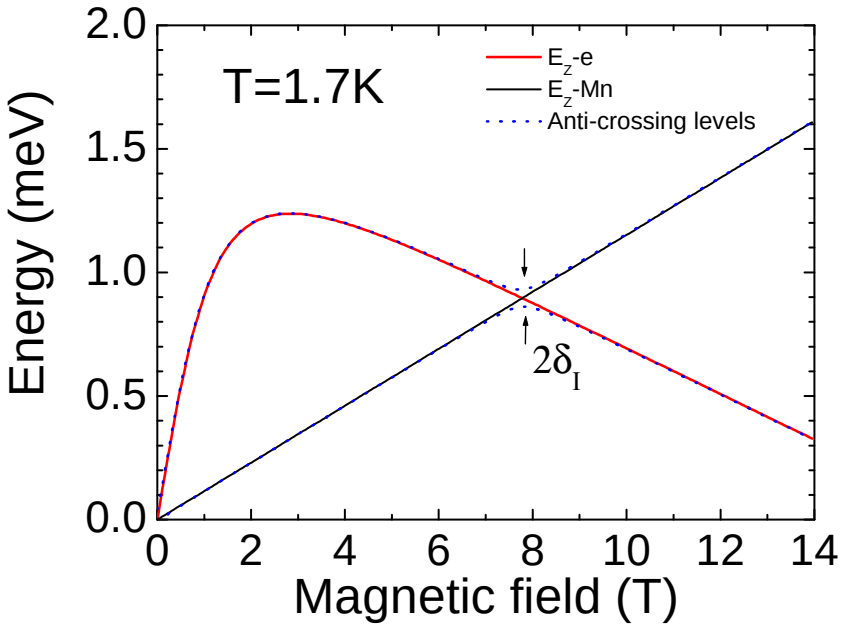

Figure 5.9: Comparison of the Zeeman energy for electrons (red line) and paramagnetic Mn^{2+} spins (black line) as a function of the magnetic field in case they cross (solid line) or they anti-cross (dot line).

As shown in Figure 5.9, E_{Mn} and E_e excitations estimated by the mean field approach for magnetic and electronic subsystems cross at a magnetic field just above 8T. However, when interaction is included, the coupled modes E_+ and E_- anticross with a smallest separation $2\delta_1$ between them, recovering the character of the modified modes resulting from the mean approach, E_{Mn} and E_e, away from the anticrossing region. Our suggestion to interpret the experimental data relies on the assumption that the EPR experiments are probing the Mn^{2+}-like coupled mode excitations, in particular around 8.1T. The resonating Mn^{2+}-like spin excitations correspond to the upper E_+ coupled mode, since for our particular case $E_e \approx E_{Mn}$ at the magnetic field range as shown in Fig.5.9.

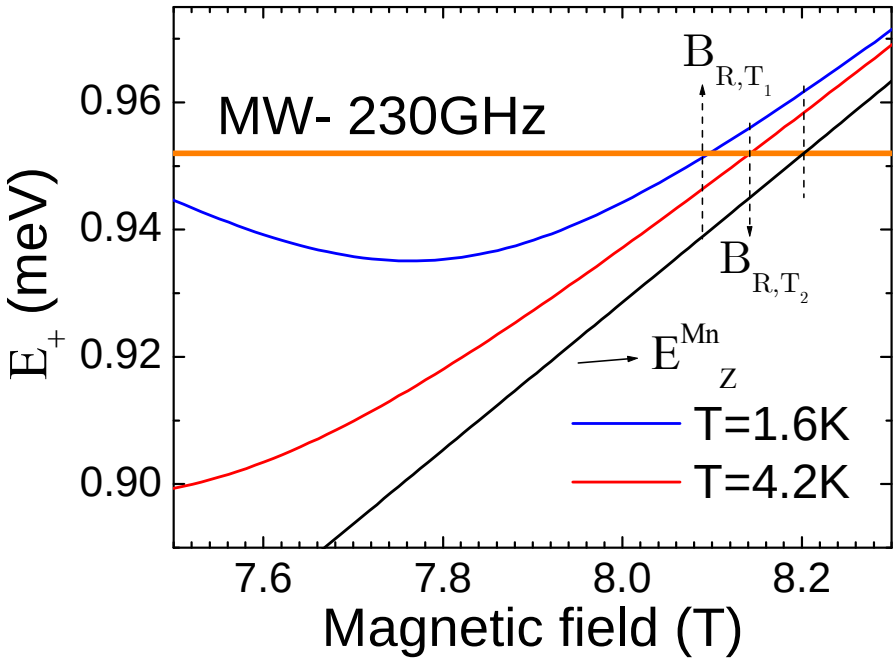

Figure 5.10: Magnetic field dependence of E_+ for two different temperatures (blue and red lines). The orange line represent the energy of the microwaves. The cross magnetic field positions with E_+ correspond to the resonant magnetic field B_R. The magnetic field dependence of the Zeeman energy of paramagnetic Mn spins is plotted for comparison (black line).

5.6.1 Resonance position at its temperature dependence in the anticrossing region

In order to quantitatively reproduce our experimental data we consider

Eq.5.4 assuming: δ_1=0.035meV (fitting parameter), g_{Mn}=1.990 obtained from the EPR experiments at low magnetic fields (at ν=10, B= ~2.45 T) and $E_{s\text{-}d}$=1.62 meV as determined from the node positions at low fields for this sample (100997A). The results of Eq.5.3 are illustrated at T=1.6 K over a large magnetic field range in Fig.5.9. A zoom of the anticrossing region (~8.1T) is shown in Figure 5.10. There, we plot the magnetic field dependence of the $E_{Mn}= g^{Mn}\mu_B B_{ext}$ as well as the E_+ excitation, the latter for two different temperatures T=4.2 and 1.6 K. For a microwave frequency of 230 GHz used in the experiment, the resonant field B_R occurs at 8.2 T for the uncoupled E_{Mn} spin excitation. Assuming that the microwaves are resonating with the mode E_+, the resonance position is shifted down in field to B_R =8.1 T for T=1.7K and B_R =8.15 T at T=4.2K. These resonant fields can once again be seen as g-factors g^{Mn2+}=2.0243 and 2.0118 or "Knight shifts" B_k=1100 G and 500 G, for T=1.7 K and T=4.2 K respectively, in qualitative agreement with the experimental observations. Therefore our phenomenological "resonant interaction model" can explain not only the large shift of the resonance position but also its strong temperature dependence.

The latter dependence comes from the fact that the mean field E_e spin excitation is temperature dependent, and consequently so are the coupled modes $E_\pm$. For these reasons, the anticrossing region shifts in field as the temperature is changed, which induces a shift in the resonance field for the coupled E_+ mode at our given frequency (230 GHz).

At this point we would like to make one comment more regarding the 230 GHz EPR data presented in Fig.5.6. The main resonance line is accompanied by a weak signal in the vicinity of B ~8.2T which is only observed in this high field region and at T=1.7 K. The reason why it appears at high fields and low temperatures may be related to the sensitivity of our detector, the 2DEG. Considering the resistance of our 2DEG simply as a sensitive bolometer, we think it cannot be excluded that the weak signal at B ~8.2 T is due to the microwave absorption of the resonant spins of Mn^{2+} ions which are located outside the quantum well. However, if this is true our previous method to determine the actual values of g-factors needs to be verified. This method relied on the assumption of a perfect linearity of the DPPH EPR with field, which is generally accepted but extremely difficult to verify. If we interpret the weak resonance at B~8.2T as being due to non interacting Mn^{2+} ions outside the quantum well, we deduce that for the main resonance the "Knight shift" is 1000 G instead of the 1700 G value estimated using the DPPH calibration procedure. In both cases, the observed Knight shift is anomalous large but well explained by our model of coupled modes.

5.6.2 EPR line shape

We have shown above that our model of "coupled modes " explains well the main experimental findings, i.e. the anomalous "Knight shift" and the strong temperature dependence observed in EPR experiments around 8.1T. This model has however some additional consequences which as we show below can be observed in the experimental data. The characteristic experimental features which we would like to comment on now concern the resonance line shape and its temperature dependence close to the anti-crossing point (i.e. B ~8.2 T). The difference in the line shape between low and high magnetic fields, and its possible asymmetry will be discussed.

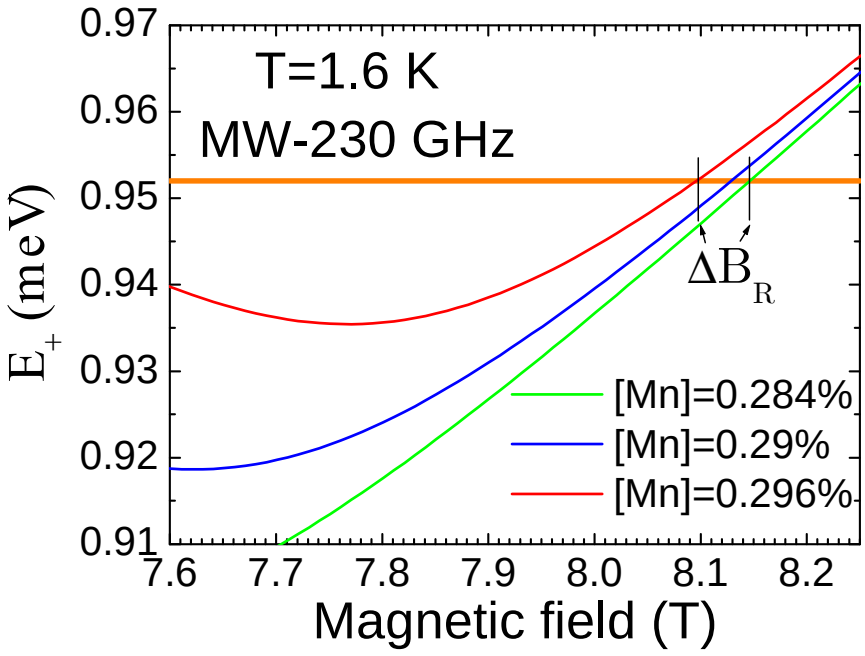

Figure 5.11: Magnetic field dependence of ω_+ for three different Mn concentrations: 0.28% (green line), 0.29% (blue) and 0.3% (red line). The orange line represents the energy of the microwaves. ΔB corresponds to the separation between crossing of different ω_+ for 0.28% and 0.3%.

Our "anticrossing model" has important consequences for the mechanism of broadening the Mn^{2+} EPR spectra. One of the main possible sources of the inhomogeneity in our samples is the fluctuation of the Mn^{2+} concentration. This, however, (in the case of low Mn compositions, i.e., where the Mn^{2+} can be treated

as isolated paramagnetic ions), should not affect the shape of the Mn^{2+} EPR. On the other hand the mean-field acting on the electronic spins is proportional to the Mn concentration and therefore the fluctuation of the manganese composition can easily be reflected in the fluctuation of the mean-field splitting of electronic states. Therefore, within the simple mean field approach, the inhomogeneity of Mn composition will influence the dispersion of the electronic spin splitting but not the Mn^{2+} spin splitting. The situation changes with the model of coupled modes. Far away from anticrossing region ($E_{Mn} \neq E_e$), the Mn^{2+}-like spin excitations are not dispersed. However, in the vicinity of the anticrossing ($E_{Mn} \sim E_e$), the coupled E_+ and E_- modes will be rather sensitive to the fluctuations of Mn composition. In particular, the resonance field for our 230 GHz EPR spectra (microwaves resonant with the E_+ coupled mode) will be a rather sensitive function of the Mn composition, which will affect the broadening of the line. As shown in Figure 5.11, the change of the Mn composition from 0.3% to 0.28% leads to a 700 G shift in the EPR resonance position at 1.7K. This shift is comparable to the observed linewidth of the 230 GHz-EPR spectrum. From the Raman experiment (see chapter 6) we estimate that the fluctuations of the Mn concentration are about 10%, which is reasonable. Therefore, we conclude that these fluctuations may provide an important contribution to the broadening of our 230-GHz EPR spectra. On the other hand, according to our model the fluctuations of Mn^{2+} composition do not affect the EPR spectra far away from the $E_e=E_{Mn}$ resonance.

The decrease in the linewidth with temperature observed in 230 GHz EPR spectra, can now be understood. As can be seen in Fig.5.11, the spread of the E_+ modes related to the fluctuations of the manganese concentration diminishes for magnetic fields away from the $E_e=E_{Mn}$ crossing point. A decrease in temperature leads to a shift of the $E_e=E_{Mn}$ crossing point towards lower fields and a larger separation from the EPR resonance field. Thus, the temperature variation induces an expected narrowing in reasonable agreement (within a factor of 2) with the experimental observation.

It is very probable, that the broadening induced by an inhomogeneous Mn distribution prevents the observation of a hyperfine splitting of the Mn^{2+} EPR at 230Ghz. On the other hand, the fluctuations of Mn^{2+} composition do not affect the EPR spectra far away from the $E_e=E_{Mn}$ resonance which agrees with our observation of the hyperfine splitting of the Mn^{2+} EPR at lower magnetic fields.

Another consequence of our broadening model is the expected asymmetry of the 230 GHz EPR spectrum. This asymmetry can be easily deduced from Fig.5.11. The increase in Mn concentration from 0.29% percent to 0.3% shifts the resonance towards lower fields whereas the decrease of Mn concentration from

0.29% to 0.28% lowers the resonance field. The upwards shift is however substantially smaller then the downwards shift and this means that a "symmetric" inhomogeneity in the Mn distribution leads to an asymmetry in the EPR line shape. Careful examination of the experimental data (Fig.5.6) reveals that indeed the 230-GHz EPR spectrum is slightly asymmetric with more spectral weight concentrated on the low field side.

Conclusion

In this chapter we have presented the resistively detected investigations of the Electron Paramagnetic Resonance of Mn^{2+} ions imbedded in CdMnTe modulation doped quantum well structure. The experiments have been performed using different microwave frequencies resulting in observed resonance positions near B ~ 8.1, 3.4, 2.8 and 2.45T. At low magnetic fields (B=3.4, 2.8 and 2.45T) the position of the EPR spectrum can be well understood in terms of the simple mean field approach. In this range of magnetic fields, the unexpected observation is the nuclear spin polarization at relatively high temperatures seen in the EPR spectra at 3.5T. This has been interpreted in terms of the dynamical effect mediated by the presence of free carriers. A large deviation from the expected position of the Mn^{2+} spin resonance has been observed in the vicinity of B=8.1 T. The EPR resonance shifts more than 1000 G from the expected field position towards lower magnetic fields showing a strong temperature dependence. The observed shift is too large to be explained by the simple mean field approach. A model based on a resonant interaction between the mean-field spin excitations for electrons and Mn^{2+} ions has been proposed in order to interpret the experimental data. This model accounts well for the experimental findings, providing the correct order of magnitude for the observed shift of the resonance position. The model also provides a possible mechanism for the temperature dependence of the resonance shape and other characteristic features (asymmetry). However, many questions remain open such as, for example, the role of the v=3 quantum Hall state in our observation or more generally the dependence of the anomalous “Knight shift” on carrier concentration.

Our proposed model of coupled modes also needs more basic experimental verifications since it remains phenomenological and the physical origin of the interaction needs to be identified. It is clear that the experimental verification of our model requires tunable measurements of Mn^{2+} (and likely electron) spin excitations. Although a powerful technique, the EPR experiments also have some disadvantages. The main disadvantage is the limited tunability with magnetic field. The microwave sources have extremely limited tunability and our detection method is limited to magnetic field regions where the longitudinal resistance is

sensitive to the electronic spin gap. Another possible method to probe spin excitations in our samples is Raman scattering experiments. Unfortunately, due to a bad surface quality, the Raman scattering experiments could not be performed on this sample. Experiments on other similar structures have however been performed and they confirm the main conclusions of this chapter. Those investigations are presented in the following chapter of this thesis.

Chapter 6

Electronic and Mn^{2+} spin flip excitations investigation using inelastic light scattering

Introduction

As described in Chapter 1, spin flip Raman scattering (SFRS) spectroscopy is a powerful tool for studying spin excitations in crystals. The energy difference between the in-coming and out-going photons corresponds to the energy cost of the spin flip processes. Wide gap DMS have good optical properties even for Mn concentration as high as 40%, which enables us to perform resonant Raman spectroscopy. Resonant Raman spectroscopy yields information about spin properties since the scattering intensity is enhanced if the in-coming and out-going photon energy matches an allowed electronic transition. Concerning the electronic subsystem, SFRS separately probes the spin splitting for the conduction and valence band spin states, in contrast to the photo-luminescence or transmission spectroscopy which determine the combined spin splitting in the conduction and valence bands. In undoped semiconductors, the electrons involved in the spin flip transitions are attached to free, bound excitons or other excitonic complexes such as the donor-bound magnetic polaron [Wolf-1984]. In this way, SRFS gives detailed information about the giant Zeeman splitting for conduction electrons in DMS quantum wells complementing the photo-luminescence studies of the ***sp-d*** exchange interaction.

Raman spectroscopy is also sensitive to the spin flip of the ***3d***-electrons of the localized Mn^{2+} ions. Therefore, this spectroscopic technique can be used to investigate magnetic excitations of the paramagnetic phase of Mn^{2+} ions, of Mn^{2+} pairs [Stühller-1996] or collective Mn^{2+}excitations [Sapega-2000]. In the paramagnetic phase on which we focus our attention, the spin flip processes are related to electronic transitions within the Zeeman multiplet shown in the Figure 1.5. Raman spectroscopy is complementary to the Electronic Paramagnetic Resonance (EPR) technique in DMS nano-structures. The flexibility of the EPR technique is limited by

the availability of frequency-tunable microwave sources, which does not permit to perform experiments at arbitrary magnetic fields. On the other hand, SFRS allows to continuously monitor the Mn resonance at any magnetic field. Nevertheless, Raman spectroscopy usually has low resolution with respect to the EPR technique, which is more sensitive and therefore permits us to extract more detailed information regarding weak interactions such as the hyperfine interaction.

In this chapter we study SFRS processes related to the electronic and magnetic spins at low temperatures and in magnetic fields up to 14 T. The magnetic field dependence of the electronic Raman shift allows us to study the effective Zeeman energy. In particular at the vanishing point where a non-zero electronic spin splitting is observed. At the same time, we study the magnetic field dependence of the Mn Raman shift especially in the magnetic field range where electronic and magnetic spin excitation energies are comparable. A model of anticrossing between both spin excitations will be presented in order to describe our observations.

6.1 Spin Flip Raman scattering

6.1.1 Experimental details

SFRS processes obey specific selection rules regarding the circular polarization of the incident and the scattered light. These processes can be observed in the so-called crossed polarization configuration, i.e., when the incident

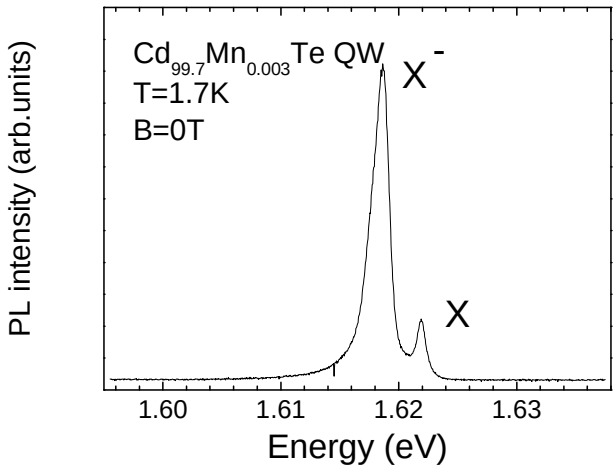

Figure 6.1. PL spectrum of the CdMnTe quantum well studied at T=1.7K and zero magnetic field. Two sharp lines can clearly be recognized: neutral X and negatively charged X^- excitons.

and the scattered light have opposite helicity [Geschwind-1984]. From the experimental point of view, this requires polarization resolved optical experiments. Details concerning the optical set-up used in the experiments can be found in the Appendix 1. The sample was mounted in back-scattering Faraday configuration using the optical mini-table system, which was then placed in a ^{4}He cryostat. Magnetic fields were generated using a super-conducting magnet. The experiments were performed in a temperature range between 1.7 and 4.2 K and for magnetic fields up to 14T. A Titanium Sapphire tunable laser pumped by an Ar^+ ion laser was used as the excitation source. The excitation power density on the sample was kept below 1mW/cm^2. The spectra were measured using a 1m focal length single grating spectrometer with a spectral resolution 0.2 Å and equipped with a CCD camera.

The system investigated was a nominally undoped CdMnTe quantum well whose structure was described in chapter 2. The effective Mn concentration determined from simple magneto-luminescence measurements was around 0.2%. A photoluminescence spectrum of our sample is shown in Fig.6.1. It indicates the presence of background electrons in the quantum well, which results in the observation of a luminescence peak associated with the negatively charged exciton X^- (see chapter 7). The electron density, estimated from optical measurements, in the sample is ~1x10^{10} electrons/cm^2.

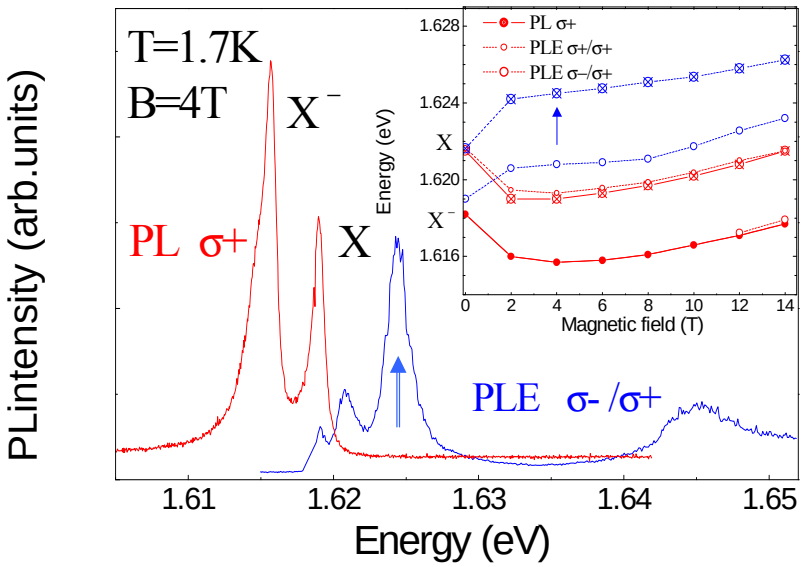

Figure 6.2. Typical polarization resolved PL (red line) and PLE (blue line) spectra at T=1.7K and B=4T. σ–/σ+ denotes the polarization configuration of the excited/emitted light. Insert: PL (solid circles) and PLE (empty circles) fanchart for cross and parallel configurations.

Strong Raman scattering signals are observed when the excitation energy coincides with the absorption peak related to the neutral exciton X. Figure 6.2 shows a typical photo-luminescence excitation spectrum (blue line) at 4T and at T=1.7K. The energy range corresponds to the absorption peak of the σ- component of the neutral exciton. The experimental procedure was to systematically use the σ- circularly polarized excitation light tuned in the vicinity of the X resonance. Figure 6.3 shows a typical Raman spectrum. The two marked peaks are identified with spin-flip Raman signals. They are observed only in the crossed polarization configuration. At a given magnetic field, these peaks have a similar width and intensity. When tuning the excitation energy, the peaks shift with the laser line which is essential for identifying them as Raman scattering signals (Stokes processes). Under conditions of resonant excitation, the SF signals are easily detected as they are comparable to luminescence lines. However, weak off-resonant SF lines can also be observed in our structure.

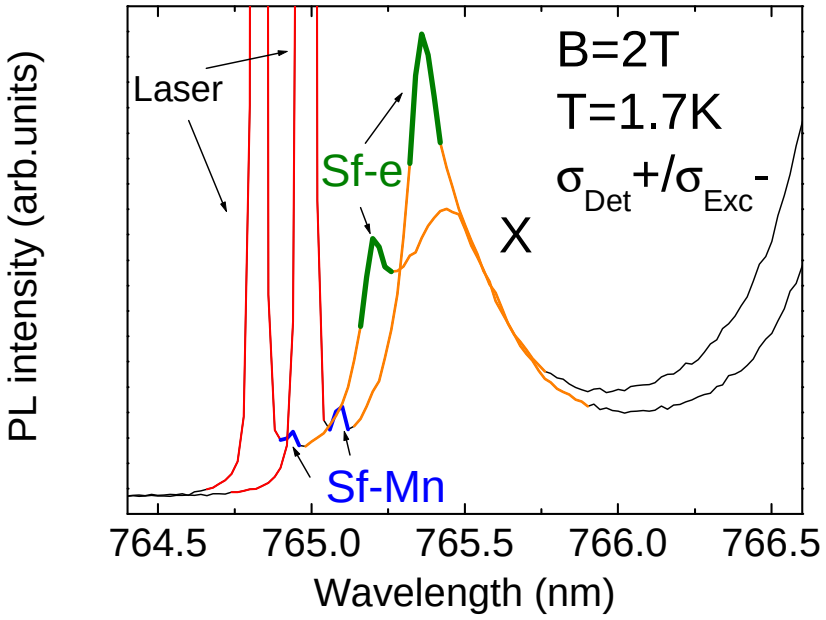

Figure 6.3. Two typical Raman spectra acquired at different excitation energy at magnetic field B=2T and temperature T=1.7K in cross polarization configuration. The SFRS lines are associated with Sf-e (green line) and Sf-Mn (blue line).

6.1.2 Experimental results

At the lowest temperature (1.7K), the magnetic field dependence of the Raman shifts for both SF transitions are shown in Figure 6.4. The different data points at a given magnetic field correspond to different excitation energies. It is clear from this picture that we can easily distinguish two types of distinct spin-flip processes. The spin flip excitations which show a linear magnetic field dependence are related to flips of Mn^{2+} spins, and we label them Sf-Mn. For these excitations, the magnetic field dependence of the Raman shift corresponds to the Zeeman energy between the spin states of the paramagnetic Mn spin S=5/2. The linear dependence shown Fig.6.4 has been fitted to the experimental points using the expression $E_Z=g^{Mn}\mu_B B$ with g^{Mn} =1.950, for the Mn g-factor. This later value is different from the bulk value (g=2.005 [Deigen-1967]) but similar to the bare Mn g-factor obtained by EPR in chapter 5. The second type of spin flip processes, labeled Sf-e, is related to spin-flip excitations of conduction band electrons. The Sf-e processes are related to the spin flip between different electronic spin states whose energetic separation varies with field as shown in Fig.1.4. We can roughly reproduce the magnetic field dependence of the Sf-e excitations (red line) using the electronic Zeeman splitting involving the ***s-d*** exchange term and given by Eq.6.1, and assuming $E_{s\text{-}d}$=1.16 meV for the ***s-d*** exchange energy, a Brillouin function $B_{5/2}(B,T)$ and g=-1.6 for the bare g-factor in CdTe:

$$E_Z(x)=g_e\mu_B B+E_{s\text{-}d}B_{5/2}(B,T) \qquad \text{Eq.6.1}$$

A closer inspection of the data presented in Fig.6.4 reveals however the important discrepancies between the experimental data and simple modeling of Zeeman energies for Sf-e and Sf-Mn excitations. The most remarkable deviation occurs in the vicinity of 6T where the Mn and electronic Zeeman splitting are expected to cross. There, the Sf-Mn data deviates from the expected linear behaviour. At the same time, the Sf-e Raman shift cannot be well described by Eq.6.1 neither at the crossing points nor at high fields where the electronic Zeeman energy is expected to vanish. Moreover, it is apparent that the values of the Raman shift associated with Sf-e excitations at given magnetic field appear to be much more dispersed than those associated with Sf-Mn excitations. These discrepancies are systematically discussed below. First we focus our attention on electronic branch and later discuss manganese spin flip data.

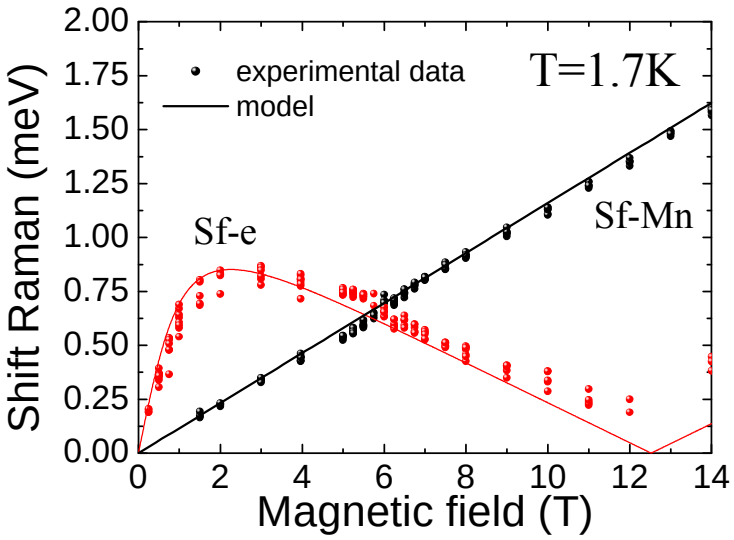

Figure 6.4. Magnetic field dependence of the observed Raman shift for Sf-e (red points) and Sf-Mn (black points) in comparison with the expected electronic (red line) and Mn (black line) Zeeman energy.

6.2 Discussion

6.2.1 Electronic spin flips

6.2.1.1 Spin-flip transitions versus excitation energy

In DMS, SF lines associated with band electrons are easily observed at very low fields due to the giant Zeeman splitting. The magnetic field dependence of the Sf-e Raman shift is plotted in Figure 6.5 for two temperatures. At a given magnetic field, the values of the Sf-e Raman shift corresponding to different excitation energies are dispersed in some cases more than 0.1meV, contrary to the data corresponding to Sf-Mn excitations which are much less scattered (note that widths and intensities of both signals are similar). Closer inspection of the experimental results indicates that the data points for Sf-e excitations are not randomly scattered. They show a systematic dependence on the excitation energy which is not the case for Sf-Mn excitations. As shown in Figure 6.6R, for a fixed magnetic field, when the energy of the incident light is tuned over the exciton X absorption peak, the energy of the Sf-e excitation increases with increasing excitation energy. Such an energy dependence cannot be explained as an experimental error.

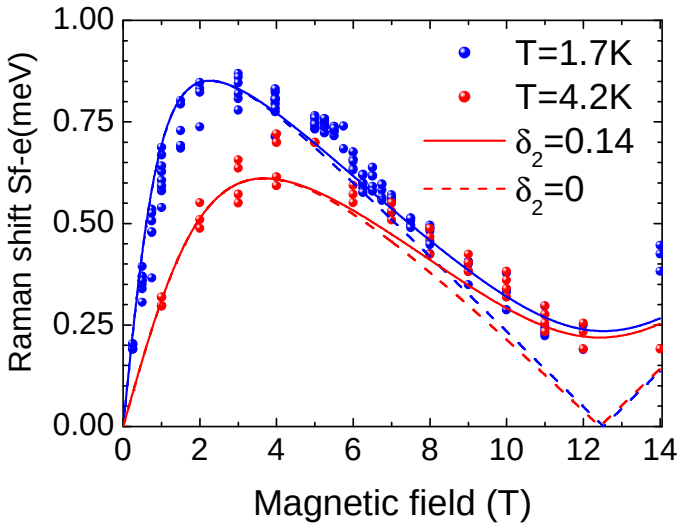

Figure 6.5. Magnetic field dependence of the Raman shift associated with Sf-e for two temperatures (circles). At a given magnetic field the different points were measured for different energy excitation. The solid (dash) line correspond to calculation using Eq.6.3 for δ_2= 0.14 (0) meV.

A possible explanation for the dispersion of the values of the Sf-e Raman shift with the energy of the incident light might be due to the fluctuations of the Mn concentration within the laser spot. Any fluctuation of the Mn concentration would result in changes of the bandgap as well as in a change of the ***s-d*** exchange splitting. As we mentioned in the introductory chapter, the bangap of DMS linearly increases with the Mn concentration x at T=4.2 K [Lee-1984] as:

$$Eg(x)=1.606+1.592\cdot x \qquad \text{Eq.6.2}$$

At low Mn concentration x, the Zeeman splitting describe by Eq.6.1 involving the ***s-d*** exchange term also increases linearly with x as:

$$E_Z(x)=g_e\mu_B B+N_0\alpha\, x S_0 B_{5/2}(B,T)> \qquad \text{Eq.6.3}$$

The fluctuations of Mn concentration can be spatially distributed along or in-plane the quantum well layer on the micro- or nano-meter scale. Over our laser spot whose diameter is of about 1 mm, we may probe distinct regions with different Mn concentrations. These regions will therefore be characterized by different bandgaps and different effective Zeeman splittings according to Eq.6.2 and 6.3. Sweeping the excitation energy over the absorption peak we expect to probe regions of low (high) Mn concentration when exciting in the low (high) energy tail

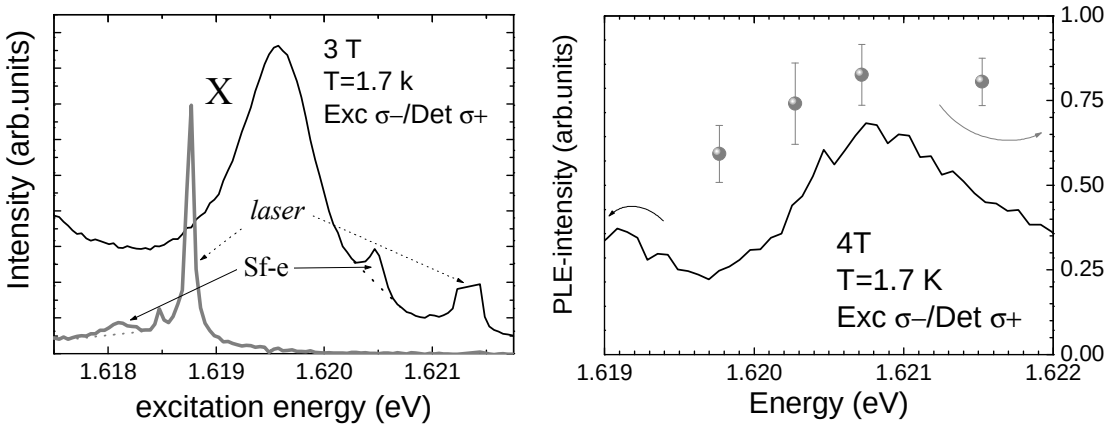

Figure 6.6. Right) Typical Raman spectra acquired under resonant (off-resonant) conditions (black and gray line, respectively) at 3T. Left) Comparison of the increase of the Raman shift value with respect to the PLE spectra at 4T.

of the absorption peak. In consequence we may expect that Sf-e Raman shift (i.e. ***s-d*** exchange splitting) is an increasing function of the excitation energy which could quantitatively account for our experimental observations. The absorption peaks observed in our sample are rather broad (1-2meV), partially due to the fluctuations of the Mn concentration as we propose. Assuming 0.2% for the effective Mn concentration of our sample, a 10% fluctuation of the Mn concentration would result in ~1meV shift of the absorption peak and ~0.2meV change in the ***s-d*** exchange splitting resulting from Eq.6.2. These estimations are in reasonable agreement with the experimental values for the width of the absorption peak and the dispersion of the values of the Sf-e Raman shifts observed, for example, at B=3T.

At this point, it is interesting to note that in spite of the large fluctuations in the Mn concentration, our resonant Raman scattering signal related to Sf-e excitations has a rather narrow linewidth. We believe that such a narrow linewidth is linked to the resonant excitation conditions, which in fact allow us to selectively probe regions with a well-defined Mn concentration. Due to the fluctuations, the electron spin splitting might be rather inhomogenous over the sample which is confirmed by off resonant Raman scattering experiments. Such an off resonant condition usually gives much broader Sf-e signals (see Fig.6.6L) and this might be a reason, why it is difficult to observe the electron spin resonance signal in EPR experiments.

6.2.1.2. The case of vanishing s-d Zeeman splitting

The data points attributed to Sf-e excitations, obtained for two different temperatures are plotted in Fig.6.5. The experimental values of Sf-e energy excitations cannot be reproduced simply by using the description given by Eq.6.1. Such a description (corresponding to the electronic Zeeman splitting) is shown by the dashed lines in Fig.6.5 and has been calculated assuming a ***s-d*** exchange constant E_{s-d}=1.16 meV and g^c=-1.6 for the bare g-factor in CdTe. The calculated ***s-d*** Zeeman splitting reproduces well the experimental data at low magnetic fields for both temperatures but fails to describe the data at high fields. In particular, close to the magnetic field where the ***s-d*** Zeeman splitting is predicted to vanish in this sample, around ~12T. The experimental data shows that there exists an interaction between the spin-split electronic Landau levels resulting in an anticrossing of these levels and consequently in a finite spin splitting at the magnetic field position for which the Zeeman splitting is predicted to vanish. In order to qualitatively describe our data, we model the effect of anticrossing between two spin split Landau levels within the simple first-order perturbation approximation. After introducing a phenomenological interaction parameter δ_2, we replace the unperturbed (N=0, $\downarrow$) and (N=0, $\uparrow$) spin-split Landau levels by the coupled ones. The energy separation Δ between these coupled levels is

$$\Delta = 2\{(E_{\downarrow} - E_{\uparrow})^2/4 + \delta_2^2\}^{1/2} \qquad \text{Eq.6.4}$$

where $E_{\downarrow}$-$E_{\uparrow}$ is the energy difference between the unperturbed spin-split levels, i.e. it corresponds to electronic spin splitting deduced from Eq.6.1. The energy separation between our coupled modes is plotted in Fig.6.5 (solid lines), assuming $2\delta_2$=0.28 meV. It can be seen that the anticrossing model significantly improves the description of the experimental data compared to the simple consideration of the simple Zeeman splitting (dashed lines).

The effect of a non-vanishing electronic Zeeman splitting has already been discussed in Chapter 4 in reference to the transport experiments. There, we consider the possibility that the electron-electron interaction might keep the spin gap open since the carrier density was appreciable. However, electron-electron interactions are not relevant in the present case since now we deal with a structure with very few electrons.

The data presented support the hypothesis that the observed anticrossing between the spin levels is related to the spin-orbit (***s-o***) interaction

characteristic for the Cd(Mn)Te band structure. Although the strength of the spin-orbit interaction in Cd(Mn)Te has not been extensively studied to date, the **s-o** interaction is generally weak and negligible for the conduction band. However, the ***s-o*** coupling can become appreciable under special conditions [Fal'ko-1993]. Recent cyclotron resonance studies [Karczewski-2001] attribute to the **s-o** interaction the observation of an appreciable resonant coupling between the cyclotron resonance and spin excitations in similar CdMnTe quantum well structures. Such observations support our proposed hypothesis.

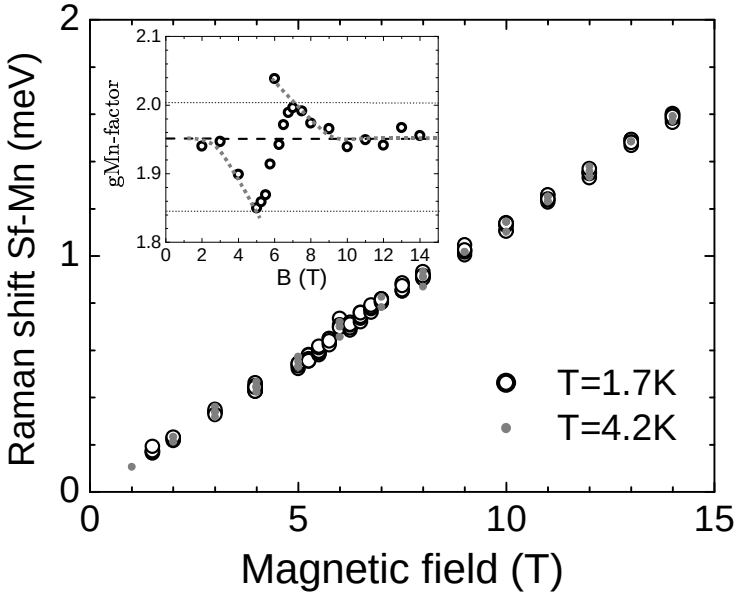

Figure 6.7. Magnetic field dependence of the Raman shift associated to Sf-Mn for two temperatures (circles). Insert: Magnetic field dependence of experimental Mn g-factor. The dotted lines are guided by eye.

6.2.2 Magnetic spin flip

The magnetic field dependence of the Raman shift of the signal attributed to Sf-Mn excitations is shown in Figure 6.7. As mentioned above, the overall dependence is linear with field and can be fitted according to the $E_Z=g_{Mn}\mu_B B$ with a Mn g-factor $g_{Mn}=1.95$. Closer inspection of the experimental data shows, however, a substantial deviation from this linear dependence. To emphasize this effect we consider the data obtained at T=1.7K. For each magnetic field, we calculate the mean value of the Raman shift (measured for different excitation energies) and determine the corresponding g-factor as a function of the magnetic

field. The obtained data are shown with closed circles in the inset of Fig.6.7. For fields well above or well below 6T, we find a Mn g-factor equal to g_{Mn} =1.95. Deviations from this mean g-factor value are observed around B=6T. On the low field side of the 6T point the g-factor is systematically smaller while on the high field side the g-factor is systematically larger. A dotted line, which serves as a guide to the eye, shown in the inset of the Fig.6.7 represents a tentative evolution of the g-factor of Sf-Mn excitations in the vicinity of 6T. This evolution clearly indicates the effect of repulsion around B=6T, where the energy of the electronic and Mn spin excitations are comparable (see Fig.6.4). As proposed in the previous chapter, such a behaviour leads us to the conclusion that we observe an anticrossing between Sf-e and Sf-Mn excitations. Such an anticrossing is already anticipated in our EPR studies on a heavily doped sample and is observed again in the case of a much smaller electron concentration. Hence, we believe that the carrier concentration is not a crucial parameter to observe such repulsion effects between electronic and Mn spin excitations.

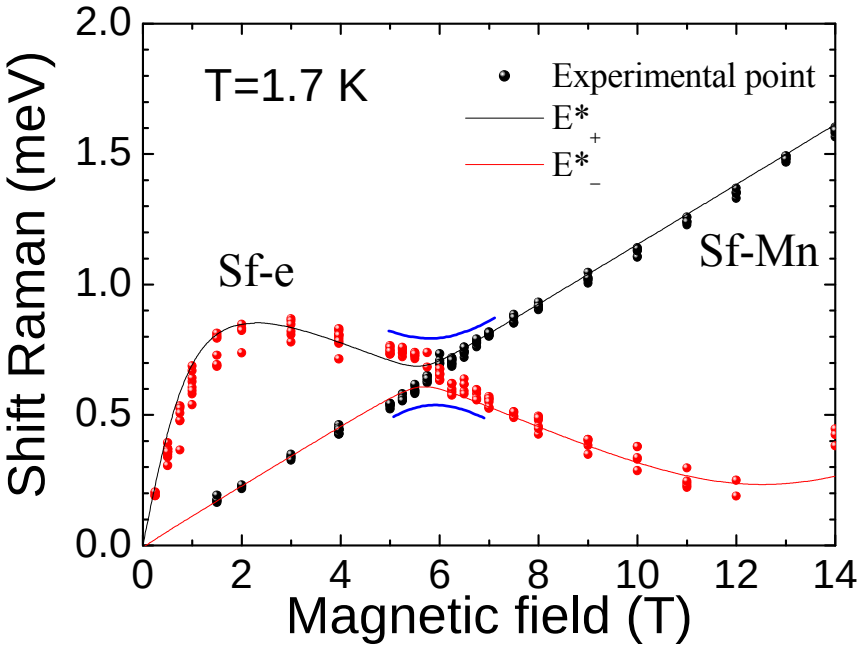

Figure 6.8. Magnetic field dependence of the Raman shift associated to Sf-Mn and Sf-e (black and red points). The red and black lines correspond to calculations of two interacting levels. The blue lines are guided by eye.

6.2.3 Coupling of magnetic and electronic spin excitations

The data analysis presented in two preceding paragraphs allowed us to draw a complete phenomenological description of manganese-like and electronic-like spin excitations observed in Raman scattering experiments. We limit our consideration to the data obtained at 1.7K and shown again in Figure 6.8. According to our analysis the usual description of this data in terms of Mn and electronic Zeeman energy is clearly insufficient. Instead, we propose a resonant coupling between both Sf-Mn and Sf-e excitations together with a resonant coupling between spin up and down electronic levels resulting in a non vanishing electronic spin gap at any magnetic fields. The complete description of our Sf-e and Sf-Mn excitations is presented with the solid lines in Fig. 6.8. In this model, as in the preceding paragraph, we assume that spin excitations in our system are given by coupled modes according to the first-order perturbation formula:

$$E^{*}_{+/-} = (E_{Mn}+\Delta)/2 \pm 2\{(E_{Mn}-\Delta)^2/4 + \delta_1^{\,2}\}^{1/2} \qquad \text{Eq.6.5}$$

where the $E_{Mn}=g_{Mn}\mu_B B$ and Δ is given by Eq.6.4 in order to account for the non vanishing electronic spin gap with a δ_2=0.14 meV, $E_{s\text{-}d}$=1.16 meV for the mean field electronic ***s-d*** exchange energy and g=-1.6 for the bare g-factor in CdTe. The value for the interaction energy δ_1 can be extracted from the experimental data when looking at the magnetic field dependence of the Mn-g factor at the anticrossing region (see insert Fig.6.7). Thus, $\delta_1 = \Delta g_{Mn}\mu_B B_{ac}$ where Δg_{Mn} is the difference of the Mn g-factor value at both extremes of the anti-crossing at the magnetic field position B_{ac}. Thus, it results δ_1 = 0.04meV for the coupling interaction parameters in Eq.6.5. As seen in Fig.6.8, our phenomenological model correctly reproduces the experimental data.

Conclusions

Spin flip Raman scattering processes associated with spin flip transitions of band electrons and spin flip transitions of manganese ions have been observed. We postulate that there is a resonant coupling between the manganese and electronic excitations as well as a resonant coupling between spin up and spin down electronic levels. Two phenomenological models have been presented in order to qualitatively describe our observations. Indeed, these models successful reproduce the experimental data. The experimental findings

corresponding to the electronic excitations presented in this chapter, are in agreement with transport data presented in chapter 4, where some features observed in tilting experiments indicate a repulsion between spin up and spin down Landau levels. The experimental finding corresponding to the Mn spin excitations are also in agreement with the EPR studies presented in chapter 5 which also suggest a resonant coupling between the Mn and electronic spin excitations. Since the experimental results presented in this chapter have been obtained using a sample with a low electron concentrations we conclude that our anticrossing effects are not very sensitive to the electron concentration. The origin of the observed anticrossing effects remains an open issue but it is likely to be related to the spin-orbit interaction.

Chapter 7

Luminescence and absorption-type studies of modulation doped $Cd_{1-X}Mn_XTe$ quantum well structures

Introduction

Magneto-optics is an important experimental tool for investigating semiconductor nanostructures. Interband optical spectroscopy has been widely applied to obtain information on 2D carriers and also for studying the magnetic properties of quantum well structures based on DMS materials, where the electronic energy spectrum can be modified via the ***sp-d*** exchange interaction. In these materials, the resulting spin levels separation leads to a giant Zeeman splitting which is strongly reflected in the optical properties, especially, in the emission spectra. Hence, one can use optical means for performing magnetization studies [Haury-1997]. The effects of manganese spin polarization on the optical properties of DMS materials are largely relevant so that they can be often studied without a deep understanding of the optical response.

However, there are still other important reasons why the optical studies of II-VI semiconductor structures have recently developed an increasing interest. The tetrahedral bondings ($s\text{-}p^3$) in the II-VI compounds are more ionic than in the III-V case which leads to an increase of the effective Rydberg constant: R=5.5 meV in GaAs, R=14 meV in CdTe. A variety of the observed effects related to the absorption and emission processes provide a valuable insight into the many-body response of a Fermi sea in the presence of a photo-created electron-hole pair. Both, absorption and emission spectra are dominated by different excitonic complexes, which are sensitive to the presence of carriers.

This chapter is divided into two distinct parts. In the first part we present the results of luminescence studies of CdMnTe quantum wells at very low temperatures and very low magnetic fields. The aim of these experiments was to use optical spectroscopy to probe the magnetic properties of our structures. In the

second part of this chapter, we present a more detailed investigation of the optical properties. We focus our investigations on the evolution of the optical response in Cd(Mn)Te QWs for different electron densities at zero field and under magnetic fields. Such studies allow to analyze later the main features of the emission and absorption spectra observed for quantum wells with relatively high electron concentration. Finally, we discuss our main experimental findings and suggest that the coexistence of "lakes of 2DEG" and "insulating islands" is necessary to interpret the data obtained in our samples.

7.1 Magnetism study by optical means

The presence of local magnetic moments in CdMnTe induces a significant realignment of the electronic spin states under magnetic field. This realignment is due to the ***sp-d*** exchange interaction and is interpreted in terms of the giant Zeeman splitting (within the mean field approach). The giant Zeeman splitting is in fact a direct measure of the magnetization of the system. In case of paramagnets, such as an ensemble of isolated Mn^{2+} ions, the magnetization M is given by a Brillouin function and follows the Curie law at low magnetic fields (M~B/T). Such magnetic field and temperature dependence of the magnetization may be reflected in photoluminescence spectra.

7.1.1 Realignment of energy bands

As described in chapter 1, CdTe is a wide gap semiconductor whose crystallization involves valence ***s*** electrons of the group II element (conduction band) and valence ***p*** electrons of the group VI element (valence band). The band extrema for the conduction band and for the valence band are located at the center of the Brillouin zone (direct band gap). The conduction and valence bands are correspondingly Γ_6 and Γ_8 symmetry whose total angular momenta are J=1/2 and J=3/2, respectively (see Figure.1.1). Under application of a magnetic field in z-direction, the spin alignment of the conduction band in CdTe is such that spin down levels (σ_z=−1/2) correspond to higher- and spin up (σ_z =+1/2) to lower-energy states due to the negative electronic g-factor [Sirenko-1997].

The incorporation of Mn^{2+} ions realigns the spin states for electrons and holes under magnetic field as shown in Fig. 7.1. The alignment of electronic spin levels inverts the sign of the effective g-factor with respect to the CdTe. The situation is more complex for the valence states due to effects of band mixing.

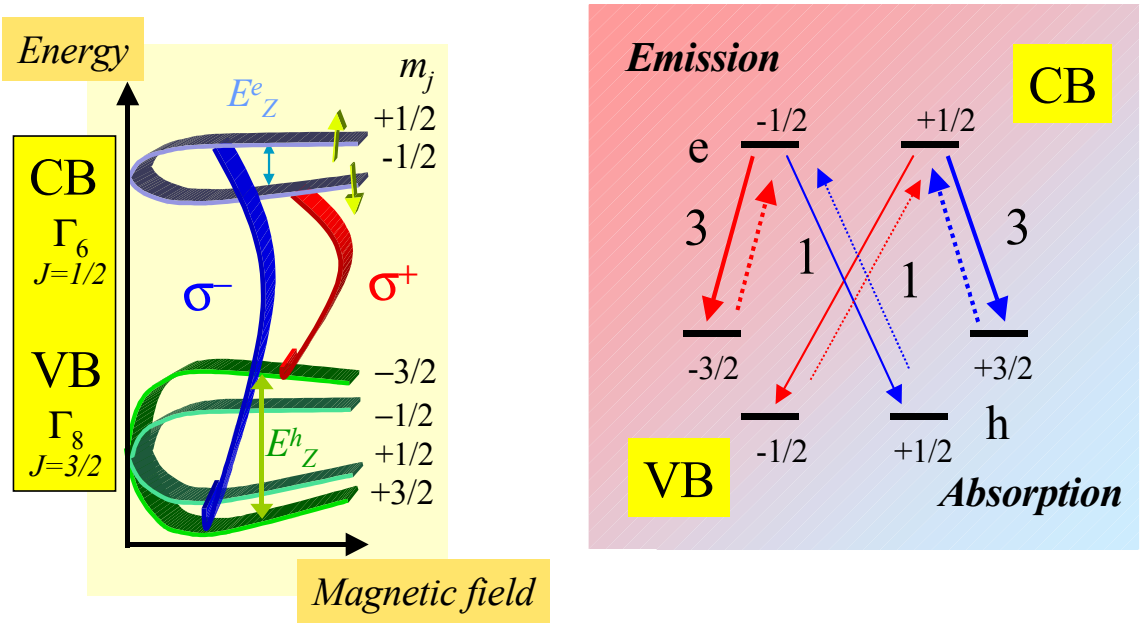

Figure.7.1: Left) Schematic illustration of the magnetic field dependence of the conduction (Γ_6) and valence (Γ_8) band structure in CdMnTe. The main observable electronic transitions (σ+/σ-) are indicated by red/blue arrow. Right) Optical selection rules for emission and absorption. The inter-band matrix. Elements are three times larger in case of transitions involving hole states ±3/2 than to states ±1/2.

For the case of quantum wells, the $J_Z=\pm 3/2$ and $J_Z=\pm 1/2$ valence states are split due to confinement effects which simplifies the description of the optical experiments since we can often consider only $J_Z=\pm 3/2$ states. On the other hand, mixing between heavy and light hole states certainly leads to a nontrivial dependence of the spin splitting as a function of the magnetic field which is not well known. However, at low magnetic fields where the ***p-d*** exchange term is the main contribution to the energy level position, the spin alignment of the valence band states is well established. As shown in Fig.7.1, it is clear that the spin splitting in the valence band Γ_8 states with J=3/2, is four times bigger than the spin splitting in the conduction band ***s-d*** exchange term. Nevertheless, the intrinsic spin structure of the valence band is less well known. In spite of these complications the selection rules for optical transitions in CdMnTe are well established and they are shown in Fig.7.1. The lower spin component of the band edge transition is observed for σ+ circularly polarized light and corresponds to the transitions between the lower electron spin level (σ_z =-1/2) and upper hole spin level (m_j=-3/2). The higher energy σ− component of the band edge transition is between the upper electron (σ_z =+1/2) and lower hole (m_j =+3/2) spin sublevels.

Therefore, the $\sigma+/\sigma-$ splitting of the band edge transitions corresponds to the sum of the spin splitting for the conduction (E^e_Z) and in the valence band (E^h_Z).

7.1.2 Experimental details

We have performed magneto-optical experiments on two similar modulation doped 10nm-thick single $Cd_{1-x}Mn_xTe$ QW structures with an effective Mn concentration $x_{eff} \approx 0.3\%$ for sample A and slightly larger $x_{eff} \approx 0.4\%$ for sample B. The electron sheet concentrations are $n_e = 5.9 \times 10^{11}$ cm^{-2} (sample A) and $n_e = 3 \times 10^{11}$ cm^{-2} (sample B). Sample A is from of the same wafer 100997A on which we performed the magneto-transport studies presented in chapter 4. Here, we concentrate on some particular features of the PL spectra. A detailed investigation of the PL as a function of both temperature and weak external field has been carried out in a dilution refrigerator mounted inside a superconducting coil. A series of measurement have been performed from 0 up to 0.3 T in the Faraday configuration, exciting and collecting luminescence using a 600-μm-diameter optical fiber. The QW luminescence was excited above the barrier by the green line (514.5 nm) of an Ar^+ laser. The density of the excitation power was kept below $80 \mu W/cm^2$ in order to avoid the effects of laser heating. The analysis of the circular polarization of the luminescence was performed using a quarter-wave plate and a linear polarizer both inserted between the sample and the tip of the fibre. After cooling the samples from room temperature, the PL experiments were carried out at fixed temperatures between 0.075 and 4.2K. The luminescence spectra were taken using a CCD camera, while the magnetic field was fixed. The PL spectra obtained are independent of the direction of the magnetic field sweep.

7.1.3 Optical determination of the giant Zeeman splitting

In the considered range of magnetic fields, the Landau quantization is not pronounced in our spectra and therefore we neglect it. The PL spectrum is a broad line as shown in Figure.7.2a. The 2DEG luminescence, attributed to recombination processes between electrons occupying states at the bottom of the e1 subband and photogenerated holes thermalized on the top of hh1 valence band state, immediately splits when magnetic field is applied (see Fig.7.2b). The band realignment induced by ***sp-d*** exchange interaction leads to a PL spectrum whose energy and intensity are very sensitive to changes in the external magnetic field and temperature, mostly driven by the spin polarization of the magnetic subsystem. At fixed magnetic field lowering the temperature, the $\sigma+$ ($\sigma-$) emission line moves to lower (higher) energy. The $\sigma+$ emission gains in intensity

whereas σ– emission becomes weaker as a consequence of increasing spin polarization of photo-excited holes. Decreasing the temperature increases the Zeeman energy and consequently most of the holes thermalize in the lowest energy level (-3/2) before recombining. Hence, the emission is strongly polarized in the σ+ component.

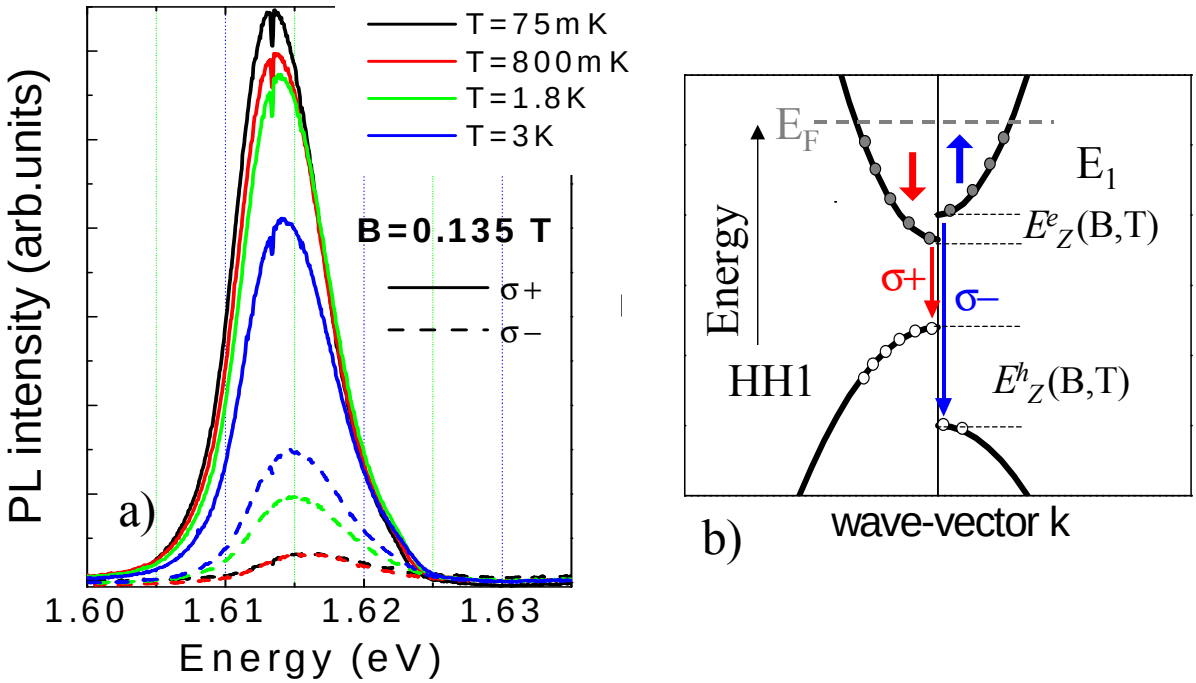

Figure.7.2.a) Temperature dependence of the σ+ (solid line) and σ– (dotted line) components of photoluminescence spectra at B=0.135T.b) Illustration of the rearrangement of the band structure at given external magnetic field B and temperature T.

The "*polarization*" of the luminescence is also obtained when increasing the magnetic field at fixed temperature. Hence, the luminescence signal at low temperatures becomes strongly σ+ polarized already at low magnetic fields. This is the main feature found in the optical response of CdMnTe quantum wells which independently of the origin of the optical transitions (excitonic or band to band transitions), is common for undoped and doped structures.

The energy positions of σ+ and σ – PL components have been followed by means of calculating the center of gravity ($\langle E \rangle = \Sigma I_i \cdot E_i / \Sigma I_i$) of the corresponding spectra. This method allows us to measure precisely relatively small, with respect to the linewidth, changes of the position of the luminescence spectrum. The σ+/σ–

splitting of the recombination line is plotted in Figure.7.3a as a function of magnetic field for different temperatures. As shown in this figure, the spin splitting of the luminescence line progressively increases as a function of decreasing temperature, reflecting the variation with temperature of the Mn^{2+} magnetization.

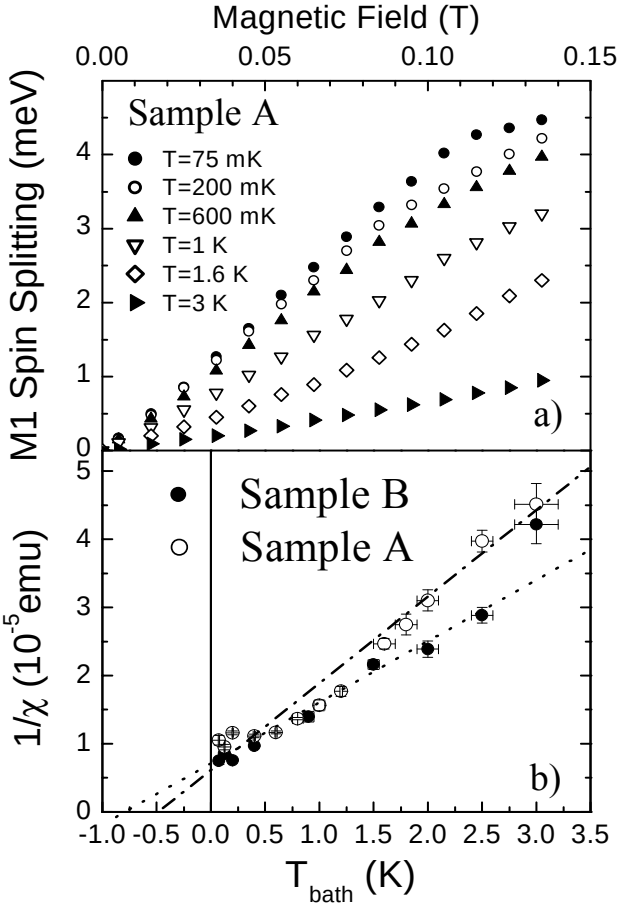

Figure.7.3. (a) Magnetic field dependence of the splitting between the σ^+ and σ^- first moment M_1 of the luminescence components for different bath temperatures. The data corresponds to the sample A. (b) Temperature dependence of the zero-field magnetic susceptibility calculated in accordance to Eq.7.1, from the results of spin splitting measurements. Open and closed circles denote the data obtained for sample A and B, respectively.

7.1.4 Magnetic susceptibility

One of the characteristic quantities used to describe the magnetic properties is the magnetic susceptibility. The derivative of the observed total spin splitting Δ with respect to the magnetic field, measured at B≈0 can be related to zero-field magnetic field susceptibility χ of Mn^{2+} ions through the following relation [Galazka-1980]:

$$\chi(T)\big|_{B\to 0} = \left(\frac{\partial M}{\partial H}\right)\Big|_{B\to 0} = \left(\frac{g\mu_B}{|\alpha-\beta|}\right)\left(\frac{\partial \Delta}{\partial H}\right)\Big|_{B\to 0} \qquad \text{Eq.7.1}$$

where g is the Landé factor of the Mn assumed here to be equal to 2; α and β are ***s-d*** and ***p-d*** exchange integrals respectively. The susceptibility of the manganese ions obtained using the above formula is shown in Fig.7.3b. As it can be seen in the figure, the temperature dependence of χ(T) follows a linear behaviour for both samples which can be described by the Curie-Weiss law $1/\chi \sim T_{Mn}$, where T_{Mn} is the effective temperature of the Mn subsystem defined as in chapter 4 ($T_{Mn}=T_{bath}+T_0$). The extracted values for T_0 are 0.6 K and 0.75 K for sample A and B respectively, of the same order as the value deduced for sample A in chapter 4 (T_0=180 mK). The disagreement between optical and transport methods could come from the determination of the Zeeman energy. Whereas the transport method based on the observation of nodes in the amplitude of the oscillations of the longitudinal resistance was very precise, the broadening of the emission spectrum (~15 meV) leads to a larger inaccuracy in the case of our optical method. The Zeeman energy used in the Eq.7.1 was estimated from the first moment calculation for both polarization components. Using this method we ignore possible changes in the spectral shape which in principle are possible, for example, due to changes in the distribution of photoexcited holes. Nevertheless, using our method to analyze the PL data, we observe the expected behavior of the magnetic susceptibility which is characteristic for the ensemble of paramagnetic Mn^{2+} ions with weak effects of antiferromagnetic coupling. These latter effects lead to an extrapolated value of $1/\chi$ which is non zero. These effects are accounted for the Curie Weiss law by a phenomenological parameter T_0 which can be considered as a correction to the "effective manganese temperature" $T_{Mn}=T+T_0$. The experimental trend to observe larger values for larger manganese concentrations is correct, however, the absolute values of parameter T_0 are probably overestimated in these experiments.

We conclude therefore that interband luminescence might be considered as an easy method to study the susceptibility of CdMnTe structures. The advantage of this method is the possibility to study the selected part of the structure (quantum well) with a small number of spins. The method is however not very accurate in case of doped structures. The accuracy of this method could probably be much better for structures with narrow luminescence lines (undoped quantum wells). Possibly, this method could also be improved by a more detailed analysis of the shape of the luminescence line. This is however a difficult task since it requires a deeper understanding of the optical response of the investigated structures.

7.2 Optical properties of II-VI quantum well structures

7.2.1. Introductory remarks

Interband optical spectroscopy has been widely applied to obtain information on 2D carriers confined in semiconductor quantum well structures. The fundamental interest has been focused on excitons, screening effects, electron-electron and electron-impurity interactions. In spite of the large number of investigations the optical properties of quantum wells are well understood only for two extreme cases:

(i) when the concentration of the excess carriers (for instance, electrons) is negligible. In this case, the exciton binding energy (E_b) is much larger than the Fermi energy (E_F), i.e. the Bohr radius is larger than $1/k_F$. The formation of excitons, i.e., electron-hole pairs bound by the Coulomb potential, is possible since the exciton radius (electron-hole distance in the bound state) is much smaller that the mean distance between the excess electrons. The excitonic spectra in quantum wells can be well described by a two-dimensional hydrogenic-like energy spectrum either in the absence [MacDonald-1986, Jarosik -1985] or in the presence of magnetic fields [Potemski-1991a].

(ii) when the excitons are completely screened. This situation occurs when E_b is much smaller than E_F, i.e. at high electron concentration. In this case, the potential fluctuations and excitonic effects are effectively screened by the Fermi sea. The emission and absorption spectra reflect the phase space filling up to the Fermi energy. In a simple approximation the optical spectra can be understood within the framework of single particle transitions whereas the effects of electron-electron interaction are included by simply considering the shrinking of the fundamental bandgap (bandgap renormalization). The optical transitions in a magnetic field are then those between discrete Landau levels for electrons and holes. The allowed transitions are those between the electron and hole Landau levels with the same

index ($\Delta N=0$). The breaking of this selection rule is often considered if the holes involved in the optical process are localized [Hawrylak-1992].

Recent works also give some insight into the understanding of optical processes at low but non-zero electron concentrations. Investigations in this regime ($E_b>E_F$) underline the possibility of the formation of bound states involving more than two-particles. The important observation is the appearance of the *charged exciton* X^- or *trion* in the optical spectra of QWs with low electron concentration. Such complexes first observed by Kheng and coworkers in 1993 in CdTe [Kheng-1993] and afterwards in GaAs [Buhmann-1995] or ZnSe [Astakhov-1999], are the simplest evidence of many-body interaction (three particles). The X^- consists of two electrons with anti-parallel spins bound to a valence hole and is similar to the hydrogen ion H^-. The trion represents the lowest energy state for a 2D dilute electron system, coexisting with the ordinary neutral exciton X in a dynamical equilibrium [Jeukens-2001]. There exists a considerable controversy whether charged excitons can exist as mobile particles or they are weakly localized in the potential fluctuations. Eytan and coworker have suggested [Eytan-1998] that trions may be localized by potential fluctuations induced by the remote ionized donors in the barriers surrounding the quantum well. The possibility to observe free trions has been reported recently in very high quality GaAs samples, in which the trion has been shown to freely drift under electric fields as any charged particle [Sanvitto-2001]. The appearance of trions in the optical spectra of quantum wells with low electron concentration is accompanied by other spectral features known as *combined exciton–electron processes* [Yakovlev-1997]. These processes may be understood in terms of exciton-electron scattering. Considering, for example, the process of exciton absorption it is assumed to be accompanied by electron excitation above the Fermi level. Therefore, such processes are expected to be responsible for the broadening of the exciton absorption peak on the high energy side. In magnetic fields, the relevant electron excitations are between Landau levels. The exciton-electron combined process then involves cyclotron excitation of an electron. This results in the observation of a weak absorption peak which develops from the high energy tail of the exciton peak. The combined exciton-electron absorption peak is observed above the exciton peak with an energy separation corresponding to the cyclotron energy. In luminescence, the exciton-electron processes are expected to activate a low energy tailing of the excitonic peak. In magnetic fields this tail can be expected to develop into a discrete line (known in literature as a shake-up line), which is now pushed down by cyclotron energy with respect to the exciton line position. The possibility to observe "*combined*" processes involving trions, rather than excitons, has also been recently considered [Ossau-2001].

The interpretation of the optical response of quantum wells seems to be most difficult in case when $E_b \approx E_F$. For the case of II-VI compounds such a regime

corresponds to the range of electron densities ~$1x10^{11}cm^{-2}$. The corresponding optical spectra show many intriguing results which however are not yet completely understood: see for example [Teran-1998, Imanaka-2001] for the works reporting the magneto-luminescence spectra and [Huard-2000a] for the work on magneto-transmission spectra.

The aim of the investigations presented in this chapter is to investigate the properties of the emission and absorption spectra of CdMnTe and CdTe quantum wells with electron concentration around $6x10^{11}cm^{-2}$. A precise interpretation of these spectra is not an easy task. In the following, we discuss our experimental results underlying the main difficulties for understanding the data and we propose a quantitative model which may possibly explain the characteristic behavior of our spectra. A characteristic experimental observation is that specific features related to excitonic effects persist in emission and absorption spectra for samples with electron concentration as high as $6.3x10^{11}cm^{-2}$. Such excitonic effects coexist with "usual band-to band transitions" expected in the limit of very high electron concentrations. We propose a model based on the coexistence of two different spatial regions: "lakes of 2DEG" and insulating islands.

We begin with the analysis of the optical response as a function of carrier density (starting with the well-known case of low electron concentration). This is crucial for the analysis of our main observations and discussion of the data obtained for samples with high electron concentrations (~$6x10^{11}$cm cm^{-2}), which are presented in the second part of this chapter. Initially, we concentrate on the data obtained at zero magnetic field before discussing the evolution of the optical response with the magnetic field.

7.2.2 Experimental details

In order to study the evolution of the optical properties with the carrier density, a special modulation-doped quantum well structure with spatial in-plane profiling of doping density was performed. As described in chapter 2, the structure consists in four different spatial regions B_i with the same quantum well (10nm $Cd_{0.998}Mn_{0.002}Te$) and spacer (10nm), but different thickness of the doping region d_i, d_1=0 nm, d_2=28 nm, d_3= 60 nm and d_4=120 nm. A set of four samples cut from the different spatial regions B_i with carrier densities from ~10^{10} up to $1.5x10^{11}$ cm^{-2} was used in the investigations. The special design of the sample structure permits to additionally control the electron concentration by excitation above or below the barrier, as described in chapter 2. Thus, we have profit out this method to change the electron concentration in the sample B_4. We increase by a factor of 2 the carrier density observed under red excitation (B_4(R) with $n_e=1.5x10^{11}cm^{-2}$) by additional

illumination with green light (B_4(G) with $n_e=3x10^{11}cm^{-2}$) at a very low power so that it does not contribute to the luminescence signal. Thus, we have B_4(R) and B_4(G) which are two different concentration in the same piece of material. The electron concentration for B_3, B_4(R), B_4(G) has been determined from the analysis of the magneto-optical data. The electron concentration for B_1, B_2 samples has been estimated by comparing the intensities of the X and X^- peaks [Jeukens-2001].

We also study two samples with higher carrier densities grown on different wafers but with a similar quantum well and spacer thickness (10 nm). One is the sample 100997A on which we have shown the transport and cyclotron resonance results in previous chapters. As determined by transport data, this sample has an effective Mn concentration $x_{eff}=0.3\%$ and a carrier density $n_e=5.9x10^{11}cm^{-2}$. The second is the sample 072897A on which we have also performed cyclotron resonance experiments. It is a CdTe quantum well whose carrier density is $n_e=6.3x10^{11}cm^{-2}$. In both samples, the electron concentrations hardly change ($<5\%$) when exciting above or below barrier.

The samples were subjected to a detailed investigation of the PL, PLE and reflectance carried out at temperatures in the range of 1.7 K and 70 K and in magnetic fields up to 25T in the Faraday configuration. The polarization resolved PL and PLE experiments were performed using the mini-optical table described in Appendix 3. A Titanium sapphire laser tunable between 695-1200 nm was used for the PLE. The magneto-reflectance experiments were performed by illuminating with unpolarized white light by an optical 200-μm-diameter optical fibre and collecting the reflected light by using a 600-μm-diameter optical fibre. The analysis of the circular polarization components of the reflected light was performed by a combination of a quarter-wave plate followed by a linear polarizer inserted between the sample and the tip of the 600-nm-fibre. The PL, PLE and reflectance spectra were taken using a CCD camera.

7.2.3 Evolution of luminescence and absorption spectra as a function of carrier density at zero magnetic field

7.2.3.1Experimental results: low density range

Representative PL using below-barrier laser excitation and PLE spectra, measured for a series samples B_i are shown in Fig. 7.4 at zero magnetic field and temperature T=1.7 K. Sample B_1 is intentionally undoped, but very likely contains ~10^{10} cm^{-2} electrons in the well. The strong PLE (absorption) peak observed for this sample is identified as the neutral exciton X peak. A second absorption peak observed at lower energies and less intense is attributed to negatively charged

exciton X^-. Luminescence shows also two emission lines. A higher energy PL line coincides with its absorption counterpart and can be clearly attributed to the free exciton X. The lower energy PL peak is most likely due to the negatively charged exciton X^-. This peak is slightly shifted down in energy with respect to its absorption counterpart. This Stokes shift between the emission and the absorption peaks indicates some degree of localization of X^- excitons observed in PL.

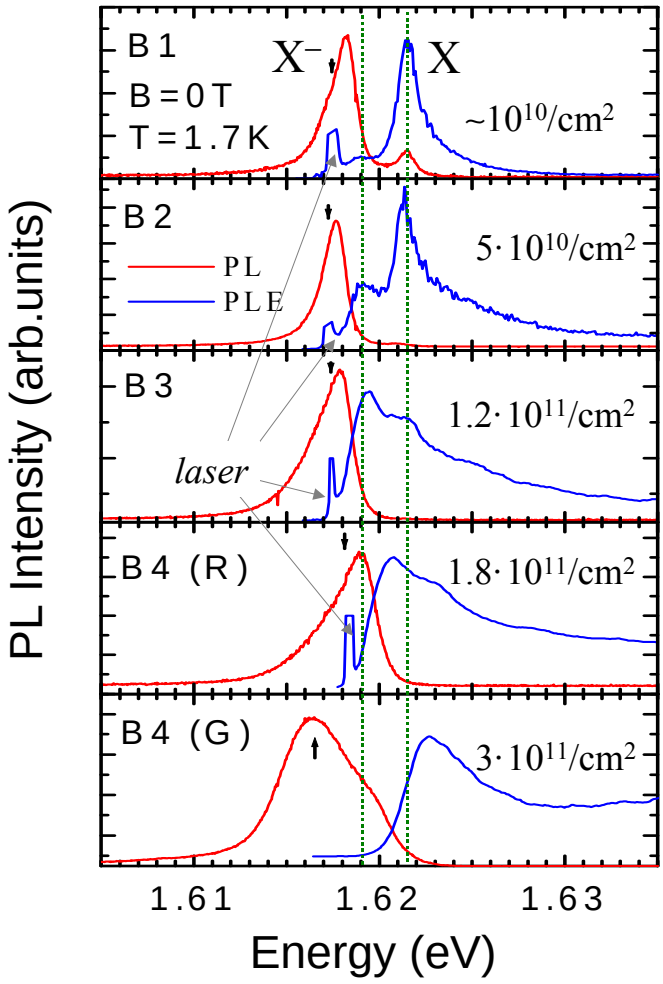

Figure.7.4 : PL and PLE spectra at zero field and T=1.7 K , for samples B_i with different concentrations. The absorption positions of the neutral and negatively charged excitons are indicated by dotted lines. The black arrows indicate the detection energy position of the PLE spectrum.

A characteristic asymmetry in the broadening of the main absorption and emission peaks is clearly observed. The broadening of the X absorption peak is more

pronounced at the high energy side, whereas the main emission peak is broadened on the low energy side. This is a clear indication of some contribution of exciton-electron scattering to the observed optical transitions (combined exciton-electron processes). The spectra for sample B_2 are qualitatively the same. We note, however, the increasing intensities of the X^- transitions with respect to intensities of X (peaks) due to the increase of the number of carrier. One may also note the narrowing of the X absorption and X^- emission peaks with respect to the spectra observed for sample B_1. This could be a consequence of the screening of the potential fluctuation by electrons, which should be more effective in sample B_2 than in sample B_1.

Further increase of electron concentration (sample B_3) leads to a remarkable broadening of the absorption spectrum, mostly on the high energy side, and an enhancement of the X^- absorption. The luminescence spectrum shows a sharp onset at the high energy side and *peaks* at the position of X^-, with a more and more pronounced low energy tail. For sample B_4(R) we can no longer distinguish the X and X^- lines in the absorption spectrum. The absorption spectrum peaks at the energy position above the X^- resonance, decrease relatively quickly on the low energy side but very slowly on the high energy side. Adding more carriers leads to a blue shift of the absorption spectrum whereas the luminescence becomes much broader and shifts towards lower energy (see B_4(G)).

At this point, we would like to emphasize the experimental fact that at any electron concentrations there is always a nonzero absorption at the energies which correspond to the positions of X^- and X excitons. Similarly, a nonzero luminescence signal exists at X and X^- positions for any value of the electron concentration. In the following we analyze in more detail the spectra for samples with high electron concentrations.

7.2.3.2 Experimental results: high density range

Characteristic features of optical spectra observed for structures with high electron concentration (sample 100997A) are shown in Figure.7.5. In the emission spectrum, we can distinguish (green line) three lines labeled as B-B for the lowest energy line associated to band-to-band transitions as will be shown later on, M-E for the middle energy line and H-E for the highest energy line (zoomed by 10 times). The two more pronounced are B-B and M-E, whereas H-E represents a clear onset on the high-energy side.

Such characteristic features of the PL spectra are observed for a large class of samples with electron concentration in the range $3\text{-}7\text{x}10^{11}$ cm^{-2}. However for this particular sample, the shape of the luminescence spectra is very much dependent

on whether we excite below or above the barrier (see red and green trace, respectively). As shown in the inset of Fig.7.5, the relative intensity of the M-E emission line, maximum under below barrier excitation, is differently pronounced by controlling the excitation, allowing distinct PL spectrum shapes, i.e. different intensity ratio of the B-B and M-E luminescence peaks. At the same time, the PLE spectra of the B-B and M-E luminescence peaks are also quite different, as seen in Fig.7.5. The onset of the PLE of the M-E luminescence line (orange line) is clearly red-shifted with respect to the onset of the PLE of the B-B luminescence (blue line). However, the main difference arises in the development of the additional absorption peak around 1.623eV in the PLE of the M-E luminescence (green arrow).

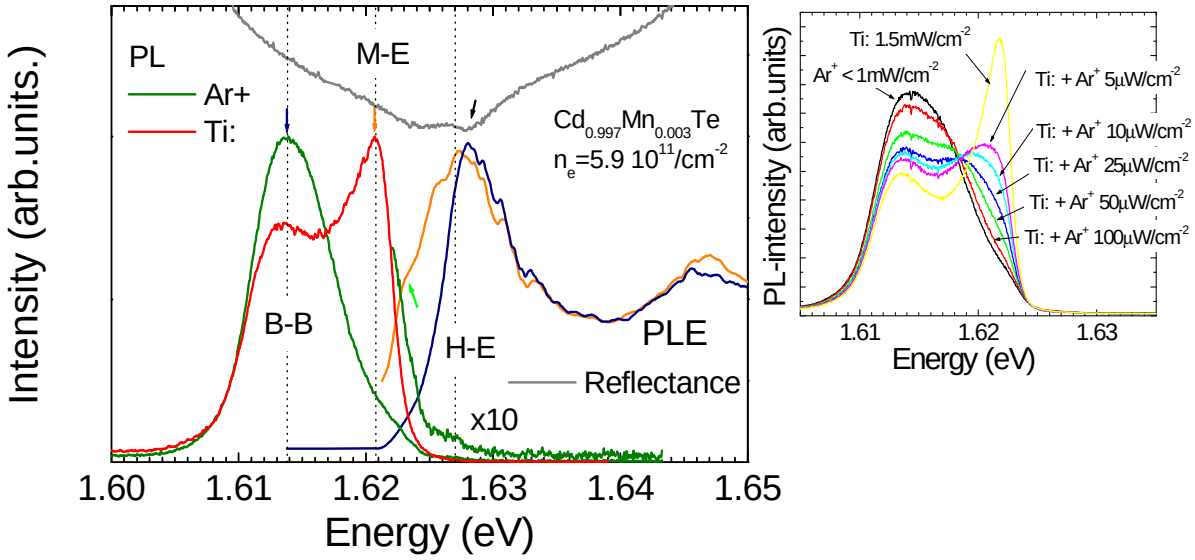

Figure.7.5 : Comparison of the PL, PLE and reflectance spectra for sample 100997A at zero field and T=1.7 K. The PL spectra correspond to different excitation conditions: above (green line) and below (red line) the barrier. PLE spectra at the detection energy positions: B-B (blue line) and M-E (orange line). The green and black arrow denotes the PLE resonances, which coincide with those of the reflectance spectrum (gray line). Inset: PL spectra taken under excitation using green (Ar^+ 514.5nm), red (Ti: 740 nm) and simultaneous red+green light with different powers of Ar^+ line.

This absorption peak also manifested in the reflectance spectra (gray line) implies clear differences for the appearance of the B-B and the M-E emission lines as shown in Fig. 7.6. The M-E luminescence is already well pronounced when exciting just above the emission line position (green and red lines) whereas the B-B luminescence increases at higher excitation energies (blue line).

7.2.3.2 Discussion: band-to-band versus exciton-like transitions

We think that the B-B luminescence together with its characteristic excitation spectrum and typical high energy onset (H-E) can be understood in terms of a simple model of one particle interband transitions, corrected for the effect of band gap renormalization. Subsequently, this assumption will be confirmed by experiments performed in magnetic field. The B-B luminescence is due to "one particle" recombination processes involving 2D electrons from the Fermi sea and photo-created holes (see inset Fig.7.6, transition 1). This luminescence peaks at the energy which corresponds to the renormalized bandgap. The high energy onset (H-E) corresponds to the recombination processes involving electrons from the vicinity of the Fermi level (see inset Fig.7.6, transition 3). Thus, the difference between the energy position of the B-B luminescence peak and the energy position of the onset of the PLE of the B-B luminescence (black arrow in Fig.7.5) corresponds to the Moss-Burstein shift $\Delta_{M\text{-}B} = E_F(1+m^*_e/m^*_h)$. From the spectrum, we obtain $\Delta_{M\text{-}B}$=14.5 meV and assuming $m^*_e=0.107m_0$ as deduced from cyclotron resonance measurements and $m^*_h=0.4m_0$ for the heavy hole mass in CdTe [Segall-1967] we obtain $n_e=5.1x10^{11}$ cm^{-2} in agreement with the transport data ($n_e=5.9x10^{11}cm^{-1}$).

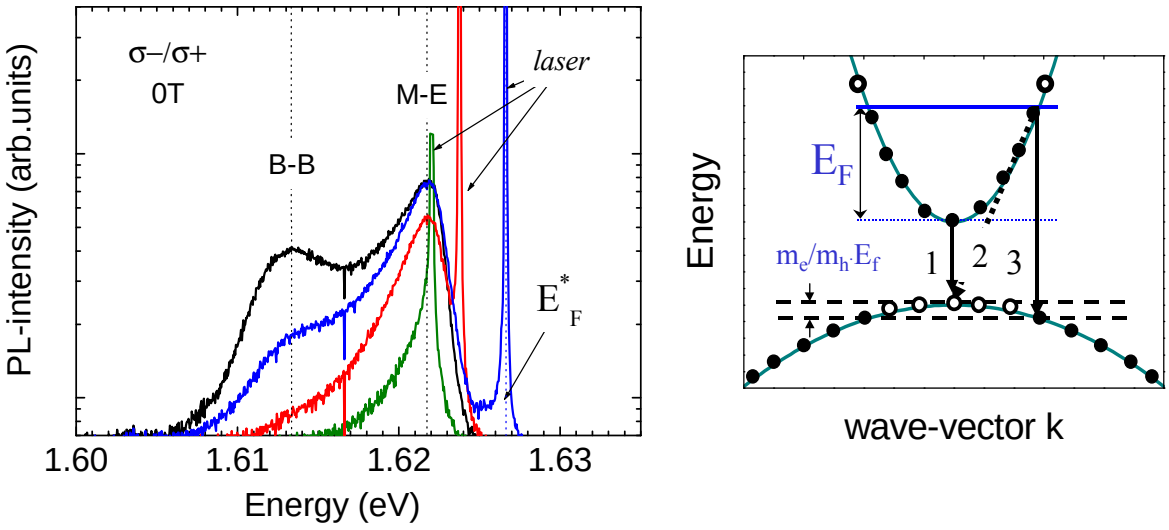

Figure.7.6 : PL spectra for different energy excitations (below barrier). Schema of possible optical transitions in the *k*-space.

The appearance of the M-E luminescence is more complex to interpret, since it can be effectively excited below the "Moss-Burstein shifted" absorption threshold. Such behavior is characteristic for undoped or lightly doped structures when excitonic effects dominate the optical spectra. Thus, we are tempted to assume that the M-E luminescence has an excitonic character. This statement will be further verified by the experiments in magnetic fields.

We note here that the anomalous M-E peak is often observed in the luminescence spectra of modulation doped quantum well structures [Kochereshko-2000, Huard-2000b]. Most often it is interpreted in terms of the observation of the so called Fermi edge singularity, i.e. in terms of the observation of the many-body enhancement of the oscillator strength of forbidden transitions involving $\boldsymbol{k}$=0 holes and electrons from the vicinity of the Fermi energy (see inset Fig.7.6, transition 2). This effect could be considered as a possible origin of the M-E luminescence peak in our sample. However, such an explanation would imply the energy position of the M-E peak at E_G+E_F. This means that we would expect that the M-E emission position to be red-shifted by $E_F m^*_e/m^*_h$ from the absorption onset (which is expected at $E_G + E_F(1+m^*_e/m^*_h)$) and blue-shifted by E_F from the B-B luminescence peak. Using the experimental values we deduce the rather unrealistic estimated for E_F=10meV and $m^*_h=0.2m_0$. Both values are in clear disagreement with the values previously estimated, and in contradiction with the results of the magneto-optical experiments presented in next section.

In Figure.7.7, we group all the information concerning the energy positions of the peaks observed in the PL and the PLE spectra measured for samples B_1, B_2, B_3 B_4(R) B_4(G) and 100997A. The peak positions are plotted as a function of the dimensionless parameter $1/r_s=a^{3D}_B/<r>$, where a^{3D}_B =50A stands for a 3D effective Rydberg in CdTe and $<r>=n_e^{-1/2}$ is the mean distance between the 2D electrons confined in the well. Excitonic-like peaks are marked with circles (open for absorption peaks and closed for luminescence peaks) and band-to band transitions are represented by triangles (open for absorption peaks and closed for luminescence peaks). The solid green line represents the renormalized bandgap BGR. It has been calculated using a generally accepted formula [Kleiman-1986]:

$$BGR = E_G - C\,(n_e^{\,2}\, a_B)^{1/3} \qquad \text{Eq.7.2}$$

where we assume C=2.5 appropriate for our quasi-2D system [Wojtowicz-1999] and the bandgap $E_G = E_X + E_{bX}$, where E_X=1.6215 eV is the resonance position for the neutral exciton X extracted from the absorption spectrum. E_{bX} is the binding energy whose value E_{bX} = 18 meV has been estimated from the energy distance between the 1s and 2s exciton states observed in PLE spectra in the sample with

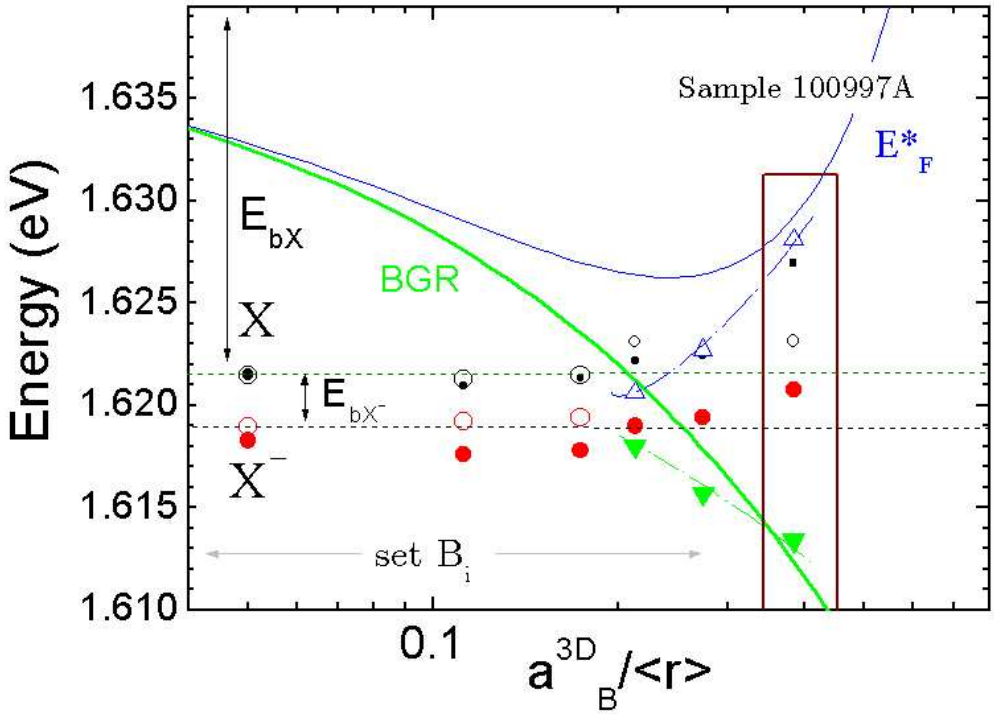

Figure.7.7 : Representation of the emission (solid circles) and absorption (empty circles) energy position extracted from the PL and PLE spectra for samples B_i (Figure 7.4) and 100997A (Figure7.5) as a function of the $a^{3D}_B/<r>$. The transitions related to X have a black color, X^- red color and band-to-band transition blue and green color. The absorption positions of the neutral (black line) and negatively charged (red line) excitons for the sample B_1 are indicated by dotted lines. The predicted bandgap renormalization position and the onset of the Fermi energy as described in the text are indicated by green and blue line, respectively. The blue and green dash-dotted lines are guided by eye.

smallest electron concentration (B_1). Thus, we obtain that the bandgap is equal to $E_G = 1.6395$ eV for zero electron concentration. The solid blue line in Fig.7.7 represented the energy position of the Moss-Burstein absorption onset:

$$E^*_F = BGR + E_F(1+m^*_e/m^*_h) \qquad \text{Eq.7.3}$$

For electron concentrations $n_e<1.2\text{x}10^{11}\text{cm}^{-2}$ ($1/r_s<0.2$) the excitonic-like transitions can be regarded as well defined X and X^- excitonic resonances. The band to band transitions appear to be visible in the spectra when the renormalized band gap crosses the excitonic resonance. The evolution of the band to band transitions with the electron concentration ($1/r_S$) (shown with dashed lines as a guide to the eye) is in good agreement with the expected changes of the bandgap and of the Moss-

Burstein absorption onset. The survival of excitonic-like resonance for electron concentrations in the range when the renormalized band gap is smaller than the energy of the exciton resonance, is nevertheless a surprising observation.

7.2.4 Studies in magnetic fields

The application of an external magnetic field significantly transforms the optical properties of CdMnTe quantum wells. On one hand, the ***sp-d*** exchange interaction leads to the giant Zeeman splitting which leads to the polarization of the emitted and absorbed light. As described in the first part of the chapter, the luminescence spectra already becomes strongly σ+ polarized at low magnetic fields due to the large spin splitting in the valence band and in consequence the strong spin polarization of the photocreated holes (see Fig. 7.1). The influence of the magnetic field on the orbital motion of electrons is equally important. It is reflected in the spectra by the observation of a diamagnetic shift for the excitonic resonances in the case of low carrier densities and in the Landau-level like structure of the optical transitions in case of high carrier densities.

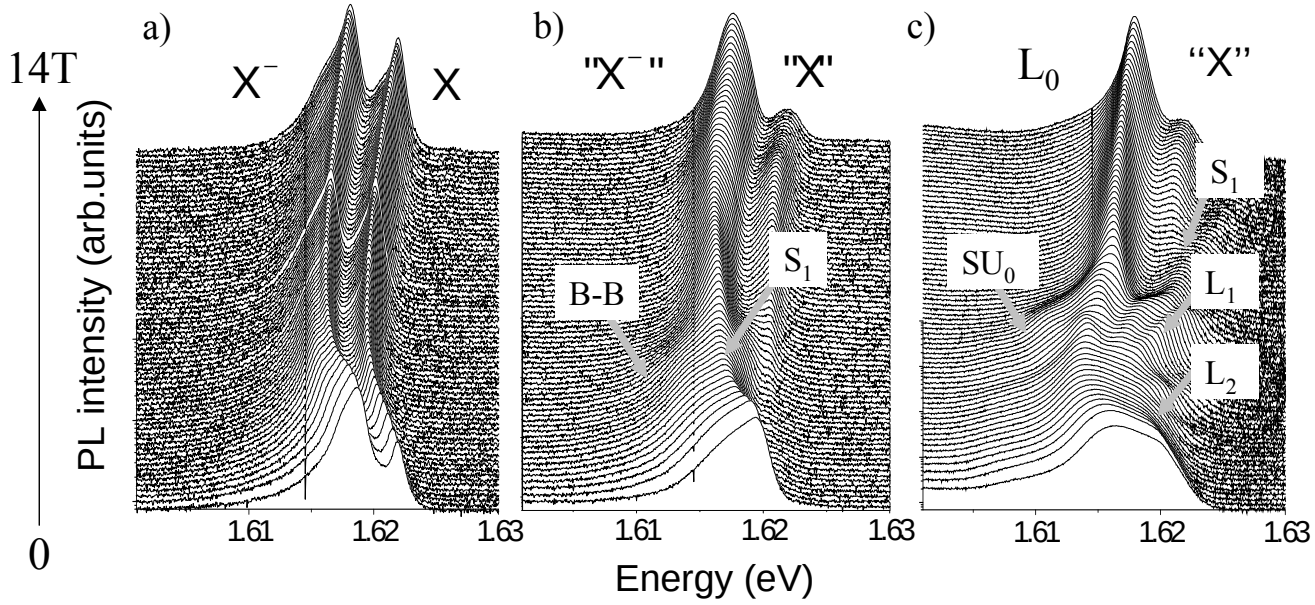

Figure.7.8 : Magnetic field evolution of the PL σ+ component at T=1.7 K for: a) $n_e \sim 10^{10}$ cm^{-2}, b) $n_e=1.8x10^{11}$ cm^{-2} and c) $n_e=3x10^{11}$ cm^{-2}.

7.2.4.1 Evolution of magneto-luminescence with the electron concentration

Figure7.8 shows the emission spectra for the σ+ polarization component of the emission at T=1.7 K under magnetic field up to 14 T for different carrier concentration (a) $1x10^{10}$ cm^{-2}, b) $1.5x10^{11}$ cm^{-2} and c) $3x10^{11}$ cm^{-2}) corresponding to the samples B_1, B_4(R), and B_4(G) respectively. A more detailed analysis of the data, extracting the energy positions of the emission and absorption peaks observed for different magnetic fields and polarization components is plotted in Fig. 7.9. The magnetic field evolution of optical transitions observed for sample B_1 with the lowest electron concentration is characteristic for transitions related to the neutral exciton X and the negatively charged exciton X^-.

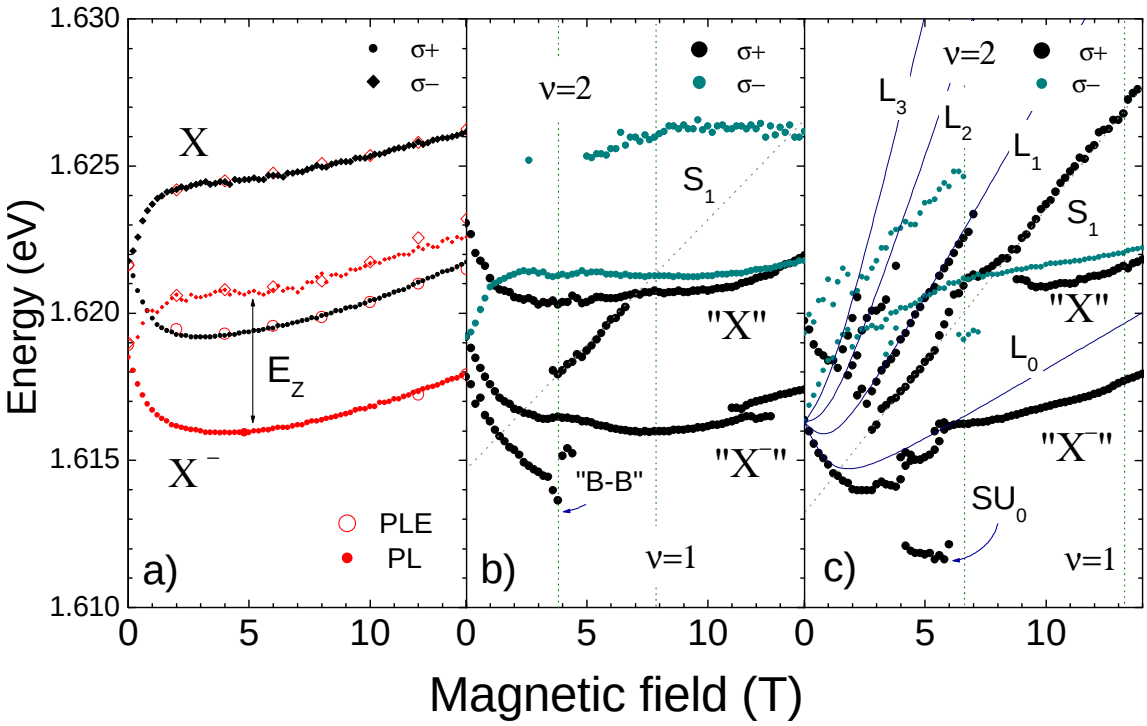

Figure.7.9. Magnetic field dependence of the PL (solid circles) and PLE (empty circles) lines of both polarization components at T=1.7 K for: a) n_e~10^{10} cm^{-2}, b) n_e=$1.8x10^{11}$ cm^{-2} and c) n_e=$3x10^{11}$ cm^{-2}.

As can be seen in Fig. 7.9a, both X and X^- transitions clearly reflect the effect of the giant Zeeman splitting. They also show a diamagnetic shift, which in case of neutral excitons is slightly steeper as compared to the X^-. Such a

difference reflects the lighter reduced mass for the neutral exciton as compared to the trion. In emission, the σ+ component is dominant for both X and X^- transitions due to the large Zeeman splitting in the valence band.

However, both σ+ and σ− components of the free exciton X are equally strongly pronounced in absorption. It is expected (chapter 1) that, the X^- absorption is mainly observed in σ+ polarization due to the effective spin polarization of the excess electrons. However, it should be noted that the σ+ absorption related to the X^- exciton is observable in magnetic fields around 12T. This observation is due to the reduced spin polarization of the excess electrons at the vanishing of the effective Zeeman splitting. In chapter 6, we showed that for an effective Mn concentration $x_{eff} \cong 0.2\%$, we expect $E_Z=0$ at magnetic fields around 12T. Although the luminescence spectra of samples B_1 and B_4(R) are very different at zero magnetic field, they become qualitatively very similar at high magnetic fields (see Fig. 7.8a,b). In such high field regions, the observed luminescence transitions have a magnetic field dependence for both polarization components very similar to X and X^- transitions observed for the sample with the lower carrier density (B_1). For this reason, we label both characteristic X^- like and X like transitions, as " X^-" and "X" in Fig.7.9. Nevertheless, in the low magnetic field region the sample B_4(R) shows richer spectra than for sample B_1. The "X" and " X^-" transitions coexist with two additional transitions: B-B and S_1. Both B-B and S_1 luminescence peaks are not very well resolved in the spectra. We anticipate that the B-B peak should be interpreted in terms of a band-to band transition involving electrons from the lowest electronic Landau level. This transition disappears from the spectra around 4 T where the magnetic field dependence of the energy position of "X^-" manifests a characteristic kink. Both effects, the disappearance of band-to band transitions and the characteristic kink seems to be related. They are commonly observed in the range of magnetic fields near filling factor ν≈2 and will become more pronounced for higher electron concentrations.

The origin of the S_1 line is not completely clear. Its dependence with the magnetic field shows a slope which roughly corresponds to the electron cyclotron energy. We could speculate that this line is due to the charged exciton – electron combined process but the S_1 line is also observed in samples with higher electron concentrations which makes such an interpretation rather doubtful. We will come back to this problem when discussing spectra for samples with higher electron concentrations.

The observation of band-to-band transitions involving subsequent Landau levels for electron and hole is clear for sample B_4(G) (see Fig. 7.8). We

can distinguish a series of luminescence peaks (L_0, L_1, L_2, L_3) whose magnetic field dependence can be described within the free particle picture:

$$E_{LN}=E_{BGR} + (N+½)\hbar\omega^{\Gamma}_{C} \pm ½ E^{*}_{Z}(B_{5/2}(B,T+T_0)) \qquad \text{Eq.7.4}$$

A series of solid navy-blue lines in Fig. 7.9c have been calculated assuming E_{BGR}=1.616 eV for the renormalized bandgap at zero magnetic field and $\hbar\omega^{\Gamma}_{C}$ =0.99meV/T for the reduced cyclotron energy. The effective Zeeman splitting E^{*}_{Z} has been calculated according to the Eq.1.11 with g^{e}=-1.6 for the electron g-factor in CdTe (g_h≈0 in our samples [Sirenko-1997]) and E^{*}_{exch}=4.2 meV for the sum of the exchange energies in the conduction and valence band. This leads to an effective Mn concentration of x_{eff}=0.19 % in good agreement with the value obtain from Raman data in chapter 6. As can be seen in Fig. 7.9c, such a free particle model of the inter-Landau level transitions qualitatively describes the set of L_N luminescence transitions among those visible in the experiment. The presence of these lines allows us to estimate the occupation of the Landau levels associated with subsequent N=0,1,2,.. We can see, for example, that for sample B_4(G), the L_1 transition disappears from the spectra around B=6.5T and therefore conclude that this magnetic field corresponds to the situation when the N=1 Landau level starts to be empty, i.e., it corresponds to filling factor ν≈2. At the same time, the main luminescence line manifests a pronounced change of character around B=6T (see Fig.7.9c). Below 6T, this dominant luminescence transition can be interpreted as the L_0 interband transition, whereas above this point the dominant luminescence transition changes its character and resembles the behavior of the X^{-} transition. Such an abrupt change in the character of the dominant luminescence line again occurs in the vicinity of filling factor ν≈2. There is also a set of emission lines, which do not enter in the Landau quantization description: S_1 and SU_0. The S_1 transition becomes more pronounced and better resolved in the spectra for sample B_4(G). The additional emission transition SU_0 on the low energy side of the dominant luminescence is nicely developed in the spectra of sample B_4(G) between filling factor 3 and 2.

Finally, we would like to underline that the high field luminescence spectra of sample B_4(G) are in fact qualitatively the same than in samples with lower electron concentrations (see Fig. 7.8). Increasing the magnetic field leads to a short appearance of "X" in the vicinity of filling factor ν=1 where the emission of "X" reaches a maximum there, and afterwards it tends to progressively disappear (see Fig.7.8). It seems that the magnetic field raises the excitonic effects not totally screened by the excess carrier phase-space filling. Thus, we

find a common "excitonic-like" behavior of luminescence transitions at high magnetic fields for three B_1, B_4(R), and B_4(G) samples with different electron concentrations.

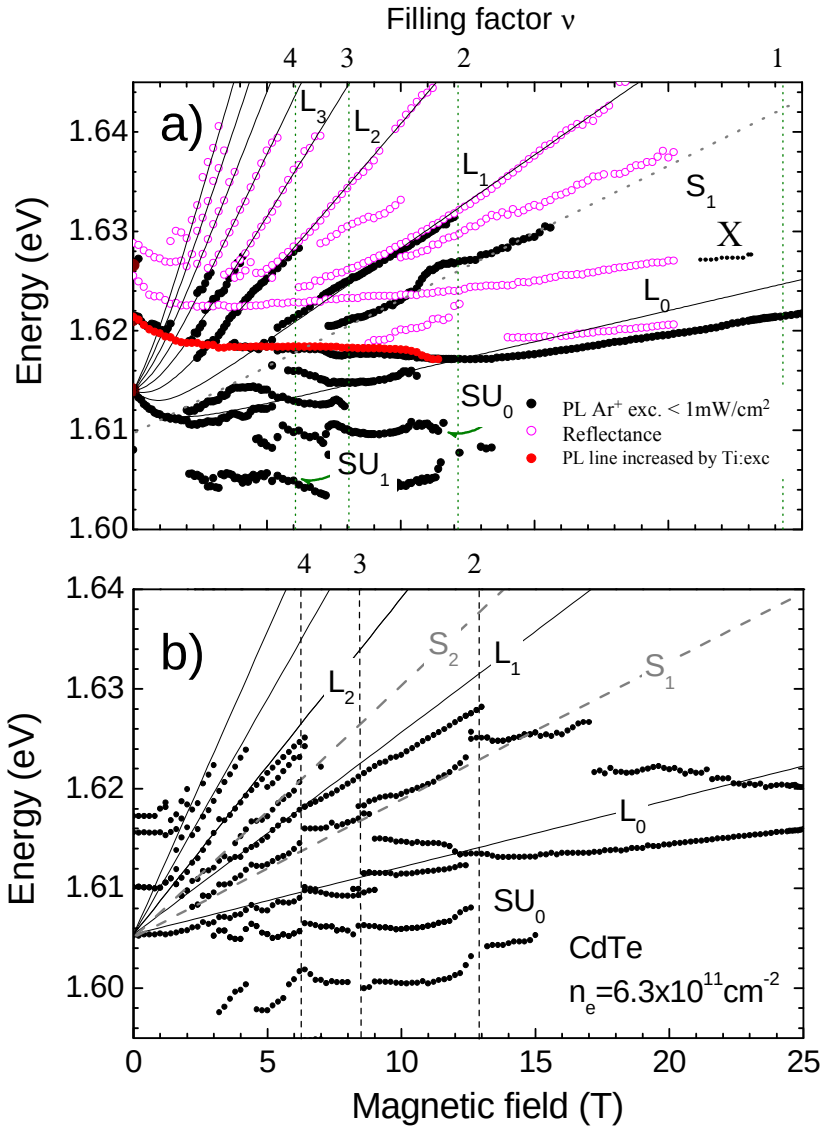

Figure.7.10 : a) Magnetic field dependence of the PL (solid circles) and reflectance (empty circles) lines corresponding to σ+ component at T=1.7 K for sample 100997A n_e=5.9x10^{11} cm^{-2}. The red points correspond to the emission transition enhanced by below barrier excitation. b) Magnetic field dependence of the PL (solid circles) lines corresponding to σ+ component at T=1.7 K for the sample 072897A with n_e=6.3x10^{11} cm^{-2} without Mn.

7.2.4.2. Magneto-optical transitions for high electron concentrations

The complexity of the magnetic field fanchart of optical transitions which has been already seen for sample B_4(G) is amplified in the case of samples with higher electron concentrations. In Figure.7.10a, we show the magneto-luminescence results obtained for the sample 100997A. In this figure, the black solid circles indicate the magnetic field dependence of the transitions observed in the luminescence spectra under above and below barrier excitation performed up to 25 T. In both cases the magnetic field fancharts of the luminescence transitions are practically the same except for the intensity of the emission line M-E which is more pronounced under red-laser excitation than under the green-laser excitation. The energy position of this particular peak can consequently be better followed in magnetic field (red solid circles). The open circles in Fig.7.10a denote the energy positions of transitions observed in reflectance measurements which were performed up to 21T. In Fig.7.10b, we show the results obtained for similar but Mn free CdTe modulation doped quantum well structure (QW). Both samples show similar emission spectra for the dominant polarization component, i.e. $\sigma-$ for CdTe and $\sigma+$ for CdMnTe. The resulting magnetic field fancharts of the emission transitions for these two samples have many similarities. This implies that the presence of manganese is not crucial to observe a great complexity in the magneto-optical spectra of II/VI modulation doped quantum wells. The many optical transitions identified in the emission spectra will be separately discussed in the next section.

7.2.4.2.1 "Regular" inter-Landau level transitions.

The set of "regular" Landau levels like transitions L_N are more visible in the case of higher electron concentration. They involve a conduction electron and a valence hole which populate Landau levels with the same index N, in order to verify the selection rules ($\Delta N=0$) as shown in Figure.7.11 (red line). The distinct allowed L_N transition can be differently probed depending on the occupation of the Landau levels. Thus, when the Landau levels are fully occupied they can be only seen by luminescence (emission) whereas the Landau levels become visible in reflectance (absorption) when the corresponding Landau levels start to get empty. Hence, the set of the L_N transitions can be qualitatively described according to the formula 7.4. The corresponding calculated traces shown with solid lines in Figs. 7.10a and b, assuming for:

- CdMnTe quantum well : $\hbar\omega^r_C$ =1.33 meV/T for the reduced cyclotron energy, E_{BGR}=1.6137 eV for the renormalized bandgap at zero magnetic field,

g^e=-1.6 for the electron g-factor in CdTe, and E_{exch}=8.5 meV for the sum of the ***s-d*** and ***p-d*** exchange energies.

- CdTe quantum well : $\hbar\omega^r_C$ =1.35 meV/T, E_{BGR}=1.605 eV, and g^e=-1.6 for the "bare" Zeeman splitting (g_h≈0 in our structures).

From the values of the reduced cyclotron resonances and considering the electron masses deduced in chapter 2, (m^*_e=0.108m_0 for 100997A and m^*_e=0.107 m_0 for the 072897A), we can deduce the effective hole mass m^*_h=0.454m_0 (0.453m_0) in CdMnTe (CdTe). As shown in Fig.7.10, the calculated L_N lines can qualitatively described the Landau level transitions despite some deviations which are remarkably pronounced in case of the lowest Landau level transition.

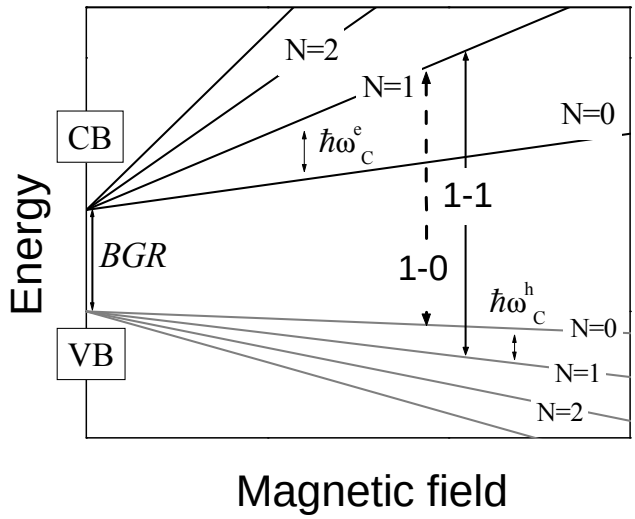

Figure.7.11: Schematic illustration of the allowed (ΔN=0) and forbidden (ΔN>0) inter-Landau level transitions. The spin splitting is neglected.

7.2.4.2.2 Oscillations of the "ground state" luminescence transition

The deviations from the linear magnetic field dependence of the L_0, L_1, L_2... can easily be found in the diagram presented in Fig.7.10. These oscillatory deviations are mostly pronounced for the dominant luminescence transition L_0 associated with the lowest electron Landau level and the upper valence band Landau level. This "ground-state" magneto-luminescence emission has been intensively studied in numerous n-type modulation doped structures whose energy dependence versus magnetic field is known to show a variety of "singularities". All studies agree that these singularities occur periodically each time the Fermi energy lies in a gap between Landau levels, i.e. periodic with integer filling factors as in our case.

Early studies of GaAs quantum wells invoked the possibility that such singularities are simply related to the effect of periodic magnetic field induced changes of the electron concentration [Vincente-1995]. This could be caused by the effect of charge transfer between the quantum well and doping region, which would therefore also imply changes in the profile of the electric field across the quantum well. Direct electron tunneling through the spacer barrier is very improbable but the possibility of an effective exchange of charge between the quantum well and the doping region cannot a priori be excluded under the conditions of optical excitation. Nevertheless, the simple test to reject this effect is to compare the behavior of ground state and higher energy transitions. In the case of charge transfer effects, all bands should shift and therefore all transitions should shift in parallel. This is not our case.

An alternative approach has been proposed suggesting that many body effect are responsible for the anomalies in the magnetic field dependence of the ground state luminescence transition in modulation doped quantum wells. The first "many-body explanation" has been proposed in terms of the effect the modulation of the band gap renormalization by the magnetic field [Katayama-1989, Uenoyama-1989]. More recent theoretical works propose an approach based on consideration of the competition between the electron-electron exchange interaction and interband exciton binding [Cooper-1997]. Many body theory also account for the observation of low energy satellites observed below the ground state luminescence transition [Manfra-1998, Gravier-1998]. Such satellites are also observed in our structures and are marked by SU_0, SU_1 in Figs. 7.10a and b. More elaborate theories underline the possibility of intriguing many body effects such as the splitting of the luminescence ground state due to a resonant interaction of a hole in the Fermi sea with spin excitations of a 2DEG [Hawrylak-1997, Asano-1998]. These theories are likely applicable in the ideal case of a disorder free 2DEG in the limit of high magnetic fields. We are tempted to say that the periodic "jumps" in the position of the ground state luminescence and development of the low energy satellites observed for our samples are due to many-body effects. At the same time, we are however surprised that these effects can be so clearly pronounced in our after all quite disordered systems. The interpretation of these many body effects is beyond the scope of this thesis. More theoretical works clarifying the role of disorder on many body effects and their manifestations in magneto-luminescence spectra of 2DEG are needed. An interesting speculation would be the possibility of enhancing the effects of electron-electron interactions by introducing some degree of disorder.

7.2.4.2.3 "Forbidden transitions"

Another characteristic feature shown in Fig.7.10 is the appearance of the so called "forbidden" transitions (S_1, S_2) [Lyo-1988]. The S_N transitions are quite pronounced in luminescence, but are not found in absorption-type spectra. As shown in Fig.7.10, S_1 and S_2 transitions are pinned below L_1 and L_2. The conventional interpretation of these transitions [Lyo-1988] is that they are due to "forbidden" recombination processes involving a valence hole and conduction electron populating Landau levels with large index ($\Delta N>0$) as shown in Fig.7.11 (blue line). Such an interpretation naturally explains the fact that S_N transitions are observed in luminescence (photo-created holes mostly accumulate at the N=0 valence band Landau level) but not in the absorption because of the small oscillator strength of these transitions [Lyo-1988]. Moreover, these "forbidden" transitions should disappear when temperature is increased.

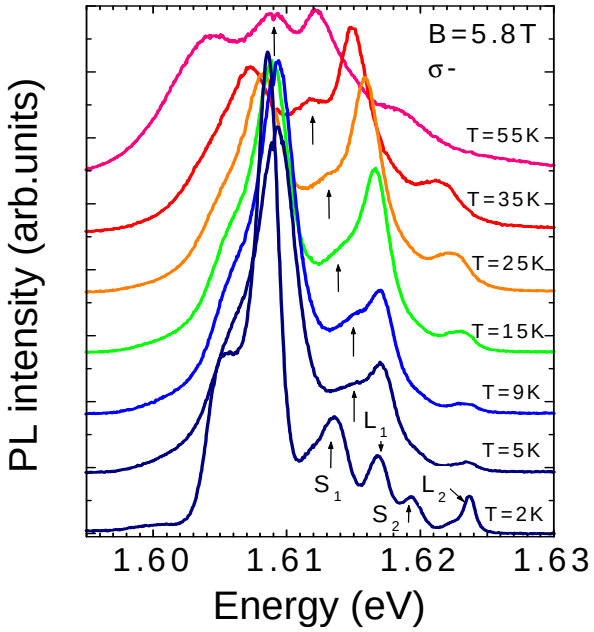

Figure.7.12: Temperature evolution of the σ– component emission at B=5.8T for sample 072897A. Different transitions L_N and S_N are indicated.

As shown in Fig. 7.12, temperature dependence experiments performed for our CdTe quantum well structures are not in agreement with this prediction. The transition S_1 remains clearly visible in the spectra even at temperatures as high as 55K when the line becomes comparable to the intensity of the allowed transition L_1. The model of "forbidden" transitions is also inconsistent with our

data when considering the characteristic slopes in the magnetic field dependence of the energy position of S_N and L_N luminescence lines. According to the model of "forbidden" transitions the differences in the slope for the L_N and S_N transitions is a direct measure of the cyclotron energy of the valence band hole (see Fig.7.11). Such a hypothesis implies, for example, that S_1 would correspond to the transition between the Landau level N=1 for electrons and N=0 for holes (transition 1-0). In this case, the energy separation between L_1 and S_1 will be directly related to the hole mass. The extracted hole mass from the difference of L_1 and S_1 slope is $m^*_h=0.17m_0$, in contradiction to our previous estimation. We speculate that a possible explanation for the appearance of these lines S_N, is that the S_1, S_2,...luminescence lines reflect the formation of certain type of bound impurity-like states which are pinned below each Landau level [Vincente-1995]. An alternative possibility would be recombination processes involving electrons localized in the tails of broadened Landau levels [Teran-2001]. These are however only speculations to explain the intriguing origin of a set of S_N lines which can be excited below the Fermi edge, as we will show later on. More theoretical work is necessary to validate our suggestions.

7.2.5 Inter-Landau level versus excitonic transitions

The properties of the magneto-optical spectra discussed in the last three paragraphs are not new effects. Although these effects are not completely understood, they have been observed in a large class of n-type modulation doped quantum wells and have been largely discussed in literature. In our opinion the new observation presented here concerns the observation of "excitonic-like" features in the optical spectra of high electron concentration samples. We have already discussed such intriguing observation when analyzing the spectra at zero field as well as when analyzing the evolution of optical spectra with the electron concentration, and in particular when analyzing the transition which occurs in the emission spectra near filling factor $\nu=2$. We will now consider in more details the experimental evidences obtained in the samples with the highest electron concentrations.

We begin by discussing the dramatic change of the character of the ground state emission observed around filling factor $\nu=2$ (see Figs.7.9b and c. and 7.10). Similar transitions have already been observed for a dilute 2DEG in GaAs quantum wells [Yoon-1992] and more recently in heavily doped ZnTe quantum well structures [Ossau-2001]. In both cases, it has been interpreted within the framework of a metal-insulator transition [Yoon-1992] or in terms of "hidden symmetry" rules for emission processes at filling factors $\nu < 2$ [Rashba-2000].

Recent ODMR experiments [Yeo-2001] have indicated that the ground state transition at filling factors $\nu < 2$ indeed resembles the X^- excitonic resonance.

We believe our experiments add new insight to this problem. As can be seen in Figs. 7.10, the transition at filling factors $\nu \approx 2$ is clearly pronounced. Indeed, such a strong effect persists up to temperatures as high as 35K (see Figure.7.13). It is instructive to reconsider in more details the results obtained for our representative 100997A sample which has been investigated using many different experimental techniques, cyclotron resonance and transport. They have shown typical features of a conducting system for all filling factors, included $\nu<2$, contrary to photoluminescence spectra, which suffer a drastic transition. This may imply that such transition exclusively corresponds to an 'optical transition' involving interband recombination of a conduction electron with a valence hole.

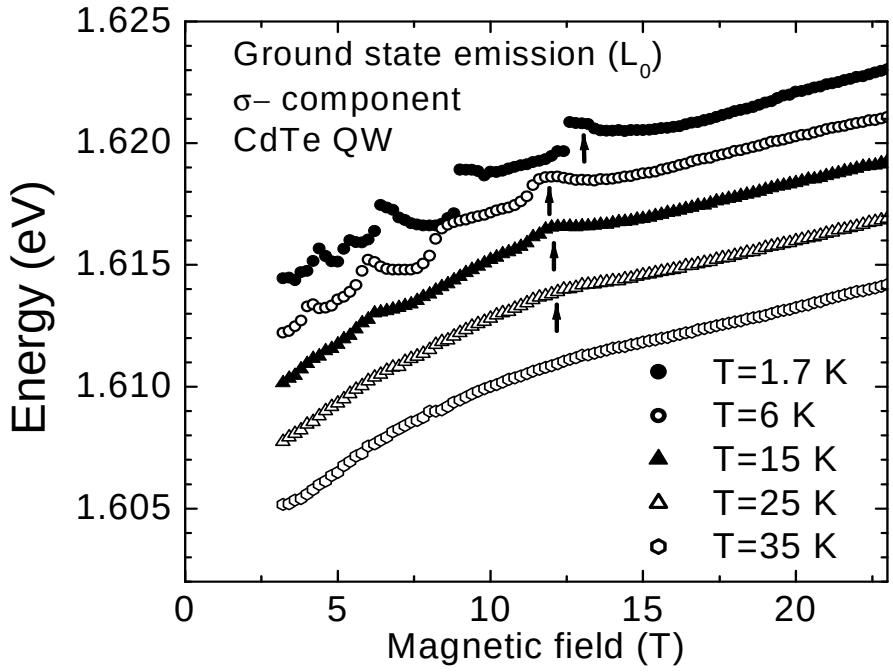

Figure.7.13 : Temperature dependence of the main emission line L_0 for the σ– component (see Fig.7.10) of a CdTe quantum well structure containing $n_e=6.3x10^{11}$ cm^{-2}. The arrow indicated the kink of the PL near filling factor $\nu=2$.

As previously discussed (see Fig. 7.5), the zero field spectrum of this sample clearly shows an emission line (M-E) which is thought to be related to excitonic effects. Indeed, the magnetic field dependence of the energy position of the M-E emission line shows a well pronounced diamagnetic shift characteristic of excitonic

transitions (see Fig. 7.10a). This line merges with the ground state luminescence transition around filling factor $\nu=2$, and beyond becomes the dominant luminescence transition at higher magnetic fields. Therefore, we label this M-E emission transition as "X^-". We observed that "X^-" is always present in the luminescence spectra. At low magnetic fields, the transition "X^-" is weakly pronounced with an energy smaller than the energy of the ground state transition (L_0). However, the emission line "X^-" becomes stronger when the energy of the ground state transition (L_0) is upper in energy than the "X^-" transition as schematically illustrated in Figure.7.14. We have considered the experimental observation at zero field where the position of the "X^-" emission line is centered in the energy range of the renormalized band-to-band transition (BGR) and the Moss-Burstein absorption onset (E^*_F). Thus, neglecting the Zeeman energy for the L_0 transition and the weak effect of the magnetic field on the position of "X^-", we obtained a crossing between both emission lines, L_0 and "X^-" in the vicinity of filling factor $\nu=2$. Such naive reasoning phenomenologically reproduce the "X^-"character of the ground state luminescence at $\nu< 2$.

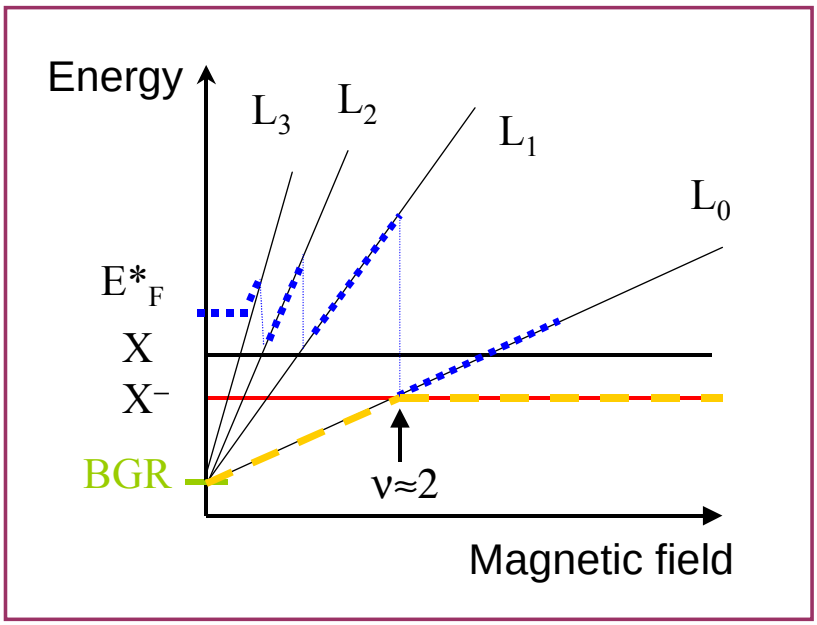

Figure.7.14. Schematic representation of the magnetic field dependence of the X, X^-, L_0 and E^*_F as described in the text. The crossing between X^- and L_0 occurs in the vicinity of $\nu = 2$.

The signature of excitonic effects in samples with high electron concentrations can be also seen in the magneto-reflectance experiments obtained

for the 100997A sample. Indeed, we observed a pronounced resonance in the reflectance spectrum below the Fermi onset already at zero magnetic field (green arrow in Fig.7.5) which becomes more relevant under magnetic field. As shown in Fig.7.10a, the magnetic field dependence of such an absorption resonance shows a distinctly diamagnetic shift confirming the excitonic character. This absorption line extrapolated to fields higher than 20T seems to link the neutral exciton emission weakly reappearing in the vicinity of filling factor ν=1. For this reason, we label this absorption transition as "X" which is also observed in PLE measurements (see Figure7.15).

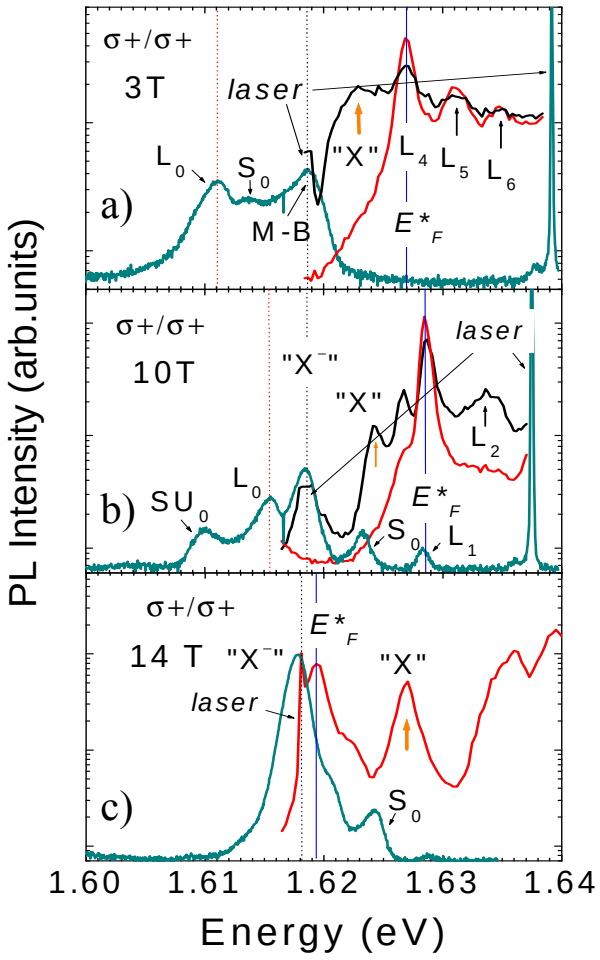

Figure.7.15: PL (green line) and PLE spectra at different magnetic field in σ+/σ+ configurations. The energy of detection positions for the distinct PLE spectra (red and black lines) correspond to the position of L_0 and "X^-" emission lines. The position of the Fermi edge (blue line) is shown for comparison.

As shown (see Fig.7.5), the PLE spectra of the M-E ("X^-") and B-B (L_0) luminescence lines are very different already at zero field what stays under magnetic field. Thus, in the PLE spectrum of the L_0 luminescence the most pronounced peaks are those related to the higher L_N transitions involving empty Landau levels as shown in Fig. 7.15a and b. However, the PLE of "X^-" shows the additional absorption peak corresponding to the "X", observed in reflectance measurements.

Nevertheless, we note that the resonant absorption at the "X^-" position is very weak at low magnetic fields becoming clearly observable at magnetic fields for which $\nu < 2$ (see Fig. 7.15c). We can therefore conclude that even in case of highly doped samples, it is still possible to distinguish optical transitions clearly related to excitonic complexes ("X" and "X^-") coexisting with free particle-like transition (L_N). The strength of such excitonic transitions in the optical spectra depends on the magnetic fields: less visible at low magnetic fields ($\nu > 2$) and dominating at high magnetic fields ($\nu < 2$).

7.2.6. Coexistence of one particle-like and excitonic-like optical transitions in modulation doped quantum wells

The observation of clear excitonic-like transitions in structures with electron concentrations as high as ~$6x10^{11}cm^{-2}$ cannot easily be explained using existing theoretical models. Our experimental findings have shown that for a high density of electrons, we can distinguish to kinds of optical transitions of a different nature. We have observed transitions that can be interpreted in a single particle picture corrected for the effect of the band gap renormalization. At zero magnetic field, these transitions result in a broad luminescence band which peaks at the energy of the renormalized bandgap and they lead to the observation of a conventional "Moss-Burstein" absorption onset. In magnetic fields, these transitions decompose into Landau levels reflecting the changes in the occupation of the subsequent Landau levels.

We have also observed transitions showing typical features of excitonic complexes: "X" and "X^-". At zero field the energies of "X" and "X^-"resonances lie in between the energy of the renormalized bandgap (peak of the luminescence) and the energy corresponding to the Moss-Burstein absorption onset. Under magnetic field, both transitions show a characteristic diamagnetic shift.

At low magnetic field the emission spectra are mainly composed of band-to band transitions. Under special conditions we can clearly observe the "X^-" luminescence, before it crosses with the dominant band-to-band transition L_0 in the vicinity of filling factor ν=2, becoming the dominant luminescence line at high

magnetic fields. These different emission processes are in fact related to distinct absorption thresholds. One threshold is associated with the absorption at the Fermi edge (E^*_F) to which the band-to-band transitions L_N and SU_N are related and the second threshold is associated with the neutral exciton "X" to which the "X^-" and S_1 luminescence lines are related as shown in Figure.7.16.

In addition, the magnetic field dependence of the energy position of the excitonic-like lines "X" and "X^-" in highly doped samples resemble the corresponding magnetic field dependence of the X and X^- excitons in samples with low electron concentration (for instance B_1). Such similarities are particularly relevant at high magnetic fields where the optical response does not seem to depend on the electron density. The coexistence of two type of transitions of a different nature, one characteristic for lightly doped samples and a second one characteristic of heavily doped structures, poses, at first sight, the question of the problem of spatial homogeneity of our structures. The essential point is whether the coexistence of band-to-band and excitonic transitions is a property of a system with a homogenous electron concentration or if such "two-phases"-like behavior is simply the consequence of a spatial separation of regions with different electron concentrations. The former possibility is very attractive but, as we already discussed, there is no theoretical model, which could be applicable to our data.

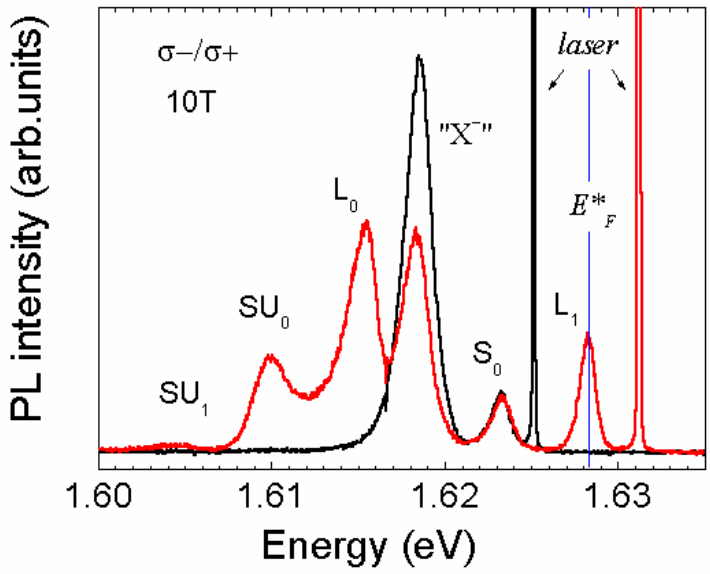

Figure.7.16 : PL spectra for different energy excitations (below barrier) at B=10T and T=1.7 K for the indicated polarization configuration.

However, the problem of the optical response in the presence of 2D electrons is far from being trivial and it is not completely solved. Notably, the case of intermediate electron concentrations ($E_F \sim E_b$) is not very well understood. It is well known that in case of high electron densities the "excitonic effects" are explained in terms of "Fermi edge singularity"[Brum-1997]. This "excitonic effect" results in the enhancement of the oscillator strength of optical transitions but does not imply the formation of bound states. However, our "excitons" are clearly bound states (showing characteristic diamagnetic shifts) and cannot be explained using a conventional "Fermi edge singularity" formalism. One may however, think that this formalism cannot be strictly applicable in the case of intermediate range of electron concentrations ($E_F \sim E_b$), and more theoretical and experimental work is needed to clarify this point.

An alternative and more speculative possibility to explain our data is to assume that our sample is spatially inhomogenous, and therefore the interband optical experiments probe different regions with distinctly different electron concentrations. Assuming such a possibility, one can imagine a simplistic picture in which electrons condense into "lakes" which are separated by insulating regions. Our samples would be composed by a mosaic of cluster of carriers which start to 'condense' as water droplets in potential fluctuations in order to form 'lakes' with a common carrier density. These clusters would be spread over all the sample and their extension would be related to the potential fluctuations and the Fermi level of a given 'lake'. Between the lakes no carriers are present. Both phases might be coupled under interband excitations with the negatively charge exciton as the corresponding correlation establishing a bridge between both phases.

The evolution of the optical response in our samples as a function of the electron concentration. The model, "lakes of electrons" and "insulating islands" can be used to qualitatively interpret our data. In particular the balance between different luminescence transitions under different excitation conditions can be explained in terms of characteristic relaxation processes between the two spatially different regions. The model has however an essential deficiency which concerns the electron concentration, which is a well defined value in our samples as the experimental data have shown (narrow linewidths of the inter Landau level transitions ~1meV). The dispersion in the electron concentration should noticeable broaden these lines due to the shift of the renormalized band-gap. On the other hand, it is difficult to explain that each lake of electrons should be characterized by very similar electron concentration. We are left with the open question concerning the possibility of forming the "lakes of electrons" with well defined electron concentration

Conclusions

We have investigated the evolution of the optical response as a function of carrier density in modulation doped II-VI quantum well structures. This study reveals a persistence of excitonic transitions for electron densities for which Fermi energy is comparable to the exciton binding energy. We observe a coexistence tuned by magnetic field of band to band and excitonic-like transitions in samples with electron concentration as high as $6.3x10^{11}cm^{-2}$. Our investigation leads to address the question whether such observations are characteristics for systems with homogenous carrier density or they involve a phase separation, i.e. "insulating islands" and "lakes of electrons" with well-defined electron concentrations.

General conclusions

We have studied the ***sp-d*** exchange interaction between 2D electrons and localized magnetic moments by investigating the electronic and magnetic properties of n-type modulation doped CdMnTe quantum well structures.

The ***electronic properties*** strongly reflect the realignment of the electronic spin states induced by the exchange interaction when a magnetic field is applied. Such band realignment leads to a giant Zeeman splitting whose magnetic field and temperature dependence is differently described at low or high magnetic fields.

In the ***low magnetic field*** region, the combination of the cyclotron resonance measurements (effective electron mass) and the characteristic beating patterns in the amplitude of the Shubnikov-de Haas oscillations of the longitudinal resistance R_{XX} allow us to determine a precise model for the magnetic field dependence of the effective Zeeman energy. This model considers the two components of the effective Zeeman energy: the standard Zeeman effect plus a ***sp-d*** exchange interaction term which is successfully described by the *mean-field approach*. This model permits to *describe* the magnetic field and temperature dependence of the transport and optical *properties* (Raman and PL) of the *electronics subsystem* in the low field regime.

In the ***high magnetic field*** range, where the effective Zeeman energy is expected to vanish (E_Z=0), we observe that a zero effective Zeeman energy does not necessarily imply a closing of the spin gap. Independently of the condition of vanishing Zeeman splitting, the spin gap always remains open for filling factors $5/2 \lesssim \nu \lesssim 7/2$ and around $\nu = 3/2$. The experimental findings corresponding to Raman scattering and transport experiments indicate a repulsion between spin up and spin down Landau levels. The effect of opening or closing the spin gap by tuning the effective Zeeman splitting can be seen as an anticrossing or

crossing of the spin split Landau levels which permit an almost complete understanding of our data. The anticrossing description complements the model of the effective Zeeman splitting based on the mean field approach at the vanishing effective Zeeman gap $\mathbf{E_Z=0}$.

The ***magnetic properties*** of the Mn^{2+} ion subsystem show an influence of the carrier presence. The Knight shift of the position of the EPR spectrum is differently understood at low and high magnetic fields. In case of ***low magnetic fields***, the mean field approach can describe the effects of electrons in the quantum Hall regime on the Mn^{2+} magnetic properties.

However, the mean field approach does not account for the large shift of the Mn^{2+} spin resonance observed at ***high magnetic fields*** in the vicinity of $\mathbf{E^{Mn}_Z=E^e_Z}$. A model based on a resonant interaction between the mean-field spin excitations for electrons and Mn^{2+} ions has been proposed in order to interpret the Raman and EPR experimental data. This model based on an anticrossing between both, electronic and magnetic spin excitations, well describes the experimental findings, providing the correct order of magnitude for the observed shift of the resonance position and its temperature dependence when $E^{Mn}_Z=E^e_Z$.

However, some questions remain open such as the role of the quantum Hall state ($\nu=3$) near the anticrossing region or more generally the origin of the observed anticrossing which seems to weakly depend on carrier concentration and is therefore most likely related to the spin-orbit interaction.

A direct consequence of the mean field approach in our samples is the existence of two particular situations: $\mathbf{E^e_Z=E^{Mn}_Z}$ and $\mathbf{E^e_Z=0}$. In both cases, ***perturbation*** effects resonantly appear due to the ***interaction*** of electronic and magnetic spin excitations of the DMS crystal.

The study of the evolution of the optical response as a function of carrier density in modulation doped II-VI quantum well structures reveals a persistence of excitonic transitions for electron densities for which Fermi energy is comparable to the exciton binding energy. We observe a coexistence tuned by magnetic field of band to band and excitonic-like transitions in samples with electron concentrations as high as $6.3\text{x}10^{11}\text{cm}^{-2}$. Our investigation leads to address the question whether such observations are characteristic of homogenous system or they involve a phase separation, i.e. “insulating islands” and “lakes of electrons” with well defined electron concentrations.

Appendix 1

Mini-optical table

Optical spectroscopy such as photo-luminescence or inelastic light scattering gives access to the spin information of the electronic states involved in the optical processes when the polarization components of the in-coming or out-going photons are resolved. In semiconductor quantum well structures, the emission or absorption transitions mainly imply circularly polarized light σ+/−.

A typical optical table for photo-luminescence experiments is shown in Figure A1.1. In the excitation path (red line), an ensemble composed by a linear polarizer plus λ/4 quarter wave plate can be used to circularly polarize (σ+ or σ-) the excitation beam on the sample. In addition, the emitted photons can be focused on a detector after analyzing their circular polarization component. When the sample is placed inside a cryostat mounted on a magnet, the optical path is sensitive to the magnetic forces, which adversely affect the stability of the optical table. Since the holders of the optical elements (lens, mirror, polarizer and λ/4 plate) are slightly magnetic, a progressive disalignment occurs on increasing the strength of the magnetic field. Similarly, the thermal contractions may also displace the sample, disaligning further the set-up. In addition, the design of magnets which facilitate high magnetic fields (> 23 T) implies large distances for the optical paths further complicating optical experiments.

With the motivation of performing stable and polarization resolved experiments in the visible-near infrared spectral regions at high field and low temperatures, a miniaturized optical table was made. The design of the mini-optical table is mainly based on the schematic shown in Fig.A.1.1. Two parallel optical axes for excitation and detection as shown Figure A.1.2a, allow us to differently polarize or analyze the excitation or emitted light respectively. The polarization analyzer ensemble is now composed of a linear polarizer (P) mounted on a tube in front of a λ/4 plate fixed on a independent support (see

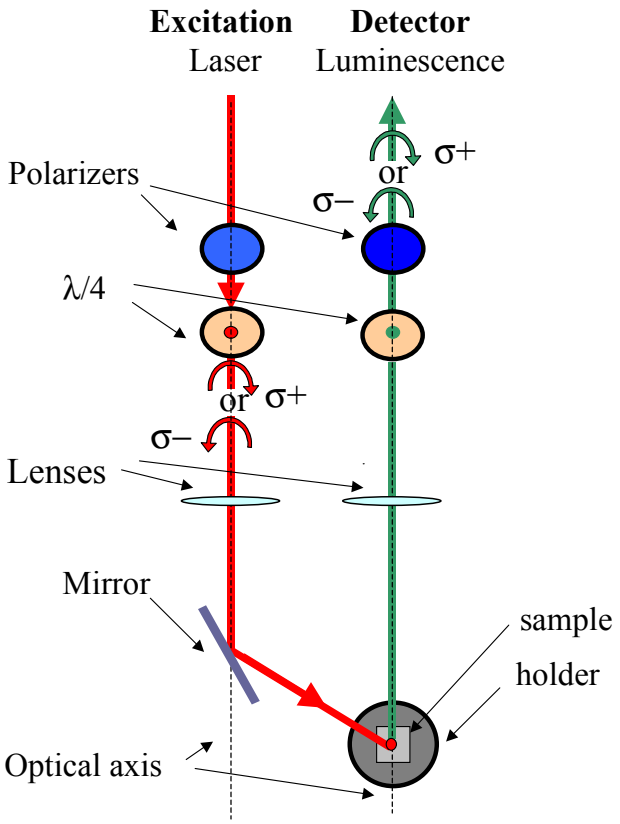

Figure A.1.1: Schematic illustration of a standard optical set-up table for photo-luminescence experiments.

Figure A1.2b). Such an arrangement allows us to change the angle between the polarizer axe with respect to the fixed optical axe of the λ/4 plate. Thus, from the polarizer position corresponding to one of the two configuration, σ+ or σ−, we select the opposite σ− or σ+ by externally turning the tube by 90°. An optical fiber (F) guides the laser to the excitation path. After polarizing σ+ or −, the beam is focused on the sample by a lens (L) and a mirror (M) as shown in Figure A.1.2c. The emitted light is focused by a lens on the tip of a second optical fiber to reach the detector after one of the two circular polarization components (σ + or −) was selected by a similar arrangement (P+λ/4). The optical components active in the infrared region (near 800nm), the materials and the design of the optical path and holders were carefully chosen in order to minimize the sensitivity to thermal contraction and magnetic forces. The spacing between the optical axes was also a handicap since the inner part of the cryostat tails do not exceed 34-37 mm. Fig.A.1.2a shows the real size of the mini-optical table.

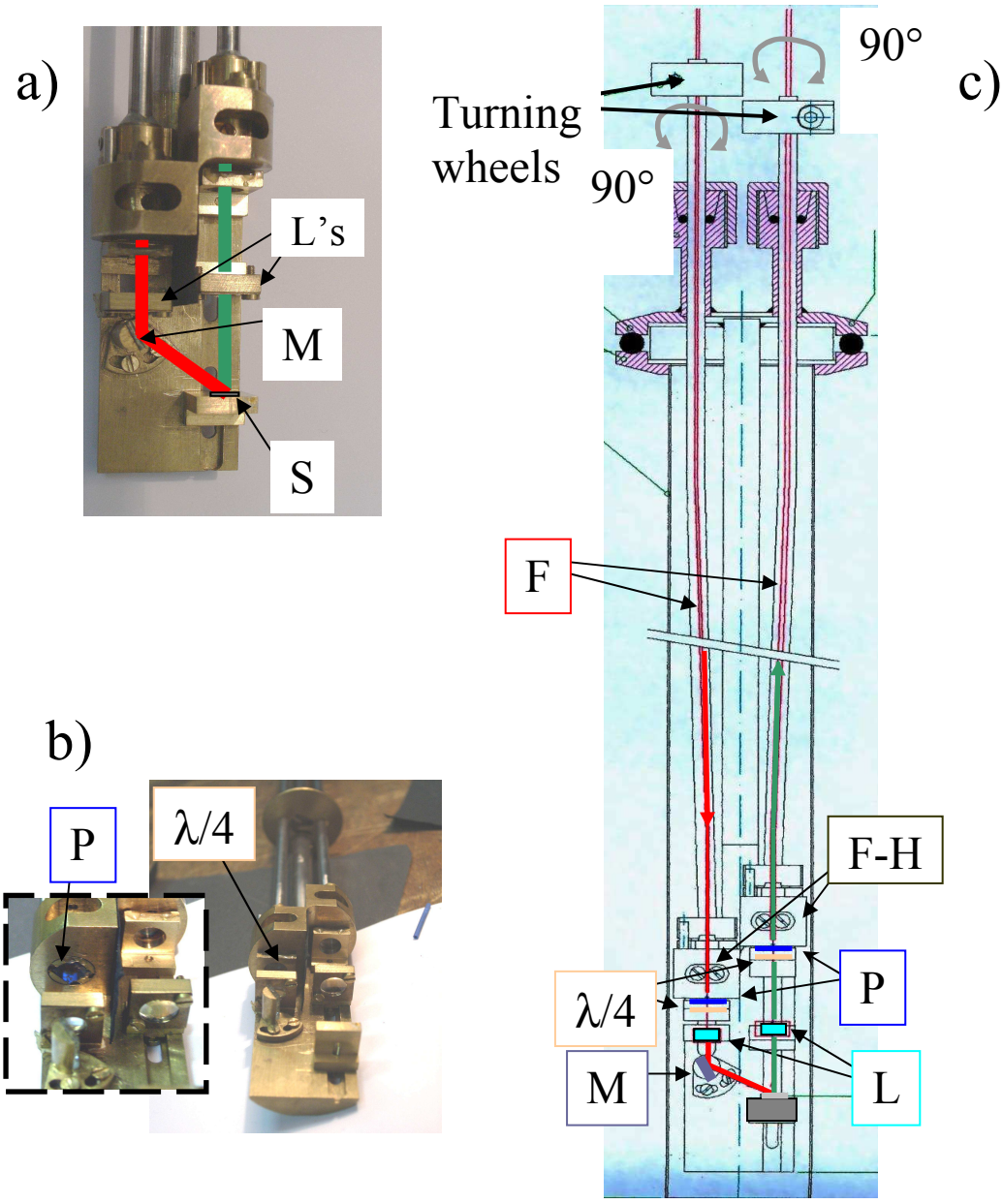

Figure A.1.2: a) Picture of the 'home made' miniaturization of the optical table (real size). b) Detail of the optical insert corresponding to the ensemble of the polarization analyzer: polarizer mounted in a tube and λ/4 plate placed in a fixed holder. c) Overall upper view of the design of the optical insert with the different parts for Faraday configuration PL experiments: optical fibers (F), lenses (L), Fiber holders (F-H), mirror (M), polarizers (P), lenses (L) and λ/4 quarter wave plates.

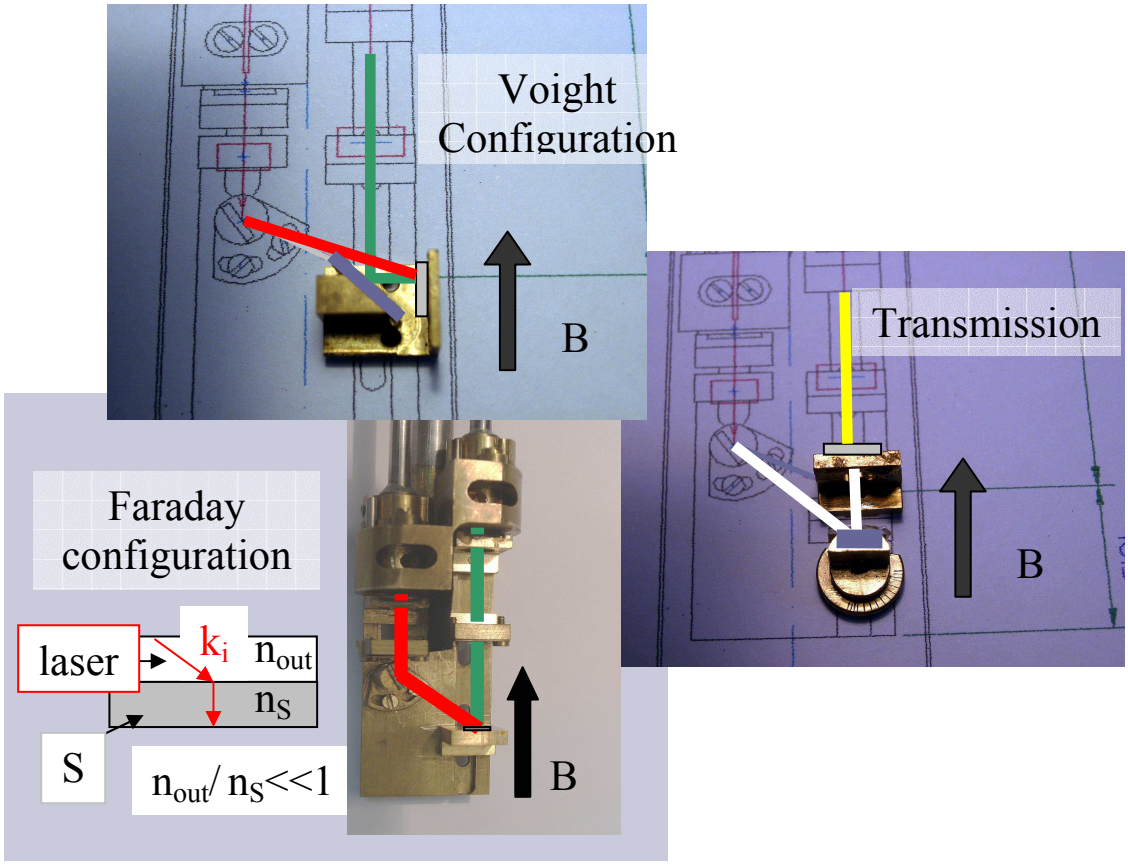

Figure A.1.3: Different arrangements for: Faraday and Voigt configuration for PL,PLE and transmission experiments.

The mini-table hangs from a solid structure fixed on a rigid central tube which maintains stable the overall insert, which is 1.5 m long and weights 1.2 kg. The insert is completely leak tight and can be plunged into a He bath. Once the optical components are well aligned and fixed, the system is easily transportable and available for use in any standard cryostat and therefore in high magnetic fields. In addition, this insert is flexible by design, offering many possibilities for different configurations. The two parallel optical axes of the optical table allows to independently install or remove different sample holders or optical components (mirror, lenses...) making easier its alignment and also opening a large number of distinct configurations of which some examples are shown in Figure A.1.3.

The Faraday configuration is widely employed for polarization resolved PL, PLE and Raman scattering experiments on quantum well structures. In

such a configuration the magnetic field direction is perpendicular to the quantum well layer and parallel to k-vector of the incident photon (red line). The fact that the values of semiconductor index refraction are generally quite large so that the ratio between the index refraction of the external medium (generally, He gas or liquid) n_{OUT} and the semiconductor n_S is much smaller than one. According to Snell's law, the incident photon will consequently travel through the sample perpendicular to the surface sample, i.e. parallel to B. Another useful configuration achievable for PL spectroscopy is the Voigt configuration (incident k-vector perpendicular to B) complemented using a second mirror which displaces the emitted light towards the detector system (see Fig.A.1.3). It enables us also to resolve the polarization both for detection and excitation. Also transmission experiments in the Faraday configuration are possible by placing a second mirror below a drilled sample holder. Illuminating by unpolarized white light, the system allows us to analyze the two polarization components (σ + and σ–) of the transmitted light through the sample.

Appendix 2

Calculations of the longitudinal resistance

In order to simulate of the longitudinal resistance of a 2DEG we start with the assumption that the energy positions of the centers of spin-resolved Landau levels are given by:

$$E_{N\uparrow,\downarrow}(B,T) = (N+\tfrac{1}{2})\,\hbar\omega_c \pm E_Z(B,T)/2 \qquad \text{Eq.Ap2.1}$$

where N corresponds to the Landau level index taking the values N=0,1,2, .., ω_C=eB/m^*_e denotes the cyclotron energy, m^*_e is the electron mass, and the spin splitting E_Z is given by Eq.4.1. The density of states related to each spin resolved Landau level is represented by a Gaussian shape with the broadening parameter (variance of the Gaussian function) Γ:

$$DOS^{E_{N\uparrow,\downarrow}} = \frac{eB}{h}\frac{1}{\sqrt{2\pi}\Gamma}e^{(-(E-E_{N\uparrow,\downarrow})^2/2\Gamma^2)} \qquad \text{Eq.Ap2.2}$$

where eB/h is the degeneracy of single spin resolved Landau level and $1/\sqrt{2\pi}\Gamma$ is a renormalization factor for a Gaussian broadening:

$$\int_{-\infty}^{+\infty}\frac{1}{\sqrt{2\pi}\Gamma}e^{(-(E-E_{N\uparrow,\downarrow})^2/2\Gamma^2)}dE = 1 \qquad \text{Eq.Ap2.3}$$

The total density of states in then given by:

$$DOS(E,B,T) = \sum_{N=0}^{\infty}\left(DOS^{E_N\uparrow} + DOS^{E_N\downarrow}\right) \qquad \text{Eq.Ap2.4}$$

The first step in our calculations is to find the Fermi energy (for each value of the magnetic field). This is done by solving the equation which defines the known value of the electron concentration n_e:

$$n_e = \int_{-\infty}^{E_F} DOS(E,B,T)dE \qquad \text{Eq.Ap2.5}$$

For our calculations on sample 100997A, we assume $m^*_e = 0.107m_0$ as determined by cyclotron resonance measurements, $n_e = 5.9\text{x}10^{11}\text{cm}^{-2}$ for the electron concentration, $E_{s\text{-}d} = 1.70$ meV for the ***s-d*** exchange constant, $T_0 = 180$mK for the "antiferromagnetic" correction to the effective temperature of manganese spins, and $g_e = -1.6$ for the "bare" electron g-factor in CdTe. The effects of non-zero temperature are not included in the electron Fermi distribution but they are taken into account for the expression for the electron spin splitting E_Z.

Simulation at the low field region

After determining the position of the Fermi energy at each magnetic field (from the eq.Ap2.5) the longitudinal resistance at low magnetic field is calculated simply by assuming that it is proportional to the total density of states at the Fermi level:

$$R_{xx} \sim DOS(E_F) \qquad \text{Eq.Ap2.6}$$

As a matter of fact the only adjustable parameters in our modeling of R_{xx} at low fields are those concerning the broadening of the Landau level. The low field data are best reproduced (see Fig.4.11) assuming a width of the Landau levels changes with the magnetic field: $\Gamma = \Gamma_0 + \Gamma_1 B^{1/2}$ [Ando-1982] where $\Gamma_0 = 0.07$ meV and $\Gamma_1 = 0.2\text{meV}/\text{T}^{1/2}$.

Simulation at the high field region

The procedure of simulating R_{xx} is more complex in the high field region. Here, we distinguish between localized and extended states, assuming that only the latter ones contribute to the conductivity. We suppose that in the central part of each Landau there exists a band of extended states which is again of a Gaussian shape and width $\Gamma_{ext}<\Gamma$. For each Landau band, the integrated density of extended states is a fixed fraction of the total density of states. The Fermi energy is calculated considering total density of states as before, but the longitudinal resistance is assumed to be proportional to the density of extended states at the Fermi level:

$$R_{xx} \sim DOS_{ext}(E_F) \qquad \text{Eq.Ap2.7}$$

Another important point in simulating the high field data is to reproduce the effect of the opening of the spin gap even in the case of vanishing ***s-d*** Zeeman splitting. To take this into account we consider the possibility of anticrossing of spin levels. We assume that for each Landau level index N, the two Zeeman components $E_{N\uparrow,\downarrow}$ are replaced by coupled levels $E^*_{N\uparrow,\downarrow}$. The coupled levels are calculated within a simple first order perturbation approach, introducing the interaction parameter $\Delta=\Delta_0/2$ (Δ_0 is the anticrossing gap, see chapter 4).

$$E^*_{N\uparrow,\downarrow} = ½(E_{N\uparrow} - E_{N\downarrow}) \pm \{¼(E_{N\uparrow} - E_{N\downarrow})^2 + (\Delta)^2)\}^{½} \qquad \text{Eq.Ap2.8}$$

In order to calculate the Fermi energy and the DOS for R_{xx}, in Eq.Ap2.7 the energy positions of the unperturbed $E_{N\uparrow,\downarrow}$ levels are replaces by those of coupled ones $E^*_{N\uparrow,\downarrow}$.

In the simulations at tilt magnetic fields we have introduced the total magnetic field B_{tot} into the equations which define the ***s-d*** Zeeman splitting. On the other hand, the Landau quantization parameter such as the cyclotron energy and the Landau level degeneracy are related to the magnetic field component $B_\perp$ perpendicular to the plane of the 2DEG.

The adjustable parameters in our simulations are: the total width of the Landau level Γ, the width of the band of the extended states and the interaction parameter Δ. We have found that that our data are best described when Γ=0.15 meV and Γ_{ext}=0.075 meV both assumed to be constant in the magnetic field

range considered (B=4-28T). The interaction parameter Δ was found to be dependent on magnetic field as discussed in chapter 4.

Appendix 3

Construction of a g-factor marker

For reliable electron paramagnetic resonance experiments a suitable standard for calibrating the magnetic field in order to determine the g-factor of the spin species under study is essential. The field determined from reading the current in a super-conducting magnet leaves some margin for error such as residual fields or hysterisis loops, etc. These experimental errors can be significant for high resolution EPR spectroscopy. For this reason we use the organic radical 2.2-diphenyl-1-picrylhydrzyl (DPPH) as a standard sample for EPR calibration [Krzystek-1997]. The EPR spectrum varies from a single narrow (<1mT) line without structure to a broader spectrum (4.8mT) depending on the sample preparation giving a g-factor value of 2.0036 [Al'tshuler-1964].

The extremely narrow linewidth with respect to our Mn^{2+} EPR spectrum (~35mT) and its strong EPR signal makes DPPH an ideal candidate for the construction of a g-factor marker on the site of the sample.

In order to measure the DPPH EPR spectrum with our experimental set-up (see chapter 5), we use a standard carbon resistance that will act as a bolometer. An Allan Bradley resistor was chosen for such purpose due to its high thermal sensitivity in the temperature range where we performed our experiments [4.2 - 1.6 K]. The resistor was polished in order to reduce its size and to obtain a thin and regular shape. In an initial test, we placed the resistor in our EPR insert, below a small amount of DPPH powder which was introduced in a 0.6mm-thick Teflon container as is schematized in Figure A.3.1. We measured the resistance value as a function of magnetic field under continuous microwave irradiation in order to obtain the EPR spectrum of DPPH at low temperatures as shown in Figure A3.2. The magnet used was a super-conducting coil with a homogeneity of 10^{-4} into a 10mm-diameter sphere

at the center field position. The resistance is very sensitive to the temperature changes due to the resonant absorption (notice the 20% change of the resistance at resonance, see Fig.A.3.2a)). This fact allows us to obtain a typical EPR spectrum composed by a single narrow line for both frequencies 230 and 95 GHz within a resolution up to 16 G (see Fig.A.3.2).

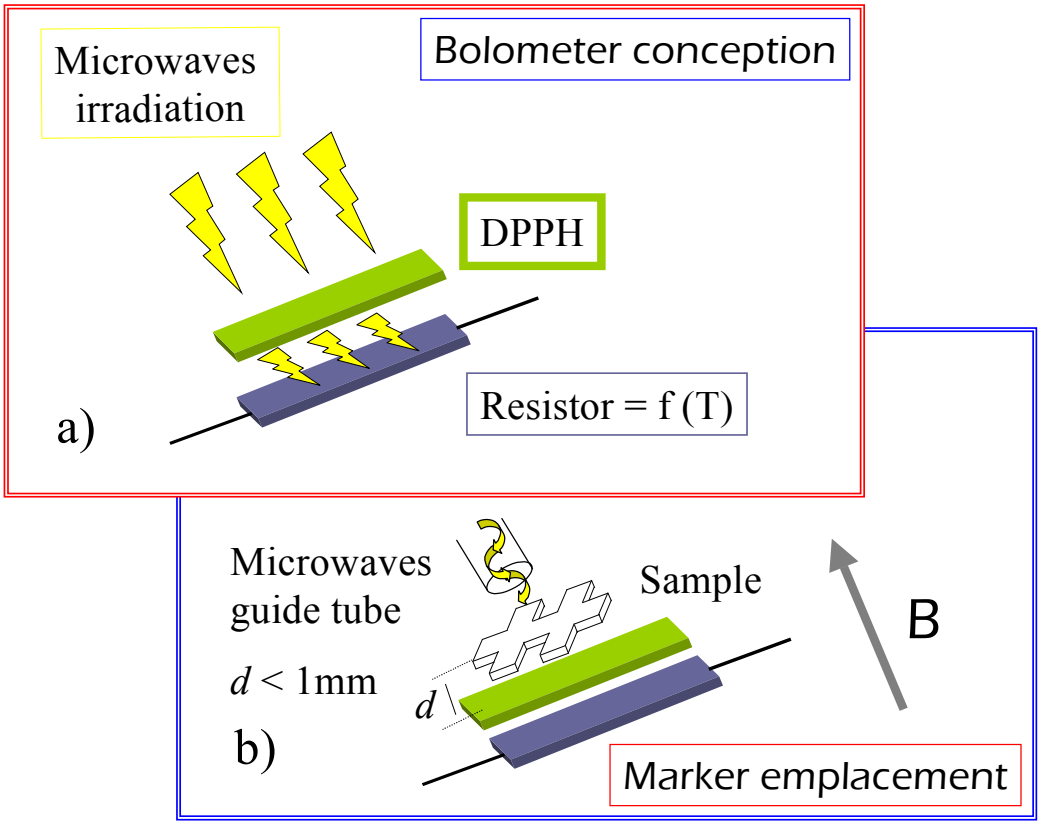

Figure A3.1. Schematic representation of the a): Bolometer conception. The resistance value is sensitive to the changes of the Microwaves intensity in and out the DPPH absorption. b) schematic view of the marker ensemble with respect to the sample.

The next step was to incorporate the g-factor marker in our experimental set-up. The ensemble DPPH-bolometer was placed below the sample, less than 1mm away, as Fig.A.3.1 shows, in order to determine as accurately as possible the magnetic field felt at the sample position.

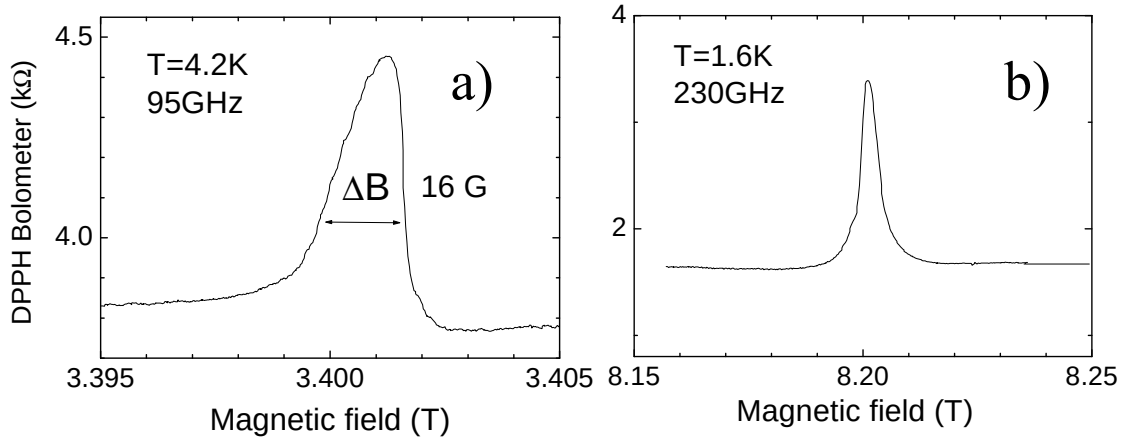

Figure A3.2. DPPH spectra measured with our made-home bolometer at a) low field region using a microwave frequency of 95GHz at 4.2K. b) High field region: microwave frequency of 230GHz at 1.6K.

This *in situ* installation of the g-marker-bolometer ensemble allowed us to calibrate the field of all data acquired and to precisely determine an absolute value for the Mn^{2+} g-factor.

References

- Abragam : A. Abragam. *The Principles of Nuclear Magnetism* (Clarendon, Oxford, 1961).

- Abrikosov-1988: A.Abrikosov. *Fundamentals of the Theory of Metals.* (North Holland, Amsterdam, 1988).

- Abstreiter-1974 : G.Abstreiter, J.P.Kotthaus, J.F.Koch, and G.Dodra. *Phys. Rev. B* **74**, 2480 (1974).

- Al'tshuler-1964: S.A.Al'tshuler and B.M.Kozyrev. *Electron Paramagnetic Resonance*. Ed.C.P.Poole. Academic Press, New York,1964.

- Ando –1974a : T.Ando and Y.Uemura. *J. Phys. Soc. Jpn* **36**,959 (1974).

- Ando –1974b : T.Ando and Y.Uemura. *J. Phys. Soc. Jpn* **37**,1044 (1974).

- Ando-1982 : T. Ando, A. B. Fowler, and F. Stern. *Rev. Mod Phys.* **54**, 437 (1982).

- Asano-1998 : K. Asano and T.Ando. *Physica B* **249-251**, 549 (1998). *Physica B* **256-258,** 319 (1998).

- Aoki-1977 : H.Aoki and K.Kamimura. *Solid State Comm*. **21**, 45 (1977).

- Ashcroft : N.W. Ashcroft and N.David Mermin. *Solid State Physics*. Saunders College Publishing, Harcourt Brace College Publishers, Orlando,1976.

- Astakhov-1999 : G. V. Astakhov, D. R. Yakovlev, V. P. Kochereshko, W. Ossau, J. Nürnberger, W. Faschinger, and G. Landwehr. *Phys. Rev. B* **60**, R8485 (1999).

- Barret-1995 : S. E. Barret, G. Dabbagh, L. N. Pfeiffer, K. W. West, and R. Tycko. *Phys. Rev. Lett.* **74**, 5112 (1995).

- Bayot-1997 : V. Bayot, E. Grivei, S. Melinte, and M. Shayegan. *Physica E* **1**,36 (1997).

- Berg-1990 : A. Berg, M. Dobers, R. R. Gerhardts, and K. v. Klitzing *Phys. Rev. Lett.* **64** , 2563 (1990).

- Brown –1996 : S. A. Brown, J.F. Young , J.A. Brum , P. Hawrylak, and Z. Wasilewski. *Phys. Rev. B* **54** , R11082 (1996).

- Brum-1997 : J.A. Brum and P.Hawrylak. *Comments on Condensed Matter Physics*,**18**, 135 (1997).

- Buhmann-1995 : H. Buhmann, L. Mansouri, J. Wang, P. H. Beton, N. Mori, L. Eaves, M. Henini, and M. Potemski. *Phys. Rev. B* **51** , 7969 (1995).

- Bychkov –1981 : Yu. A. Bychkov, S. V. Iordanskii, and G. M. Eliashberg. *JETP Lett*. **33**, 152 (1981).

- Chemla-1993 : D.S. Chemla. *Physics Today*, **46**, 22 (1993).

- Chen-1992 : W. Chen, M. Fritze, W. Walecki, A. V. Nurmikko, D. Ackley, J. M. Hong, and L. L. Chang. *Phys. Rev. B*, **45**, 8464 (1992).

- Chiu – 1976 : K.W. Chiu, T.K. Lee, and J.J. Quinn. *Surf. Sci.* **58**, 182 (1976).

- Coleridge – 1989 : P.T. Coleridge, R. Stoner, and R. Fletcher. *Phys. Rev. B* **39** 1120 (1989).

- Cooper-1997 : N.R. Cooper and D. B. Chklovskii. *Phys. Rev. B* **55** 2436 (1997).

- Crooker-1995 : S.A. Crooker, D.A. Tulchinsky, J. Levy, D.D. Awschalom, R. Garcia, and N. Samarth. *Phys. Rev. Lett.* **75**, 505 (1995).

- Daneshvar-1997 : A.J. Daneshvar, C.J.B. Ford, M.Y. Simmons, A.V. Khaetskii, A.R. Hamilton, M. Pepper, and D.A. Ritchie. *Phys. Rev. Lett.***79**, 4449, (1997).

- Das Sarma and Pinczuk –1997 : *Perspectives in Quantum Hall effects*. Ed. S. Das Sarma and A. Pinczuk. Wiley (1997).

- Datta-1985 : S. Datta, J.K.Furdyna, R.L. Gunshor. *Superlattices and Microstructures* **1,**327 (1985).

- Deigen –1967 : M.F. Deigen, V.Ya. Zevin,V.M. Maevskii,I.V. Potykevich, and D. Shanina. *Sov.Phys.Solid State* **9**,773 (1967).

- Dietl-1995 : T. Dietl, P. Peyla, W. Grieshaber, and Y. Merle d'Aubigné. *Phys. Rev. Lett.* **74**, 474 (1995).

- Dietl-1997 : T. Dietl, A. Haury, and Y. Merle d'Aubigné. *Phys. Rev. B* **55**, R3347 (1997).

- Dietl-2000 : T. Dietl, H.Ohno, F.Matsukura, J.Cibert, and D.Ferrand. *Science* **287**,1019 (2000).

- Dingle-1978 : R. Dingle, H.L. Störmer, A.C. Gossard, and W. Wiegmann. *Appl.Phys.Lett.* **33**, 655 (1978).

- Dolpogolov-1997 : V. T. Dolgopolov, A. A. Shashkin, A. V. Aristov, D. Schmerek, W. Hansen, J. P. Kotthaus, and M. Holland. *Phys.Rev.Lett*.**79**, 729 (1997).

- Einsenstein – 1990 : J.P. Einsenstein and H.L.Stormer, *Science* **248**, 1461 (1990).

- Eom –2000 : J.Eom, H.Cho,W.Kang,K.L.Campman, A.C.Gossard, M.Bichler, and W. Wegcheider. *Nature* **289**, 2320 (2000).

- Eytan-1998 : G. Eytan, Y. Yayon, M. Rappaport, H. Shtrikman, and I. Bar-Joseph. *Phys. Rev. Lett.* **81**, 1666 (1998).

- F'alko-1993 : V. F'alko. *Phys.Rev.Lett*. **71**, 141 (1993).

- Ferrand –2000 : D. Ferrand, C. Bourgognon, J. Cibert, A. Wasiela, S. Tatarenko, Y. Merle d'Aubigné, A. Bonnani, D. Stifter, H. Sitter, Le Van Khoi, S. Kolesnik, J. Jaroszynski, M. Sawicki, T. Andrearczyk, and T. Dietl. *Physica B* **284-288**, 1177 (2000).

- Ferrand-2001 : D. Ferrand, J. Cibert, A. Wasiela, C. Bourgognon, S. Tatarenko, and G. Fishman, T. Andrearczyk, J. Jaroszynski, S. Kolesnik, T. Dietl, B. Barbara, and D. Dufeu. *Phys. Rev. B* **63** 085201 (2001).

- Fiederling-1999 : R. Fiederling, M. Keim, G. Reuscher, W. Ossau, G. Schmidt, A. Waag, and L.W. Molenkamp. *Nature* **402**, 787 (1999).

- Fleury-1968 : P.A. Fleury and R. Loudon. *Phys. Rev*. **166**, 514 (1968).

- Fowler – 1966 : A.B. Fowler, F.F. Fang, W.E. Howard, and P.J. Stiles. *Phys. Rev. Lett.* **16**, 901 (1966).

- Furdyna – 1988a : *Semiconductors and Semimetals* (Academic Press, London), Vol. 25 Ed. J.K. Furdyna and J. Kossut (1988).

- Furdyna-1988b : J.K. Furdyna. *J. Appl. Phys.* **64** R29 (1988).

- Furdyna-2000 : J.K. Furdyna, P. Schiffer, Y. Sasaki, S.J. Potashnik, and X.Y. Liu. *Proceed. Nato Advanced Research Workshop. Nato ASI series.3.High Technology*, **81**, 211 (2000).

- Gaj – 1978 : J.A. Gaj, P. Byszewski, M.Z. Cieplak, G. Fishman, R.R. Galazka, J. Ginter, M. Nawrocki, N. Guyen The Khoi, R. Planel, R. Ranvaud, and A. Twardowski. *Phys. Stat. Sol*. (b) **89**, 655 (1978).

- Gaj-1979 : J. Gaj, R. Planel and G. Fishman. *Solid State Comm*. **29**, 435 (1979).

- Galazka –1980 : R.R. Galazka,S. Nagata, and P.H. Keesom. *Phys.Rev.B* **22**, 3344 (1980).

- Gerschütz –1996 : J. Gerschütz, S. Scholl, and G.Landwehr. *12th Proceed.of Int. Conf. High Magn. Field in Sem. Phys. World Scientific.* Ed. G.Landwehr and W.Ossau. **1** , 399 (1996).

- Geschwind-1984 : S. Geschwind and R. Romestain. Cap.3 . *Light Scattering in solids IV*. Topics in Physics. Ed. M.Cardona and G. Güntherodt. Springer-Verlag (1984).

- Gravier-1998 : L. Gravier, M. Potemski, P. Hawrylak, and B. Etiene. *Phys. Rev. Lett*. **80**, 3125 (1998).

- Godlewski-1996 : M. Godlewski, A. Wittlin, R.R. Galazka, B. Monemar, T. Gregorkiewicz, C.A.J. Ammerlaan, P.H.M. van Loosdrecht, and J.A.A.J. Perenbomm. *Proceed. of 23th Int. Conf. Phys. Sem.*. World Scientific. Ed. M. Scheffler and R. Zimmermann. **1**, 393 (1996).

- Goldberg-1989 : B. B. Goldberg, D. Heiman, and A. Pinczuk. *Phys. Rev. Lett*. **63**, 1102 (1989).

- Guéron-1959 : M.Guéron and Ch.Ryter. *Phys. Rev. Lett.* **3**,338 (1959).

- Haury – 1997 : A. Haury, A. Wasiela, A. Arnoult, J. Cibert, S. Tatarenko, T. Dietl, and Y. Merle d'Aubigné. *Phys. Rev. Lett*. **79**, 511 (1997).

- Haury-1997b : Ph.D. Thesis Université Joseph Fourier, Grenoble 1,1997.

- Hawrylak –1991 : P. Hawrylak. *Phys. Rev. B* **44** , 3821 (1991).

- Hawrylak –1992 : P. Hawrylak, N. Pulsford, and K. Ploog. *Phys. Rev. B* **46** , 15193 (1992).

- Hawrylak –1997 : P. Hawrylak and M. Potemski. *Phys. Rev. B* **56**, 12386 (1997).

- Huard-2000a : V. Huard, R.T. Cox, K. Saminadayar, C. Bourgognon, A. Arnoult, J. Cibert, S. Tatarenko and M. Potemski. *Phys. Stat.Sol.* (*a*) **178**,95 (2000).

- Huard-2000b : V. Huard, R.T. Cox, K. Saminadayar, C. Bourgognon, A. Arnoult, J. Cibert, and S. Tatarenko. *Physica E* **6**,161 (2000).

- Huard-2001 : V. Huard, R.T. Cox, K. Saminadayar, A. Arnoult, and S. Tatarenko. *Phys. Rev. Lett* **84**, 187 (2001).

- Imanaka-2001 : Y. Imanaka, T. Takamasu, G. Kido, G. Karczewski, T. Wojtowicz, and J. Kossut. *Physica E* **10**, 336 (2001).

- Jaczynski –1978: M. Jaczynski, J. Furdyna, and R.R. Galazka. *Phys. Stat. Sol.(b)* **88**, 73 (1978).

- Janak –1969 : J.F. Janak. *Phys. Rev.* 178, 1416 (1969).

- Jarosik -1985 : N. C. Jarosik, B. D. McCombe, B. V. Shanabrook, J. Comas , John Ralston, and G. Wicks. *Phys. Rev. Lett.* **54**, 1283 (1985).

- Jaroszynski –1998: J. Jaroszynski, G.Karczewski, J.Wrobel, T.Andrearczyk, A. Srtycharczuk, T.Wojtowicz, J.Kossut, and T.Dietl. *Proceed.of 24th Int. Conf. Phys. Sem.*, World Scientific, Singapore (1999).

- Jeukens-2001: C.R.L.P.N. Jeukens, P.C.M. Christianen, J.C.Maan, D.R. Yakovlev, W. Ossau, T. Wojtowicz, G. Karczewski, and J. Kossut. *Proceed. of 25th Int. Conf. Phys. Sem.* Springer-Verlag Ed. N. Miura and T. Ando. **2**, 979 (2001).

- Jungwirth –1998 : T. Jungwirth,S. P. Shukla, L. Smrcka, M. Shayegan, and A. H. MacDonald. *Phys. Rev. Lett.* **81**, 2328 (1998).

- Kallin-1984 : C. Kallin and B.I. Halperin. *Phys. Rev. B* **30**,5655 (1984).

- Karczewski –1998 : G.Karczewski, J.Jaronszynski,M.Kutrowski, A.Barcz, T.Wojtowicz, and J.Kossut. *Acta Phys. Pol. A* **92**, 829 (1997). *J. Cryst. Growth* **184/185**, 814 (1998).

- Karczewski-2001 : G. Karczewski and Y. Wang. *Physica B* **298**, 402 (2001).

- Katayama – 1989 : S. Katayama and T. Ando. *Solid State Comm*.**70**, 97 (1989).

- Kleiman-1986 : D.A. Kleiman. *Phys. Rev. B* **33**,2540 (1986).

- Knight-1949 : W.D.Knight. *Phys.Rev* **76**, 1259 (1949).

- Kittel-1996 : C. Kittel. *Introduction to the Solid State Physics*. 7th Edicion. Wiley (1996).

- Kheng-1993 : K. Kheng, R.T. Cox, Merle Y. d' Aubigné, F. Bassani, K. Saminadayar, and S. Tatarenko. *Phys. Rev. Lett*. **71**,1752 (1993).

- Koch-1976: J.F. Koch. *Surf. Sci.* **58**, 104 (1976).

- Koch –1993 : S. Koch, R.J. Haug, K. v. Klitzing, and M. Razeghi. *Phys.Rev.B* **47**, 4048 (1993).

- Kochereshko-2000 : V.P. Kochereshko, G.V. Astakhov, D.R. Yakovlev, W.Ossau, G. Landwehr, T. Wojtowicz, G. Karczewski, and J. Kossut. *Phys. Status Solidi (b)* **221**, 345 (2000).

- Kohn-1961: W.Kohn. *Phys. Rev*. **123**, 1242 (1961).

- König-2000 : J. König, H. Lin, and A.H. MacDonald. *Phys. Rev. Lett.* **84**, 5628 (2000).

- Köning – 2000 : B. König, I. A. Merkulov, D. R. Yakovlev, W. Ossau, S. M. Ryabchenko, M. Kutrowski, T. Wojtowicz, G. Karczewski, and J. Kossut. *Phys. Rev. B* **61**, 16870 (2000).

- Korringa-1950 : J.Korringa. *Physica* **16**, 601 (1950).

- Krzystek-1997 : J. Krzystek, A. Sienkiewicz, L. Pardi, and L.C. Brunel. J.Magn.Reson. **125**, 207 (1997).

- Kuhn-Heinrich –1993 : B. Kuhn-Heinrich, W. Ossau, H. Heinke, F. Fischer, T. Litz, A. Waag, and G. Landwehr. *Appl. Phys. Lett.***63**, 2932 (1993).

- Lambe-1960 : J. Lambe and C. Kikuchi. *Phys. Rev*. **119**, 1256 (1960).

- Lampert-1958 : M.A. Lampert. *Phys. Rev. Lett* **1**, 450 (1958).

- Landau-1930 : L.D.Landau *Z. Physik* **64**,629 (1930).

- Landwehr-2000 : G. Landwehr. *Physica B*, **298**, 384 (2000).

- Larson –1990 : B.E. Larson and H. Ehreich. *J. Appl. Phys.* **67,** 5084 (1990).

- Laughlin-1981 : R. Laughlin. *Phys. Rev. Lett.* **22**,5632 (1981).

- Laughlin-1983 : R. Laughlin. *Phys. Rev. Lett.* **50**,1559 (1983).

- Leadley – 1998 : D. R. Leadley, R. J. Nicholas, and J. J. Harris C. T. Foxon. *Phys. Rev. B* **58**,13036 (1998).

- Lee-1984 : Y.R. Lee and A.K. Ramdas, *Solid State Com*. **51**,861 (1984).

- Lyo-1988 : S. K. Lyo, E. D. Jones, and J. F. Klem . *Phys. Rev. Lett.* **61**, 2265 (1988).

- MacDonald-1986 : A.H. MacDonald and D.S.Ritchie. *Phys. Rev. B*. **33**, 8336 (1986).

- MacDonald –1998 : A.H. MacDonald, R. Rajaraman, and T. Jungwirth . *Phys. Rev. B*. **60**, 8817 (1998).

- Mackh – 1996 : G.Mackh, W.Ossau, A.Waag, and G.Landwehr. *Phys. Rev. B* **54**, 5227, (1996).

- Manfra-1998 : M.Manfra, B.B.Goldberg, L.Pfeiffer, and K.West. *Phys. Rev. B* **57** , R9467 (1998).

- Marple-1963 : D.T.F. Marple. *Phys.Rev* **129**, 2466 (1963).

- Maude-1996 : D. K. Maude, M. Potemski, J. C. Portal, M. Henini, L. Eaves, G. Hill, and M. A. Pate. *Phys. Rev. Lett.* **77**, 4604 (1996).

- Merkulov-1999 : I. A. Merkulov, D. R. Yakovlev, A. Keller, W. Ossau, J. Geurts, A. Waag, G. Landwehr, G. Karczewski, T. Wojtowicz, and J. Kossut. *Phys. Rev. Lett.* **83**, 1431 (1999).

- Nachtwei-1999 : G. Nachtwei. *Physica E*, **4**,79 (1999).

- Nawrocki-1980 : M. Nawrocki, R. Planel, G. Fishman, and R. Galazka. *J.Phys.Soc. Jap.* **49**, 823 (1980).

- Nicholas-1988 : R.J. Nicholas, R.J. Haug, K.v.Klitzing, and G. Weimann. *Phys. Rev. B* **37**, 1294 (1988).

- Nurmiko and Pinczuk-1993 : A. Nurmiko and A. Pinczuk. *Physics Today*, **46**, June 1993.

- Ohno-1992 : H. Ohno, H. Munekata, T. Penney, S. von Molnár, and L. L. Chang. *Phys. Rev. Lett.* **68**, 2664 (1992).

- Ohno-1998 : H. Ohno. *Science* **281**,951 (1998).

- Ohno-1999 : Y. Ohno, D. K. Young, B. Beschoten, F. Matsukura, H. Ohno, and D. D. Awschalom. *Nature* **402**, 790 (1999).

- Osbourn-1987 : G. Osbourn in *Semiconductors and Semimetals.* Ed. R. Dingle, (Academic Press, London), Vol **24**, 459(1987).

- Ossau-2001 : W. Ossau, V. P. Kochereshko, G. V. Astakhov, D. R. Yakovlev, G. Landwehr, T. Wojtowicz, G. Karczewski, and J. Kossut. *Physica B* **298**, 315 (2001).

- Overhauser-1953: A. Overhauser. *Phys. Rev.* **92**, 411 (1953).

- Paget –1977 : D. Paget, G. Lampel, B. Sapoval, and V.I. Safarov. *Phys. Rev. B* **15**, 5780 (1977).

- Peeters – 1992 : F.M. Peeters, X.G. Wu, J.T. Devreese, C.J.G.M. Langerak, J. Singleton, D.J. Barnes, and R.J. Nicholas. *Phys. Rev. B* **45**, 4296 (1992).

- Potemski – 1991a : M. Potemski, L. Viña, G. E. W. Bauer, J. C. Maan, K. Ploog, and G. Weimann. *Phys.Rev.B* **43**, 14707 (1991).

- Potemski-1991b : M. Potemski, R. Stepniewski, J. C. Maan, G. Martinez, P. Wyder, and B. Etienne. *Phys. Rev. Lett*. **66**,2239 (1991).

- Prange-1990 : R.E. Prange and S.M.Girvin,1990, Eds. *The Quantum Hall Effect*,2nd Ed. (Springer,New York).

- Prechtl-2000 : G. Prechtl, W. Heiss, A. Bonanni, W. Jantsch, S. Mackowski, E. Janik, and G. Karczewski. *Phys. Rev. B* **61**, 15617 (2000).

- Ramdas-1988 : A.K. Ramdas, and S. Rodriguez in Cap.9. *Semiconductors and Semimetals* (Academic Press, London), Vol. **25** Ed. J.K. Furdyna and J. Kossut (1988).

- Rashba-2000 : E. I. Rashba and M. D. Sturge. *Phys. Rev. B* **63**, 045305 (2000).

- Rigal-1999 : L. B. Rigal, D. K. Maude, M. Potemski, J. C. Portal, L. Eaves, Z. R. Wasilewski, G. Hill, and M. A. Pate. *Phys. Rev. Lett.* **82**, 1249 (1999).

- Sadowski –1999 : M.L. Sadowski, F.J. Teran, M. Potemski, G. Karczewski, M. Kutrowski, J. Jaroszynski, and T. Wojtowicz. *Proceed.of 24th Int. Conf. Phys. Sem.*, World Scientific, Singapore (1999).

- Sanvitto-2000 : D. Sanvitto, R. A. Hogg, A. J. Shields, D. M. Whittaker, M. Y. Simmons, D. A. Ritchie, and M. Pepper. *Phys.Rev B* **62**, R13294 (2000).

- Sanvitto-2001 : D. Sanvitto, F. Pulizzi, A.J. Shields, P.C. M. Christianen, S.N. Holmes, M.Y. Simmons, D. A. Ritchie, J.C. Maan, and M. Pepper. *Science* **294**, 837 (2001).

- Sapega-2000 : V.P.Sapega, T.Ruf, and M.Cardona. *Solid Stat. Commun.* **114**, 573 (2000).

- Segall-1967 : B. Segall and D.T.F. Marple in *Physics and Chemistry of II-VI Compounds*. Ed. M. Aven and J.S. Prener. p. 317 Wiley, New York. (1967).

- Shapira-1990 : Y. Shapira. *J. Appl. Phys*. **67**, 5090 (1990).

- Scherbakov –1999 : A. V. Scherbakov, A. V. Akimov, D. R. Yakovlev, W. Ossau, A. Waag, G. Landwehr, T. Wojtowicz, G. Karczewski, and J. Kossut. *Phys. Rev. B*, **60**, 5609 (1999).

- Scherbakov –2000 : A. V. Scherbakov, A. V. Akimov, D. R. Yakovlev, W. Ossau, G. Landwehr, T. Wojtowicz, G. Karczewski, and J. Kossut. *Phys. Rev. B* **62,** R10641 (2000).

- Schmeller –1995 : A. Schmeller, J.P. Eisenstein, L.N. Pfeiffer, and K.W. West. *Phys. Rev. Lett*. **75**, 4290 (1995).

- Shields –1995 : A.J. Shields , M. Pepper, D.A. Ritchie, M.Y. Simmons, and G.A.C. Jones. *Phys. Rev. B* **51**,18049 (1995).

- Shubnikov-1930 : L. Shubnikov and W.J. de Haas. *Leiden Comm.* 207a, 207c, 207d, 210a (1930).

- Skolnick –1987 : M. S. Skolnick, J. M. Rorison, K. J. Nash, D. J. Mowbray, P. R. Tapster, S. J. Bass, and A. D. Pitt. *Phys. Rev. Lett*. **58**, 2130 (1987).

- Sirenko-1997 : A.A. Sirenko, T. Ruf, M. Cardona, D.R. Yakolev, W. Ossau, A. Waag, and G. Landwehr. *Phys. Rev B* **56**,2114 (1997).

-Sondhli-1993 : S. L. Sondhi, A. Karlhede, S. A. Kivelson, and E. H. Rezayi. *Phys. Rev B* **47**, 16419 (1993).

- Störmer-1979 : H.L. Störmer, R. Dingle, A.C. Gossard, and W. Wiegmann. *Solid State Com.* **29**, 705 (1979).

- Story-1986 : T. Story and R.R. Galazka, R.B. Frankel, and P.A. Wolff. *Phys. Rev. Lett.* **56**,777 (1986).

- Story – 1996 : T. Story, C.H.W. Swüste, P.J.T. Eggenkamp, H.J.M. Swagten, and W.J.M de Jonge. *Phys. Rev. Lett.* **77**,2802 (1996).

- Slusher-1967 : R. E. Slusher, C. K. N. Patel, and P. A. Fleury. *Phys. Rev. Lett.* **18**, 77 (1967).

- Stühler-1996 : J. Stühller, M. Dahl, G. Schaak, A. Waag, G. Landwehr, K.V. Kavokin, and I.A. Merkulov. *12Th Proceed.of Int. Conf. High Magn. Field in Sem. Phys*. World Scientific. Ed. G.Landwehr and W.Ossau. **1** , 449 (1996).

- Svoboda –1992 : P. Svoboda, P. Streda, G. Nachtwei, A. Jaeger, M. Cukr, and M. Láznicka. *Phys. Rev. B* **45**, 8763 (1992).

- Teran-1998 : F.J. Teran, M.L. Sadowski, M. Potemski, G. Karczewski, S. Mackowski, and J. Jaroszynski. *Physica B* **256-258,** 577 (1998).

- Teran – 2001: F.J.Teran, M.Potemski, P.Kossacki, P.Hawrylak, and G.Karczewski. *Proceed. of 25th Int. Conf. Phys. Sem.* Springer-Verlag Ed. N. Miura and T. Ando. **1**, 723 (2001).

- Thilagam-1997 : A. Thilagam. *Phys. Rev. B* **55**, 7804 (1997).

- Tsui-82 : D.C. Tsui, H.L. Stormer, and A.C. Gossard. *Phys. Rev. Lett.* **48**, 1559 (1982).

-Uenoyama – 1989 : T. Uenoyama and L. J. Sham. *Phys.Rev. B* **39**, 11044 (1989).

- Usher-1990 : A.Usher, R.J. Nicholas, J.J. Harris, and C.T. Foxon. *Phys. Rev. B* **41**, 1129 (1990).

- Van der Burgt –1995 : M. van der Burgt, V. C. Karavolas, F. M. Peeters, J. Singleton, R. J. Nicholas, F. Herlach, J. J. Harris,M. Van Hove, and G. Borghs. *Phys. Rev. B* **52**, 12218 (1995).

- Vincente-1995: P. Vincente, A. Raymond, M.K. Saadi, B. Couzinet, M. Kubisa, W. Zawadzki, and B. Etienne. *Solid State Comm.*, **96**, 901 (1995).

- Von Klitzing-80 : K. Von Klizting, G.Dorda, and M.Pepper. *Phys. Rev. Lett.* **45**, 494 (1980).

- Weisbuch : C.Weisbuch. in *Semiconductors and Semimetals*. Ed. R. Dingle, (Academic Press, London), Vol. **24**, (1987).

- Willardson-1966 : *Semiconductors and Semimetals* (Academic Press, London), Vol. **2** Ed. R.K.Willardson and A.C.Beer (1988).

- Wojtowicz-1998 : T.Wojtowicz, M. Kutrowski, G. Karczewski, and J. Kossut. *Appl. Phys. Lett.* **73**, 1379 (1998).

- Wojtowizc-2000 : T. Wojtowicz, M. Kutrowski, G. Karczewski, J. Kossut, B. König, A. Keller, D.R. Yakovlev, A. Waag, J. Geurts, W. Ossau, G. Landwehr, I.A. Merkulov, F.J.Teran, and M. Potemski. *J. Cryst. .Growth* **214-215** 378 (2000).

- Wolf-1966 : P.A.Wolf. *Phys. Rev. Lett*. **16**, 225 (1966).

- Wolf-1984 : P.A. Wolf and J.Warnock. *J. Appl. Phys*. **55** 2300 (1984).

- Wolff-1988 : P.A. Wolff in *Semiconductors and Semimetals* (Academic Press, London), Vol. **25** Ed. J.K. Furdyna and J. Kossut (1988).

-Yang-2000 : G. Yang, J.K. Furdyna, and H. Luo. *Phys.Rev. B* **62** 4226 (2000).

- Yakovlev-1997 : R. Yakovlev, V. P. Kochereshko, R. A. Suris, H. Schenk, W. Ossau, A. Waag, G. Landwehr, P. C. M. Christianen, and J. C. Maan. *Phys.Rev.Lett.* **79**,3974 (1997).

-Yeo-2001 : T.Yeo, H.A.Nickel, G.Comanescu, H.D.Cheong, M.Furis, A.Petrou, B.D. McCombe. *Proceed.of 25th Int. Conf. Phys. Sem.* Springer-Verlag Ed. Miura and Ando. Vol.II, 519 (2001).

- Yoon-1992 : H.W. Yoon, M.D. Sturge, and L.N. Pfeiffer. *Solid State Comm.* **104**, 287 (1992).

- Yu-Cardona : P.Y.Yu and M.Cardona. *Fundamentals of Semiconductors*. Springer (1996).

Publications

Books

"Propiedades de transporte de un gas de electrones bidimensional confinado en semiconductores semimagnéticos diluidos"
F.J.Teran. *Colección Becas de Investigación. Ed.Obra Social de Caja Segovia.* Vol.**16** (2001).

Scientific articles

1. *"Quantum Hall states under conditions of vanishing Zeeman energy*"
   F.J.Teran, M.Potemski, D.K.Maude, T.Andrearczyk, J.Jaroszynski, and G.Karczewski.
   Submitted to Physical Review B

2. *"Pauli paramagnetism and Landau level crossing in a modulation doped CdMnTe/CdMgTe quantum well*"
   F.J.Teran, M.Potemski, D.K.Maude, T.Andrearczyk, J.Jaroszynski, and G.Karczewski.
   Submitted to Physical Review B

3. *"Scaling of the quantum Hall effect in highly spin polarised electron gas"*
   T. Andrearczyk, J. Jaroszynski, G. Karczewski, J.Wrobel, T.Wojtowicz, T.Dietl, E.Papis, E.Kaminska, A.Piotrowska, D.K. Maude**, F.J.Teran**, and M. Potemski.
   Submitted to Physical Review B

4. *"Effective spin diffusion across hugely lattice mismatched heterointerfaces"*
   M.Ghali, J.Kossut, E.Janik, K.Reginski, L.Klopotowski, S.Mackowski, G.Cywinski, P.Dluzewski, M.Potemski, and **F.J.Teran**.
   To be published in Physica E.

5. *"Trions as a probe of spin injection through II-VI magnetic/non magnetic interface".*
   M.Ghali, J.Kossut, E.Janik, M.Kutrowski, L.Klopotowski, M.Potemski, and **F.J.Teran**.
   To be published in Thin Solid Films.

6. *"Resistively detected EPR of Mn^{2+} ions coupled to a 2DEG in quantum Hall regime*"
   F.J.Teran, M.Potemski, D.K.Maude, A.K.Hassan, T.Andrearczyk, J.Jaroszynski, Z.Wilamowski, T.Wojtowicz, and G.Karczewski.
   To be published in Physica E.

7. *"Band-Gap renomalization and photoluminescence from an interacting 2DEG in a magnetic field*"
   P.Hawrylak**, F.J.Teran**, M.Potemski, and G.Karczewski.
   To be published in Physica E.

8. *"Effects of the nonlinear spin-splitting on the quantum transport of a 2DEG confined in CdMnTe/CdMgTe MDQWs"*
   F.J.Teran, M.Potemski, D.K.Maude, T.Andrearczyk, J.Jaroszynski, and G.Karczewski.
   Proceed.of the 25th International Conference on the Physics of Semiconductors. Word Scientific Publications. Ed. N. Miura and T. Ando. (Springer-Verlag, Heidelberg,2001). **2**, 943 (2000).

9. *"Polarization of magnetopolaritons in a semiconductor microcavity"*
   M.D. Martin, S. Burgas, M. Alonso, L. Viña, **F.J. Teran**, M. Potemski, and E.E.Mendez.
   Proceed.of the 25th International Conference on the Physics of Semiconductors. Word Scientific Publications. Ed. N. Miura and T. Ando. (Springer-Verlag, Heidelberg,2001).**1**, 671 (2001).

10. *"Magnetooptical evidence of many-body effects in spin-polarized 2D electron gas"*
    C.Testelin, A.Lemaître, C.Rigaux, T.Wojtowicz, G.Karczewski, **F.Teran**, and M.Potemski.
    Proceed.of the 25th International Conference on the Physics of Semiconductors. Word Scientific Publications. Ed. N. Miura and T. Ando. (Springer-Verlag, Heidelberg,2001). **1**, 551 (2001).

11. *"Magneto-optical transitions involving 2DEG confined in Cd(Mn)Te/CdMgTe quantum wells"*
    F.J.Teran, M.Potemski, P.Kossacki, P.Hawrylak, and G.Karczewski.

Proceed.of the 25th International Conference on the Physics of Semiconductors. Word Scientific Publications. Ed. N.Miura and T.Ando. (Springer-Verlag, Heidelberg,2001). **1**, 723 (2001).

12. *"Two-dimensional electron gas coupled to Mn2+ ions: a magneto-optical study of CdMnTe/CdMgTe MDQWs"*
F.J.Teran, M.L.Sadowski, D.K.Maude and M.Potemski, G.Karczewski, S.Mackowski, and J. Jaroszynski.
Physica E **6** 775 (2000).

13. "II-VI quatum structres with tunable electron g-factor"
T.Wojtowicz, M.Kutrowski, G.Karczewski, J.Kossut, B.König, A.Keller, D.R.Yakolev, A.Waag,J. Geurts, W. Ossau, G. Landwehr, I.A. Merlukov, **F.J.Teran**, and M.Potemski. *J.Cryst.Growth **214-215** (2000) 378.*

14. "Cyclotron resonance and photoluminescence of CdMnTe/CdMgTe modulation doped quantum wells"
M.L.Sadowski, **F.J.Teran**, M.Potemski, G.Karczewski, M.Kutrowski, J.Jaroszynski, and T.Wojtowicz.
Proceed.of the 24th International Conference on the Physics of Semiconductors. (Word Scientific Publications,1999).

15. *"Magnetooptical properties of graded quantum well structures made of diluted magnetic semiconductors"*
M.Kutrowski, T.Wojtowicz, G.Karczewski, J.Kossut, D.R.Yakolev, V.P.Kochereshko,W.Ossau, A.Waag, **F.J.Teran**, and M.Potemski.
Nato Advanced Research Workshop 1999. Nato ASI series.3.High Technology,Vol.**81** (1999).

16. "*g-factor dependence of the evolution of magneto-optical spectra with density of the quasi-two dimensional electrons in CdMnTe/CdMgTe heterostructures"*
T.Wojtowicz, M.Kutrowski, G.Karczewski, J.Kossut, **F.J.Teran**, and M.Potemski.
Physical Review B **59**, R10437 (1999).

17. "*Magneto-optics of a two dimensional electron gas confined in CdMnTe quantum wells"*
F.J.Teran, M.L.Sadowski, M.Potemski, G.Karczewski, S.Mackowski, and J.Jaroszynski. *Physica B* **256-258**, 577 (1998).

Résumé

Phénomènes dépendants du spin dans des structures à un puits quantique CdMnTe à modulation de dopage de type-n

L'étude des propriétés électroniques et magnétiques des structures à un puits quantique CdMnTe à modulation de dopage de type-n nous a permis d'explorer l'interaction d 'échange sp-d entre les électrons 2D délocalisés et les moments magnétiques localisés des ions Mn^{2+}. Cette interaction d'échange sépare les états de spin électronique induisant un splitting Zeeman géant lequel modifie profondément les propriétés électroniques et optiques du semi-conducteur. A faible champ magnétique, l'interaction sp-d peut être décrite par une approximation de champ moyen. Néanmoins, à fort champ magnétique nous observons qu'une énergie effective Zeeman nulle n'entraîne pas la disparition complète du gap de spin. En effet, des expériences de transport et de spectroscopie Raman montrent une répulsion entre les niveaux de spin up et down. Nos résultats peuvent être expliqués dans le cadre d'un modèle basé sur l'anti-croisement des niveaux de Landau résolus en spin. Les propriétés magnétiques du sous-système d'ions Mn^{2+} sont fortement influencées par la présence des porteurs. Le 'Knight shift' observé pour la position du spectre RPE peut être décrit par l'approximation de champ moyen pour de faibles champs. Cependant, cette approximation ne permet pas de décrire la valeur importante du 'Knight shift' à fort champ au voisinage de $E^{Mn}{}_Z=E^e{}_Z$. Pour interpréter nos résultats expérimentaux de spectroscopie Raman et de RPE nous proposons un modèle basé sur l'interaction résonante entre les excitations de spin pour les électrons et pour les ions Mn^{2+}. Finalement, une étude de l'évolution de la réponse optique des puits quantiques CdMnTe en fonction de la concentration d'électrons montre une persistance des effets excitoniques lorsque l'énergie de Fermi est comparable à l'énergie de liaison excitonique. Suite à nos recherches, l'homogénéité de nos systèmes est remise en cause.

Mots-clés : semiconducteurs, spin, ion Mn^{2+} localisé, électron délocalisé, interaction d'échange sp-d, propriétés optiques, effet Hall quantique, excitons.

Abstract

Spin dependent phenomena in n-type modulation doped CdMnTe quantum well structures

The study of the electronic and magnetic properties of n-type modulation doped CdMnTe quantum well structures has allowed to investigate the *sp-d* exchange interaction between 2D electrons and localized magnetic moments of Mn^{2+} ions. Such exchange interaction realigns the electronic spin states leading to a *giant Zeeman splitting* which deeply modifies the optical and electronic properties of the semiconductor host. At low magnetic fields, the *sp-d* exchange interaction term can be successfully described by the mean-field approach. However, in the high magnetic field region, we observe that a zero effective Zeeman energy ($E_Z=0$) does not necessarily imply a closing of the spin gap. Raman scattering and transport experiments indicate a repulsion between spin up and spin down Landau levels. A model based on an anticrossing of the spin split Landau levels permits an almost complete understanding of our data. The magnetic properties of the Mn^{2+} ion subsystem show an influence of the carrier presence. The *Knight shift* of the position of the EPR spectrum can be described by the mean field approach in the low magnetic field region. However, the mean field approach does not account for the large shift of the Mn^{2+} spin resonance observed at high magnetic fields in the vicinity of $E^{Mn}{}_Z=E^e{}_Z$. A model based on a resonant interaction between the mean-field spin excitations for electrons and Mn^{2+} ions has been proposed in order to interpret the Raman and EPR experimental data. Finally, a study of the evolution of the optical response as a function of carrier density in modulation doped II-VI quantum well structures reveals a persistence of excitonic transitions for electron densities for which Fermi energy is comparable to the exciton binding energy. Our investigation leads to address the question whether such observations are characteristic of homogenous system or they involve a phase separation.

Key-words: semiconductor, spin, localized Mn^{2+} ion, delocalized electron, sp-d exchange interaction, optical properties, quantum Hall effect, excitons.